Norwegian University of Life Sciences
Faculty of Science and Technology

Philosophiae Doctor (PhD)
Thesis 2018:40

Multiscale modeling of the early visual pathway

Multiskalamodellering av den tidlige synsbane

Thomas Heiberg

Multiscale modeling of the early visual pathway

Multiskalamodellering av den tidlige synsbane

Philosophiae Doctor (PhD) Thesis

Thomas Heiberg

Norwegian University of Life Sciences
Faculty of Science and Technology

Ås (2018)

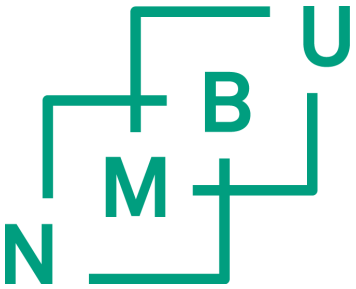

Thesis number 2018:40
ISSN 1894-6402
ISBN 978-82-575-1512-6

Acknowledgements

This thesis represents work carried out at the Norwegian University of Life Sciences from August 2010 to April 2018 funded by a three year university PhD grant and the Research Council of Norway (eNeuro, NOTUR). The work was accomplished under the supervision of Associate Professor Hans Ekkehard Plesser and Professor Gaute T. Einevoll.

During my masters (siv.ing) at NTNU, I took a psychology class that triggered my interest in the brain. While the models presented were interesting enough, there seemed to be little or no relation between them and what neurons do. To learn more, I took several other psychology classes and started reading neuroscience literature on the side. Then, as fate would have it, I got in touch with Keith Downing who at the time headed the research group now called "Data and Artificial Intelligence" (DART) at NTNU who recommended me to contact Gaute Einevoll and the computational neuroscience group here at NMBU. They soon after had an open position as a PhD student that I was offered.

First of all, I would like to thank my supervisors Hans Ekkehard Plesser and Gaute T. Einevoll for seeing this through to the end. A special thanks goes to the co-authors on my papers, who in addition to my supervisors were Birgit Kriener, Tom Tetzlaff, Espen Hagen, Geir Halnes, and Alex Casti. I would also like to thank all my colleagues at NMBU during my period there, including Espen Hagen, Birgit Kriener, Torbjørn Ness, Geir Halnes, Klas Pettersen, Tom Tetzlaff, Håkon Enger, Eivind Nordheim, Henrik Lindén, Szymon Łęski, Maria Stavrinou, and Amir Khosrowshahi for insightful discussions and an enjoyable workplace. Finally, I would like to thank my family and friends, respectively, for getting me interested in science and reminding me every once in a while that I was still not finished.

Ås, April 2018
Thomas Heiberg

Abstract

The human brain contains billions of neurons connected through synapses, making it a highly complex system that researchers have been trying to understand for centuries. One way of increasing our understanding of the brain is through modeling. Different modeling techniques and tools support modeling at different levels of scale, from biophysically detailed models of specific properties in single neurons to large-scale population models where the rate of action-potential firing is modeled.

Vision is by far the most important sense for humans and a large fraction of the brain's capacity is engaged in visual perception. The retina, the lateral geniculate nucleus (LGN) and the primary visual cortex comprise the first few steps in visual processing and are collectively known as the *early visual pathway*. The thalamus, of which the LGN is a part, has been said to represent "the final bottleneck of information flow before it gets into cortex". It has mostly been thought of as a relay station for sensory signals on the way to cortex, but with its central position in the brain right on top of the brainstem, it seems to be a natural location to perform filtering and modulation of the sensory signals based on attention and other behavioral requirements.

A central theme of this thesis is to extend our understanding of the signal processing in the early visual pathway through modeling and to bridge the gap between biology and models at different levels of scale. Three main topics are addressed: First, we investigate how spiking point-neuron models relate to firing-rate models at the retinogeniculate synapse. With two spiking neuron models as the starting point of our analysis, we study how well firing-rate models capture the essential response properties of LGN relay cells. Second, we apply the same approach to more complex neuron models that can be parameterized to exhibit a wide range of different spiking patterns and thereby can be configured to represent many different neuron types in the early visual system and elsewhere in the brain. Finally, we explore the effects of different inhibitory actions from local interneurons on the relay cells in a biophysically detailed network model of the LGN circuit. Large-scale parameter scans are central to all three projects. They are managed efficiently by support tools developed as part of this work.

Although the models and findings presented here may have taken our understanding a small step forward, the early visual pathway and the brain in general is still far from understood. Hence, we hope that these results will prove useful as starting points for future investigations.

Sammendrag

Menneskehjernen består av flere milliarder nevroner som er koblet sammen via synapser. Resultatet er et komplekst system som forskere har forsøkt å forstå i en årrekke. En fremgangsmåte for å øke forståelsen av hjernen, er å benytte seg av modellering. Forskjellige modelleringsteknikker og -verktøy støtter modellering på forskjellige nivåer, fra detaljerte biofysiske modeller av enkeltnevroner i den ene enden av skalaen til fyringsratemodeller for populasjoner av nevroner i den andre.

Synet er uten tvil den viktigste av menneskets sanser og en stor del av hjernen benyttes til å behandle synsinntrykk. Netthinnen bakerst i øyet, LGN ("lateral geniculate nucleus") og det primære synssenteret i hjernebarken utgjør de første stegene i synsprosesseringen og omtales gjerne som *den tidlige synsbane*. Thalamus, som LGN er en del av, har blitt omtalt som "den siste flaskehalsen i informasjonsflyten inn til hjernebarken". Den har stort sett blitt ansett som kun en reléstasjon for signaler på vei til hjernebarken, men med sin sentrale plassering på toppen av hjernestammen, fremstår dette som et naturlig sted for filtrerering og modulering av signaler fra sansene.

Hovedmålet med denne avhandlingen er å øke vår forståelse av prosesseringen som foregår i den tidlige synsbane gjennom modellering og å bygge bro mellom biologien og modeller på forskjellige detaljeringsnivåer. Vi tar for oss tre temaer: Først undersøker vi i hvilken grad punktnevnronmodeller av reléceller i LGN kan forenkles til fyringsratemodeller. Vi tar utgangspunkt i to eksisterende punktnevnronmodeller som vi tilpasser forenklede fyringsratemodeller til og sammenligner simuleringsresultater fra de to modelltypene. Videre benytter vi samme fremgangsmåte for å analysere mer komplekse nevronmodeller som kan tilpasses mange forskjellige adferdsmønstre. Til slutt bygger vi en biofysisk detaljert nettverksmodell av LGN-kretsen for å undersøke hvordan forskjellige typer inhibisjon fra lokale internevroner påvirker relécellene. Nødvendige støtteverktøy utvikles underveis for å understøtte storskala parametersøk som står sentralt i alle tre prosjektene.

Modellene og funnene som presenteres her bidrar forhåpentligvis til å ta vår forståelse av hjernen et lite steg videre. Samtidig gjenstår det fortsatt mye før den tidlige synsbane og hjernen generelt er fullt ut forstått. Vi håper derfor at disse resultatene også kan danne et godt utgangspunkt for fremtidige undersøkelser.

Contents

Acknowledgements iii

Abstract v

Sammendrag vii

List of Papers xi

List of Figures xiii

1 Introduction 1

2 Multiscale modeling 5
2.1 Level 1: Biophysically detailed models . . . 5
2.2 Level 2: Spiking point-neuron models . . . 6
2.3 Level 3: Firing-rate models . . . 7

3 Early visual system 9
3.1 Biological background . . . 9
3.2 Receptive-field modeling . . . 12
3.3 Mechanistic modeling . . . 16

4 Methods 19
4.1 Simulation . . . 19
4.2 Large-scale parameter scans . . . 19

5 Summary of papers 27
5.1 Summary of Paper I . . . 27
5.2 Summary of Paper II . . . 29
5.3 Summary of Paper III . . . 29

6 Perspectives 33

Bibliography 35

Attached papers 43
Paper I . . . 45
Paper II . . . 75
Paper III . . . 107

List of Papers

I **Heiberg T**, Kriener B, Tetzlaff T, Casti A, Einevoll GT, Plesser HE (2013) Firing-rate models capture essential response dynamics of LGN relay cells. Journal of Computational Neuroscience 35(3):359–375, doi: 10.1007/s10827-013-0456-6

II **Heiberg T**, Kriener B, Tetzlaff T, Einevoll GT, Plesser HE, Firing-rate models for neurons with a broad repertoire of spiking behaviors. Submitted to Journal of Computational Neuroscience, under revision

III **Heiberg T**, Hagen E, Halnes G, Einevoll GT (2016) Biophysical Network Modelling of the dLGN Circuit: Different Effects of Triadic and Axonal Inhibition on Visual Responses of Relay Cells. PLoS Comput Biol 12(5):e1004929, doi: 10.1371/journal.pcbi.1004929

List of Figures

1.1 Mapping of primate visual areas 2

2.1 Consecutive simplification of neuron structure. 6

3.1 Overview of the mammalian early visual system 10
3.2 Center-surround receptive fields 11
3.3 Spatial receptive fields in the early visual pathway 14
3.4 Spatiotemporal receptive field profiles (x-t plots) 15

4.1 Parameter spaces 22
4.2 Basic workflow steps 25
4.3 PyScan components overview 25

5.1 Firing-rate modeling setup sketch 28

1 Introduction

The human brain consists of billions of neurons connected in a complex network. While the human brain essentially has been the same for thousands of years, insight into its inner workings is fairly recent. The invention of the microscope and staining techniques in the late 1800s sparked the foundation of neuroscience as a scientific field. Since then, new tools and techniques have contributed to an enormous growth in our knowledge about the brain and its components. More recently, optogenetics have enabled the study of increasingly smaller neurons and parts of neurons. Experimenters can not only observe, but also manipulate neurons and neural circuits by activating and disabling components down to individual synapses in real time (Deisseroth et al, 2006; Packer et al, 2012). Helping to clarify our understanding of retinal structure and function, adaptive optics allows direct visualization of individual rod and cone photoreceptors in the human eye (Godara et al, 2010; Miller et al, 1996). At the other end of the scale, the resolution of non-invasive imaging techniques keeps increasing. The Human Connectome Project aims to map the anatomical and functional connectivity between brain areas (Sporns et al, 2005; Van Essen et al, 2013). The Allen Institute for Brain Sciences builds multiple *brain atlases* to better understand gene expression and connectivity in the brain (e.g. Lein et al, 2006; Hawrylycz et al, 2012; Oh et al, 2014) These advances in unraveling the structure of the brain together with system level experiments yield unprecedented insight into the emergence of function and behavior. Pivotal in building a mechanistic understanding of brain functioning is complementary theoretical analysis and modeling, especially detailed computer simulations made possible by the rapid increase in computational power.

Of the five senses, vision is by far the most important to humans (Palmer, 1999). Using cortical area as measure of relative importance, the visual cortex (including visual association areas) occupies 55% of the neocortex in macaque monkeys, whose visual system in many ways rivals that of humans (Felleman and Van Essen, 1991). Visual perception starts when the lens in the eye focuses an image onto the retina where photoreceptors detects the photons. From the retina, the main visual pathway to the cortex is via *retinal ganglion cells* that project through the optic nerve to *relay cells* (or thalamocortical cells) in the *lateral geniculate nucleus* (LGN), which in turn pass their axons to the primary visual cortex (V1). In the cortex, visual processing is spread out across a complex network of regions (Figure 1.1). The retina, LGN, and V1 are commonly collectively referred to as the *early visual pathway*. While the retina transformes light into electrical signals for processing in the brain, the functional role of the LGN is not as obvious. The name used for its main neuron class indicates that the nucleus primarily has been seen as a relay station for visual signals, but why does retinal input not project directly to cortex? While effective, the retinal input accounts for only a few percent of the synaptic inputs onto the relay cells. The remaining 90%-95% is approximately equally divided between

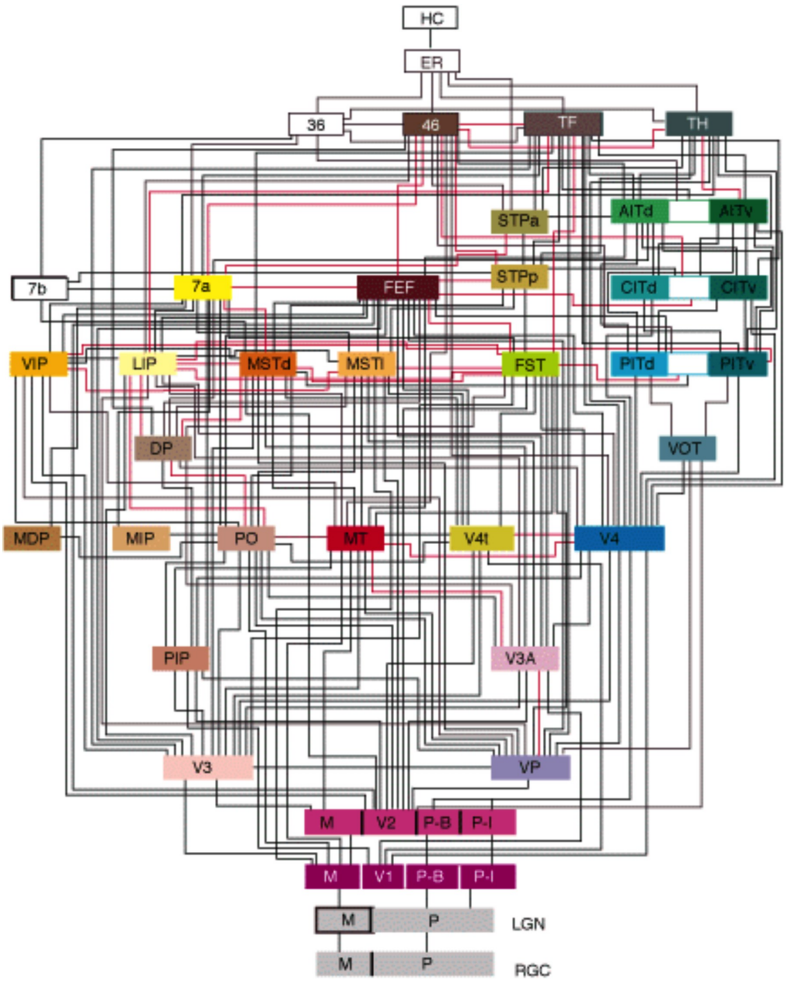

Figure 1.1: **Mapping of primate visual areas.** The hierarchy shows the retinal ganglion cell (RGC) layer, the LGN, 32 visual cortical areas, and several nonvisual areas. Reprinted from Felleman and Van Essen (1991), by permission of Oxford University Press.

local inhibitory inputs, cortical feedback, and brainstem inputs (Van Horn et al, 2000).

The thalamus, of which the LGN is a part, is known to be involved in regulating sleep and wakefulness (Steriade and Llinás, 1988). Changes between drowsy and alert states are generally associated with changes in activity of brainstem afferents that cause relay cells to switch between two response modes, tonic and burst. The response modes affect how information is passed on to the cortex. In brief, cells in tonic mode reliably relay information, while cells in burst mode might be more capable of detecting a stimulus. Initially, response mode was thought to be linked with arousal state and that only tonic firing is seen in the awake, alert animals. However, more recent research suggests that bursting may also occur (Ramcharan et al, 2000; Sherman, 2001) and that cortical feedback may be involved in controlling the response mode selectively in different regions of the visual field (Sherman and Guillery, 2005).

The thalamus is made up of more than 30 separate nuclei that can be grouped into *first order* and *higher order* relays (Sherman and Guillery, 2005). First order relays are those, like LGN, that send information about the environment through sensory pathways and messages about events in the subcortical parts of the brain to the cortex, while higher order relays provide a transthalamic relay from one part of cortex to another. In primates, the higher order nuclei make up more than half the thalamus. Although there is little direct interaction between individual relay cells, modulation by interneurons occurs at multiple levels. First, with some variation between species, the LGN comprises up to 30% local interneurons that act on the relay cells (Sherman and Guillery, 2005). The circuitry is complex and depends not only on the precise connections that are established, but also on the transmitters, the receptors, and the membrane properties that are involved in the synaptic interactions. Further, projection in both directions between thalamus and cortex give off collaterals in the *thalamic reticular nucleus* (TRN) — a structure that forms a capsule around the thalamus. The TRN receives excitatory branches from corticothalamic and thalamocortical axons and sends inhibitory connections back to the thalamus to form an additional source of inhibition (Jones, 1985). Interaction between TRN regions even allows for modulation of LGN relay cells by higher order relays (Sherman and Guillery, 2005).

Although the full range of relay properties affected by the lateral geniculate nucleus circuitry is far from understood, it is generally accepted that the LGN "does not simply perform a trivial, machine-like passing on of retinal inputs" (Guillery and Sherman, 2002). The main objective of this thesis has been to extend our understanding of the early visual system through modeling and to bridge the gap between biology and models at different levels of scale.

The following sections will introduce modeling techniques at different levels and provide additional background on the early visual system.

2 Multiscale modeling

Mathematical models in neuroscience can be categorized into three types: mechanistic, descriptive, and interpretive (Einevoll and Halnes, 2014). *Mechanistic* (physics-type) models aim to account for observed neural properties on the basis of known neural physiology and anatomy. *Descriptive* (statistical) models summarize experimental data compactly in a mathematical form. *Interpretive* (normative) models aim to model the functional roles of neural systems.

Mechanistic modeling, the main focus in the present thesis, can be done at different *levels*. Biophysically detailed models, spiking point-neuron models, and firing-rate models are three common modeling techniques that operate at different levels of detail.

2.1 Level 1: Biophysically detailed models

Compartmental models are the most detailed model type. By including morphologies that describe the branching structure of the dendrites and physiological properties such as the distributions of ion channels, these models enable modeling of detailed dendritic processing (Koch and Segev, 1998). The structure is divided into compartments that are modeled as small electrical circuits. Within the volume of each compartment, the membrane potential V is assumed to be equal. The membrane voltage V_n of compartment n with two neighboring segments in a multi-compartment neuron model can be described by

$$g_{n,n+1}(V_{n+1} - V_n) - g_{n-1,n}(V_n - V_{n-1}) = C_n \frac{dV_n}{dt} + \sum_s I_n^s(t) + \sum_j I_n^j(t) \ . \tag{2.1}$$

The left hand terms represent current contributions from neighboring compartments where g is the conductance between the compartments. On the right hand side, the first term is the capacitive current through the membrane (due to changes in the membrane potential) for compartment n. The final terms represents other currents due to synaptic input (s) and activity in other ion channels (j) in compartment n. As an example, in the well known Hodgkin-Huxley (HH) model (Hodgkin and Huxley, 1952) of the mechanisms underlying the initiation and propagation of action potentials in the squid giant axon, three ion channels currents were included: a sodium channel, a potassium channel and a *leak* channel accounting for other non-specified currents. Compartmental models can be used to quantitatively fit dynamics of real neurons, but they are defined by a large number of variables and are highly nonlinear, which makes mathematical analysis difficult and makes large scale network simulations computationally intensive. Two compartmental

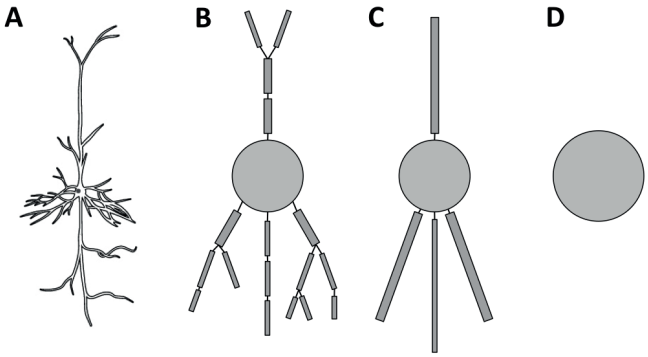

Figure 2.1: **Consecutive simplification of neuron structure. A:** Cortical pyramidal neuron. **B:** Multicompartment model of the pyramidal neuron. **C:** Reduced multicompartment model ("ball-and-stick"). **D:** Point neuron. Panel A © CNX OpenStax / https://cnx.org / CC-BY-4.0

models with different number of compartments are illustrated in Figure 2.1 panels B and C. The latter is often referred to as a "ball-and-stick" model.

2.2 Level 2: Spiking point-neuron models

In point neuron models, the compartmental structure is collapsed into a single compartment (Figure 2.1D). The validity of this simplification depends on the neuron properties as the membrane potential and transmembrane currents are assumed to be the same throughout the cell. Other models in this class include both reductions of the HH-model and more phenomenological models. The leaky integrate-and-fire (LIF) neuron (Knight, 1972a; Brunel and van Rossum, 2007) is the simplest and most widely used model in this class:

$$C\frac{dV}{dt} = -g_L(V - E_L) - \sum_s I_s(t) \ , \tag{2.2}$$

g_L is the ohmic leak current and the I_s sum represents current due to synaptic input. Because of its simplicity, the IAF model has a limited repertoire of spiking behaviors compared to real neurons. On the other hand, its simplicity makes it suitable for mathematical analysis and numerical simulations in large networks. Between these two extremes, a broad range of models have been developed with different tradeoffs between keeping most of the dynamic behavior and reducing complexity to become computationally cheaper and more amenable to mathematical analysis.

Spiking models are deterministic in response to current stimuli or synaptic input and can predict precise spike times, assuming that all parameters are known. As this is not always the case, this apparent precision may not be realized in practice.

2.3 Level 3: Firing-rate models

In firing-rate models, the probability of action-potential firing is modeled rather than individual spikes. They can be used to model both individual neurons and dynamics in populations of neurons. By avoiding the short timescale dynamics of action-potential firing, the number of parameters needed may be reduced and they can be efficiently implemented in terms of differential or integral equations (Dayan and Abbott, 2001). Firing-rate models are comparatively easy to study analytically and simple enough to be suitable for studying network dynamics at a large scale.

A common way to approach firing-rate modeling, is to study the dynamics in a limited region of the state space. Under the assumption that a system remains linear for small perturbations around a working point, it can be treated like a linear, time-invariant (LTI) system that is completely characterized by its *impulse response*. That is, for any input, the output can be calculated as a convolution of the input and the system's impulse response. Thus, one can describe the time-dependent output firing-rate $r(t)$ of a population of neurons, or an ensemble of trials for a single neuron, in response to an input signal $a(t)$ near the stationary working point (a_0, r_0) for small perturbations $\Delta a(t) = a(t) - a_0$. Once the impulse response h_0 is known, the output rate $r(t)$ can be predicted for small stimulus perturbations $\Delta a(t)$,

$$r(t) = (a * h_0)(t) = r_0 + (\Delta a * h_0)(t). \tag{2.3}$$

In the frequency domain, the *transfer function* (or frequency response) $H_0(f)$ is given by the Fourier transform of the impulse response,

$$H_0(f) = \mathcal{F}[h_0(t)](f) = \int_{-\infty}^{\infty} \mathrm{d}t \; h_0(t) e^{-2\pi i f t}. \tag{2.4}$$

Obtaining the transfer function is useful as convolution in the time domain corresponds to multiplication in the frequency domain (Eq 2.3).

3 Early visual system

3.1 Biological background

As the eye focuses an image onto the retina at the back of the eye, light is converted to an electrical signal as photoreceptors detects the photons (Figure 3.1, top right). *Rods* and *cones* are the two main types of photoreceptors and are responsible for night and day vision, respectively. Rods have a high sensitivity to light, but have low temporal resolution and do not differentiate between colors. Cones perform better than rods on all visual tasks except detection of dim stimuli (Kandel et al, 2000). They are more numerous at the fovea and therefore provide better acuity, they provide better temporal resolution, and they provide color vision as there are three types of cones that are sensitive to different parts of the light spectrum. The three cone types are referred to as S (short), M (medium), and L (long) due to the wavelength of the light they are most sensitive to.

From the photoreceptors, the main (vertical) pathway through the retina is via *bipolar cells* to ganglion cells (Lee et al, 2010; Dowling, 1987). Along the way, the visual signal is shaped by feedback and feedforward inhibition by two main types of interneurons: *horizontal cells* and *amacrine cells*.

Bipolar cells come in two main varieties, *ON* and *OFF*. When photoreceptors directly above them are active, ON bipolar cells depolarize, while OFF cells hyperpolarize. When surrounding photoreceptors are active, the response of bipolar cells are the opposite of that evoked by illumination of the center. Cones typically connect to both types of bipolar cells and each type of bipolar cell makes excitatory connections with the corresponding type of ganglion cell. This arrangement enables two parallel pathways from cones to ganglion cells that help later processing stages detect weak contrasts and rapid changes in light intensity. The rod circuitry is slightly different. Rod bipolar cells have only been found to be of the ON type and these connect with ganglion cells via amacrine cells. OFF responses are created as rods directly contact OFF cone bipolar cells or via amacrine cells. In addition, rods and cones can form gap junctions that allow rod signals to flow through cone bipolar cells.

Horizontal cells connect nearby photoreceptors, and in some species bipolar cells (Hubel, 1995). They contribute to adjust the eyes to see well in a wide range of lighting conditions and, in particular, they establish the center-surround receptive-field properties through inhibitory feedback to photoreceptors (Figure 3.2A).

Amacrine cells, like horizontal cells, primarily work laterally. They receive synaptic input from bipolar cells and other amacrine cells, and in turn provide input to amacrine and ganglion cells as well as feedback to bipolar cells. Amacrine cells are the most diverse

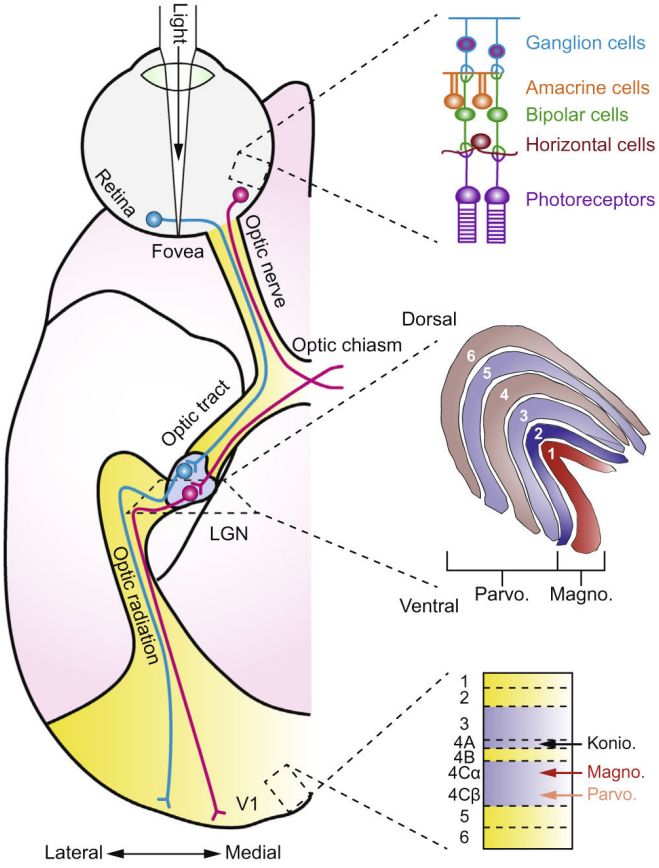

Figure 3.1: **Overview of the mammalian early visual system (macaque monkey). Left:** The early visual pathway from retina via the lateral geniculate nucleus (LGN) to the primary visual cortex (V1). Nerve fibers cross at the optic chiasm such that signals originating from the right visual field of both eyes are processed in the left part of the visual system, and vice versa. **Right top:** Light is absorbed by photoreceptors and the signals are passed through bipolar cells and multiple types of interneurons to retinal ganglion cells whose axons exit the eye and form the optic nerve. **Right center:** The LGN is a layered structure with 6 main layers. The bottom two layers (1 and 2) are called the magnocellular layers and receive input from rod photoreceptors. The upper four (3 to 6) are the parvocellular layers and receive input from cone photoreceptors. Between each of these six layers are the koniocellular layers (not shown). **Right bottom:** LGN relay cells mainly project to layer 4, with koniocellular cells also targeting more superficial cortical layers. Reprinted from Jeffries et al (2014), with permission from Elsevier. Adapted by permission from Springer Customer Service Centre GmbH: Nature Reviews Neuroscience 8(4):276–286, The machinery of colour vision. Solomon and Lennie (2007)

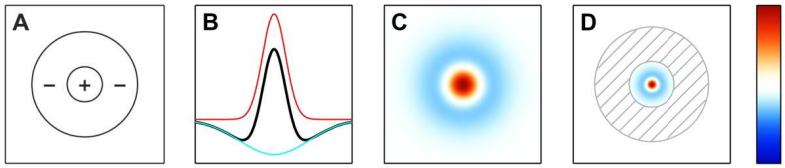

Figure 3.2: **Center-surround receptive fields. A:** Classical receptive field with a central on region and a surrounding off region. On-center cells are excited by stimulation of the central region (+) and inbibited by stimulation in the surrounding region (-). For off-center cells the opposite is true. **B:** The center-surround receptive field can be modeled as the difference of two Gaussians (DOG). An on-center receptive field is shown (black) composed of a narrow excitatory region (red) and a wider inhibitory region (blue). **C:** A two dimensional plot of the DOG model from panel B. **D:** The extra-classical receptive field (ECRF), a region much larget than the classical receptive field (CRF). Stimuli in the ECRF are thought to affect the response to stimuli in the CRF without directly generating spikes. Reprinted from Jeffries et al (2014), with permission from Elsevier.

class of neurons in the retina.

Most ganglion cells in the primate retina can be grouped into one of two main categories, P cells (*parvi*; small) or M cells (*magni*; large). Each class include both on-center and off-center cells. M cells respond optimally to large objects and are able to follow rapid changes in the stimulus. P cells are known as midget retinal ganglion cells, based on the small sizes of their cell bodies and dendritic trees. They receive input from relatively few rods and cones. As a result they have small receptive fields and are thought to be responsible for the analysis of fine detail in the visual image, while M cells appear to be concerned with the analysis of the gross features of the stimulus and its movement (Kandel et al, 2000). *Bistratified* ganglion cells are a more recent discovery, possibly due to their small size. These cells have large receptive fields that only have centers (i.e., no surrounds) and are always ON to blue cones and OFF to both red and green cones. Finally, some retinal ganglion cells are themselves photosensitive, but contribute little or nothing to vision. Instead, they contribute to circadian rhythms and pupillary light reflex, the resizing of the pupil. For further details on retinal processing, see e.g. Lee et al (2010).

Axons from retinal ganglion cells exit the eye through the optic nerve and pass the optic chiasm where half of them cross to the opposite side. This causes signals originating from the right visual field of both eyes to be processed in the left part of the visual system, and vice versa.

There are two separate pathways into the brain on each side. A few percent of the fibers go to the *superior colliculus* which is involved eye movement, but the main pathway leads to the lateral geniculate nucleus (LGN). The LGN is part of the *thalamus*, a sub-cortical structure which serves as a gateway for most sensory signals bound for the cortex – with the notable exception of olfaction.

Whereas the ganglion cells form a two-dimensional sheet that receive input from nearby cells in the same eye, the LGN is a three-dimensional structure that receives input from both eyes (Palmer, 1999). Individual LGN cells, however, respond to stimulation from just one eye. The LGN has a laminar (layered) architecture consisting of multiple sheets of

neurons. Six distinct layers are folded as shown in Figure 3.1 (right center) and organized such that the same point in visual space is stacked on top of each other in each layer. The bottom two layers (1 and 2) are called the magnocellular layers, while the upper four (3 to 6) are called parvocellular layers. Between each of these six layers are koniocellular layers.

Different kinds of retinal ganglion cells project selectively to these layers. Magnocellular and parvocellular layers in the LGN correspond with similarly named types of retinal ganglion cells. That is, retinal M cells synapse onto magnocellular LGN cells and the two layers receive input from one eye each. Likewise, cells in the parvocellular layers are innervated by retinal P cells and the four layers alternate between left and right eye input. Bistratified ganglion cells are thought to project to the koniocellular layers of the LGN (Lee et al, 2010). Due to the selective connectivity from retina via LGN to primary visual cortex, one commonly refers to the parvocellular (P), magnocellular (M), and koniocellular (K) pathways. These pathways have been suggested to process different aspects of the visual scene in parallel (Casagrande, 1994). Note that separate pathways are found in other species as well, but that they have somewhat different properties and are labeled differently. In cats, for example, three pathways called *X*, *Y*, and *W* have been found that roughly correspond to the M, P, and K pathways in primates, respectively (Sherman and Guillery, 2005).

The LGN cells that integrate inputs from one or a few ganglion cells and transmit the processed information though the *optic radiations* to the middle layers of the primary visual cortex (V1), are collectively known as *relay cells* (RCs). The synapses between ganglion cells and relay cells are so strong that only a few spikes in close succession are required to cause the relay cell to fire. While effective, the retinal inputs account for only a few percent of the synaptic inputs onto the relay cells. Interneurons (INs) receive the same retinal signal and modify the relay cell response in several ways. One construct that seems to be unique for the thalamic interneurons is called "triads". These are particular synaptic terminals on the interneuron dendrites where the ganglion cell connects to both a relay cell and the interneuron. Both the relay cell and the interneuron are excited by the ganglion cell, but in addition the relay cell is inhibited by the interneuron. This inhibition has been observed to consistently follow the excitation with a delay of about 1 ms and effectively serves to tune the input to the relay cell (Blitz and Regehr, 2005). This type of inhibition has been termed "locked" (or local) inhibition. In addition, most interneurons have an axon that can inhibit nearby relay cells in a more conventional way when the interneuron fires. As this type of inhibition typically requires integration of several input spikes, it is not directly linked to any one input spike and has become known as "non-locked" (or "global") inhibition. The details of the interaction between relay cells and interneurons has not been clear and is the topic of Paper III in this thesis.

3.2 Receptive-field modeling

Neurons in the visual system respond to light stimuli within a limited region of the visual field called their *receptive field*. Within a neuron's receptive field, there are regions where brightness above the background illumination causes increased firing, and others where lower illumination increases firing. The layout of these regions determine how the neuron responds to different stimuli. The early visual system is organized such that adjacent

neurons have receptive fields that include slightly different, but overlapping visual regions. This arrangement forms a topographic map of the visual field known as a *retinotopic map* that is preserved along the visual pathway, from the retina via LGN to the primary visual cortex (V1) and further.

In "classic" receptive field illustrations, only the spatial dimension is considered. However, neurons in the visual pathway generally exhibit dynamics in both space and time. Given that the receptive field is a spatiotemporal entity, it is relevant to determine how space and time interact to form a cell's response — whether or not it is space-time separable. If the receptive field $D(x, y, \tau)$ can be described as the product of two independent functions, a spatial and a temporal receptive field, it is said to be space-time separable:

$$D(x, y, \tau) = D_s(x, y)D_t(\tau) \tag{3.1}$$

Retinal ganglion cells and LGN relay cells have (spatial) receptive fields that are approximately circular. This concentric receptive field structure is known as center-surround organization. There are two main variants of this scheme. On-center cells (Figure 3.2A) respond maximally to bright spots surrounded by a dark background and vice versa for off-center cells. These spatial structures can be described with a difference-of-Gaussians model

$$D_s(x, y) = \pm \left(\frac{1}{2\pi\sigma_{\text{cen}}^2} \exp\left(-\frac{x^2 + y^2}{2\sigma_{\text{cen}}^2} \right) - \frac{B}{2\pi\sigma_{\text{sur}}^2} \exp\left(-\frac{x^2 + y^2}{2\sigma_{\text{sur}}^2} \right) \right) \tag{3.2}$$

where the first and last Gaussian function describe the center and the surround, respectively (Rodieck, 1965). σ_{cen} determines the size of the central region, while σ_{sur} determines the surround. B controls the balance between the center and surround contributions. The $\pm$ sign enables both on (+) and off (-) center cases to be represented. The on center case is illustrated in Figure 3.2 panels B and C.

Hubel and Wiesel (1959) studied receptive fields of cells in the primary visual cortex and categorized the cells as either *simple* or *complex*. Simple cells have spatially oriented receptive fields with alternating elongated regions that are responsive to bright or dark stimuli. It is thought that the responses are formed from an array of LGN center-surround receptive fields. Complex cell responses are assumed to be formed by non-linear combinations of subunits that resemble simple cells (DeAngelis et al, 1995).

Using white-noise techniques, the receptive fields in the early visual system can be mapped experimentally (DeAngelis et al, 1995). Figure 3.3 illustrates schematic (left) and measured (right) spatial profiles of the center-surround type typically found in the retina and LGN (A) along with cortical simple (B) and complex (C) cells.

A compact way to illustrate the dynamics of the receptive field structure is to construct an *x-t plot* that summarizes how the one-dimensional spatial organization of the receptive field (along the axis perpendicular to the cell's preferred orientation) changes with time.

Representative examples are illustrated in Figure 3.4: For the two LGN cells (A and B), the x-t profiles are approximately space-time separable, with center-surround organization in space (horizontal) and a biphasic structure in time (vertical). However, the temporal component may be different for the center and surround parts, making the whole receptive

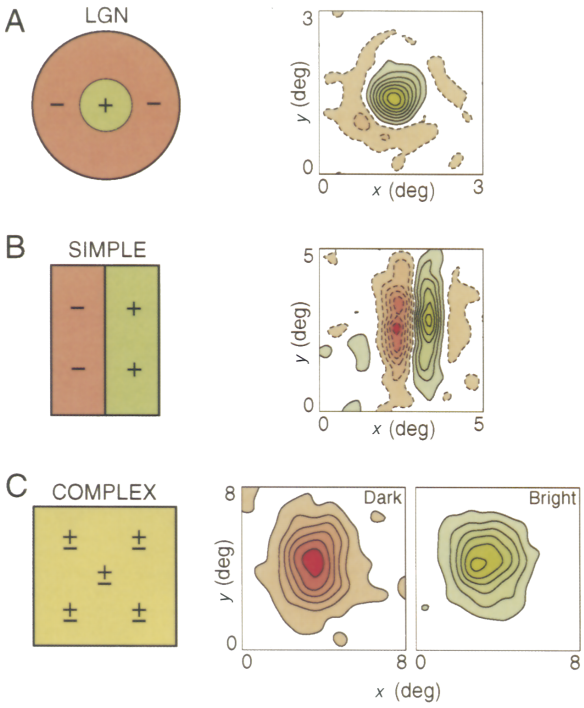

Figure 3.3: **Spatial receptive fields in the early visual pathway.** The left column illustrates spatial classical receptive field sketches for three different neuron types, while the right column shows experimentally recorded profiles for the same neuron types. **A:** Center-surround receptive field from LGN relay neuron with a central on region (green, +) and a surrounding off region (red, -). **B:** Receptive field of a cortical simple cell with elongated subregions that are responsive to either bright (green, +) or dark (red, -) stimuli. **C:**. Receptive field of a cortical complex cell that responds to both light and dark stimuli across large (overlapping) regions. Recorded profiles were measured from cat cells. Reprinted from DeAngelis et al (1995), with permission from Elsevier.

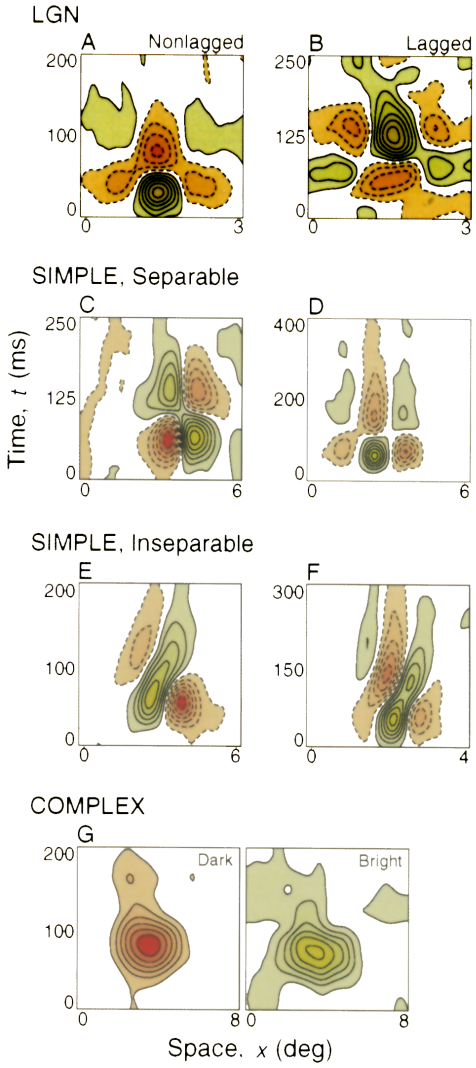

Figure 3.4: **Spatiotemporal receptive field profiles (x-t plots) for neurons recorded from LGN and visual cortex.** In each panel, the horizontal axis represents space (x) along the axis perpendicular to the cell's preferred orientation, and the vertical axis represents time (t). See Figure 3.3 for details. Reprinted from DeAngelis et al (1995), with permission from Elsevier.

field non-separable. Likewise, some simple cells (C and D) have spatial profiles that can be modeled by Gabor functions (Daugman, 1985) and have a biphasic structure in time. All four (A-D) can be well approximated by the product of a spatial and a temporal profile. Note that simple cells with multiphasic temporal receptive field profiles have bandpass temporal frequency tuning, whereas cells with monophasic profiles exhibit low-pass tuning (DeAngelis et al, 1995). In general, though, simple cells are space-time inseparable, like those shown in panels E and F. In x-t plots, this is evidenced by tilted light- and dark-excitatory regions, which means they gradually change with time. For the complex cell (G), note that there are no distinct subregions and that light- and dark-excitatory regions overlap extensively in the space-time domain.

Finally, studies of receptive field dynamics have provided some insight into the underlying mechanisms of motion sensitivity. Cells with space-time inseparable receptive field profiles (i.e., tilted x-t profile; Figure 3.4 E and F) typically show a directional preference, while cells with space-time separable receptive fields do not (DeAngelis et al, 1993).

3.3 Mechanistic modeling

Numerous mechanistic models of the early visual system have been developed. An overview of existing models that focus on LGN neurons and circuitry is provided below.

Multiple relay cell models have been developed to explore specific aspects of neuron activity. The impact of dendritic morphology on integration of synaptic inputs have been investigated in models with passive (Bloomfield and Sherman, 1989; Briska et al, 2003) and active (Perreault and Raastad, 2006) dendrites. McCormick and Huguenard (1992) investigated the various effects of a large ($\sim$10) number of active conductances on somatic response properties in a single-compartment model. The ability to switch between two different firing modes (tonic and bursting) has been studied both in single-compartment (Destexhe et al, 1993; Huguenard and McCormick, 1992) and multicompartment models (Destexhe et al, 1998). The most comprehensive relay cell models are reconstructed multicompartment models with multiple active conductances both in the soma and dendrites (Antal et al, 1997; Emri et al, 2000, 2003; Rhodes and Llinás, 2005). Direct fitting of neuron models to experimental data has been less common, but there are examples from the connection between retinal ganglion cells and relay cells. A spike-response model (Gerstner and Kistler, 2002) was fitted to data from the retinogeniculate synapse in macaque(Carandini et al, 2007) and a leaky integrate-and-fire model was used to fit corresponding data from cat (Casti et al, 2008).

Fewer models have been developed for LGN interneurons than for relay cells. Signal propagation in the elaborate dendritic structure of the interneurons have been investigated using models with passive (Bloomfield and Sherman, 1989; Briska et al, 2003) and active (Casale and McCormick, 2011; Perreault and Raastad, 2006) dendrites. Two relatively general, multicompartment models with realistic morphologies (Zhu et al, 1999; Halnes et al, 2011) are able to capture a range of somatic response properties.

Mechanistic network models of the early visual system have mainly focused on the primary visual cortex. In such models, the processing in the LGN has generally been ignored or simplified. Models that focus on LGN cells include networks of spiking relay cells (Kirkland and Gerstein, 1998; Köhn and Wörgötter, 1996; Wörgötter et al, 1998) receiving

input from grids of retinal ganglion cells and feedback from cortical cells. Similar studies have been performed with firing-rate models (Einevoll and Heggelund, 2000; Hayot and Tranchina, 2001; Yousif and Denham, 2007). Finally, the processing of visual signals in the LGN circuit has been modeled as neural mass (Norheim et al, 2012) and neural field models (Einevoll and Plesser, 2002, 2012).

4 Methods

Multiple tools for neural simulation have been created by and are available for use by the computational neuroscience community. The following sections will introduce the main tools used and provide an overview on how we managed the large-scale parameter scans, an area where we found the range of existing tools to be limited.

4.1 Simulation

Simulations were performed in two different neural simulation tools. NEST (Gewaltig and Diesmann, 2007) was used in all three projects to generate spike spike trains with the desired properties and to simulate multiple (hundreds) trials of spiking point neuron models in parallel (Paper I and II). Interaction with NEST was performed through its Python programming interface, PyNest (Eppler et al, 2008). For the network model (Paper III), the whole LGN circuit was implemented in the NEURON simulation environment (Carnevale and Hines, 2006; Carnevale, 2007; Hines et al, 2009) with retinal ganglion cell input generated by a non-stationary Poisson spike generator (rather than a neuron model) in NEST. A common denominator in the three projects was that each simulation was relatively small and independent of the other simulations, which allowed for efficient parallelization and use of compute clusters.

4.2 Large-scale parameter scans

Parameter scans of more than a few dimensions can quickly lead to combinatorial explosion. For each of the three projects the present thesis is based on, several 100.000 simulations were run (Table 4.1). Exploration of parameter spaces of this magnitude necessitates some degree of automation and means of keeping track of progress. Readily available tools covered parts of the problem (e.g., `NeuroTools Parameters` package (Muller et al, 2009), Sumatra (Davison, 2012), and Mozaik (Antolik and Davison, 2013)), but no single solution was found to sufficiently fit our needs. To fill the gaps, we developed a Python package (`PyScan`). The main challenges experienced and how we overcame them are summarized below.

Table 4.1: Parameter scan magnitudes.

Project	LGN rate models	Multi-behavior models	LGN circuit
Dimensions	6	6	9
Subspaces	2	2	3
Parameter combinations	~ 350.000	~ 650.000	$> 1.000.000$

Problem description

For smaller problems, the brute force approach of running all simulations in a single batch is simple and works well. If one decides to change a parameter, the complete scan can always be rerun. Given 10.000 tasks each lasting one minute, the job would take nearly one week to complete on a single computer. With problem sizes more than an order of magnitude larger, the naive approach is no longer feasible.

Furthermore, parameter scans are often exploratory, as we try to uncover the relation between stimulus and model parameters on the one, and model responses on the other hand. One will frequently explore certain parts of a parameter space first, e.g., responses to stationary stimuli, and later proceed to more complicated stimuli described by more parameters. To obtain an overview, one may want to sample the parameter space on a coarse grid first, before zooming in on interesting regions at higher resolution. All parameter combinations are not necessarily considered meaningful. For instance, there is no need to vary modulation frequency in an input signal if the modulation depth is zero. Ignoring such "singular" dimensions saves time. During the course of a project one may also want to modify parameters that were originally considered model constants.

To provide this flexibility in large-scale parameter scans, a way to identify and track status and results for each parameter combination is needed to avoid re-running already completed tasks.

At this scale, the use of compute clusters becomes a necessity. While by no means a unique problem for parameter scans, keeping configuration and data synchronized and having to switch back and forth between a local workstation and one or more remote compute clusters certainly adds to the complexity. In addition to automating most steps in the workflow and making it simple to invoke those commands, a second goal in terms of automation was to be able to control them all from the local workstation.

Rather than reinventing the wheel, utilising existing tools is preferable where possible. With that in mind, over the course of the projects we built a solution that allows us to

1. generate, aggregate and analyze data from hundreds of thousands of parameter sets and randomized trials in parallel;
2. progress from coarse-scale to fine-scale scans, continuously monitoring progress and adapting scan resolution;
3. avoid re-running any parameter set that has been tested before;
4. drop scans along "singular" dimensions;
5. run a very large number of very small jobs efficiently on large clusters;

6. control parameter scans on remote clusters from the desktop with a small set of simple commands.

Solution overview

To facilitate the parameter scan process, we developed `PyScan` — a lightweight Python package. `PyScan` consists of three main parts. The first is a "parameter space" concept with the necessary flexibility to support an iterative workflow. Second, it assists in data management. Finally, it is a command line tool that simplifies common and repetitive tasks, both locally and on remote clusters.

Parameter spaces

The NeuroTools Parameters module (Muller et al, 2009) supports iteration over parameter spaces at a high level of abstraction. The module introduces useful constructs like Parameters, ParameterRanges and ParameterSets. Iteration over a parameter space returns readable, possibly nested, name-value dictionaries for one parameter set at a time.

The major weakness of the Parameters module relative to our requirements is that it provides no support for selectively iterating over a subset of dimensions, or a subset of values along a given dimension, and that modifying any parameter range leads to an entirely new parameter space. `PyScan` builds on the NeuroTools parameters module and extends it with five concepts:

1. A **Space** is the top-level structure in any project using `PyScan` and represents all possible parameter combinations. It is comparable to a NeuroTools ParameterSpace, but offers additional capabilities.
2. Each parameter that is (potentially) to be varied in a parameter scan, is represented by a **Dimension**. `PyScan` Dimensions are similar to NeuroTools ParameterRanges, but support slicing.
3. A **Subspace** represents a part of a Space defined by constraining one or several Dimensions to subsets of their values. One may view a Subspace as a slice of the full Space.
4. The **structure** component of a Space contains all constant parameters of the model under study, i.e., parameters that are to remain fixed during all parameter scans.
5. Each parameter set is **hashed** to a unique identifier.

The principal idea is that the Space comprises all parameter combinations (or parameter sets) that might possibly be of interest under some aspect of the project, while a suitable Subspace is defined for each specific investigation within the project. As one of the main goals of `PyScan` is to manage combinatorial explosion, one will typically not iterate over the full Space, but rather the union of parameter sets contained in all defined Subspaces. That is, parameter combinations contained in both Subspace A and B in Figure 4.1 will only be run once.

Results and other data related to each parameter set are tagged with a "fingerprint" unique to the parameter set. This fingerprint, implemented as a hash, allows `PyScan`

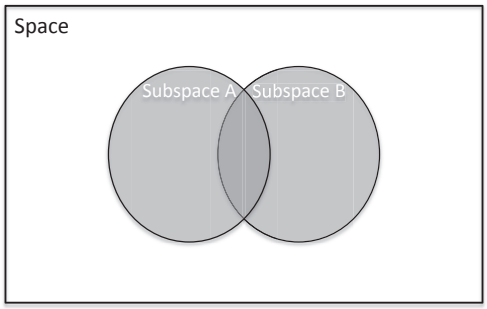

Figure 4.1: **Parameter spaces.** A parameter Space with two overlapping Subspaces. `PyScan` makes sure parameter combinations found in multiple Subspaces (i.e., center region) are run once only.

to keep track of progress across changes in parameter range resolution, addition of new Subspaces, etc. Iteration over parameter (sub)spaces can use this information to skip already completed tasks.

Data management

Parameter scans may produce large amounts of results which we need to store persistently for future analysis. In this section we will discuss some of our experiences with different approaches to data management and persistence.

In parameter scans, we typically execute a large number of trials in parallel, each generating a small amount of data. We thus require a way of efficiently storing large amounts of data generated in small portions by many processes in parallel.

A naive approach would be to write the data from each trial into a separate file and collect results afterwards. While this is easily implemented, it puts a tremendous strain on operating systems and file systems. At the other extreme are relational database systems (RDBMS) such as MySQL/PostgreSQL and other document-oriented databases (or NoSQL data stores in general) which write all data to a single or few files managed by the database. Using databases to collect simulations results from parallel tasks is by no means impossible, but running on a time-shared cluster environment raises a number of technical and practical challenges.

We thus concluded that the best approach is to start one process per node that is provided a set of tasks and to have each such process write to one file. This avoids any bottlenecks during simulation and results in a manageable number of files, typically a few hundred. After the simulations are complete, data is merged across files. This solution has the added benefit of reduced startup time per task, as well as being simple to use locally as well, e.g., for initial testing on a laptop.

Parameter scans in computational neuroscience may generate spike trains and/or voltage traces, as raw output, while often only derived quantities such as firing rates and measures of variability or correlation will be of immediate interest. At the same time, the raw data may be required for subsequent, detailed investigation, particularly in the case

of surprising observations. Because moving large amounts of raw data between remote compute clusters and local machines used for analysis and visualization is tedious, we found it useful to perform initial data analysis as part of the parameter scan. As a result of each trial simulation, `PyScan` expects the raw data (spike trains) and the compact result of the initial analysis. It then stores analysis results and raw data in separate files, maintaining references from analysis results to the corresponding raw data. In this way, only the comparatively small files containing the analysis results need to be moved, while raw data can be accessed if necessary.

A number of technologies were reviewed, including Pickle, SQLite, NumPy record arrays (recarrays), Shelve, and HDF5. Support was added for the latter two, with HDF5 as the primary option.

HDF5 is a data model, library, and file format for storing and managing data. There are two main Python libraries for HDF5, h5py (Collette, 2013) and PyTables (Alted et al, 2002–). Their feature sets are overlapping, but the APIs are quite different. In the following, we will describe PyTables. Two main data types can be represented; tabular data and homogenous arrays. For tabular data, its format must be defined upon table creation as a list of NumPy dtypes (Oliphant, 2006). Arrays must be homogenous, but each element can be of a composite NumPy dtype. In our experience, PyTables is a good solution for storing typical neuroscience data: Structured data, such as parameters, can be stored in tables, while spike trains of varying length can be stored as variable length arrays (VLArrays). Any number of tables or arrays can be stored in a hierarchy inside a single file.

`PyScan` provides a merge operation that combines data from all processes into a single file.

Automation and cluster management

In our experience, a few tasks are repeated a large number of times and they tend to be more or less the same across projects. Some tasks, such as file synchronization, are typically initiated from the workstation, while others require an established connection to the compute cluster. Communication with remote clusters is often done over SSH through a login node. Once connected, interaction typically involves running programs or shell scripts at the command prompt.

By creating a small library of scripts, many of these tasks can be automated and with little extra effort reused across similarly structured projects. For projects utilizing the Python programming language, scripting these tasks using the same language would be useful — particularly when command line tasks need to access project code. Also, it would be advantageous if they could be initiated from the same location, i.e., that connecting to remote hosts was handled implicitly.

We found *Fabric* to fit our needs (Hansen and Forcier, 2013). Fabric is a Python library and command-line tool "for streamlining the use of SSH for application deployment or systems administration tasks". Typical use involves creating functions and executing them via the *fab* command-line tool. During the course of the projects, we built a library of such commands for synchronizing files between hosts, preparing and posting jobs to remote clusters, checking job status, etc. This enabled us to initiate all common operations,

whether local or remote, from within the project directory on the local workstation. Commands are defined as functions in a file called "fabfile.py". Fabric can be invoked from the command line anywhere in the project file structure.

Basic usage would involve the commands **init**, **upload**, **queue**, and **download** as illustrated in Figure 4.2 and briefly described below.

- **init**: Create local directory structure and perform common initialization based on project settings. Also, project specific initialization code could be called to e.g. validate configuration files or create databases or other project files that should be in place before parallel execution of the simulation.
- **upload**: Update files to a remote cluster. Uploading files can be done with `rsync`. A remote project folder can also be updated from a version control system (VCS) by executing the necessary shell commands remotely. An SSH connection is set up by Fabric and terminated once the operation has finished.
- **queue**: Adding a job to a queue at a compute cluster typically requires parameters such as the number of nodes and/or cores, run time, memory requirement, etc. to be specified either at the command line or in a job script. Job script templates are reused across projects. As part of the queueing task, they are parameterized at the workstation, sent to the compute cluster and submitted to the job queue. The queueing system starts the job on the compute nodes once the necessary resources become available and informs the user when the job completes.
- **download**: Download results from a remote cluster. The process would be similar to uploading files, except that other directories are involved to simplify synchronization. That is, configuration files are kept separate from data files as they are mainly moved in opposite directions.

Further analysis was typically performed locally on the aggregated data. Larger post processing tasks or tasks that required access to raw data that was not initially dowloaded, were performed on the compute clustering using IPython.parallel (Perez and Granger, 2007).

In summary, by creating a thin layer on top of selected existing tools (Figure 4.3), we were able to support a flexible workflow with minimal effort.

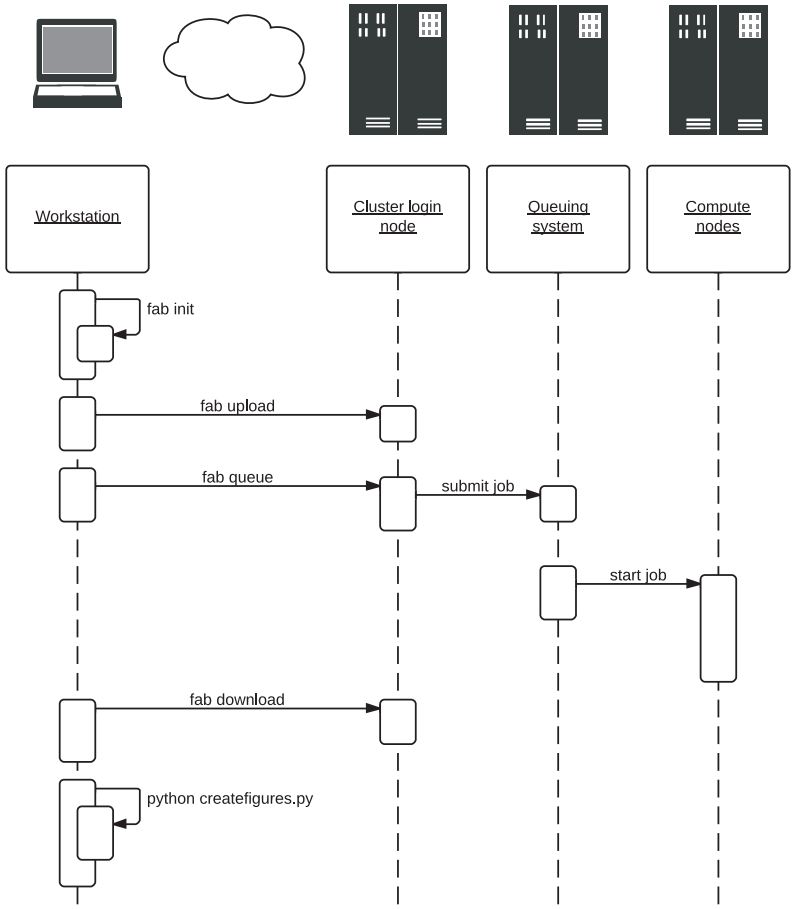

Figure 4.2: **Basic workflow steps.** Tasks are initiated on the workstation. Where relevant, Fabric interacts with the cluster login node. To run jobs on compute nodes, computation time is requested from the login node via the cluster queueing system.

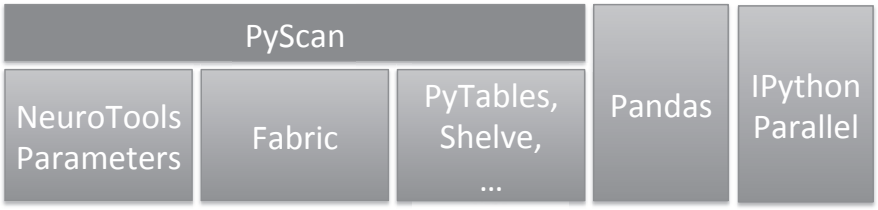

Figure 4.3: **PyScan components overview.** `PyScan` is built on top of the NeuroTools Parameters package, Fabric, PyTables and Shelve. Pandas and IPython Parallel is typically used together with the other tools for data analysis tasks without any direct dependencies.

5 Summary of papers

The present thesis is based on three papers. All three involve models at different levels (see Chapter 2). Paper I investigates how spiking point-neuron models (level 2) are related to firing-rate models (level 3) at the retinogeniculate synapse. With two spiking neuron models as the starting point of our analysis, we study how well firing-rate models capture the essential response properties of LGN relay cells. Paper II investigates how levels 2 and 3 are connected for more complex neuron models. We study spiking two spiking neuron models that can be parameterized to exhibit a wide range of different spiking patterns, as defined in terms of specific current input (Izhikevich, 2003), and thereby can be configured to represent many different neuron types in the early visual system and elsewhere in the brain. We investigate how the models behave in different noise regimes when driven by spiking input and how well the different model parameterizations can be approximated by firing-rate models. In Paper III, we explore the effects of different inhibitory actions from local interneurons on the relay cells in a biophysically detailed network model (level 1) of the LGN circuit driven by firing-rate input from descriptive models converted into spikes.

5.1 Summary of Paper I

The dynamics of neuron populations have been studied extensively both experimentally (Knight, 1972b; Silberberg et al, 2004; Köndgen et al, 2008; Blomquist et al, 2009; Boucsein et al, 2009) and theoretically (Knight, 1972a; Gerstner, 2000; Brunel et al, 2001; Fourcaud and Brunel, 2002; Mattia and Giudice, 2002; Fourcaud-Trocmé et al, 2003; Richardson, 2007). Previous studies have primarily investigated population rates resulting from time-varying noisy current injected into the soma of the cells. The current amplitudes for the ensemble of neurons (or trials) are assumed to be uncorrelated and follow a normal distribution at each instance in time, which corresponds to a scenario where spikes arrive at the target cells independently with infinite rate, and where the impact of each spike on the postsynaptic neuron is infinitesimal (Nordlie et al, 2010). In this situation, the problem can be approximated by a *diffusion process* (Johannesma, 1968). For many biological neural systems, however, these assumptions cannot be justified. In the early visual system, synapses between retinal ganglion cells and LGN relay cells are often much stronger and even single retinal spikes have been reported to reliably initiate action potentials in the thalamic targets (Cleland et al, 1971; Sirovich, 2008).

Nordlie et al (2010) investigated the response properties of the leaky integrate-and-fire (LIF) neuron in a regime beyond the diffusion limit. Unlike most previous studies, the in-

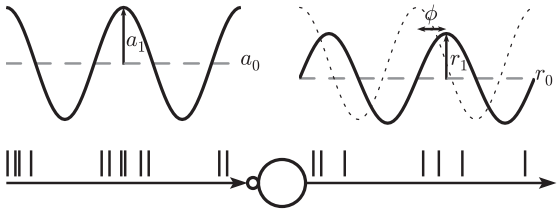

Figure 5.1: **Firing-rate modeling setup sketch.** A model neuron is driven by a spike train with sinusoidally modulated rate $a(t)$ with mean a_0, modulation depth a_1, and frequency f_{stim}. As a first-order approximation, the output spike train of the neuron can be characterized by the sinusoidally modulated response firing rate $r(t)$ with mean r_0, amplitude r_1, frequency f_{stim} and phase ϕ. Reprinted from Heiberg et al (2013).

put signal was represented as spike trains with relatively low rates received through strong excitatory synapses. Thus, no assumptions about the distributions of input currents were made.

Here, we use spiking LGN relay cell models configured to account for experimental data as a starting point to investigate how well firing-rate models can explain the processing performed by these cells. We selected two existing, simplified spiking models of LGN relay cells (Carandini et al, 2005; Casti et al, 2008). Both models had been parameterized to respond like cells that have been measured experimentally. These parameterizations, 23 in total, were probed systematically and the measured responses were used to create firing-rate models.

We base our analysis on the framework introduced by Nordlie et al (2010). In summary, the procedure for rate model derivation introduced there is a two-step process. In the *stationary analysis*, a model neuron is stimulated with random spike trains with constant rate and mean response rates are measured (Figure 5.1). This is repeated for a range of input rates to create a (typically nonlinear) response function describing how the output rate varies with input rate (transfer ratio). In the *non-stationary analysis*, the neuron is stimulated with random spike trains with sinusoidally modulated rate. This is repeated for a range of modulation frequencies to measure the transfer function (frequency response), a measure of output magnitude as a function of frequency (see Section 2.3). The transfer function is in turn approximated with a known filter. In its simplest form, this can be a first-order low-pass filter as described in Nordlie et al (2010).

The resulting linear-nonlinear firing-rate models of the relay cells were tested by comparing results for the spiking models with the predictions of the firing-rate models when exposed to novel stimuli. The responses could be well described by first-order low-pass filters with delay; filters characterized by the three parameters gain, cut-off frequency and delay. The properties of the low-pass filter depend only on the average input rate, but not on the modulation depth of the input. Furthermore, we found that the cutoff frequencies, and thus the filter time constants, of the rate-based model are unrelated to the membrane time constants of the spiking models.

5.2 Summary of Paper II

Simulation of large networks of spiking neurons on the scale of cortical columns, or even whole areas of the cortex, are increasingly becoming feasible due to advances in computer technology and simulator software (Helias et al, 2012; Kunkel et al, 2014; Jordan et al, 2018). In order to relate simulation results to experimental findings, it is important to employ neuron models that accurately capture actual neuron dynamics in response to realistic stimuli. However, there is generally a tradeoff to be made between biological plausibility and computational cost. As a measure of biological plausibility, Izhikevich (2004) mapped out 20 characteristic responses commonly used to classify neuron response types in experiments (such as tonic, phasic and rebound spiking and bursting, or adaptation). The *Izhikevich* model (Izhikevich, 2003) and the *augmented multi-timescale adaptive threshold* (AMAT) model (Yamauchi et al, 2011) are two models that balance this tradeoff well by being able to reproduce all 20 characteristic responses with relatively low computational cost and thus are attractive for large-scale network simulations. The characteristic responses are defined in terms of current injection protocols. It is not entirely clear whether the same classification would make sense when the neurons are driven by more realistic stimuli. In Paper II, therefore, we studied how these neuron models behave in different noise regimes when driven by spiking input.

Large-scale network dynamics are often analyzed mathematically in terms of rate and field models. Examples include neural mass models, such as the Jansen-Rit model (Jansen and Rit, 1995), and neural field models, such as the Wilson-Cowan model (Wilson and Cowan, 1972). In these models, specific spike times and heterogeneities in network structure are ignored and the dynamics of large populations of neurons are substituted by rate variables in a mean-field manner (Ermentrout, 1998; Coombes, 2005). Development of such models include the substitution of the spiking activity of a neuron with an appropriate rate function. Common choices are threshold-linear or sigmoidal functions, but the parameters of the gain function are often chosen qualitatively, and it is uncertain how well they match single-neuron properties or biophysics. To allow for better comparisons between spiking neuron network simulations and reduced neural mass or field models, an adequate quantitative expression for the neuronal gain function is needed. It is therefore of interest to understand if and how the activity of individual spiking neurons in response to arbitrary inputs can be described by a rate-model. Hence, we also investigated how well the different parameterizations of the two neuron models could be approximated by firing-rate models. As part of this work, the method for deriving firing-rate models was extended to allow for filters with multiple time constants.

5.3 Summary of Paper III

In Paper III we seek to better understand how the geniculate circuitry modifies the retinal input signal. Results from previous studies (e.g. Ruksenas et al (2000)) suggest that the spatial receptive-field properties can be explained by a simplified circuit model where a relay cell receives (i) direct excitation from a single retinal ganglion cell, and (ii) indirect feedforward inhibition from several retinal ganglion cells via interneurons.

Einevoll and Heggelund (2000) developed a firing-rate model that could account for additional experimental observations and made predictions "regarding receptive-field sizes of interneurons, the amount of center-surround antagonism for interneurons compared to relay cells, and distance between neighboring retinal ganglion cells providing input to interneurons" that were compatible with data available in the literature. The model consisted of five ganglion cells providing input to one relay cell each and a single interneuron receiving input from all five ganglion cells.

Here, we developed a circuit model of spiking neurons that were stimulated by the same retinal model used in Einevoll and Heggelund (2000). The relay cells and the interneuron have dendrites of comparative physical length, but the two neuron types differ in electrotonic size. The relay cells are electrotonically *compact*, meaning that if modeled as passive cables, steady-state voltage changes applied at distal synaptic sites attenuate by less than 50% on the way to the soma (Sherman and Guillery, 2005). The main reason for this is that relay cells have relatively thick dendrites that cause less current to leak out through the membrane and all synapses regardless of location influence the soma. Hence, the cell is doing large-scale summation of all active synapses and can be modeled as a point neuron. For the present study, we adapted an existing relay cell model by Destexhe et al (1996) obtained from ModelDB (McDougal et al, 2016), accession number 3343.

Interneurons on the other hand have much thinner dendrites and are said to be electrotonically *extensive*, implying that input from distal dendrites will be significantly attenuated before the signal reaches the soma. In electrotonically compact neurons, dendritic inputs are integrated and the soma eventually fires an action potential. This event is passed on to postsynaptic neurons through the axon. If input from distal synapses does not reach the soma, why would a neuron have extensive dendritic arbors? In the case of interneurons, the dendrites serve as outputs too. The thalamic interneurons typically have axons, but also dendro-dendritic terminals that form inhibitory synapses onto relay cells. Sherman and Guillery (2005) argue that it seems likely that clusters of such terminals are isolated from each other and the soma, enabling local dendritic circuits to perform independent input/output operations. Hence, the neuron may not need the axon to function.

For this study, a multicompartment interneuron model (Halnes et al, 2011) previously developed in our group was used as a starting point (ModelDB accession number 140249). The morphology was simplified to a ball-and-sticks configuration with five equal dendrites to make results less sensitive to synapse positioning, while neuron properties otherwise were kept close to the original. Each of the dendrites was configured with a distal dendro-dendritic terminal (triad) that provided the interneuron with excitatory input from one retinal ganglion cell and an inhibitory synapse onto one relay cell. As expected from the discussion above, inputs from these distal synapses had a negligible effect on the soma. Therefore, another excitatory synapse was added close to the soma. The interneuron also had an axon that provided inhibition to all five relay cells. Spatial responses were recorded from this circuit and qualitatively reproduced the results from Einevoll and Heggelund (2000). In addition, synaptic weights were systematically adjusted to study the effects of relative changes in excitation and different types of inhibition (local vs. global).

Our results suggest a possible role of the dual inhibitory actions in providing separate mechanisms for overall gain control (triadic inhibition) and regulation of spatial resolution (axonal inhibition) of visual signals sent to cortex. In addition to providing new biological insight into the roles of the distinct forms of inhibition in the LGN, the model in itself

should be useful as a starting point for use in further network simulations of early visual processing.

6 Perspectives

Nordlie et al (2010) studied leaky integrate-and-fire (LIF) models with strong current-based synapses and showed that a first-order low-pass filter fit to the frequency response together with a nonlinear activation function yielded linear-nonlinear rate models that predicted responses to arbitrary inputs with high accuracy. The framework for rate-model derivation introduced there was adapted for use with LGN relay cell models (Paper I) and extended to allow for other filter kernels (Paper II). In particular, the more complex frequency responses of Izhikevich and AMAT model parameterizations were modeled as bandpass filters. Firing-rate models have previously typically used first-order low-pass (exponential) kernels. While attractive for their simplicity, such models have a limited repertoire of behaviors. Here, by essentially combining two such kernels, we have demonstrated firing-rate models with a broader range of behaviors while retaining most of the simplicity associated with rate models. Application of the rate-model derivation framework to other spiking neuron models would be a straight forward extension of this work. Also, if necessary to get rate models with the desired properties, other or more complex filter kernels can be fitted by following the same procedure.

Several neuron models can reproduce a wide range of experimentally observed spike response patterns when stimulated with current injections. However, how these neurons behave with more natural synaptic inputs has so far not been studied systematically. In Paper II, we investigated the response properties of the Izhikevich model and the AMAT model to noisy spiking input in three different background noise regimes. We observed that neuron models can show very similar responses to spike input, even though they show very different responses to current injections, and in particular that models of different mathematical nature (i.e., Izhikevich and AMAT models), showing identical current responses can respond very differently to spiking input. Given that neurons are mainly driven by spike input in vivo, it seems as if a systematic classification based on a neuron's response to spiking input may be required. We found that the response complexity observed under current injection collapses to only a few response types when the neurons are driven by stationary or sinusiodally modulated Poisson input. Classification based on k-means clustering resulted in clearly different groupings for the Izhikevich and AMAT model classes. However, our classification was far from perfect and further investigation into this topic is necessary.

Until recently, LGN circuit models lacked a key ingredient, namely an interneuron model incorporating the key dual-action inhibitory features of this cell type. Building upon the first multi-compartment dual-action interneuron model (Halnes et al, 2011) and an existing single-compartment relay cell model (Destexhe et al, 1996), we were able model the LGN circuitry at a new level of biological realism (Paper III). We consider the present investigation to be the first of several applications of the present modeling approach that

will not only enable elucidation of the role of LGN circuitry in shaping spatial response features like here, but also the key role played by the circuit in temporal processing of the incoming spike trains from retina. Neurons in the LGN receive modulatory input from other parts of the brain. Some of these inputs cause the LGN circuit to shift between drowsy and attentive states, which in turn can switch the firing mode of the LGN cells between tonic and bursty. One obvious step in future investigations would be to explore how the conclusions we arrived at in the current work depend on the processing state of the LGN. Both relay cells and interneurons receive excitatory feedback from cortex and inhibitory feedback from the thalamic reticular nucleus. The effect of the feedback on circuit behaviour will likely depend strongly on whether the feedback arrives on distal dendrites or close to the soma. This question can be investigated with a network model of the present type, possibly with a more more comprehensive, multicompartmental model for the relay cells. Finally, the present model assumes static synapses, while *in vitro* studies have demonstrated short-term synaptic plasticity throughout the circuit. Investigation of synaptic plasticity and the resulting dynamics in the LGN circuit would require a detailed model of our type.

The three projects in the present study all included large parameter scans. By combining existing tools and libraries along with a small custom library developed as part of the study, we were able to manage the simulation configurations and results efficiently. The setup enabled us to define and work with meaningful subspaces of parameters. Rather than making a detailed plan up front, we performed coarse scans of interesting regions first and refined the search grid iteratively to fit our needs. Central to this flexibility was the use of *fingerprinting* of parameter sets that allowed us to skip simulations that already had been run. While essentially a *brute force* approach for large-scale parameter scans, these additional features contribute to limit computing resource consumption by avoiding reruns and enable an agile workflow.

Bibliography

Alted F, Vilata I, et al (2002–) PyTables: Hierarchical datasets in Python. URL `http://www.pytables.org/`, last accessed 2018.04.10

Antal K, Emri Z, Tóth TI, Crunelli V (1997) Model of a thalamocortical neurone with dendritic voltage-gated ion channels. Neuroreport 8(4):1063–1066

Antolik J, Davison A (2013) Mozaik: a framework for model construction, simulation, data analysis and visualization for large-scale spiking neural circuit models. Frontiers in Neuroinformatics 7, doi: 10.3389/conf.fninf.2013.09.00018

Blitz DM, Regehr WG (2005) Timing and specificity of feed-forward inhibition within the lgn. Neuron 45(6):917–928, doi: 10.1016/j.neuron.2005.01.033

Blomquist P, Devor A, Indahl UG, Ulbert I, Einevoll GT, Dale AM (2009) Estimation of thalamocortical and intracortical network models from joint thalamic single-electrode and cortical laminar-electrode recordings in the rat barrel system. PLoS Computational Biology 5(3):e1000328, doi: 10.1371/journal.pcbi.1000328

Bloomfield SA, Sherman SM (1989) Dendritic current flow in relay cells and interneurons of the cat's lateral geniculate nucleus. Proceedings of the National Academy of Sciences 86(10):3911–3914, doi: 10.1073/pnas.86.10.3911

Boucsein C, Tetzlaff T, Meier R, Aertsen A, Naundorf B (2009) Dynamical response properties of neocortical neuron ensembles: multiplicative versus additive noise. J Neurosci 29(4):1006–1010, doi: 10.1523/JNEUROSCI.3424-08.2009

Briska AM, Uhlrich DJ, Lytton WW (2003) Computer model of passive signal integration based on whole-cellin vitrostudies of rat lateral geniculate nucleus. European Journal of Neuroscience 17(8):1531–1541, doi: 10.1046/j.1460-9568.2003.02579.x

Brunel N, van Rossum MCW (2007) Lapicque's 1907 paper: from frogs to integrate-and-fire. Biol Cybern 97(5-6):337–339, doi: 10.1007/s00422-007-0190-0

Brunel N, Chance FS, Fourcaud N, Abbott LF (2001) Effects of synaptic noise and filtering on the frequency response of spiking neurons. Phys Rev Lett 86(10):2186–2189, doi: 10.1103/PhysRevLett.86.2186

Carandini M, Demb JB, Mante V, Tolhurst DJ, Dan Y, Olshausen BA, Gallant JL, Rust NC (2005) Do we know what the early visual system does? J Neurosci 25(46):10577–10597, doi: 10.1523/JNEUROSCI.3726-05.2005

Carandini M, Horton JC, Sincich LC (2007) Thalamic filtering of retinal spike trains by postsynaptic summation. J Vis 7(14):20.1–2011, doi: 10.1167/7.14.20

Carnevale NT, Hines ML (2006) The NEURON Book. Cambridge University Press

Carnevale T (2007) Neuron simulation environment. Scholarpedia 2(6):1378, doi: 10.4249/scholarpedia.1378

Casagrande V (1994) A third parallel visual pathway to primate area v1. Trends in Neurosciences 17(7):305–310, doi: 10.1016/0166-2236(94)90065-5

Casale AE, McCormick DA (2011) Active action potential propagation but not initiation in thalamic interneuron dendrites. Journal of Neuroscience 31(50):18289–18302, doi: 10.1523/jneurosci.4417-11.2011

Casti A, Hayot F, Xiao Y, Kaplan E (2008) A simple model of retina-lgn transmission. J Comput Neurosci 24(2):235–252, doi: 10.1007/s10827-007-0053-7

Cleland BG, Dubin MW, Levick WR (1971) Simultaneous recording of input and output of lateral geniculate neurones. Nature New Biology 231(23):191–192, doi: doi:10.1038/newbio231191a0

Collette A (2013) Python and HDF5: Unlocking Scientific Data. O'Reilly Media, Inc.

Coombes S (2005) Waves, bumps, and patterns in neural field theories. Biological Cybernetics 93(2):91–108, doi: 10.1007/s00422-005-0574-y

Daugman JG (1985) Uncertainty relation for resolution in space, spatial frequency, and orientation optimized by two-dimensional visual cortical filters. Journal of the Optical Society of America A 2(7):1160, doi: 10.1364/josaa.2.001160

Davison AP (2012) Automated capture of experiment context for easier reproducibility in computational research. Computing in Science and Engineering 14:48–56, doi: 10.1109/MCSE.2012.41

Dayan P, Abbott LF (2001) Theoretical Neuroscience : Computational and Mathematical Modeling of Neural Systems. Massachusetts Institute of Technology Press, Cambridge, MA

DeAngelis GC, Ohzawa I, Freeman RD (1993) Spatiotemporal organization of simple-cell receptive fields in the cat's striate cortex. i. general characteristics and postnatal development. Journal of Neurophysiology 69(4):1091–1117, doi: 10.1152/jn.1993.69.4.1091

DeAngelis GC, Ohzawa I, Freeman RD (1995) Receptive-field dynamics in the central visual pathways. Trends Neurosci 18(10):451–458, doi: 10.1016/0166-2236(95)94496-R

Deisseroth K, Feng G, Majewska AK, Miesenbock G, Ting A, Schnitzer MJ (2006) Next-generation optical technologies for illuminating genetically targeted brain circuits. Journal of Neuroscience 26(41):10380–10386, doi: 10.1523/jneurosci.3863-06.2006

Destexhe A, Babloyantz A, Sejnowski T (1993) Ionic mechanisms for intrinsic slow oscillations in thalamic relay neurons. Biophysical Journal 65(4):1538–1552, doi: 10.1016/s0006-3495(93)81190-1

Destexhe A, Bal T, McCormick DA, Sejnowski TJ (1996) Ionic mechanisms underlying synchronized oscillations and propagating waves in a model of ferret thalamic slices. Journal of Neurophysiology 76(3):2049–2070, doi: 10.1152/jn.1996.76.3.2049

Destexhe A, Neubig M, Ulrich D, Huguenard J (1998) Dendritic low-threshold calcium currents in thalamic relay cells. The Journal of Neuroscience 18(10):3574–3588, doi: 10.1523/jneurosci.18-10-03574.1998

Dowling JE (1987) The Retina: An Approachable Part of the Brain. Harvard University Press

Einevoll GT, Halnes G (2014) Lateral geniculate nucleus (LGN) models. In: Encyclopedia of Computational Neuroscience, Springer New York, pp 1–7, doi: 10.1007/978-1-4614-7320-6_556-1

Einevoll GT, Heggelund P (2000) Mathematical models for the spatial receptive-field organization of nonlagged x-cells in dorsal lateral geniculate nucleus of cat. Vis Neurosci 17(6):871–885

Einevoll GT, Plesser HE (2002) Linear mechanistic models for the dorsal lateral geniculate nucleus of cat probed using drifting-grating stimuli. Network 13(4):503–530, doi: 10.1088/0954-898X_13_4_305

Einevoll GT, Plesser HE (2012) Extended difference-of-gaussians model incorporating cortical feedback for relay cells in the lateral geniculate nucleus of cat. Cognitive Neurodynamics 6(4):307–324, doi: 10.1007/s11571-011-9183-8

Emri Z, Antal K, Tóth T, Cope D, Crunelli V (2000) Backpropagation of the δ oscillation and the retinal excitatory postsynaptic potential in a multi-compartment model of thalamocortical neurons. Neuroscience 98(1):111–127, doi: 10.1016/s0306-4522(00)00068-3

Emri Z, Antal K, Crunelli V (2003) The impact of corticothalamic feedback on the output dynamics of a thalamocortical neurone model: the role of synapse location and metabotropic glutamate receptors. Neuroscience 117(1):229–239, doi: 10.1016/s0306-4522(02)00759-5

Eppler JM, Helias M, Muller E, Diesmann M, Gewaltig MO (2008) Pynest: A convenient interface to the nest simulator. Front Neuroinformatics 2:12, doi: 10.3389/neuro.11.012.2008

Ermentrout B (1998) Neural networks as spatio-temporal pattern-forming systems. Reports on Progress in Physics 61(4):353–430, doi: 10.1088/0034-4885/61/4/002

Felleman DJ, Van Essen DC (1991) Distributed hierarchical processing in the primate cerebral cortex. Cereb Cortex 1(1):1–47, doi: 10.1093/cercor/1.1.1-a

Fourcaud N, Brunel N (2002) Dynamics of the firing probability of noisy integrate-and-fire neurons. Neural Comput 14(9):2057–2110, doi: 10.1162/089976602320264015

Fourcaud-Trocmé N, Hansel D, Van Vreeswijk C, Brunel N (2003) How spike generation mechanisms determine the neuronal response to fluctuating inputs. Journal of Neuroscience 23(37):11628–11640

Gerstner W (2000) Population dynamics of spiking neurons: fast transients, asynchronous states, and locking. Neural Comput 12(1):43–89, doi: 10.1162/089976600300015899

Gerstner W, Kistler WM (2002) Spiking Neuron Models: Single Neurons, Populations, Plasticity. Cambridge University Press, Cambridge, doi: 10.1017/CBO9780511815706

Gewaltig MO, Diesmann M (2007) NEST (NEural Simulation Tool). Scholarpedia 2(4):1430, doi: 10.4249/scholarpedia.1430

Godara P, Dubis AM, Roorda A, Duncan JL, Carroll J (2010) Adaptive optics retinal imaging: Emerging clinical applications. Optometry and Vision Science 87(12):930–941, doi: 10.1097/opx.0b013e3181ff9a8b

Guillery R, Sherman S (2002) Thalamic relay functions and their role in corticocortical communication. Neuron 33(2):163–175, doi: 10.1016/s0896-6273(01)00582-7

Halnes G, Augustinaite S, Heggelund P, Einevoll GT, Migliore M (2011) A Multi-Compartment Model for Interneurons in the Dorsal Lateral Geniculate Nucleus. PLoS Computational Biology 7(9), doi: 10.1371/journal.pcbi.1002160

Hansen CV, Forcier JE (2013) Fabric — fabric 1.6 documentation. URL `http://fabfile.org`, last accessed 2018.04.03

Hawrylycz MJ, Lein ES, Guillozet-Bongaarts AL, Shen EH, Ng L, Miller JA, van de Lagemaat LN, Smith KA, Ebbert A, Riley ZL, Abajian C, Beckmann CF, Bernard A, Bertagnolli D, Boe AF, Cartagena PM, Chakravarty MM, Chapin M, Chong J, Dalley RA, Daly BD, Dang C, Datta S, Dee N, Dolbeare TA, Faber V, Feng D, Fowler DR, Goldy J, Gregor BW, Haradon Z, Haynor DR, Hohmann JG, Horvath S, Howard RE, Jeromin A, Jochim JM, Kinnunen M, Lau C, Lazarz ET, Lee C, Lemon TA, Li L, Li Y, Morris JA, Overly CC, Parker PD, Parry SE, Reding M, Royall JJ, Schulkin J, Sequeira PA, Slaughterbeck CR, Smith SC, Sodt AJ, Sunkin SM, Swanson BE, Vawter MP, Williams D, Wohnoutka P, Zielke HR, Geschwind DH, Hof PR, Smith SM, Koch C, Grant SGN, Jones AR (2012) An anatomically comprehensive atlas of the adult human brain transcriptome. Nature 489(7416):391–399, doi: 10.1038/nature11405

Hayot F, Tranchina D (2001) Modeling corticofugal feedback and the sensitivity of lateral geniculate neurons to orientation discontinuity. Vis Neurosci 18(6):865–877

Heiberg T, Kriener B, Tetzlaff T, Casti A, Einevoll GT, Plesser HE (2013) Firing-rate models capture essential response dynamics of lgn relay cells. Journal of Computational Neuroscience 35(3):359–375, doi: 10.1007/s10827-013-0456-6

Helias M, Kunkel S, Masumoto G, Igarashi J, Eppler JM, Ishii S, Fukai T, Morrison A, Diesmann M (2012) Supercomputers ready for use as discovery machines for neuroscience. Frontiers in Neuroinformatics 6, doi: 10.3389/fninf.2012.00026

Hines ML, Davison AP, Muller E (2009) Neuron and python. Front Neuroinform 3:1, doi: 10.3389/neuro.11.001.2009

Hodgkin AL, Huxley AF (1952) A quantitative description of membrane current and its application to conduction and excitation in nerve. The Journal of physiology 117(4):500–544

Hubel DH (1995) Eye, Brain, and Vision. Scientific American Library/Scientific American Books

Hubel DH, Wiesel TN (1959) Receptive fields of single neurones in the cat's striate cortex. The Journal of Physiology 148(3):574–591, doi: 10.1113/jphysiol.1959.sp006308

Huguenard JR, McCormick DA (1992) Simulation of the currents involved in rhythmic

oscillations in thalamic relay neurons. Journal of Neurophysiology 68(4):1373–1383, doi: 10.1152/jn.1992.68.4.1373

Izhikevich E (2004) Which model to use for cortical spiking neurons? IEEE Transactions on Neural Networks 15(5):1063–1070, doi: 10.1109/tnn.2004.832719

Izhikevich EM (2003) Simple model of spiking neurons. IEEE Trans Neural Netw 14(6):1569–1572, doi: 10.1109/TNN.2003.820440

Jansen BH, Rit VG (1995) Electroencephalogram and visual evoked potential generation in a mathematical model of coupled cortical columns. Biol Cybern 73(4):357–366, doi: 10.1007/BF00199471

Jeffries AM, Killian NJ, Pezaris JS (2014) Mapping the primate lateral geniculate nucleus: A review of experiments and methods. Journal of Physiology-Paris 108(1):3–10, doi: 10.1016/j.jphysparis.2013.10.001

Johannesma PIM (1968) Diffusion models for the stochastic activity of neurons. In: Caianiello ER (ed) Neural Networks: Proceedings of the School on Neural Networks Ravello, June 1967, Springer-Verlag Verlag, pp 116–144, doi: 10.1007/978-3-642-87596-0_11

Jones EG (ed) (1985) The Thalamus. Springer US, doi: 10.1007/978-1-4615-1749-8

Jordan J, Ippen T, Helias M, Kitayama I, Sato M, Igarashi J, Diesmann M, Kunkel S (2018) Extremely scalable spiking neuronal network simulation code: From laptops to exascale computers. Frontiers in Neuroinformatics 12, doi: 10.3389/fninf.2018.00002

Kandel ER, Schwartz JH, Jessell TM, Siegelbaum SA, Hudspeth AJ, et al (2000) Principles of Neural Science, vol 4. McGraw-Hill New York

Kirkland KL, Gerstein GL (1998) A model of cortically induced synchronization in the lateral geniculate nucleus of the cat: a role for low-threshold calcium channels. Vision Res 38(13):2007–2022

Knight BW (1972a) Dynamics of encoding in a population of neurons. The Journal of General Physiology 59(6):734–766, doi: 10.1085/jgp.59.6.734

Knight BW (1972b) The relationship between the firing rate of a single neuron and the level of activity in a population of neurons. experimental evidence for resonant enhancement in the population response. J Gen Physiol 59(6):767–778, doi: 10.1085/jgp.59.6.767

Koch C, Segev I (1998) Methods in Neuronal Modeling: From Ions to Networks. MIT press

Köhn J, Wörgötter F (1996) Corticofugal feedback can reduce the visual latency of responses to antagonistic stimuli. Biol Cybern 75(3):199–209, doi: 10.1007/s004220050

Kunkel S, Schmidt M, Eppler JM, Plesser HE, Masumoto G, Igarashi J, Ishii S, Fukai T, Morrison A, Diesmann M, Helias M (2014) Spiking network simulation code for petascale computers. Frontiers in Neuroinformatics 8, doi: 10.3389/fninf.2014.00078

Köndgen H, Geisler C, Fusi S, Wang XJ, Lüscher HR, Giugliano M (2008) The dynamical response properties of neocortical neurons to temporally modulated noisy inputs in vitro. Cerebral Cortex 18(9):2086–2097, doi: 10.1093/cercor/bhm235

Lee BB, Martin PR, Grünert U (2010) Retinal connectivity and primate vision. Progress in retinal and eye research 29(6):622–639, doi: 10.1016/j.preteyeres.2010.08.004

Lein ES, Hawrylycz MJ, Ao N, Ayres M, Bensinger A, Bernard A, Boe AF, Boguski MS, Brockway KS, Byrnes EJ, Chen L, Chen L, Chen TM, Chin MC, Chong J, Crook BE, Czaplinska A, Dang CN, Datta S, Dee NR, Desaki AL, Desta T, Diep E, Dolbeare TA, Donelan MJ, Dong HW, Dougherty JG, Duncan BJ, Ebbert AJ, Eichele G, Estin LK, Faber C, Facer BA, Fields R, Fischer SR, Fliss TP, Frensley C, Gates SN, Glattfelder KJ, Halverson KR, Hart MR, Hohmann JG, Howell MP, Jeung DP, Johnson RA, Karr PT, Kawal R, Kidney JM, Knapik RH, Kuan CL, Lake JH, Laramee AR, Larsen KD, Lau C, Lemon TA, Liang AJ, Liu Y, Luong LT, Michaels J, Morgan JJ, Morgan RJ, Mortrud MT, Mosqueda NF, Ng LL, Ng R, Orta GJ, Overly CC, Pak TH, Parry SE, Pathak SD, Pearson OC, Puchalski RB, Riley ZL, Rockett HR, Rowland SA, Royall JJ, Ruiz MJ, Sarno NR, Schaffnit K, Shapovalova NV, Sivisay T, Slaughterbeck CR, Smith SC, Smith KA, Smith BI, Sodt AJ, Stewart NN, Stumpf KR, Sunkin SM, Sutram M, Tam A, Teemer CD, Thaller C, Thompson CL, Varnam LR, Visel A, Whitlock RM, Wohnoutka PE, Wolkey CK, Wong VY, Wood M, Yaylaoglu MB, Young RC, Youngstrom BL, Yuan XF, Zhang B, Zwingman TA, Jones AR (2006) Genome-wide atlas of gene expression in the adult mouse brain. Nature 445(7124):168–176, doi: 10.1038/nature05453

Mattia M, Giudice PD (2002) Population dynamics of interacting spiking neurons. Physical Review E 66(5), doi: 10.1103/physreve.66.051917

McCormick DA, Huguenard JR (1992) A model of the electrophysiological properties of thalamocortical relay neurons. Journal of Neurophysiology 68(4):1384–1400, doi: 10.1152/jn.1992.68.4.1384

McDougal RA, Morse TM, Carnevale T, Marenco L, Wang R, Migliore M, Miller PL, Shepherd GM, Hines ML (2016) Twenty years of ModelDB and beyond: building essential modeling tools for the future of neuroscience. Journal of Computational Neuroscience 42(1):1–10, doi: 10.1007/s10827-016-0623-7

Miller DT, Williams DR, Morris GM, Liang J (1996) Images of cone photoreceptors in the living human eye. Vision Research 36(8):1067–1079, doi: 10.1016/0042-6989(95)00225-1

Muller E, Davison AP, Brizzi T, Bruederle D, Eppler JM, Kremkow J, Pecevski D, Perrinet L, Schmuker M, Yger P (2009) NeuralEnsemble.Org: Unifying neural simulators in Python to ease the model complexity bottleneck. In: Frontiers in Neuroscience Conference Abstract: Neuroinformatics 2009, doi: 10.3389/conf.neuro.11.2009.08.104

Nordlie E, Tetzlaff T, Einevoll GT (2010) Rate dynamics of leaky integrate-and-fire neurons with strong synapses. Front Comput Neurosci 4:149, doi: 10.3389/fncom.2010.00149

Norheim ES, Wyller J, Nordlie E, Einevoll GT (2012) A minimal mechanistic model for temporal signal processing in the lateral geniculate nucleus. Cognitive Neurodynamics 6(3):259–281, doi: 10.1007/s11571-012-9198-9

Oh SW, Harris JA, Ng L, Winslow B, Cain N, Mihalas S, Wang Q, Lau C, Kuan L, Henry AM, Mortrud MT, Ouellette B, Nguyen TN, Sorensen SA, Slaughterbeck CR, Wakeman W, Li Y, Feng D, Ho A, Nicholas E, Hirokawa KE, Bohn P, Joines KM, Peng H, Hawrylycz MJ, Phillips JW, Hohmann JG, Wohnoutka P, Gerfen CR, Koch C,

Bernard A, Dang C, Jones AR, Zeng H (2014) A mesoscale connectome of the mouse brain. Nature 508(7495):207–214, doi: 10.1038/nature13186

Oliphant TE (2006) A guide to NumPy, vol 1. Trelgol Publishing, USA

Packer AM, Peterka DS, Hirtz JJ, Prakash R, Deisseroth K, Yuste R (2012) Two-photon optogenetics of dendritic spines and neural circuits. Nature Methods 9(12):1202–1205, doi: 10.1038/nmeth.2249

Palmer SE (1999) Vision Science: Photons to Phenomenology. MIT press, Cambridge, MA

Perez F, Granger BE (2007) IPython: A system for interactive scientific computing. Computing in Science & Engineering 9(3):21–29, doi: 10.1109/mcse.2007.53

Perreault MC, Raastad M (2006) Contribution of morphology and membrane resistance to integration of fast synaptic signals in two thalamic cell types. The Journal of Physiology 577(1):205–220, doi: 10.1113/jphysiol.2006.113043

Ramcharan EJ, Gnadt JW, Sherman SM (2000) Burst and tonic firing in thalamic cells of unanesthetized, behaving monkeys. Visual Neuroscience 17(1):55–62

Rhodes PA, Llinás R (2005) A model of thalamocortical relay cells. The Journal of Physiology 565(3):765–781, doi: 10.1113/jphysiol.2004.070888

Richardson MJE (2007) Firing-rate response of linear and nonlinear integrate-and-fire neurons to modulated current-based and conductance-based synaptic drive. Physical Review E 76(2), doi: 10.1103/physreve.76.021919

Rodieck RW (1965) Quantitative analysis of cat retinal ganglion cell response to visual stimuli. Vision Res 5(11):583–601, doi: 10.1016/0042-6989(65)90033-7

Ruksenas O, Fjeld IT, Heggelund P (2000) Spatial summation and center-surround antagonism in the receptive field of single units in the dorsal lateral geniculate nucleus of cat: comparison with retinal input. Vis Neurosci 17(6):855–870

Sherman S (2001) Tonic and burst firing: dual modes of thalamocortical relay. Trends in Neurosciences 24(2):122–126, doi: 10.1016/s0166-2236(00)01714-8

Sherman SM, Guillery RW (2005) Exploring the Thalamus and Its Role in Cortical Function, 2nd edn. Cambridge, Mass. ; London : The MIT Press

Silberberg G, Bethge M, Markram H, Pawelzik K, Tsodyks M (2004) Dynamics of population rate codes in ensembles of neocortical neurons. Journal of Neurophysiology 91(2):704–709, doi: 10.1152/jn.00415.2003

Sirovich L (2008) Populations of tightly coupled neurons: The rgc/lgn system. Neural Computation 20(5):1179–1210, doi: 10.1162/neco.2007.03-07-482

Solomon SG, Lennie P (2007) The machinery of colour vision. Nature Reviews Neuroscience 8(4):276–286, doi: 10.1038/nrn2094

Sporns O, Tononi G, Kötter R (2005) The human connectome: A structural description of the human brain. PLoS Computational Biology 1(4):e42, doi: 10.1371/journal.pcbi.0010042

Steriade M, Llinás RR (1988) The functional states of the thalamus and the associated neuronal interplay. Physiological Reviews 68(3):649–742, doi: 10.1152/physrev.1988.68.3.649

Van Essen DC, Smith SM, Barch DM, Behrens TE, Yacoub E, Ugurbil K (2013) The WU-minn human connectome project: An overview. NeuroImage 80:62–79, doi: 10.1016/j.neuroimage.2013.05.041

Van Horn SC, Erişir A, Sherman SM (2000) Relative distribution of synapses in the a-laminae of the lateral geniculate nucleus of the cat. J Comp Neurol 416(4):509–520, doi: 10.1002/(SICI)1096-9861(20000124)416:4<509::AID-CNE7>3.0.CO;2-H

Wilson HR, Cowan JD (1972) Excitatory and inhibitory interactions in localized populations of model neurons. Biophys J 12(1):1–24, doi: 10.1016/S0006-3495(72)86068-5

Wörgötter F, Suder K, Zhao Y, Kerscher N, Eysel UT, Funke K (1998) State-dependent receptive-field restructuring in the visual cortex. Nature 396(6707):165–168, doi: 10.1038/24157

Yamauchi S, Kim H, Shinomoto S (2011) Elemental spiking neuron model for reproducing diverse firing patterns and predicting precise firing times. Front Comput Neurosci 5:42, doi: 10.3389/fncom.2011.00042

Yousif N, Denham M (2007) The role of cortical feedback in the generation of the temporal receptive field responses of lateral geniculate nucleus neurons: a computational modelling study. Biol Cybern 97(4):269–277, doi: 10.1007/s00422-007-0171-3

Zhu J, Uhlrich D, Lytton W (1999) Burst firing in identified rat geniculate interneurons. Neuroscience 91(4):1445–1460, doi: 10.1016/s0306-4522(98)00665-4

Attached papers

Paper I

Heiberg T, Kriener B, Tetzlaff T, Casti A, Einevoll GT, Plesser HE (2013) Firing-rate models capture essential response dynamics of LGN relay cells. Journal of Computational Neuroscience 35(3):359–375, doi: 10.1007/s10827-013-0456-6

J Comput Neurosci
DOI 10.1007/s10827-013-0456-6

Firing-rate models capture essential response dynamics of LGN relay cells

Thomas Heiberg · Birgit Kriener · Tom Tetzlaff · Alex Casti · Gaute T. Einevoll · Hans E. Plesser

Received: 30 November 2012 / Revised: 2 April 2013 / Accepted: 25 April 2013

Abstract Firing-rate models provide a practical tool for studying signal processing in the early visual system, permitting more thorough mathematical analysis than spike-based models. We show here that essential response properties of relay cells in the lateral geniculate nucleus (LGN) can be captured by surprisingly simple firing-rate models consisting of a low-pass filter and a nonlinear activation function. The starting point for our analysis are two spiking neuron models based on experimental data: a spike-response model fitted to data from macaque (Carandini et al. J. Vis., 20(14), 1–2011, 2007), and a model with conductance-based synapses and afterhyperpolarizing currents fitted to data from cat (Casti et al. J. Comput. Neurosci., 24(2), 235–252, 2008). We obtained the nonlinear activation function by stimulating the model neurons with stationary stochastic spike trains, while we characterized the linear filter by fitting a low-pass filter to responses to sinusoidally modulated stochastic spike trains. To account for the non-Poisson nature of retinal spike trains, we performed all analyses with spike trains with higher-order gamma statistics in addition to Poissonian spike trains. Interestingly, the properties of the low-pass filter depend only on the average input rate, but not on the modulation depth of sinusoidally modulated input. Thus, the response properties of our model are fully specified by just three parameters (low-frequency gain, cutoff frequency, and delay) for a given mean input rate and input regularity. This simple firing-rate model reproduces the response of spiking neurons to a step in input rate very well for Poissonian as well as for non-Poissonian input. We also found that the cutoff frequencies, and thus the filter time constants, of the rate-based model are unrelated to the membrane time constants of the underlying spiking models, in agreement with similar observations for simpler models.

Keywords LGN · Retina · Visual system · Rate model · Linear-nonlinear model

Action Editor: David Golomb

Partially funded by the Research Council of Norway (Grant 178892/V30 eNeuro), the Helmholtz Alliance on Systems Biology, and EU Grant 269921 (BrainScaleS). Simulations were performed using NOTUR resources.

Electronic supplementary material The online version of this article (doi:10.1007/s10827-013-0456-6) contains supplementary material, which is available to authorized users.

T. Heiberg (✉) · B. Kriener · G. T. Einevoll · H. E. Plesser
Department of Mathematical Sciences and Technology, Norwegian University of Life Sciences, P.O. Box 5003, 1432 Ås, Norway
e-mail: thomas.heiberg@umb.no

T. Tetzlaff
Institute of Neuroscience and Medicine (INM-6), Research Center Jülich, Jülich, Germany

A. Casti
Department of Mathematics, Gildart-Haase School of Computer Sciences and Engineering, Fairleigh Dickinson University, Teaneck, NJ, USA

1 Introduction

The thalamus is the central gateway for information passing from our sensory organs to cortex (Sherman and Guillery 2001). In particular, relay cells in the lateral geniculate nucleus (LGN) receive visual signals from retinal ganglion cells and transmit processed information to the primary visual cortex. These first stages of the visual system have been studied extensively. Since Rodieck (1965) introduced the difference-of-Gaussians (DOG) model for the spatial

Published online: 20 June 2013

receptive field of retinal ganglion cells, most modeling of the response properties of cells in the early visual system has been *descriptive* in the sense that the main purpose has been to summarize experimental data compactly in a mathematical form.

Various stimuli including random white noise, flashing spots, and drifting gratings have been applied to obtain receptive field models, and numerous spatiotemporal receptive-field filters have been suggested (see Ch.2 in Dayan and Abbott 2001). Generalized linear models (GLM) are a class of simplified descriptive models often used to describe neurons in the early stages of sensory processing (Pillow et al. 2005, 2008), or to characterize neural responses with white-noise stimuli (Chichilnisky 2001). Mechanistic models, on the other hand, aim to account for observed neural properties on the basis of known neural physiology and anatomy. Mechanistic models of the early visual system exist both in the form of spiking neuron models (e.g. Casti et al. 2008; Carandini et al. 2007; Kirkland and Gerstein 1998; Köhn and Wörgötter 1996) and firing-rate models (Einevoll and Heggelund 2000; Einevoll and Plesser 2002; Hayot and Tranchina 2001; Yousif and Denham 2007).

The main motivation for using firing-rate models rather than spiking neuron models is to reduce the dimensionality and complexity of the microscopic dynamics in order to allow for analytical tractability, efficient simulation, and intuitive understanding. The majority of rate-based neural population models have been justified by the diffusion approximation (see references in Nordlie et al. 2010), assuming a large number of tiny incoming synaptic inputs. This approach is valid for neurons that receive input spikes at a high rate through weak synapses (Johannesma 1968), but synapses between retinal ganglion cells and LGN relay cells are often much stronger and even single retinal spikes have been reported to initiate action potentials in the thalamic targets (Cleland et al. 1971; Sirovich 2008). In the present study, we investigate how firing-rate models perform in the context of LGN relay cells.

Nordlie et al. (2010) have recently investigated the firing-rate response properties of leaky integrate-and-fire (LIF) neurons receiving current input through strong synapses. They demonstrated that neuronal responses to sinusoidally modulated inhomogeneous Poisson processes could be described well by a combination of a linear first-order low-pass filter with a nonlinear activation function. This linear-nonlinear firing-rate model accurately predicted the population response for a variety of non-sinusoidal test stimuli.

In the present study, we use the same approach to investigate whether linear-nonlinear firing-rate models can describe the firing rate properties of LGN relay neuron models fitted to experimental data. In particular, we investigate spiking models with conductance-based synaptic currents and after-hyperpolarizing currents (Casti et al. 2008) as well as more abstract spike-response models (Carandini et al. 2007; Gerstner and Kistler 2002).

Moreover, we study the effect of input spike train regularity on the rate model, parameterized by the shape parameter of the gamma process. More regular input than Poisson, as observed in actual recordings (Troy and Robson 1992; Casti et al. 2008), increases the linearity of the activation function for high input rates, while low rates effectively become rectified.

In the Methods section, we introduce the spiking LGN neuron models along with a description of stimulation and response characteristics. We further summarize our simulation setup and detail how we extract linear-nonlinear firing-rate models from the results of simulations with spiking neuron models. In the Results section, we first show the results from stationary (unmodulated) stimulation to illustrate the shape of the activation function. Results from sinusoidal stimulation are presented along with optimized low-pass model filters that illustrate the high quality of the fits. We finally test the performance of the extracted rate models by comparing the actual responses to novel stimuli with the responses predicted by the firing-rate models.

2 Methods

2.1 Spiking models for LGN cells

The rate models of LGN cells investigated in this study are based on spiking neuron models of LGN cells proposed by Casti et al. (2008) and Carandini et al. (2007). We refer to these models as the *Casti* and *Carandini* models.

Casti et al. (2008) and Carandini et al. (2007) fitted their models to experimental data obtained from LGN relay neurons in cat and macaque, respectively. In both studies, retinal input and LGN output spike trains of a number of relay cells were recorded using a single electrode. This is possible because signal transmission across the strong retino-geniculate synapses can be recorded as S potentials using extracellular electrodes (Kaplan and Shapley 1984). The models of specific cat and macaque relay cells thus obtained are the starting point of our study.

Both model neurons receive input only through a single, excitatory synapse. Casti et al. (2008) initially included "locked inhibition" (Blitz and Regehr 2005), i.e., inhibition following excitation with a fixed delay, but observed that their model could fit the experimental data equally well with locked inhibition removed. They thus concluded that locked inihibition was not relevant under the stimulus regime studied and fixed the inhibitory conductance to zero. Carandini et al. (2007) designed their model with excitatory input only. In both cases, the resulting model neurons transform a single

input spike train $\{s_j\}$ arriving through a single synapse into an output spike train $\{t_k\}$. When interpreting results later, one should keep in mind that the model by Casti et al. (2008) matched experimental data best for LGN relay cells with moderate-to-high transfer ratios (Carandini et al. (2007) do not provide transfer ratios).

The models are summarized in Table 1 following the template suggested by Nordlie et al. (2009).

2.1.1 Casti model

The Casti model is a modified leaky integrate-and-fire (LIF) model with conductance-based excitatory and inhibitory synapses; for the sake of brevity, we have removed the (unused) inhibitory synapse in our sketch of the model.

The sub-threshold membrane potential $V(t)$ of the model neuron is governed by

$$C\frac{\mathrm{d}V}{\mathrm{d}t} = -G_L(V-V_L) - G_E(t)(V-V_E) - G_A(t)(V-V_A)\,, \quad (1)$$

$$G_E(t) = \sum_{\{s_j\}} g_E(t-s_j)\Theta(t-s_j)\,, \quad (2)$$

$$G_A(t) = \sum_{\{t_k\}} g_A(t-t_k)\Theta(t-t_k)\,, \quad (3)$$

$$g_X(t) = \bar{g}_X\left(\frac{t}{\tau_X}\right)e^{-\frac{t-\tau_X}{\tau_X}}\,. \quad (4)$$

Here, C is the membrane capacitance, G_L the persistent leakage conductance, $G_E(t)$ the total excitatory synaptic

Table 1 Overview of the neuron models. See Table 2 for parameters

A. Model summary	
Neuron model	Casti model and Carandini model
Input model	Spike trains realised by inhomogeneous Poisson and gamma point processes
B. Casti model	
Type	Leaky integrate-and-fire, conductance-based synapses, afterhyperpolarization (AHP)
	$C\frac{\mathrm{d}V}{\mathrm{d}t} = -G_L(V-V_L) - G_E(t)(V-V_E) - G_A(t)(V-V_A)$
	$G_E(t) = \sum_{\{s_j\}} g_E(t-s_j)\Theta(t-s_j)$
	$G_A(t) = \sum_{\{t_k\}} g_A(t-t_k)\Theta(t-t_k)$
Subthreshold dynamics	$g_X(t) = \bar{g}_X\left(\frac{t}{\tau_X}\right)e^{-\frac{t-\tau_X}{\tau_X}}$.
	Integrated using Runge-Kutta-Fehlberg 4/5 integration with adaptive step size
Spiking	Spike emission in time step of threshold crossing ($V(t_k) \geq V_{\mathrm{th}}$). Precise spike time found using linear interpolation.
Parameters	See Table 2A,B.
C. Carandini model	
Type	Spike-response model
	$V(t) = \sum_{\{s_j\}} V_{\mathrm{syn}}(t-s_j) + \sum_{\{t_k\}} V_{\mathrm{spike}}(t-t_k) + n(t)$
Subthreshold dynamics	$V_{\mathrm{syn}}(t) = V_{\mathrm{EPSP}}\,\frac{t}{\tau_{\mathrm{EPSP}}}e^{-\frac{t-\tau_{\mathrm{EPSP}}}{\tau_{\mathrm{EPSP}}}}\Theta(t)$
	$V_{\mathrm{spike}}(t) = \delta(t) - V_{\mathrm{reset}}\,e^{-t/\tau_{\mathrm{reset}}}\Theta(t)$
	Exact integration (Rotter and Diesmann 1999) with temporal resolution dt
Spiking	Spike emission at times $t_k \in \{n\,\mathrm{d}t \mid n \in \mathbb{N}\}$ with $V(t_k) \geq V_{\mathrm{th}}$
Parameters	See Table 2C
D. Input model	
Type	Spike train generated by an inhomogeneous Poisson/gamma point process
Details	Instantaneous rate: $a(t) = a_0 + a_1\cos(2\pi\, f_{\mathrm{stim}}\, t)$
Parameters	See Table 2D.

conductance evoked by the incoming spike train $\{s_j\}$, and $G_A(t)$ the total after-hyperpolarizing (AHP) conductance triggered by the outgoing spike train $\{t_k\}$. The associated reversal potentials are V_L, V_E, and V_A. The time course $g_X(t)$ of an individual conductance activation is modeled as an α-function with maximum $\bar{g}_X$ at $t = \tau_X$. $\Theta(t)$ is the Heaviside step-function.

A spike is fired when the membrane potential reaches the fixed threshold $V(t) = V_{\text{th}}$ from below. Instead of a voltage reset immediately after a spike, a transient activation of the AHP conductance $G_A(t)$ models the reset mechanism and subsequent refractory period. Modeling reset and refractoriness in this way ensures that the membrane potential $V(t)$ remains continuous upon threshold crossing. Because the membrane potential is not reset, it may remain above threshold for some time after a spike.

Figure 1 illustrates the dynamics of the model. From resting potential, this neuron comes close to threshold as a result of one incoming retinal spike. Excitability varies between the neurons, but a single incoming spike results in an increase in membrane potential by more than 50 % of the difference between resting potential and threshold for all the neurons in the study. Hence, we are clearly outside the diffusive regime.

Casti et al. (2008) recorded from two X-On and eight X-Off cells from six anesthetized adult cats. By recording S potentials along with spikes, input $\{s_j\}$ to and output $\{t_k\}$ from the cells could be recorded simultaneously (Kaplan and Shapley 1984). Although S potentials do not represent the entire input to an LGN relay cell, it is known that the LGN does not fire if retinal ganglion spikes are silenced. It is therefore reasonable to assume that the S potentials are the dominant monosynaptic excitatory input. The cells were stimulated with temporally modulated, spatially homogeneous circular spots of various diameters.

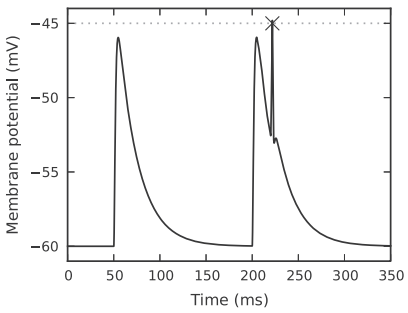

Fig. 1 Membrane potential $V(t)$ (*solid line*) for the Casti model with input spikes at 50 ms, 200 ms, and 220 ms. The *third input spike* evokes and output spike at 221.8 ms, marked by a cross. The *dotted horizontal line* marks the threshold V_{th}

In Casti et al. (2008), the model specified by Eqs. (1)–(4) was fitted as follows for each cell recorded: Most model parameters were fixed to plausible values, cf. Table 2A. The model neuron was then stimulated with the recorded S potential trains, and the response of the model neuron was compared to the experimentally recorded response using a cost function sensitive to spike-timing mismatches. They then used the Simplex algorithm (Nelder and Mead 1965) to find the values of $(\tau, \tau_A, \bar{g}_E, \bar{g}_A)$ that minimized the cost function. Here, $\tau = C/G_L$ is the passive membrane time constant of the model neuron. For details of the fitting procedure, see Casti et al. (2008).

Table 2B shows four sets of optimized parameter values, which were obtained in Casti et al. (2008) by fitting the responses of three neurons, of which one was fit for two different flashing spot sizes. These four cases span the range of response types studied here of all data reported by Casti et al. (2008), so we will use them for illustration in the remainder of this study. Complete data for all 14 optimized parameter sets from Casti et al. (2008) is given in the supplementary material (Supplementary Table 1).

We implemented this model neuron in the NEST Simulator (Gewaltig and Diesmann 2007) as model `iaf_cxhk_2008` using a Runge-Kutta-Fehlberg 4/5 ODE solver with adaptive step-size control from the GNU Science Library (Galassi et al. 2001). Minor modifications to the original model in Casti et al. (2008) are described in the supplementary material.

2.1.2 Carandini model

The Carandini model is a spike-response model (Gerstner and Kistler 2002), i.e., the membrane potential is given as a sum of stereotyped events:

$$V(t) = \sum_{\{s_j\}} V_{\text{syn}}(t - s_j) + \sum_{\{t_k\}} V_{\text{spike}}(t - t_k) + n(t) \qquad (5)$$

$$V_{\text{syn}}(t) = V_{\text{EPSP}} \frac{t}{\tau_{\text{EPSP}}} e^{-\frac{t-\tau_{\text{EPSP}}}{\tau_{\text{EPSP}}}} \Theta(t) \,, \qquad (6)$$

$$V_{\text{spike}}(t) = \delta(t) - V_{\text{reset}}\, e^{-t/\tau_{\text{reset}}} \Theta(t) \,. \qquad (7)$$

$V_{\text{syn}}(t)$ is the postsynaptic potential, $V_{\text{spike}}(t)$ the waveform describing a spike and the subsequent after-hyperpolarization with initial amplitude V_{reset} and decay time constant τ_{reset}, and $V_{\text{syn}}(t)$ the response to incoming spikes, with maximal response V_{EPSP} at time τ_{EPSP}. As before, $\{s_j\}$ and $\{t_k\}$ are the incoming and outgoing spike trains, respectively. $n(t)$ is Gaussian-distributed white noise. The model produces a spike when the membrane potential exceeds the spike threshold, $V(t) > V_{\text{th}}$.

The dynamics of the model is illustrated in Fig. 2. Given a neuron at rest, a single incoming spike results in an increase

Table 2 Parameters

A. Casti model, common parameters					
τ_E	Excitatory synaptic time constant				1 ms
C	Membrane capacitance				1 nF
G_L	Persistent leak conductance				0.1 μS
V_L	Resting potential				−60 mV
V_{th}	Spike threshold				−45 mV
V_E	Excitatory reversal potential				20 mV
V_A	AHP reversal potential				−95 mV
B. Casti model, specific parameters					
		Neuron 1	Neuron 1*	Neuron 6	Neuron 8
τ	Membrane time constant	17.8 ms	11.7 ms	16.3 ms	7.2 ms
τ_A	AHP time constant	0.47 ms	0.60 ms	1.00 ms	0.26 ms
$\bar{g}_E$	Exc. conductance	0.16 μS	0.11 μS	0.08 μS	0.07 μS
$\bar{g}_A$	AHP conductance	0.42 μS	0.56 μS	0.60 μS	0.44 μS
C. Carandini model					
τ_{EPSP}	Time constant for excitatory PSPs				6.0 ms
τ_{reset}	Time constant of AHP potential				12.0 ms
V_{EPSP}	Amplitude of excitatory PSPs				0.56
V_{reset}	Amplitude of AHP potential				0.82
V_{th}	Spike threshold				1.00
V_{noise}	Noise amplitude				0.25
D. Input parameters					
a_0	Input rate				$\{0, 5, \ldots, 160\}\,\text{s}^{-1}$
a_1	Input amplitude				$\{0, 20, \ldots, 100\}\,\text{s}^{-1}$
f_{stim}	Input frequency				$\sim 10^{\{0.0, 0.1, \ldots, 3.0\}}$ Hz
Γ	Input regularity (Γ order)				{1, 3, 6}
E. Simulation parameters					
$\text{d}t$	Time resolution				0.1 ms
T	Simulation time				100 s

A: Fixed parameters common to all models from Casti et al. (2008).

B: Optimal parameter sets for neurons no. 1, 6, and 8 from Casti et al. (2008). Parameters were obtained under stimulation with flashing small spots, except for Neuron 1*, which was obtained with a full-field stimulus.

C: Optimal parameter set for neuron 122R4-5 from Carandini et al. (2007); potentials are in arbitrary units.

D: Input parameters used to test the model.

E: Simulation parameters. Data in A–C are from Casti et al. (2008, Table 1, 2) and Carandini et al. (2007, Table 1), respectively.

in membrane potential by more than 50 % of the distance between resting potential and threshold for all neurons in the Carandini study. As with the Casti neurons, we operate outside the diffusive regime.

Carandini et al. (2007) fitted this model to nine cells (seven On, two Off; three P, four M, two unclassified) recorded from six adult macaques. Both input and output spike trains ($\{s_j\}$, $\{t_k\}$) were recorded. The cells were stimulated with spatially homogeneous light spots restricted to the receptive field center and varying continuously in time.

Optimal parameter sets for the four free parameters of the model (τ_{EPSP}, V_{EPSP}, τ_{reset}, V_{reset}) were obtained by minimizing the difference between the low-pass filtered output spike trains recorded from experiment and simulation. Minimization was performed by a custom procedure described in Carandini et al. (2007). The optimal noise level (V_{noise}) was obtained by simulating the model response at a number of amplitudes for the noise term $n(t)$ and by finding the noise level that yielded the best fit. Table 2C shows the optimal parameter set for one neuron from the Carandini study. Complete data for all nine neurons from Carandini et al. (2007) is given in the supplementary material (Supplementary Table 2).

We implemented this model neuron in the NEST Simulator (Gewaltig and Diesmann 2007) as model `iaf_chs_2007` using exact integration (Rotter and Diesmann 1999; Plesser and Diesmann 2009). Minor modifications to the original model are described in the supplementary material.

2.2 Characterization of response properties

2.2.1 Stimulation

We stimulated model neurons with sinusoidally modulated inhomogeneous Poisson or gamma process spike trains, as illustrated in Fig. 3. Specifically, we considered spike

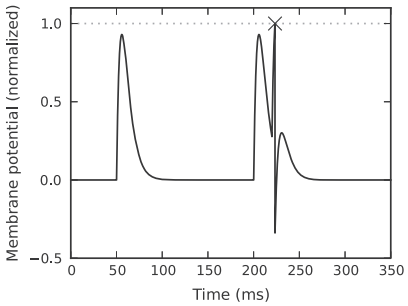

Fig. 2 Membrane potential $V(t)$ (*solid line*) for the Carandini model with input spikes at 50 ms, 200 ms, and 220 ms. The *third input spike* evokes and output spike at 223.4 ms, marked by a cross. The *dotted horizontal line* marks the threshold V_{th}

trains that are realizations of point processes with rate (or intensity)

$$a(t) = a_0 + a_1 \sin 2\pi f_{\text{stim}} t \ . \tag{8}$$

Mean rates were in the range $0 < a_0 \leq 160\,\text{s}^{-1}$, while we limited the modulation depth to $0 \leq a_1 \leq a_0$ to avoid rectification issues. Modulation frequencies f_{stim} varied from 0 Hz to 1 kHz.

Input spike times $\{s_1, s_2, \dots\}$ were chosen such that the time-rescaled spike trains $\{u_1, u_2, \dots\} = \{u_j | u_j = A(s_j)\}$ form homogeneous Poisson or gamma processes of the desired order (Brown et al. 2002). Here,

$$A(t) = \int_0^t a(s)\text{d}s = a_0 t - \frac{a_1}{2\pi f_{\text{stim}}} \cos 2\pi f_{\text{stim}} t \tag{9}$$

is the cumulated rate (cumulated intensity) of the process. For brevity, we occasionally refer to Poisson processes as gamma processes with order $\Gamma = 1$.

The `sinusoidal_gamma_generator` model in the NEST Simulator (Gewaltig and Diesmann 2007) generates spike trains using this algorithm.

2.2.2 Response characteristics

We characterized the response of the neurons by a sinusoidal rate model

$$r(t) = r_0 + r_1 \cos(2\pi f_{\text{stim}} t + \phi_1) + \sum_{m=2}^{\infty} r_m \cos(2m\pi f_{\text{stim}} t + \phi_m) \ , \tag{10}$$

as illustrated in Fig. 3. For a purely linear response, r_0 represents the background firing rate of the neuron, r_1 the stimulus response amplitude (with phase shift ϕ_1), and we expect $r_m = 0$ for all higher harmonics ($m \geq 2$).

We will quantify the linearity of the response to periodic stimuli using Fourier analysis. Spectra of spike trains

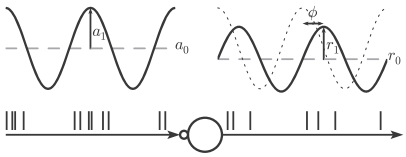

Fig. 3 A model neuron is driven by a spike train with sinusoidally modulated rate $a(t)$ with mean a_0, modulation depth a_1, and frequency f_{stim}, cf. Eq. (8). As a first-order approximation, the output spike train of the neuron can be characterized by the sinusoidally modulated response firing rate $r(t)$ with mean r_0, amplitude r_1, frequency f_{stim} and phase ϕ, cf. Eq. (10). Adapted from Nordlie et al. (2010), Fig. 1

have a continuous component due to the jitter in spike times. For Poisson spike trains this spectrum is perfectly flat. For spike trains including refractory effects (such as trains with gamma ISI-statistics for $\Gamma > 1$), the spectra have a dip near the origin (Franklin and Bair 1995). To test whether the neuronal response is indeed linear, we compare the Fourier amplitudes at higher harmonics r_m ($m \geq 2$) with the continuous background component B, as illustrated in Fig. 4.

Estimates of the Fourier amplitudes r_m, phases ϕ_m and continuous background component B were obtained as follows: We recorded output spike trains $\{t_k^{(n)}\}$ for $n = 1, \dots, N$ trials of duration T, with temporal resolution $dt = 0.1$ ms. We then computed per-trial spectra

$$S^{(n)}(f) = \sum_{t \in \{t_k^{(n)}\}} e^{-i2\pi f t} \tag{11}$$

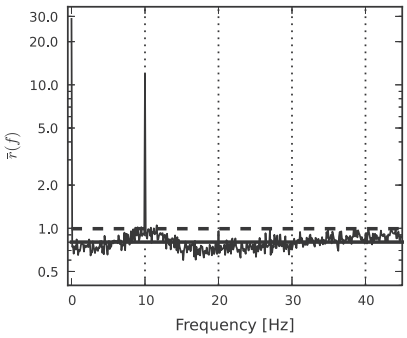

Fig. 4 Spectrum of response amplitudes $\bar{r}(f)$ obtained from $N = 50$ trials of $T = 100$ s duration, recording from a *Casti 1* model neuron stimulated by a sinusoidally modulated gamma process ($a_0 = 40\,\text{s}^{-1}$, $a_1 = 10\,\text{s}^{-1}$, $f_{\text{stim}} = 10$ Hz, $\Gamma = 3$); for this figure, $\Delta f = 0.1$ Hz and $f_{\text{max}} = 45$ Hz. The *horizontal solid line* is the estimated background B, while the dashed line marks the 99 % confidence limit for signals exceeding the background, cf Eq. (23). *Thin dotted lines* mark the harmonics. This spectrum shows no significant power at the second, third or fourth harmonic

at frequencies $f = j\Delta f$ chosen such that the stimulation frequency f_{stim} is an integer multiple of Δf. We thus obtained per-trial Fourier amplitudes

$$r^{(n)}(f) = \begin{cases} |S^{(n)}(0)|/T & f = 0 \\ 2|S^{(n)}(f)|/T & f > 0 \end{cases} \tag{12}$$

and phases

$$\phi^{(n)}(f) = \arg S^{(n)}(f) \, . \tag{13}$$

The factor 2 in the amplitudes for $f > 0$ accounts for the power at negative frequencies. We averaged across trials to obtain estimates of the true Fourier amplitudes and their standard deviations

$$\bar{r}(f) = \frac{1}{N} \sum_{n=1}^{N} r^{(n)}(f) \tag{14}$$

$$\sigma_r(f) = \sqrt{\frac{1}{N-1} \sum_{n=1}^{N} \left(r^{(n)}(f) - \bar{r}(f)\right)^2} \, . \tag{15}$$

Phases were averaged on the unit circle (Goldberg and Brown 1969)

$$\bar{\phi}(f) = \arg \sum_{n=1}^{N} e^{i\phi^{(n)}(f)} \, . \tag{16}$$

Estimates of the response amplitudes at the harmonics are thus given by

$$\bar{r}_m = \bar{r}(mf_{\text{stim}}) \tag{17}$$

and correspondingly for the standard deviations σ_m and phases $\bar{\phi}_m$.

In estimating the amplitude B of the continuous background of the spectrum, we exploited the fact that the spectrum excluding the harmonics essentially is flat. Instead of estimating the background at each harmonic by a linear fit to $\bar{r}(f)$ in the vicinity of each harmonic, we thus simply averaged across the entire spectrum, excluding the harmonics, and obtained

$$B = \frac{1}{|F_B|} \sum_{f \in F_B} \bar{r}(f) \, , \tag{18}$$

where

$$F_B = \{j\Delta f | 0 < j\Delta f < f_{\max} \wedge j\Delta f \neq mf_{\text{stim}} \forall m \in \mathbb{N}\} \, . \tag{19}$$

Here $f_{\max}$ is the upper limit of the spectrum we computed; unless otherwise noted, we used $\Delta f = 0.1\, f_{\text{stim}}$ and $f_{\max} = 10.5\, f_{\text{stim}}$. The standard deviation of B is then given by

$$\sigma_B = \sqrt{\frac{1}{|F_B|} \sum_{f \in F_B} \sigma_r^2(f)} \, . \tag{20}$$

A higher harmonic ($m \geq 2$) carries significant signal power if the mean response amplitude $\bar{r}_m$ at the harmonic exceeds the mean background amplitude B in a statistically significant way. A one-sided z-test with test statistic

$$z = \frac{\bar{r}_m - B}{\Sigma} \, , \tag{21}$$

where

$$\Sigma = \sqrt{\frac{\min_{m \geq 2} \sigma_m^2}{N} + \frac{\sigma_B^2}{N|F_B|}} \tag{22}$$

suffices to test for significance, because we collect data across $N > 30$ trials (Walpole and Myers 1993, Ch. 8.5). This statistic combines the standard deviations of harmonics (one data point from each of N trials) and background ($|F_B|$ data points from each of N trials). To obtain a test that can be applied to all higher harmonics and is sensitive for non-linearities, we use the smallest σ_m across all higher harmonics. This minimizes Σ and thus maximizes z. As a consequence, the test may indicate significant power at a higher harmonic even if there is none, but we consider such false positives less problematic than false negatives that may occur if we, e.g., choose the largest σ_m in our definition of Σ.

Then, $\bar{r}_m > B$ with 99 % confidence if $z > 2.34$ or, equivalently, if

$$\bar{r}_m > B + 2.34\Sigma \, . \tag{23}$$

We will use this criterion to identify significant nonlinearities in model responses.

2.3 Simulation

Simulations for all 23 model configurations reported by Casti et al. (2008) and Carandini et al. (2007) were performed with the NEST Simulator (Gewaltig and Diesmann 2007).

In practice, we simulated N trials by creating N mutually independent generator-neuron pairs in a single NEST simulation. Membrane potentials were randomized upon network initialization and data collection started only after an equilibration period of 1 s simulated time. All simulations were performed with a spike-time resolution of 0.1 ms.

Simulations were performed on a system with Intel Xeon 2 CPUs running Linux 2.6.18 using NEST 2.1.r9693. Software was compiled with the GNU Compiler v. 4.1.2 and linked against the GNU Science Library v. 1.14. Trials were configured using the NeuroTools.parameters package (Muller et al. 2009). Data analysis was performed on the same computers and Apple MacBook Pro computers using NumPy 1.5.1 and 1.6.2 and Matplotlib 1.0.1 and 1.1.1 under Python 2.7.1 and 2.7.3.

2.4 Rate model description

A linear, time-invariant (LTI) system is completely characterized by its *impulse response*. That is, for any input, the output can be calculated as a convolution of the input and the impulse response. A wide class of non-linear systems can be described by a linear convolution with a kernel $h(t)$ followed by a non-linear *activation function* $g(\cdot)$, so that the response is given by

$$r(t) = g(h(t) * a(t)) \ . \tag{24}$$

For each model neuron described by Carandini et al. (2007) and Casti et al. (2008), we need to find the activation function $g(\cdot)$ and the kernel $h(t)$. For constant input, $a(t) = a_0$, the convolution becomes the identity operation, provided the kernel is normalized ($\int h(t)dt = 1$). We thus determine $g(\cdot)$ by measuring the response to input with fixed rate, $r_0 = g(a_0)$ for a range of a_0 and obtain a continuous representation of $g(\cdot)$ by spline interpolation. In practice, we use $a_0 \in \{0, 5, \ldots, 160\}\text{s}^{-1}$.

To obtain the kernel $h(t)$, we linearize the activation function around a given *working point* (a_0, r_0) using Taylor expansion. The response to $a(t) = a_0 + a_1 s(t)$ can then be expressed as

$$\begin{aligned} r(t) &= g(h(t) * (a_0 + a_1 s(t))) \\ &= g(a_0) + g'(a_0)h(t) * (a_1 s(t)) + \mathcal{O}(a_1^2) \\ &\approx r_0 + h_0(t) * (a_1 s(t)) \ , \end{aligned} \tag{25}$$

where we have introduced the linear impulse response function

$$h_0(t) = g'(a_0)h(t) \tag{26}$$

which combines the normalized kernel with the linear gain. For general $g(\cdot)$, $h(t)$ and $s(t)$, this approximation is only valid for small-amplitude signals ($|a_1 s(t)| \ll |a_0|$).

Based on this approximation, we can obtain $h_0(t)$ as follows: We record model responses to sinusoidally modulated input ($s(t) = \sin 2\pi f_{\text{stim}} t$, cf. Eq. (8)) for fixed a_0 and $a_1 \leq a_0$ at a range of logarithmically spaced frequencies f_{stim} (see Table 2D). The Fourier amplitude $\bar{r}(f_{\text{stim}})$ and phase $\bar{\phi}(f)$ of the response, computed according to Eqs. (14) and (16), then yield the complex transfer function, i.e., the Fourier transform of the linear impulse response $h_0(t)$

$$H_0(f_{\text{stim}}) = \frac{\bar{r}(f_{\text{stim}})}{a_1} e^{i\bar{\phi}(f_{\text{stim}})} \ . \tag{27}$$

We then fit a first-order low-pass filter

$$\tilde{H}_0(f) = \frac{\gamma}{(1 + i\frac{f}{f_c})} e^{-2\pi i f d} \tag{28}$$

to the empirical transfer function to capture it with as few parameters as possible: the cutoff frequency f_c, the low-frequency gain γ and the delay d; see Nordlie et al. (2010) for details of the fitting procedure. For each set of stimulus parameters (a_0, a_1, f_{stim}), we obtained five independent fits, from which we computed mean values and standard deviations of the fitted parameters f_c, γ and d. In the time domain, Eq. (28) corresponds to a delayed exponential kernel

$$h_0(t) = \mathcal{F}[\tilde{H}_0(f)](t) = \gamma \tau^{-1} e^{-\frac{t-d}{\tau}} \Theta(t - d) \tag{29}$$

where $\Theta(\cdot)$ is the Heaviside function and $\tau = 1/(2\pi f_c)$ the filter time constant.

We now define our linear-nonlinear rate model as

$$r_{\text{NL}}(t) = g(h_0(t) * a(t)) \ . \tag{30}$$

Two approximations were made in deriving Eq. (30) from the original model defined by Eq. (24): the linearization of $g(\cdot)$ and the assumption that $h_0(t)$ is a first-order low-pass filter. Therefore, even though a comparison of Eqs. (26) and (29) suggests that $\gamma = g'(a_0)$ should depend only on a_0, while $h_0(t)$ should be independent of all stimulus parameters, this may not hold true in practice, due to the approximations involved. We will discuss this further in Section 3.2.

We note that the linear-nonlinear model of Eq. (24) can be mapped to the following delay differential equation using the linear chain trick (Nordbø et al. 2007):

$$\tau \dot{u}(t) = -u(t) + a(t - d), \quad r(t) = g(u(t)). \tag{31}$$

Here, $u(t) = (a * h)(t)$ and $h(t)$ is an exponential kernel.

3 Results

We initially present representative results from simulations using the Casti model (Casti et al. 2008). Later, we show that the results generalize to the Carandini model (Carandini et al. 2007). Additional results from both models can be found in the supplementary material.

3.1 Stationary response

With only stationary excitatory input, the output rate r_0 is expected to increase monotonically with increasing input rate a_0. This is indeed the case when the model operates under normal conditions (Fig. 5). Refractoriness entails that the firing rate curve will flatten out for high input rates. Curiously, output rates start to decrease for high inputs rates for certain configurations of the Casti model as shown in Fig. 5 G–I). This is a consequence of the repolarizing mechanism of the Casti model and the absence of inhibitory input: The model has no explicit reset or refractory time. Instead, the neuron remains unable to fire as long as the membrane potential remains above threshold. Thus, if the

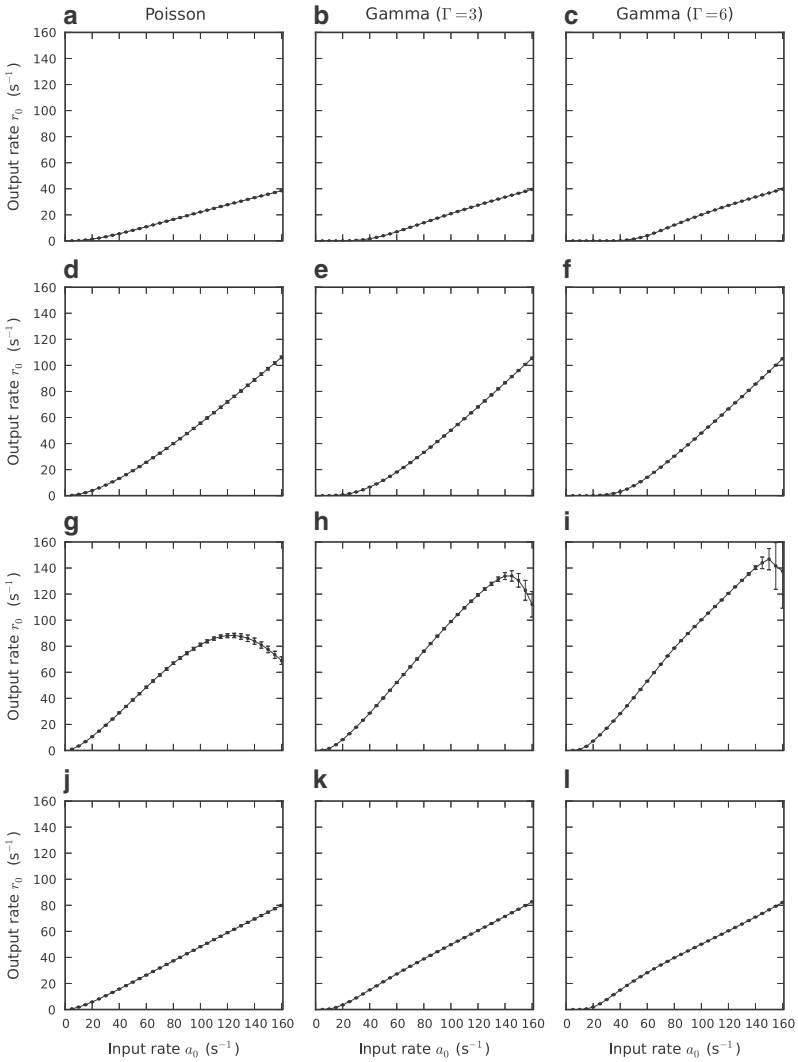

Fig. 5 Stationary response for selected Casti neurons. Symbols illustrate mean output rates r_0 across trials. *Error bars* denote one standard deviation in either direction. Each row contains results from one neuron configuration, from top to bottom: neuron 6, neuron 8, neuron 1, neuron 1*. The first and second neurons have low and high throughput ratio respectively. The third and fourth row contain responses from the same neuron, but with parameters obtained from stimulation with different spot sizes (see Section 2.1.1). Columns represent different input regularities, from left to right: Poisson ($\Gamma = 1$), gamma ($\Gamma = 3$) and gamma ($\Gamma = 6$)

neuron receives a volley of input sufficiently strong to push it so far across threshold that the afterhyperpolarizing current activated after an output spike does not repolarize the neuron to a subthreshold membrane potential, then the neuron will remain refractory until a lapse in input occurs that is long enough to allow the leak current to repolarize the neuron. This effect also increases output rate variability, as the time spent above threshold may vary considerably from trial to trial. As this effect only occurs with persistent high input rates, we will not discuss it further.

The output rates are observed to be lower than the input rates, meaning that the neurons have to integrate several incoming spikes to reach threshold. The neurons differ considerably in transfer ratio r_0/a_0, as illustrated by the difference between the top two rows in Fig. 5.

Stimulation within the receptive field center and stimulation of the whole receptive field lead to quantitatively different activation functions (Fig. 5G, J).

The more input spikes the neurons need to integrate to produce a response, the more rectified-linear the stationary response curves become. For example, the neurons in the two top rows of Fig. 5 hardly produce any output for low input rates, but above a certain level output rates start to increase nearly linearly with the input rate.

Input signals with high-order gamma statistics causes stationary responses to change in two ways because short interspike intervals (ISIs) are rarer. First, as spikes arrive more evenly, higher input rates are needed to evoke any response. Second, neurons are less likely to stay above threshold for extended periods of time as evidenced by the linearization of the stationary response curve with increasing gamma order in Fig. 5 G–I.

3.2 Response to sinusoidal stimuli

In principle, measuring the linear response $H_0(f)$ of a nonlinear system at a working point a_0 requires infinitesimally small perturbations. In practice, one needs to determine empirically the perturbation amplitudes up to which response nonlinearities may be neglected. To this end, we quantified the frequency contents of the response $r(t)$. For a linear system, a sinusoidal stimulus with frequency f_{stim} will give rise to a single peak in the response spectrum at the same frequency f_{stim}. Any nonlinearities in the system will produce higher harmonics in the response rate.

To measure the degree of nonlinearity, we compared the amplitudes of the principal and second harmonics, r_1 and r_2, with the background-firing/"noise" level $z = 2.34$ (Fig. 6). The first-order low-pass filter provides an overall good fit to the base harmonic in the response, while the higher harmonics (second harmonic included in figure) show little or no significant power.

When a neuron with a rectified-linear stationary response curve (e.g., Fig. 5C) operates near the kink in the response curve, the second harmonic of the non-stationary response becomes more pronounced with increasing regularity for some neurons (see Fig. 6, third column). Overall, we conclude that the low power found at higher harmonics

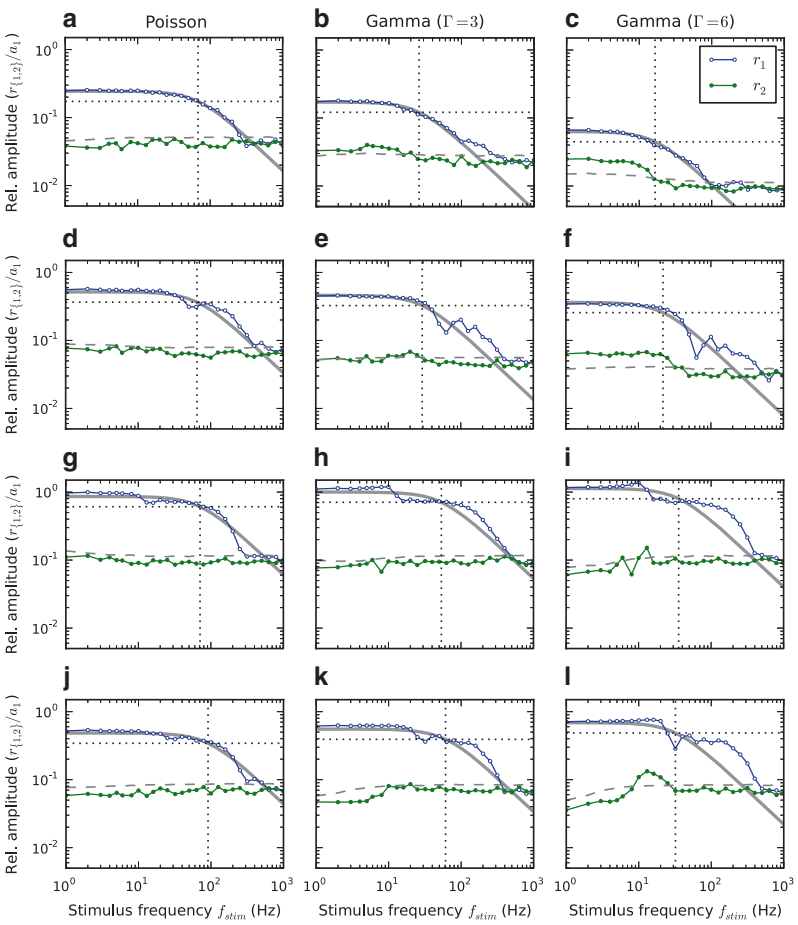

Fig. 6 Low-pass characteristic of the response to sinusoidal stimuli ($a_1 > 0$) for representative Casti neurons. The figure illustrates how a first-order low-pass filter with cutoff frequency f_c, low-frequency gain γ, and delay d fits the response of the Casti model to time varying input. Symbols represent measured responses $r_n(f_{\text{stim}})/a_1$ for principal (*blue*) and second (*green*) harmonics ($n \in \{1, 2\}$). Gray curves show fitted first-order low-pass filters. Dotted vertical lines mark fitted cutoff frequencies f_c. Dashed horizontal lines represent noise level $z = 2.34$. Stimulus parameters: $a_0 = 40\ \text{s}^{-1}$, $a_1 = 10\ \text{s}^{-1}$. Same panel arrangement as in Fig. 5

indicates that the dynamics of the Casti model are linear beyond the rectification point and thus can be captured by a linear-nonlinear model as proposed here.

As pointed out in Section 2.4, the gain of the low-pass filter should fulfill $\gamma = g'(a_0)$, while the cutoff frequency f_c and delay d should be independent of both mean input rate a_0 and modulation amplitude a_1 for a linear system. Nordlie et al. (2010) found that these expectations are reasonably fulfilled for integrate-and-fire neuron models of retinogeniculate transmission.

To investigate whether this decomposition holds for the models studied here, we obtained response parameters γ, f_c, and d for a range of stimulus parameters (a_0, a_1) with $a_1 \leq a_0$. Results for two typical neurons as shown in Fig. 7 demonstrate that the response properties are largely independent of modulation depth a_1 for given mean input rate a_0. Data in Fig. 7 are for Poisson input, but we found similar results for higher order gamma input ($\Gamma = 3$, $\Gamma = 6$; data not shown).

We observed further that $\gamma \approx g'(a_0)$ holds across neuron models and stimulus parameters, with mild deviations for cases with very high throughput (data not shown), providing further evidence that the linearization in Eq. (25) and the low-pass filter approximation in Eq. (28) are reasonable for the Casti and Carandini models. Given that the stationary response curves in Fig. 5 have approximately constant slope $g'(a_0)$, we expect constant low-frequency gain γ. Fig. 7 A, B indicates that this expectation is fulfilled to a reasonable degree.

The cutoff frequency f_c (Fig. 7 C, D) and, in some cases, the delay d (Fig. 7 F), depend on the mean input rate a_0. The latter applies to the high-throughput neurons (Casti neurons 1, 2, and 5) in particular. The neuronal responses for the models considered here thus cannot be decomposed into a gain dependent on the working point and a kernel independent of it.

However, the parameters γ, f_c, and d of our linear-nonlinear model are independent of modulation depth a_1. This is a key property of the model: Parameters obtained for one value of a_1 will apply to any modulation depth $a_1 \leq a_0$, rendering the model applicable to a wide range of stimuli provided the fixed mean input rate is approximately constant. Furthermore, as the dependence of the cutoff frequency f_c on input rate a_0 is rather weak, the rate models are expected to generalize well when driven with other stimuli. Also, in those cases where delay d depends on a_0, f_c increases along with d. The difference between rate models for different working points may effectively be reduced: As

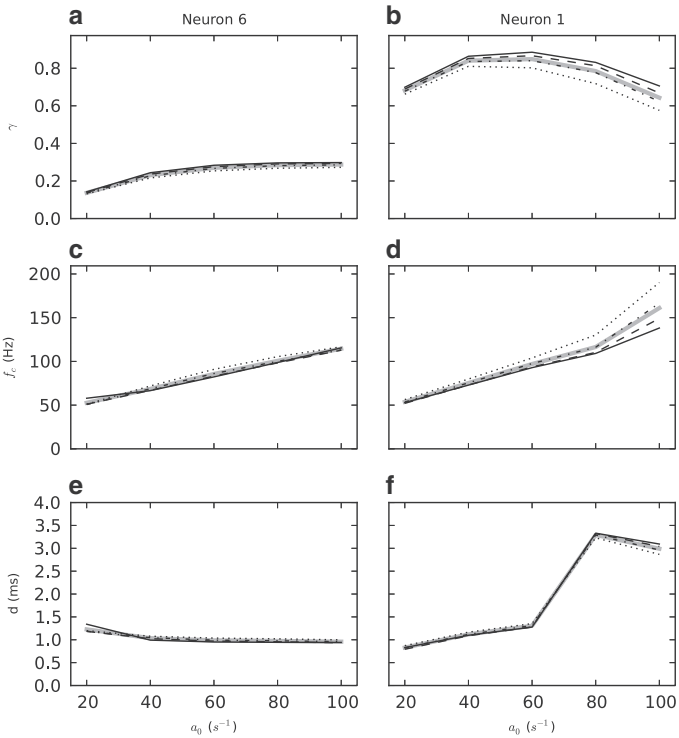

Fig. 7 Rate model parameters (γ, f_c and d) for Poisson ($\Gamma = 1$) input for two Casti neurons. The left column illustrates typical parameter variation (neuron 6). The right column illustrates the results from a high throughput neuron (neuron 1). *Solid, dashed, dash dotted and dotted black lines* represent $a_1 = \{0.25, 0.5, 0.75, 1.0\} \times a_0$ respectively. Thick, *grey lines* indicate mean values

input rate changes, an increased cutoff frequency f_c entails faster responses, which are compensated by an increased delay d.

3.2.1 Cutoff frequencies

Low-frequency signals pass through low-pass filters essentially unchanged, while signals with frequencies higher than the cutoff frequency are attenuated. The cutoff frequency of a fitted low-pass filter hence describes the tracking speed of a neuron model.

Values for all neurons studied are listed in Table 3. In summary, for Poisson input with a mean rate $a_0 = 40\ \mathrm{s}^{-1}$ (consistent with the S potential recordings and retinal ganglion cells in general) and modulation depth $a_1 = 10\ \mathrm{s}^{-1}$, cutoff frequencies f_c for the Casti neurons ranged from 48.7 to 93.9 Hz. This corresponds to rate-model time constants $\tau = 1/(2\pi f_c)$ from 3.3 to 1.7 ms.

Table 3 Cutoff frequencies in Hz

Model	Poisson	$\Gamma = 3$	$\Gamma = 6$
Casti			
1	70.9	53.6	35.7
1*	91.0	61.0	32.1
2	93.9	93.2	91.2
2*	73.0	45.3	24.1
3	68.9	31.9	21.3
3*	48.7	25.0	18.8
4	49.9	23.2	14.5
5	71.4	61.7	40.7
6	68.0	26.1	16.6
6*	89.5	37.0	23.8
7	81.4	32.8	20.1
8	64.7	29.4	21.8
9	88.6	33.5	21.5
10	91.7	32.7	20.5
Carandini			
120L15-1	30.4	24.0	19.8
121R11-1	18.4	16.7	16.7
121R13-4	32.5	26.1	24.9
121R14-4	15.7	15.0	14.7
121R15-5	34.6	32.8	36.2
121R7-1	32.8	56.6	46.6
122R4-2	53.5	46.0	42.3
122R4-3	45.4	33.1	29.3
122R4-5	35.6	24.9	20.4

The asterisk indicates that the neuron parameters were obtained from stimulation extending beyond the neuron's receptive field center. Stimulus parameters: $a_0 = 40\ \mathrm{s}^{-1}$, $a_1 = 10\ \mathrm{s}^{-1}$.

With few exceptions, the cutoff frequency drops with increased input regularity (Table 3). However, at higher input rates, increased input regularity results in higher cutoff frequencies for neurons with high transfer ratios (Supplementary Figure 4). This behavior is typically seen in neurons where AHP has relatively little effect. Across the full set of Casti neurons and input rates, cutoff frequencies varied from approximately 30 Hz to approximately 230 Hz (data not shown).

3.3 Test of linear-nonlinear model

3.3.1 Step test

As a first test of the rate model of Eq. (24), we drove it with a step in the input firing rate. Population-averaged responses of 50,000 independent Casti neurons (black curves) are shown in Fig. 8 along with the predictions of the firing-rate models (gray curves). The step response is seen to be well predicted by the firing-rate model.

An overshoot can be seen in the simulation results for some of the neurons following the step in the input rate. The magnitude of the overshoot increases with input regularity (Fig. 8). The maximal overshoot observed exceeded 30 % of the sustained post-step output rate (Supplementary Figure 5C), but for most input/neuron combinations it was much lower.

The overshoot occurs when a significant number of neurons prior to the input-rate step have a membrane potential close to threshold. As the input rate suddenly increases, many of these neurons will receive an input spike within the time frame required to produce an output spike. In cases with strong refractoriness (large AHP conductance $\bar{g}_\mathrm{A}$ and/or time constant τ_A), this leaves few neurons to spike until the refractory effects wane. Different neurons exhibit this behavior at different input rates.

3.3.2 Recorded retinal spike trains

To further validate the performance of the LGN rate models, we tested them on recorded retinal spike trains with low baseline firing rates and transients exceeding 150 s^{-1}. The spike trains were derived from S potentials captured by an electrode whose tip was extremely close to the relay cell soma (see Section 2.1). As in Casti et al. (2008), such a recording was deemed suitable for this analysis if the following conditions were met: (1) The recording was stable over a period of hours, indicating that the cell was not damaged by the electrode, (2) the S potentials stood out well above the extracellular membrane potential noise and could easily be identified by simple thresholding and subsequent principal components analysis, and (3) there was an absence of short inter-event intervals ($<$ 2 ms), giving

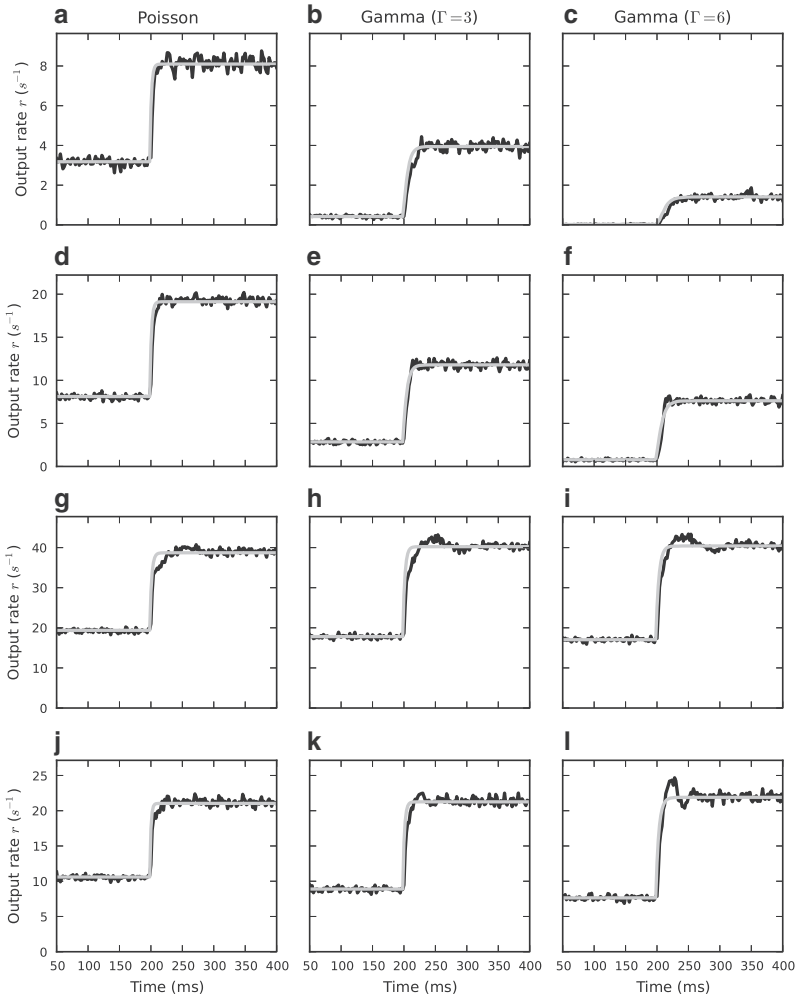

Fig. 8 Population-averaged step responses for selected Casti neurons. Firing rate $r(t)$ in response to an instantaneous increase in the input firing rate $a(t)$ at time $t = 100$ ms from 30 to 50 s^{-1}. Comparison between simulation results (black curves; population-averaged response of 50000 neurons, bin size $dt = 2.0$ ms) and prediction of the linear-nonlinear model (24) (*gray curves*) with measured activation function $g(a_0)$ and transfer kernel $h(t)$. Same panel arrangement as in Fig. 5

strong evidence that the S potentials were elicited by a single retinal ganglion cell. Each of the relay cells recorded had a moderate-to-high transfer ratio (ratio of LGN output spikes to S potential input events) between 0.15 and 0.7, a range for which the Casti model was accurate.

The monitor stimulus used to drive the ganglion cells was a noisy flashing spot modulated at 160 Hz by a naturalistic distribution of light intensities (van Hateren 1997) relative to a gray background in the photoptic range (~ 25 cd/m^2). A stimulus run consisted of a single 8-second realization of this stimulus repeated 128 times. The spot size was fixed for a set of 128 repeat trials, but was varied between runs from sub-receptive-field center sizes to full field. All cells were located within 15 degrees of area centralis in the adult cat.

To compare the perfomance of the spiking and rate-based models, we obtained comparable responses from both types of models as follows. For the rate-based model, we pooled experimental spike trains across trials and determined the averaged response rate by means of kernel density estimation (Shimazaki and Shinomoto 2010), using the *fixed kernel* method to optimize the kernel bandwith. We thus obtained a continuous rate function $a_{\mathrm{RGC}}(t)$ describing responses of real retinal ganglion cells. Applying Eq. (24) to this rate yields the reponse of the rate model $r_{\mathrm{rate}}(t)$. For the spike-based models, we drove the models with spike trains from individual experimental trials, pooled the resulting output spike trains and applied kernel density estimation to obtain the response rate $r_{\mathrm{spike}}(t)$, as shown in Fig. 9.

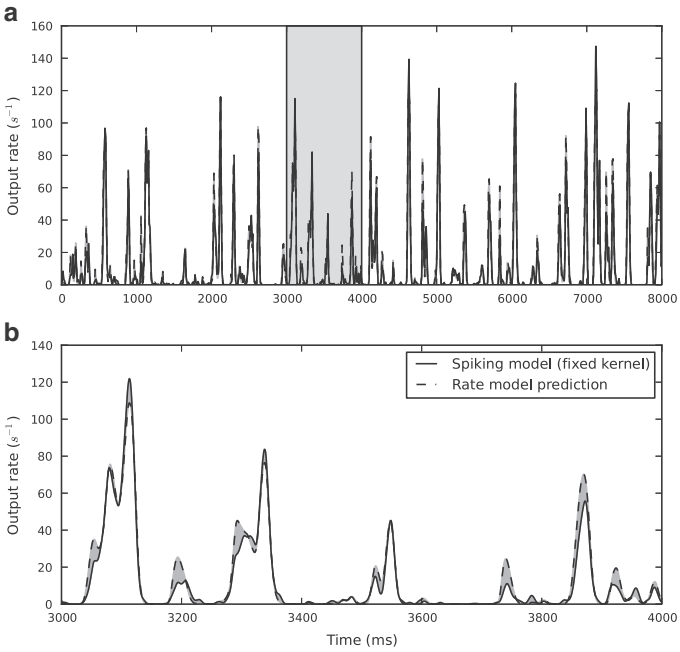

Fig. 9 Firing-rate model prediction quality E_r. Population-averaged response (*solid*) from 128 neurons and prediction of the linear-nonlinear model (24) (*dashed*). Panel A illustrates the response to a complete 8 second stimulus sequence (neuron 1, dataset 1), while panel B shows 1 s (*shaded area*) of the same data in more detail

We then quantified the difference between responses obtained from rate-based and spiking models as the mean square error normalized by the variance of the response of the spiking model (Pillow et al. 2005)

$$E_r = 1 - \frac{\frac{1}{T}\int_0^T (r_{\text{rate}}(t) - \text{r}_{\text{spike}}(t))^2 \text{d}t}{\frac{1}{T}\int_0^T \left(r_{\text{spike}}(t) - \bar{r}_{\text{spike}}\right)^2 \text{d}t} \tag{32}$$

where $\bar{r}_{\text{spike}}$ is the average response rate of the spiking model. Note that $E_r = 100$ % indicates perfect agreement between the models.

We tested the rate model on three separate datasets with different mean rate a_0 and regularity Γ and observed good agreement between rate and spiking models. Scores for the four example neurons are listed in Table 4. Across all 14 model neurons reported by Casti et al. (2008), median E_r scores for the three datasets were 96.5 %, 93.0 %, and 89.3 %, respectively, with $E_r \geq 85.0$ % for 39 of a total of 42 scores, and a minimum score of $E_r = 74.8$ %.

3.4 Carandini results

We found the results for the Carandini model to be equivalent to the results presented above. Both the stationary and non-stationary responses have the same qualitative features, but there are some quantitative differences worth pointing out. In particular, the cutoff-frequencies are lower for the Carandini neurons, implying longer time constants. This

Table 4 Rate-model prediction quality E_r

Neuron	Fits	
	Default	Best
Set 2 ($a_0 = 17.9$, $\Gamma = 2.1$, fit: 20/10)		
6	91.9	92.0
8	98.7	98.8
1	94.0	94.2
1*	97.8	97.8
Set 2 ($a_0 = 27.8$, $\Gamma = 3.5$, fit: 30/15)		
6	82.9	85.0
8	97.0	98.1
1	86.3	89.4
1*	95.7	95.7
Set 2 ($a_0 = 12.5$, $\Gamma = 0.9$, fit: 20/10)		
6	85.0	85.0
8	88.7	88.7
1	90.9	90.9
1*	95.6	95.6

For each neuron, prediction scores are listed for default and best fit. Default fit is selected based on nearest mean rate (rounded up) and 50 % modulation depth. Mean rate, regularity, and default fit is specified for each dataset

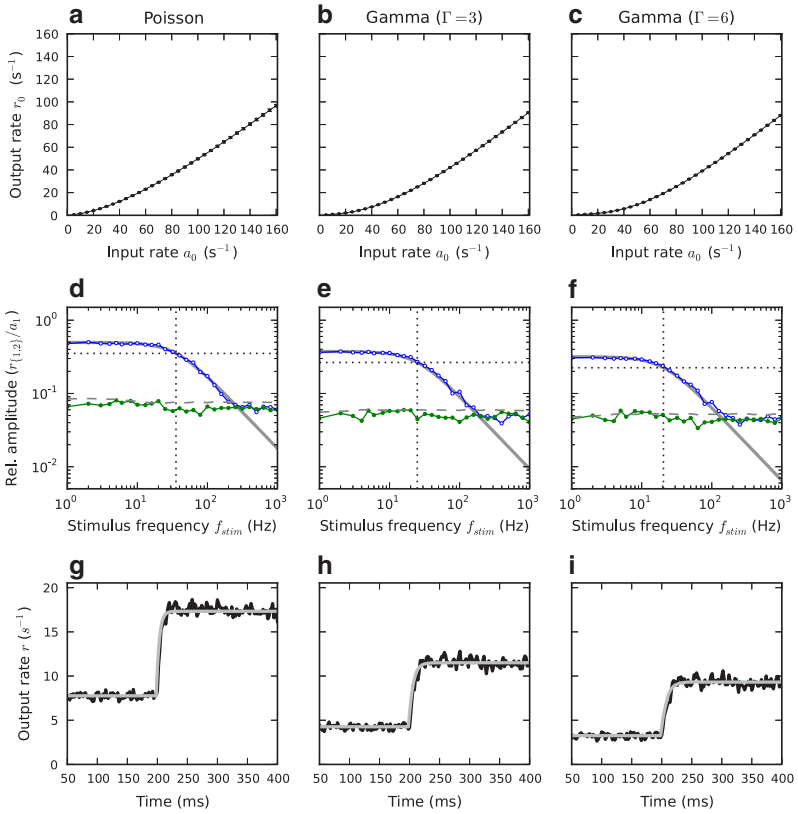

Fig. 10 Stationary response (*top*), non-stationary response (*middle*) and population-averaged step responses (*bottom*) for one Carandini neuron (122R4-5). Same row arrangement as in Fig. 5. See Figs. 5, 6 and 8 for detailed legend

is especially pronounced for Poisson input (Table 3). The stationary response, non-stationary response, and resulting firing-rate model's predicted response to a step increase in the input rate for one of the neurons in the Carandini study (122R4-5) are illustrated in Fig. 10. Results for more neurons from the Carandini study are shown in Supplementary Figures 1–3 and 6–7.

4 Discussion

In the present study, we have shown that linear-nonlinear firing-rate models can capture the essential response dynamics of data-fitted spiking LGN relay neuron models.

Our use of data-fitted models allowed us to calculate the rate-model time constants for the cat and macaque LGN relays cells studied as shown in Table 3. For Poisson input with a mean rate $a_0 = 40\,\mathrm{s}^{-1}$ and modulation depth $a_1 = 10\,\mathrm{s}^{-1}$, time constants $\tau = 1/(2\pi f_c)$ ranged from 1.7 to 3.3 ms for the cat neurons and from 3.0 to 10.1 ms for the macaque neurons. These values were found to decrease somewhat with increasing firing rates and, with some exceptions, increase with increased input regularity. In accordance with earlier work (Gerstner 2000; Nordlie et al. 2010), we found no connection between the rate-model time constants and membrane time constants.

While the neurons operate outside of the diffusive regime (numerous tiny synaptic inputs), responses to stationary stimuli show that all the studied neurons require integration of at least two input spikes to produce an output spike. This result is in line with previous studies of LGN relay neurons (Sirovich 2008; Casti et al. 2008; Carandini et al. 2007).

Since the work of Wilson and Cowan (1972), firing-rate models with exponential kernels (i.e., first-order low-pass filters) have become a standard tool in neuroscience. Nordlie et al. (2010) demonstrated that for an ensemble of unconnected LIF neurons with strong synapses, a simple first-order model yields accurate predictions of the population-averaged response for a wide range of stimulus, neuron, and synapse parameters. Because of its simplicity, we used the same filter model and our results indicate that it produces reasonable predictions for the two models studied.

The exact shape of the transfer function has been less of a concern to us than the low-frequency gain and the cutoff frequency required for a simple and accurate firing-rate model.

Previous studies have found that cutoff frequencies f_c increase with firing rate for small synaptic time constants τ_s (Knight 1972; Brunel et al. 2001; Nordlie et al. 2010). We see such an increase as well (Fig. 7), but input regularity has a larger impact: For most neurons, the cutoff frequency is reduced with increasing input regularity. At high input rates, though, the cutoff frequencies of neurons with high transfer ratios increase with input regularity and thus behave more like the neurons with supercritical weights studied by Nordlie et al. (2010).

To assess the overall validity of our rate-based models, we drove the rate models with novel stimuli. First, rate model predictions were compared to simulated step responses. The predictions were found to be good overall. Sustained rates were predicted well for all input regularities, but some combinations of neuron parameters and input parameters resulted in an overshoot immediately following the step in input rate. Our firing-rate models are unable to account for this effect. The overshoot occurs because many of the neurons that are close to threshold spike shortly after the sudden increase in the input rate. If this happens to a large proportion of the neurons, few neurons will be able to spike until the refractory effects wane. This effect can be understood from the properties of Poisson processes with refractoriness (see Deger et al. 2010). A variant of the model in which we replaced the low-pass with a band-pass filter captured the overshoot well (data not shown), but given the excellent agreement between spiking and model neurons observed of realistic input as shown in Section 3.3.2, we consider this an unnecessary complication.

Second, we used recorded retinal spikes as input to the rate models and compared the results to the output from the spiking relay cell models. Results varied between datasets and neurons, but prediction quality was good overall with median E_r scores of 96.5 %, 93.0 %, and 89.3 % for the three datasets tested. Neurons with low transfer ratios generally scored worse than neurons with high transfer ratios. Shimazaki and Shinomoto (2010) proposed rate estimators based on fixed and variable kernels. We found that estimates based on variable kernels, which capture abrupt changes in activity better, resulted in even better scores for our models than fixed rate kernels (data not shown). Due to the computational burden and the experimental status of the variable kernel methods, though, we used the fixed kernel method for all data reported here.

Overall, our rate-based model fits the experimentally constrained spiking models by Carandini et al. (2007) and Casti et al. (2008) equally well, even though the models differ in their mathematical form (spike response vs. conductance-based) and the species modeled (monkey vs cat). This universality—which may seem surprising at first—reflects the fact that both studies investigate responses to comparable stimuli, to which relay cells in cat and monkey LGN respond in a similar fashion. Thus, our model abstracts away details of the Casti and Carandini models that are insignificant to the response properties investigated. One should keep in mind, though, that the model by Casti et al. (2008), which our rate-based model match well, captures responses of neurons with moderate-to-high transfer ratios best.

Our results indicate that simple firing-rate models produce acceptable predictions for LGN relay neurons. The approach used here could therefore be a useful tool for further exploration of the firing-rate response properties of neurons.

Acknowledgments We would like to thank Matteo Carandini for valuable discussions on how to replicate his model and two anonymous referees for constructive comments.

Conflict of interest The authors declare that they have no conflict of interest.

References

Blitz, D.M., & Regehr, W.G. (2005). Timing and specificity of feed-forward inhibition within the L.G.N. *Neuron*, *45*(6), 917–928.

Brown, E.N., Barbieri, R., Ventura, V., Kass, R.E., Frank, L.M. (2002). The time-rescaling theorem and its application to neural spike train data analysis. *Neural Computation*, *14*(2), 325–346.

Brunel, N., Chance, F.S., Fourcaud, N., Abbott, L.F. (2001). Effects of synaptic noise and filtering on the frequency response of spiking neurons. *Physical Review Letters*, *86*(10), 2186–2189.

Carandini, M., Horton, J.C., Sincich, L.C. (2007). Thalamic filtering of retinal spike trains by postsynaptic summation. *Journal of Vision*, *20*(14), 1–2011.

Casti, A., Hayot, F., Xiao, Y., Kaplan, E. (2008). A simple model of retina-LGN transmission. *Journal of Computational Neuroscience*, *24*(2), 235–252.

Chichilnisky, E.J. (2001). A simple white noise analysis of neuronal light responses. *Network*, *12*(2), 199–213.

Cleland, B.G., Dubin, M.W., Levick, W.R. (1971). Simultaneous recording of input and output of lateral geniculate neurones. *Nature New Biology*, *231*(23), 191–192.

Dayan, P., & Abbott, L.F. (2001). *Theoretical neuroscience*. Cambridge: Massachusetts Institute Of Technology Press.

Deger, M., Helias, M., Cardanobile, S., Atay, F.M., Rotter, S. (2010). Nonequilibrium dynamics of stochastic point processes with refractoriness. *Physical Review E*, *82*(2 Pt 1), 021–129.

Einevoll, G.T., & Heggelund, P. (2000). Mathematical models for the spatial receptive-field organization of nonlagged X-cells in dorsal lateral geniculate nucleus of cat. *Visual Neuroscience*, *17*(6), 871–885.

Einevoll, G.T., & Plesser, H.E. (2002). Linear mechanistic models for the dorsal lateral geniculate nucleus of cat probed using drifting-grating stimuli. *Network*, *13*(4), 503–530.

Franklin, J., & Bair, W. (1995). The effect of a refractory period on the power spectrum of neuronal discharge. *SIAM Journal on Applied Mathematics*, *55*, 1074–1093.

Galassi, M., Davies, J., Theiler, J., Gough, B., Jungman, G., Booth, M., Rossi, F. (2001). *GNU scientific library reference manual*. Bristol: Network Theory.

Gerstner, W. (2000). Population dynamics of spiking neurons: fast transients, asynchronous states, and locking. *Neural Computation*, *12*(1), 43–89.

Gerstner, W., & Kistler, W.M. (2002). *Spiking neuron models*. Cambridge: Cambridge University Press.

Gewaltig, M.O., & Diesmann, M. (2007). NEST (NEural simulation tool). *Scholarpedia*, *2*(4), 1430.

Goldberg, J.M., & Brown, P.B. (1969). Response of binaural neurons of dog superior olivary complex to dichotic tonal stimuli: Some physiological mechanisms of sound localization. *Journal of Neurophysiology*, *32*, 613–636.

Hayot, F., & Tranchina, D. (2001). Modeling corticofugal feedback and the sensitivity of lateral geniculate neurons to orientation discontinuity. *Visual Neuroscience*, *18*(6), 865–877.

Johannesma, P.I.M. (1968). Diffusion models for the stochastic activity of neurons. In E.R. Caianiello (Ed.), *Networks neural: Proceedings of the school on neural networks* (pp. 116–144). Springer-Verlag.

Kaplan, E., & Shapley, R. (1984). The origin of the S (slow) potential in the mammalian lateral geniculate nucleus. *Experimental Brain Research*, *55*(1), 111–116.

Kirkland, K.L., & Gerstein, G.L. (1998). A model of cortically induced synchronization in the lateral geniculate nucleus of the cat: a role for low-threshold calcium channels. *Vision Research*, *38*(13), 2007–2022.

Knight, B.W. (1972). Dynamics of encoding in a population of neurons. *The Journal of General Physiology*, *59*(6), 734–766.

Köhn, J., & Wörgötter, F. (1996). Corticofugal feedback can reduce the visual latency of responses to antagonistic stimuli. *Biological Cybernetics*, *75*(3), 199–209.

Muller, E., Davison, A.P., Brizzi, T., Bruederle, D., Eppler, J.M., Kremkow, J., Pecevski, D., Perrinet, L., Schmuker, M., Yger, P. (2009). NeuralEnsemble.Org: Unifying neural simulators in Python to ease the model complexity bottleneck. In *Frontiers in neuroscience conference abstract: Neuroinformatics 2009*.

Nelder, J.A., & Mead, R. (1965). A simplex method for function minimization. *Computer Journal*, *7*, 308–313.

Nordbø, Ø., Wyller, J., Einevoll, G.T. (2007). Neural network firing-rate models on integral form: effects of temporal coupling kernels on equilibrium-state stability. *Biological Cybernetics*, *97*(3), 195–209.

Nordlie, E., Gewaltig, M.O., Plesser, H.E. (2009). Towards reproducible descriptions of neuronal network models. *PLoS Computational Biology*, *5*(8), e1000456.

Nordlie, E., Tetzlaff, T., Einevoll, G.T. (2010). Rate dynamics of leaky integrate-and-fire neurons with strong synapses. *Frontiers in Computational Neuroscience*, *4*, 149.

Pillow, J.W., Paninski, L., Uzzell, V.J., Simoncelli, E.P., Chichilnisky, E.J. (2005). Prediction and decoding of retinal ganglion cell responses with a probabilistic spiking model. *Journal of Neuroscience*, *25*(47), 11003–11013.

Pillow, J.W., Shlens, J., Paninski, L., Sher, A., Litke, A.M., Chichilnisky, E.J., Simoncelli, E.P. (2008). Spatio-temporal correlations and visual signalling in a complete neuronal population. *Nature*, *454*(7207), 995–999.

Plesser, H.E., & Diesmann, M. (2009). Simplicity and efficiency of integrate-and-fire neuron models. *Neural Computation*, *21*, 353–359.

Rodieck, R.W. (1965). Quantitative analysis of cat retinal ganglion cell response to visual stimuli. *Vision Research*, *5*(11), 583–601.

Rotter, S., & Diesmann, M. (1999). Exact digital simulation of time-invariant linear systems with applications to neuronal modeling. *Biological Cybernetics*, *81*(5–6), 381–402.

Sherman, S.M., & Guillery, R.W. (2001). *Exploring the thalamus*. New York: Academic Press.

Shimazaki, H., & Shinomoto, S. (2010). Kernel bandwidth optimization in spike rate estimation. *Journal of Computational Neuroscience*, *29*(1–2), 171–182.

Sirovich, L. (2008). Populations of tightly coupled neurons: the RGC/LGN system. *Neural Computation*, *20*(5), 1179–1210.

Troy, J.B., & Robson, J.G. (1992). Steady discharges of X and Y retinal ganglion cells of cat under photopic illuminance. *Visual neuroscience*, *9*(6), 535–53.

van Hateren, J.H. (1997). Processing of natural time series of intensities by the visual system of the blowfly. *Vision Research*, *37*(23), 3407–3416.

Walpole, R.E., & Myers, R.H. (1993). *Probability and Statistics for Engineers and Scientists*, 5th edn. Englewood Cliffs: Prentice Hall.

Wilson, H.R., & Cowan, J.D. (1972). Excitatory and inhibitory interactions in localized populations of model neurons. *Biophysical Journal*, *12*(1), 1–24.

Yousif, N., & Denham, M. (2007). The role of cortical feedback in the generation of the temporal receptive field responses of lateral geniculate nucleus neurons: a computational modelling study. *Biological Cybernetics*, *97*(4), 269–277.

Supplementary material for *Firing-rate models capture essential response dynamics of LGN relay cells*

Thomas Heiberg*, Birgit Kriener, Tom Tetzlaff, Alex Casti,
Gaute T. Einevoll, Hans E. Plesser

*Department of Mathematical Sciences and Technology, Norwegian University of Life Sciences
P.O. Box 5003, NO-1432 Ås, Norway, thomas.heiberg@umb.no

Model implementation differences

The following sections summarize any differences between the original model implementations and our implementations in NEST.

Casti model

According to Casti et al (2008), the afterhyperpolarization is modelled as alpha-function conductances that are added for each spike (see Section 2.1.1). The source code obtained from the authors, however, only keeps track of the conductance resulting from the most recent spike. The NEST implementation adds the conductances as described in the model equations. This difference causes noticeable differences in the output only at high input rates. As an option, the NEST implementation allows the user to behave like the original.

Also, Casti et al use a second-order Runge-Kutta integrator and linear interpolation to determine the spike times. In the NEST model, a fourth-order integrator and linear interpolation is used. This difference seems to have negligible effects.

Carandini model

The main difficulties in implementing the Carandini model in NEST, was related to the noise signal $n(t)$. It had to be generated and filtered in advance, resulting in a memory-intensive model. And the noise signal was not described in the paper, but the source code detailing the signal parameters and the filtering process was obtained from the authors. However, we were not able to run the original simulator and therefore unable to directly compare the results of the two implementations.

Tables and figures

Optimal parameter sets for all neurons from Casti et al (2008) and Carandini et al (2007) are listed in 1 and 2 respectively.

In the main text, we presented a number of figures illustrating the results for four Casti neurons, while the results from the Carandini model were summarized in a single figure. Here, stationary response (Figure 1), response to sinusoidal stimuli (Figure 2), and rate-model prediction (Figure 3) figures are included for four representative Carandini neurons.

Figures illustrating the response to sinusoidal stimuli and rate-model prediction at a different working point are included for both neuron models (Figures 4–7).

References

Carandini M, Horton JC, Sincich LC (2007) Thalamic filtering of retinal spike trains by postsynaptic summation. J Vis 7(14):20.1–2011

Casti A, Hayot F, Xiao Y, Kaplan E (2008) A simple model of retina-LGN transmission. J Comput Neurosci 24(2):235–252

Table 1: Optimal parameter sets for all neurons modeled by Casti et al (2008). Neurons were stimulated with small spots, except for those with an asterisk suffix, which were obtained with a larger than optimal stimulus. After Casti et al (2008, Table 2).

Neuron	τ (ms)	τ_A (ms)	$\bar{g}_E$	$\bar{g}_A$
1	17.8	0.47	0.16	0.42
1*	11.7	0.60	0.11	0.56
2	17.1	0.40	0.16	0.48
2*	17.3	0.50	0.13	0.54
3	12.6	0.25	0.08	0.54
3*	13.6	0.14	0.07	0.49
4	19.5	0.37	0.09	0.55
5	22.0	0.41	0.19	0.60
6	16.3	1.00	0.08	0.60
6*	11.8	1.00	0.07	0.57
7	14.4	1.07	0.08	0.28
8	7.2	0.26	0.07	0.44
9	12.4	0.60	0.08	0.52
10	15.3	0.65	0.10	0.60

Table 2: Optimal parameter set for all neurons modeled by Carandini et al. After Carandini et al (2007, Table 1).

Neuron	τ_{EPSP} (ms)	V_{EPSP}	τ_{reset} (ms)	V_{reset}	V_{noise}
120L15-1	7.4	0.77	6.3	4.39	0.15
121R11-1	14.2	0.86	20.9	2.37	0.35
121R13-4	8.4	0.62	9.5	6.64	0.30
121R14-4	17.2	0.57	33.4	0.78	0.00
121R15-5	5.8	0.93	7.5	1.34	0.10
121R7-1	5.8	0.97	6.3	2.54	0.05
122R4-2	6.3	0.91	29.9	0.85	0.20
122R4-3	5.6	0.73	12.3	1.04	0.20
122R4-5	6.0	0.56	12.0	0.82	0.25

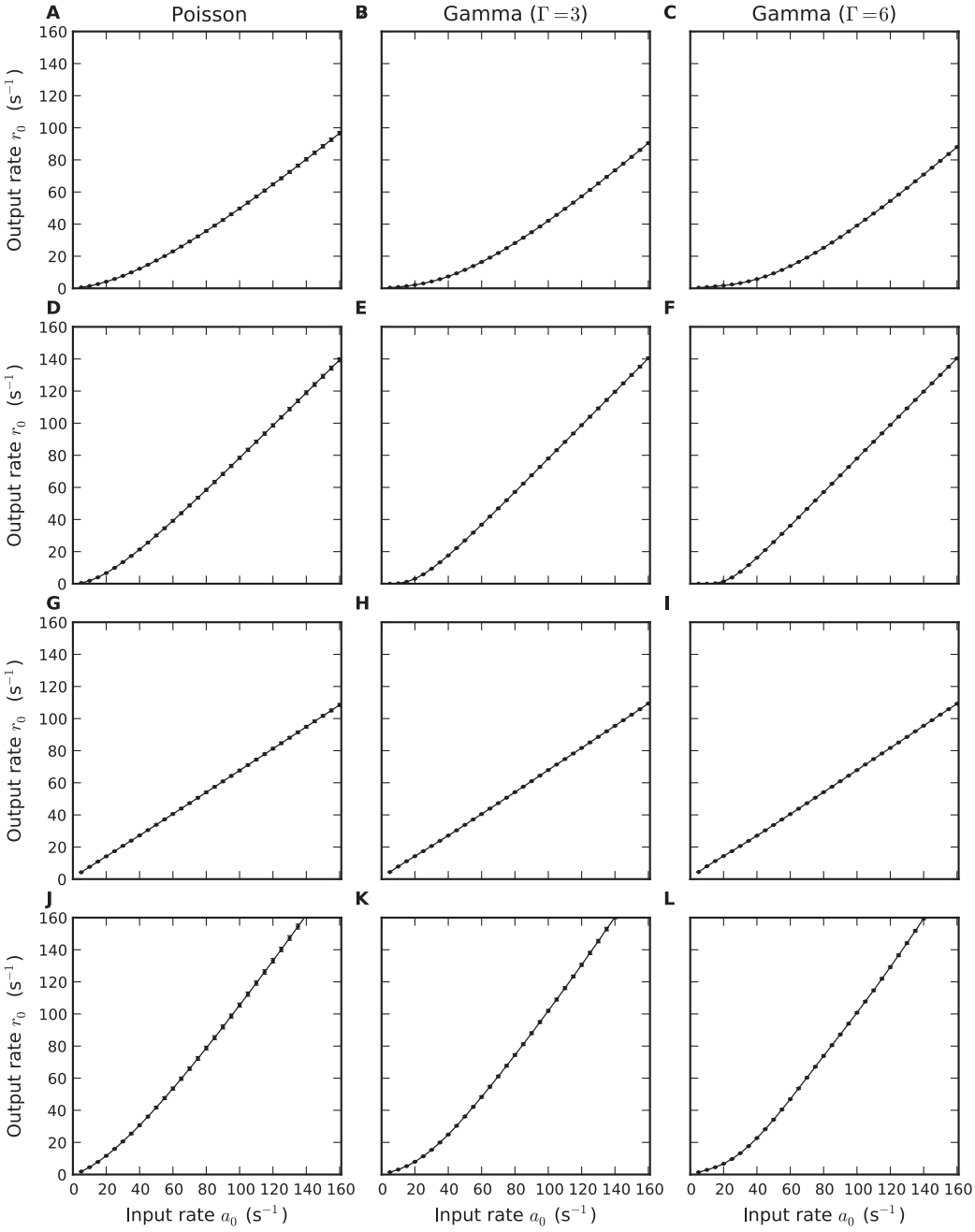

Figure 1: Stationary response for selected Carandini neurons. Symbols illustrate mean output rates r_0 across trials. Error bars denote one standard deviation in either direction. Each row contain results from one neuron configuration, from top to bottom: 122R4-5, 121R14-4, 121R11-1 and 121R15-5. Columns represent different input regularities, from left to right: Poisson ($\Gamma = 1$), gamma ($\Gamma = 3$) and gamma ($\Gamma = 6$).

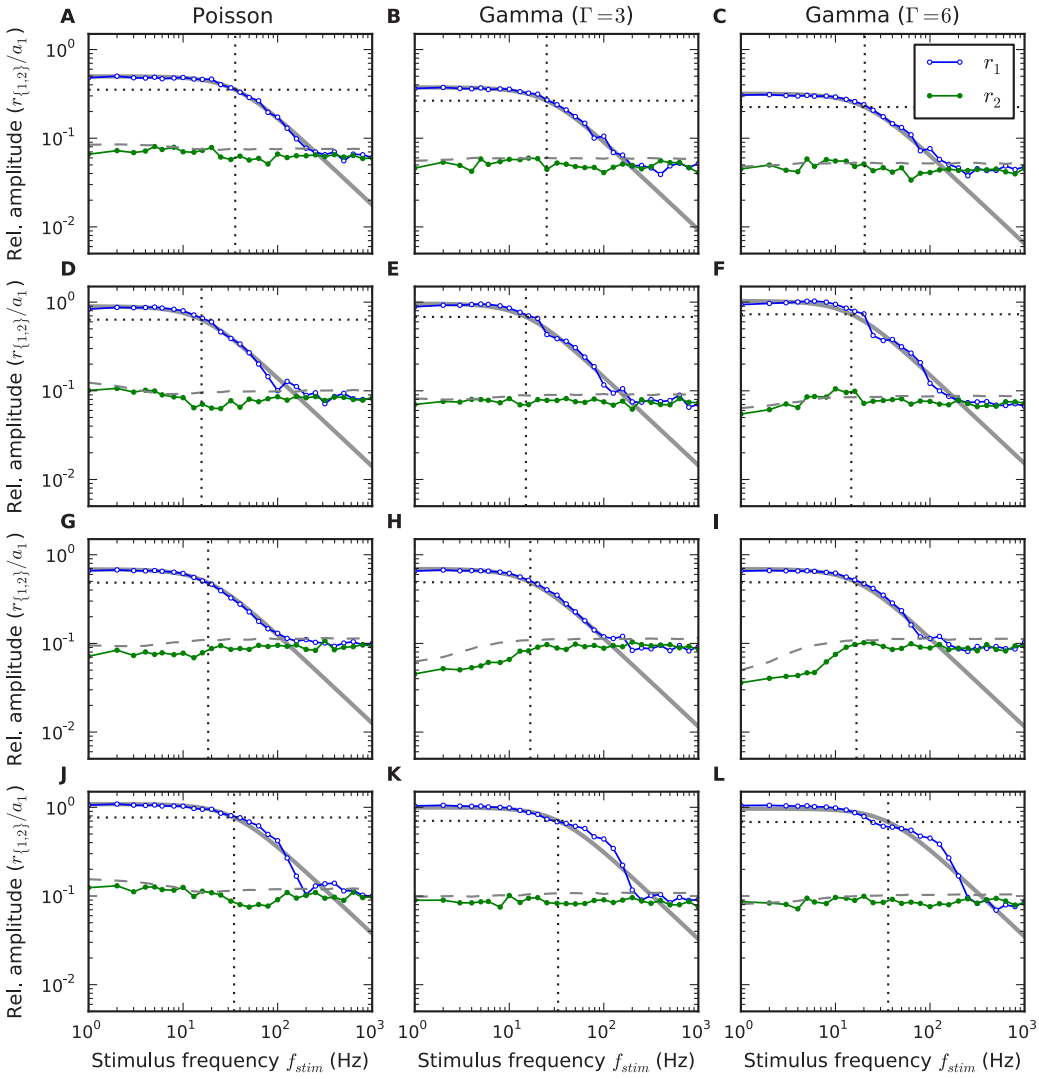

Figure 2: Low-pass characteristic of the response to sinusoidal stimuli ($a_1 > 0$) for representative Carandini neurons. The figure illustrates how a first-order low-pass filter with cutoff frequency f_c, low-frequency gain γ, and delay d fits the response of the Carandini model to time varying input. Symbols represent measured responses $r_n(f_{\text{stim}})/a_1$ for principal (blue) and second (green) harmonics ($n \in \{1, 2\}$). Gray curves show fitted first-order low-pass filters. Dotted vertical lines mark fitted cutoff frequencies f_c. Dashed horizontal lines represent noise level $z = 2$. Stimulus parameters: $a_0 = 40\,s^{-1}, a_1 = 10\,s^{-1}$. Same panel arrangement as in Figure 1.

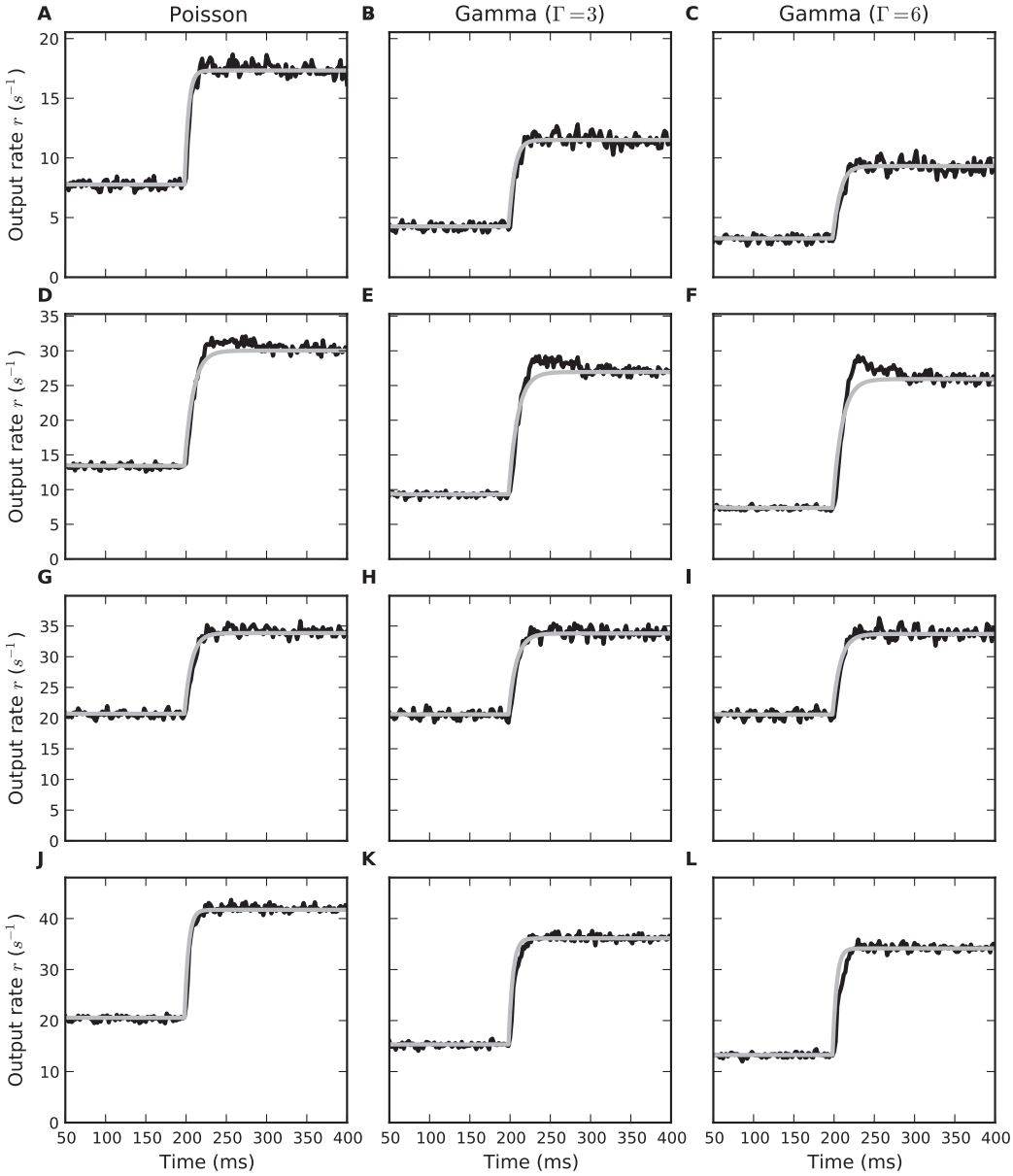

Figure 3: Population-averaged step responses for selected Carandini neurons. Firing rate $r(t)$ in response to an instantaneous increase in the input firing rate $a(t)$ at time $t = 100$ ms from 30 to 50 s^{-1}. Same panel arrangement as in Figure 1.

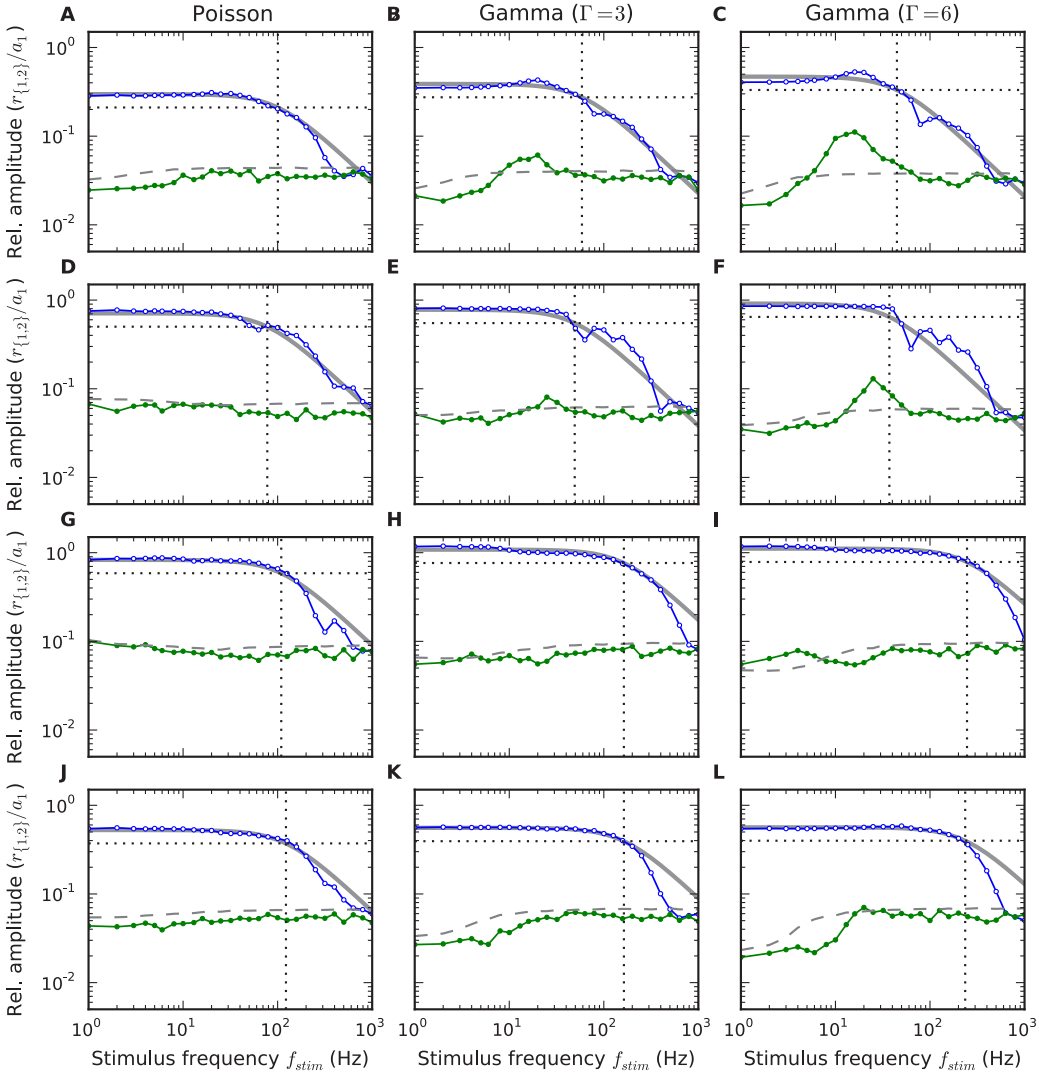

Figure 4: Low-pass characteristic of the response to sinusoidal stimuli ($a_1 > 0$) for representative Casti neurons (high input rate). Stimulus parameters: $a_0 = 80\,s^{-1}, a_1 = 20\,s^{-1}$. Same panel arrangement as in Figure 1.

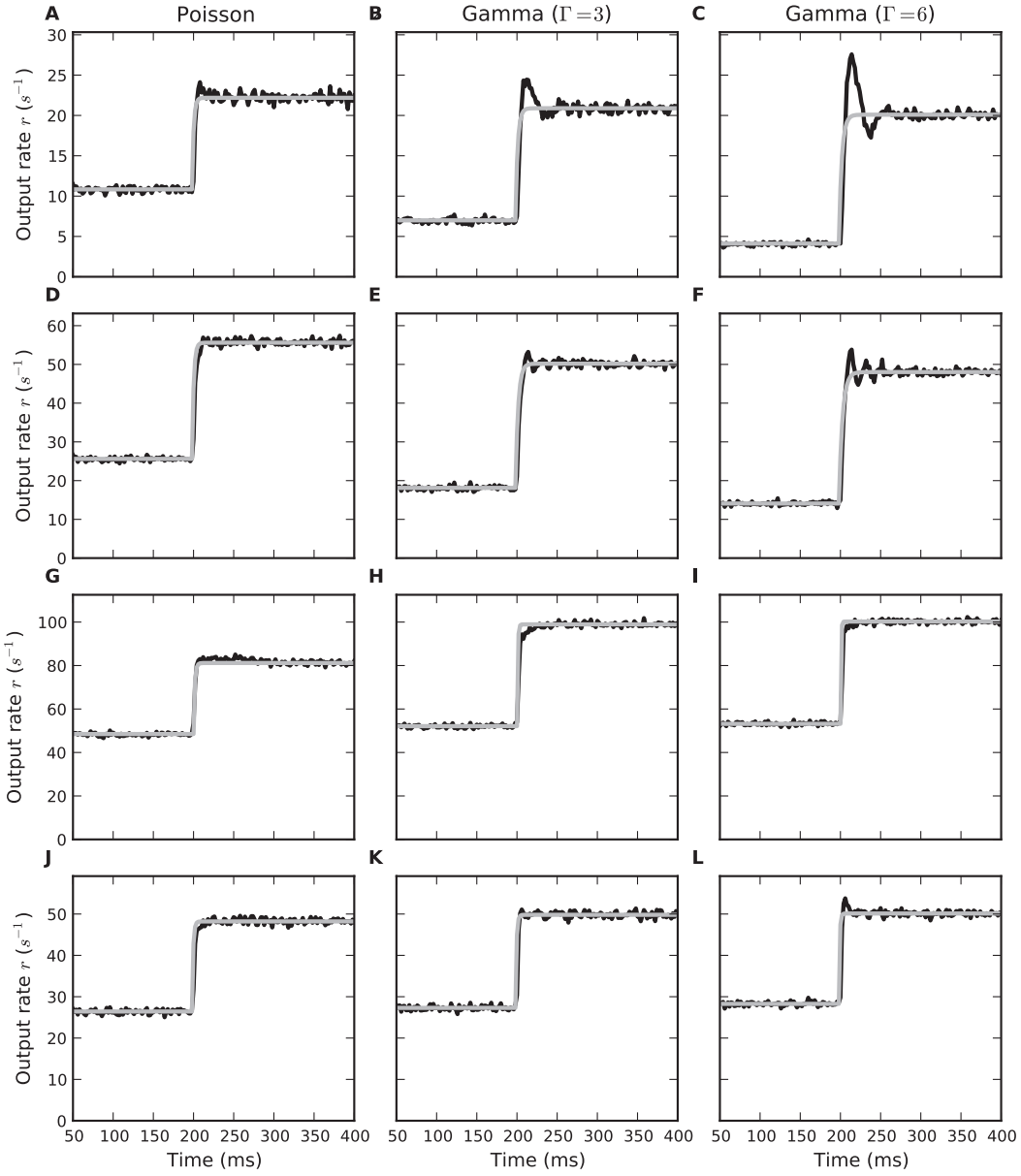

Figure 5: Population-averaged step responses for selected Casti neurons (high input rate). Firing rate $r(t)$ in response to an instantaneous increase in the input firing rate $a(t)$ at time $t = 100$ ms from 60 to 100 s^{-1}. Same panel arrangement as in Figure 1.

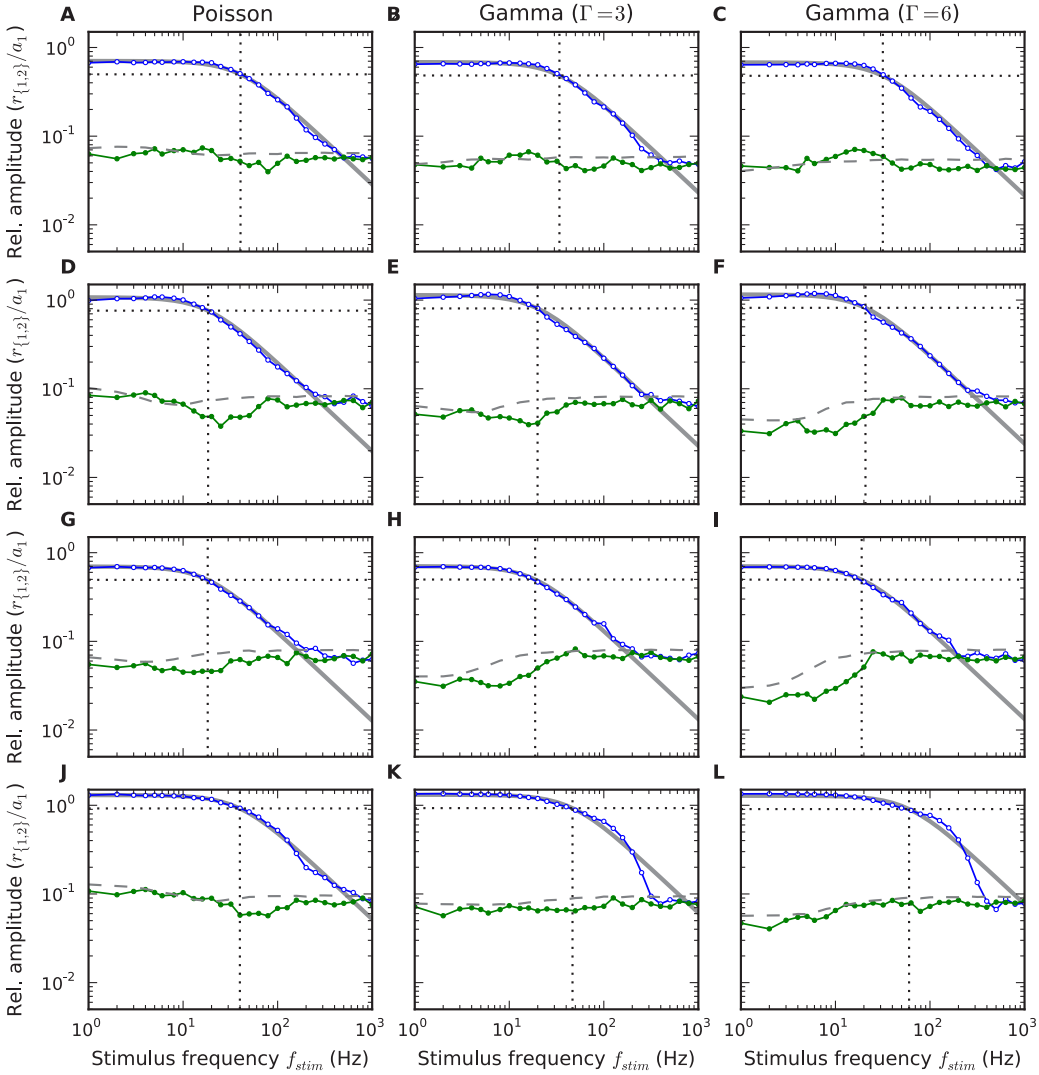

Figure 6: Low-pass characteristic of the response to sinusoidal stimuli ($a_1 > 0$) for representative Carandini neurons (high input rate). Stimulus parameters: $a_0 = 80\,s^{-1}, a_1 = 20\,s^{-1}$. Same panel arrangement as in Figure 1.

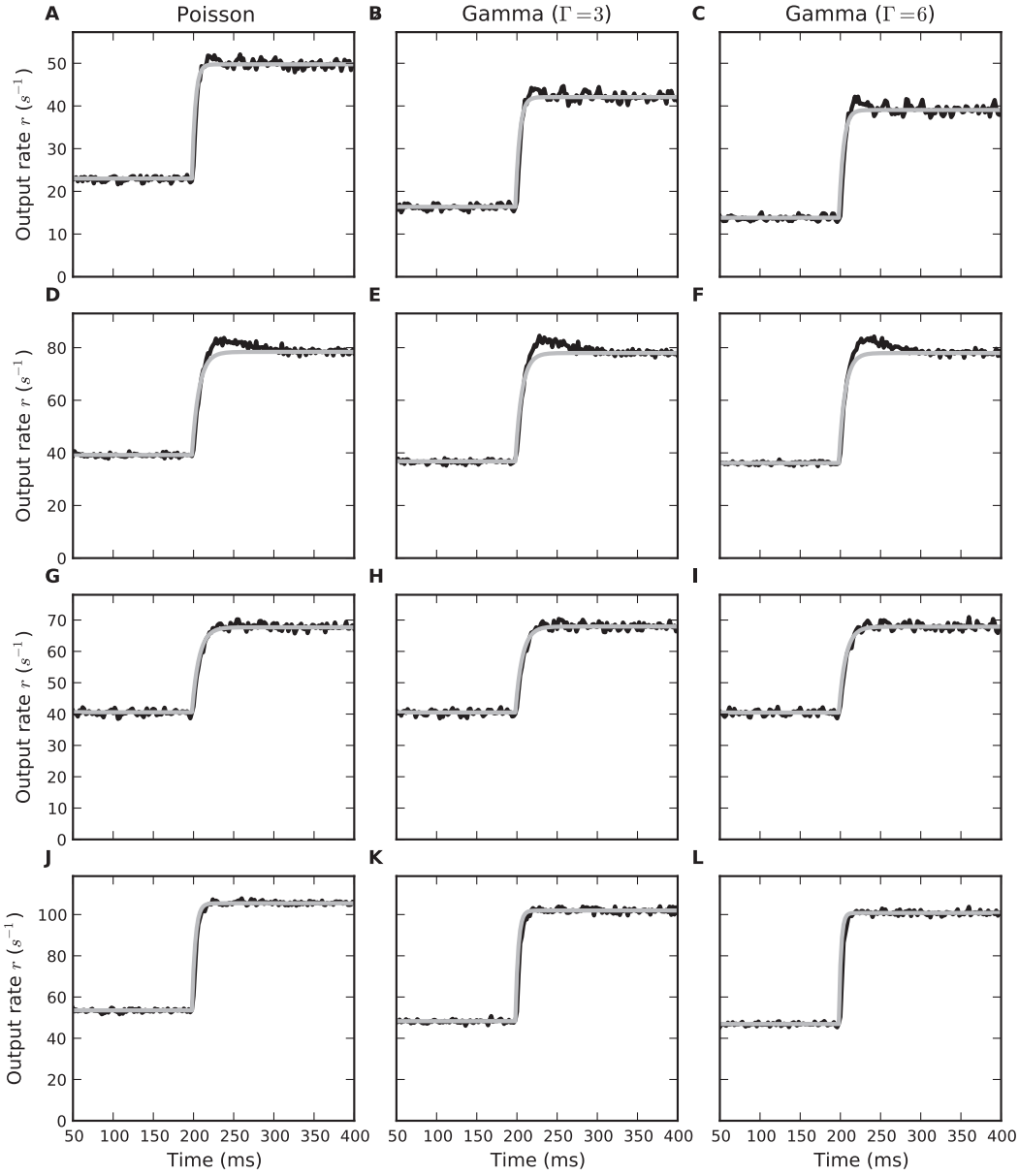

Figure 7: Population-averaged step responses for selected Carandini neurons (high input rate). Firing rate $r(t)$ in response to an instantaneous increase in the input firing rate $a(t)$ at time $t = 100$ ms from 60 to 100 s^{-1}. Same panel arrangement as in Figure 1.

Paper II

Heiberg T, Kriener B, Tetzlaff T, Einevoll GT, Plesser HE, Firing-rate models for neurons with a broad repertoire of spiking behaviors. In revision in Journal of Computational Neuroscience

J Comput Neurosci manuscript No.
(will be inserted by the editor)

Firing-rate models for neurons with a broad repertoire of spiking behaviors

Thomas Heiberg · Birgit Kriener · Tom Tetzlaff · Gaute T. Einevoll · Hans E. Plesser

Received: date / Accepted: date

Abstract Capturing the response behavior of spiking neuron models with rate-based models facilitates the investigation of neuronal networks using powerful methods for rate-based network dynamics. To this end, we investigate the responses of two widely used neuron model types, the Izhikevich and augmented multi-adapative threshold (AMAT) models, to a range of spiking inputs ranging from step responses to natural spike data. We demonstrate that a combination of a non-linear firing rate model with a linear filter, fitted to test data, provides models that generalize well to responses to realistic spike trains. We also find that the broad range of spiking behaviors obtained from Izhikevich and AMAT models driven by current injection protocols reduces to a smaller set of response classes under more natural stimulus conditions.

Thomas Heiberg
Faculty of Science and Technology, Norwegian University of Life Sciences, Ås, Norway

Birgit Kriener
Faculty of Science and Technology, Norwegian University of Life Sciences, Ås, Norway
Present address: Institute of Basic Medical Sciences, University of Oslo

Tom Tetzlaff
Institute of Neuroscience and Medicine (INM-6) and Institute for Advanced Simulation (IAS-6) and JARA Institute Brain Structure-Function Relationships (INM-10), Jülich Research Centre, Jülich, Germany

Gaute T. Einevoll
Faculty of Science and Technology, Norwegian University of Life Sciences, Ås, Norway
Department of Physics, University of Oslo, Norway

Hans E. Plesser
Faculty of Science and Technology, Norwegian University of Life Sciences, Ås, Norway
Institute of Neuroscience and Medicine (INM-6), Jülich Research Centre, Jülich, Germany
E-mail: hans.ekkehard.plesser@nmbu.no

Keywords Rate model · linear-nonlinear model · Izhikevich model · AMAT model

1 Introduction

The simulation of large networks of spiking neurons on the scale of cortical columns or even whole areas of the cortex has become feasible due to advances in computer technology and simulator software (Helias et al, 2012; Kunkel et al, 2014). In order to relate simulation results to experimental findings, it is important to employ neuron models that accurately capture actual neuron dynamics in response to realistic stimuli. Dynamical models that reproduce the responses of individual neurons to injected currents go back to the seminal work by Hodgkin and Huxley (1952). Their conductance-based model quantitatively described the action potential initiation and propagation in the squid giant axon in response to depolarizing currents and spawned many variants and simplifications that have been analyzed and used in computational neuroscience ever since. Examples are the Fitzhugh-Nagumo (FitzHugh, 1961) and the Morris-Lecar model (Morris and Lecar, 1981). On the more abstract side of neuron modeling, Lapicque's neuron model (Lapicque, 1907), widely known as the leaky integrate-and-fire (IAF) neuron, models the membrane potential $V(t)$ as a passive current integrator with leak, emitting a spike whenever $V(t)$ reaches a threshold value θ, followed by a membrane potential reset (Tuckwell, 1988; Burkitt, 2006a,b).

These simple integrate-and-fire neuron models have particular appeal to computational neuroscientists because they capture the essential function of a neuron, while still being amenable to mathematical analysis in many input and network scenarios.

Yet, the ideal model would be a neuron model that is both simple in its dynamical equations and still captures most of the actual response dynamics of a real neuron to a wide range of stimuli. To this end, Izhikevich suggested a two-dimensional neuron model that is able to reproduce at least twenty different characteristic responses that are commonly used to classify neuron response types in experiments, such as tonic, phasic and rebound spiking and bursting, or adaptation (Izhikevich, 2010). The response types are illustrated in Figure 1. The stimuli used to induce these spiking behaviors are direct current injections, ramp current injections or short direct current steps or pulses as indicated at the bottom of all panels.

In a network context, however, neurons usually receive noisy input currents. Moreover, they are known to respond highly reliably to repeated injections of the same frozen noise injection, while responses vary widely across trials when neurons receive identical direct current (Mainen and Sejnowski, 1996). Neurons thus respond stereotypically to certain temporal input features rather than to mere current amplitude.

Motivated by such findings, Gerstner and colleagues showed that nonlinear IAF models, including the spike-response model and the adaptive exponential IAF model, can succesfully be mapped to experimental spike data in a noisy input regime and even have good spike-time prediction power (Brette and Gerstner, 2005; Jolivet et al, 2006). Yet, the nonlinearity and the number of parameters in general make fitting a difficult task. The *International Competition on Quantitative Neuron Modeling* has challenged modelers to fit their neuron models to a set of spike data recorded from neurons stimulated with noisy input currents (Jolivet et al, 2008). The resulting neuron models were tested with a noisy input current that was not included in the training set, and the predicted spike times were compared to those of the actually emitted spikes. The *multi-timescale adaptive threshold model* (MAT model) introduced by Kobayashi et al (2009), a surprisingly simple model with linear subthreshold dynamics, solved this task best. Despite its simplicity, the MAT model can generate type-I and type-II excitability, as well as burst firing. Moreover, an extended version of the MAT model, the *augmented MAT* (AMAT) model, which incorporates threshold dynamics that depend on the membrane-potential history, is able to reproduce all twenty spike response patterns described for the Izhikevich model (Yamauchi et al, 2011). Because of its few parameters and simple dynamics, the AMAT model has low computational cost while providing a large dynamical repertoire, and is thus highly attractive for large-scale network simulations.

In an actual neuronal network, neurons typically integrate spikes from thousands of presynaptic neurons, yet not all spikes might necessarily have a strong impact on the membrane potential. In many spiking network models, the effect of individual spikes on the membrane potential is assumed to be small, and spiking activity asynchronous and irregular. In this limit it is indeed possible to substitute the input current by, e.g., Gaussian white noise or an Ornstein-Uhlenbeck process (Johannesma, 1968). However, experimental findings have repeatedly demonstrated that, even though most synapses are weak, synaptic weight distributions typically have heavy tails, with some corresponding to post-synaptic potentials of up to 10 mV (Song et al, 2005; Lefort et al, 2009; Avermann et al, 2012; Ikegaya et al, 2013). It is thus important to extend the analysis of neuronal response dynamics to input spike trains that elicit large individual post-synaptic potentials.

At an even higher level of abstraction are models that ignore specific spike times and heterogeneities in network structure, i.e., rate and field models. In contrast to high-dimensional networks of spiking neurons, such models are often easier to analyze mathematically due to their low dimensionality, and hence can offer insight into steady states of network activity and bifurcations that give rise to complex spatio-temporal phenomena, such as oscillatory dynamics, traveling waves or activity bump formation. Prominent examples are neural mass models, such as the Jansen-Rit model (Jansen and Rit, 1995), and neural field models, such as the Wilson-Cowan model (Wilson and Cowan, 1972), which include spatial interactions between neurons. In these models, the dynamics of large, possibly heterogeneous, populations of neurons are substituted by rate variables in a mean-field manner (Ermentrout, 1998; Coombes, 2005).

An important conceptual step in the derivation of these models is the substitution of the spiking activity of a neuron in response to a certain input current $I(t)$ by an appropriate rate function[1] mapping the input history $\{I(s)|s \leq t\}$ to the response rate at time t. Common choices are abstract models such as threshold-linear or sigmoidal functions $F(I(t))$ depending only on the input current at time t. The threshold-linear form is often chosen because of mathematical convenience, but also because it mimics to first order the gain function of many individual neurons in experiments (Chance et al, 2002; Blomquist et al, 2009), while the sigmoidal also models the saturation at very high firing rates. Yet, parameters of the gain function such as time constants, activation thresholds, or slope are often chosen rather qualitatively, and it is uncertain how well they match single-neuron properties or biophysics.

A first step towards a stringent comparison of spiking neuron network simulations with reduced neural mass or field

[1] Strictly speaking, this is a *functional*, not a function, but we ignore such mathematical detail here as we focus on instantaneous transformations in what follows.

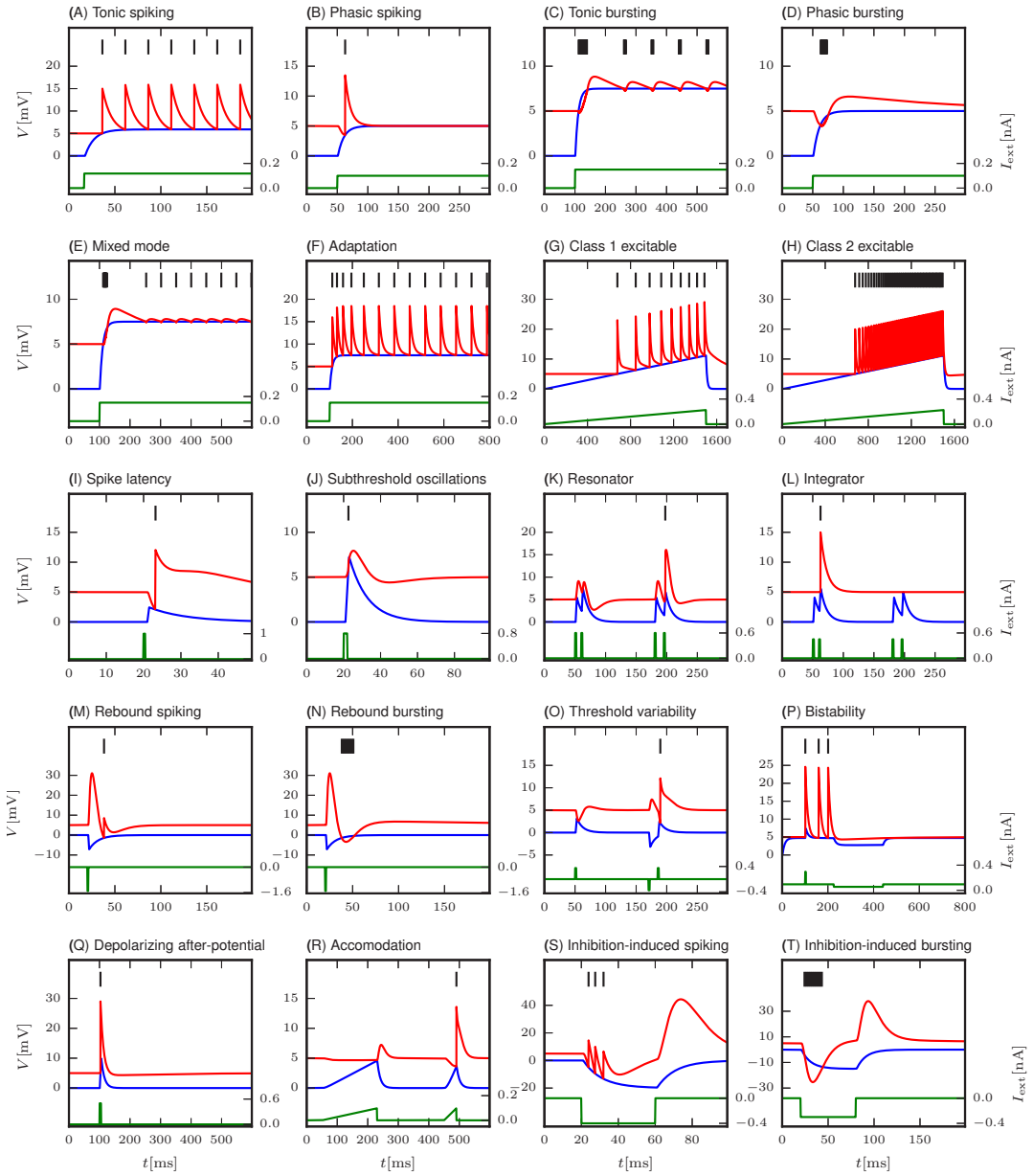

Fig. 1 Response types for current input as defined by Izhikevich (2004). This illustration was created with our NEST implementation of the augmented MAT model (Yamauchi et al, 2011). Some model and stimulus parameters differ from those given by Yamauchi et al (2011), see the Appendix. Membrane potential V_m is shown in blue, the threshold V_{th} in red, and the input current in green, while emitted spikes are shown as black bars; after Yamauchi et al (2011). Subfigures are labeled as in Izhikevich (2004, Fig. 1).

models is to obtain an adequate quantitative expression for the neuronal gain function $F(I(t))$. It is hence of interest to understand if and how the activity of individual spiking neurons in response to arbitrary input currents can be described truthfully by a rate-model formulation. Several point neuron models are simple enough to allow for an analytical derivation of the gain function, assuming that input currents are Gaussian white noise, sinusoidally modulated input, or shot noise of a given structure (see, e.g., Gerstein and Mandelbrot, 1964; Stein, 1965; Brunel, 2000; Brunel et al, 2001; Burkitt, 2006b; Richardson, 2007; Richardson and Swarbrick, 2010; Roxin, 2011; Ostojic and Brunel, 2011). However, more complex nonlinear neuron models, such as the Izhikevich model or even the AMAT model, often render such analyses futile, especially in the presence of large-amplitude post-synaptic current events that are beyond the realm of perturbation-based theories. This holds to an even larger degree for the second step towards a stringent comparison of spiking network and neural field models, namely capturing the temporal response properties of the models. A thorough understanding of complex nonlinear models thus requires simulation studies.

We provide here an analysis of the response to spike train input of the models proposed by Izhikevich (2003b) and by Yamauchi et al (2011), following the approach by Nordlie et al (2010) and Heiberg et al (2013). Both models actually represent an entire class of models that can be tuned to a wide range of reponses by adjusting model parameters. We will thus refer to the Izhikevich and AMAT *model classes*, respectively, when we refer to the set of equations and spike-generation rules, while we will call each of the approximately 20 different parameterization a *model*. Each of the two model classes comprises some 20 models.

In Section 3.1 we present how the different models respond to spike train input.

In Section 3.2, we present fits of a linear-nonlinear firing-rate model to the spike responses of Izhikevich and AMAT models to stationary and temporally modulated stochastic spike trains across a range of input rates, synaptic weights, and modulation frequencies and amplitudes under different background noise regimes.

We group the different models according to the filter parameters obtained in Section 3.3, before we in Section 3.4 explore how well the linear-nonlinear rate models capture the response of their spiking counterparts to novel stimuli, such as steps in the input firing rate and more complex temporally modulated input.

Finally, in Section 3.5 we investigate whether we can generalize models fitted to a specific input regime to a broader set of stimuli, before we summarize our findings in Section 4.

2 Methods

2.1 Neuron models

We study response behavior for two neuron model classes, the Izhikevich model (Izhikevich, 2003b) and the augmented MAT model (Yamauchi et al, 2011). As both model classes are well described in the original publications, we just summarize them briefly in Tables 1 and 2. Both models are able to reproduce 20 of the most prominent features of biological spiking neurons in response to injected current input as illustrated in Figure 1. These response types were first summarized in tabular form by Izhikevich (2004); see also Markram et al (2004). Tables 3 and 4 present the parameter values required to obtain the model responses displayed for each class; note that certain models only differ in the stimulus injected, while neuron parameters are identical. All models are implemented on a fixed time grid ($dt = 0.1\,\mathrm{ms}$).

We integrate the Izhikevich model class using the forward Euler algorithm as in the original publications on the model. Izhikevich (2003b) used a 1 ms time step, but splitting the update of the membrane potential (but not the recovery variable) into two steps of 0.5 ms "for numerical stability". Figure 1 of Izhikevich (2004), on the other hand, was generated using different time steps for different cases, ranging from 0.1 ms to 0.5 ms without substepping, as evidenced by the source code used to generate that figure (Izhikevich, 2003a). We extracted model parameters as shown in Table 3 from that source code, including an external current I_{ext} injected into the model for some variants in addition to the stimulus current.

Izhikevich's source code also revealed that model variants G, L, and R use other equations than Eqs. 1–2 for $V(t)$ or $U(t)$. We therefore excluded these variants from our study. We also excluded variants I and O, since they have the same parametes as variants A and M, respectively, and differ only in the test stimulus injected to create Fig. 1 of Izhikevich (2004).

Furthermore, we observed that response patterns depend on the precise time step used. In particular, the response for case T, *Inhibition induced bursting*, is unstable for time steps shorter than 0.5 ms. We could obtain a response similar to the original publication for our fixed 0.1 ms time step by changing parameter d from $d = -2$ to $d = 0$.

The Izhikevich model class is not defined with consistent units in the original publication (Izhikevich, 2003b). While a time unit of milliseconds is implied and membrane potential is specified in millivolts, no units are given for the parameters or explicit constants. The model equations imply that input currents have units of mV/ms, which is rather

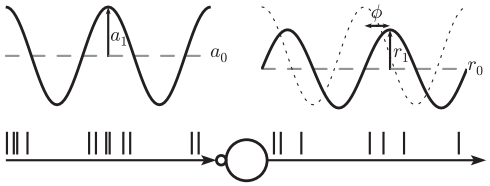

Fig. 2 A model neuron is driven by a spike train with sinusoidally modulated rate $a(t)$ with mean a_0, modulation depth a_1, and frequency f_{stim}, cf. Eq. (7). As a first-order approximation, the output spike train of the neuron is characterized by the sinusoidally modulated response firing rate $r(t)$ with mean r_0, amplitude r_1, frequency f_{stim} and phase ϕ, cf. Eq. (10). Adapted from Nordlie et al (2010), Figure 1.

exotic. In the spirit of Izhikevich (2003b) we therefore treat all quantities except time and membrane potential as unitless for the Izhikevich model class.

The AMAT class is implemented in NEST as model `amat2_psc_exp` using exact integration (Rotter and Diesmann, 1999). The implementation follows the NEST convention of parameterizing the membrane potential equation Eq. 4 in terms of membrane time constant τ_{m} and membrane capacitance C_{m} and an explicit reversal potential E_{L}, while Yamauchi et al (2011) parameterize their Eq. 1 in terms of τ_{m} and membrane resistance R and define $E_{\text{L}} = 0\,\text{mV}$. The parameterizations are related by $C_{\text{m}} = \tau_{\text{m}}/R$ and a shift of the membrane potential V and the resting value of the threshold ω by E_{L}. Some parameter values were adjusted to be able to reproduce Figs. 6 and 7 in Yamauchi et al (2011) as discussed in the Appendix. Model variants L and R are excluded from the study as they have identical parameters to variants A and O, respectively.

In all simulations reported here, a single neuron is stimulated with spike train input. For the Izhikevich model class, this spike input results in instantaneous jumps in the membrane potential v. For the AMAT class, each incoming spike evokes an exponentially decaying synaptic current. For details, see Tables 1 and 2 and Sec. 2.2.

Output spikes are recorded with NEST device `spike_detector`.

2.2 Stimulation

We briefly summarize here the sinusoidal stimulation protocol and response characterization based on Nordlie et al (2010) and presented in detail in Heiberg et al (2013). More general stimulation protocols are described in Sec. 2.5.

Model neurons are stimulated with sinusoidally modulated inhomogeneous Poisson process spike trains (Figure 2) with rate (or intensity)

$$a(t) = a_0 + a_1 \sin(2\pi f_{\text{stim}} t)\ . \tag{7}$$

Mean rates a_0, modulation depth a_1, and modulation frequency f_{stim} are varied systematically; modulation depth is limited to $0 \le a_1 \le a_0$ to avoid rectification. We used NEST device `sinusoidal_poisson_generator` to generate the input spike trains.

The weights $w > 0$ of the synapses transmitting the stimulus spike train $a(t)$ are varied from about 10% to about 75% of the synaptic weight w_θ required if a single incoming excitatory spike shall evoke a threshold crossing from rest. For the AMAT model class, w_θ is the same for all model variants and we use weights between 100 pA and 900 pA in our experiments.

For the Izhikevich model class, in contrast, model parameters do influence the response to isolated spikes. We therefore define a weight factor ξ for each model variant as the smallest weight for which a single excitatory input spike triggers the spike initiation process. Synaptic weights w are set to fractions of this value, ranging from 0.1 to 0.75, i.e., within the same range as for the AMAT model.

In addition to the resulting current stimulus, $I_{\text{stim}}(t)$, we consider stationary noisy background input currents $I_{\text{bg}}(t)$, representing unspecific weak network input. This allows us to study neuronal responses to $I_{\text{stim}}(t)$ in different total input scenarios. The full input a neuron receives is thus given by $I(t) = I_{\text{stim}}(t) + I_{\text{bg}}(t)$. We characterize the background current by its mean μ_{bg} and standard deviation σ_{bg}.

The NEST implementation of the Izhikevich neuron model is equipped with instantaneous current-based synapses. Assuming high rates and small synaptic strength, balanced spiking input can be approximated well by Gaussian white noise. We thus inject approximate Gaussian white noise realizations of defined mean μ_{bg} and standard deviation σ_{bg} using NEST's `noise_generator`[2].

The AMAT model, as used here, has current-based exponential synapses with characteristic time constants $\tau_{\text{syn,E}} = 1\text{ms}$ and $\tau_{\text{syn,I}} = 3\text{ms}$. We inject background current as Poisson spike trains through synapses with small, fixed weight $w_{\text{E,bg}} = 1\,\text{pA}$ and $w_{\text{I,bg}} = -4/3\,\text{pA}$, respectively, using NEST model `poisson_generator`. The resulting noise input current has mean and standard deviation

$$\mu_{\text{bg}} = w_{\text{E,bg}} \nu_{\text{E}} \tau_{\text{syn,E}} + w_{\text{I,bg}} \nu_{\text{I}} \tau_{\text{syn,I}} \tag{8}$$

$$\sigma_{\text{bg}} = \sqrt{w_{\text{E,bg}}^2 \nu_{\text{E}} \tau_{\text{syn,E}}/2 + w_{\text{I,bg}}^2 \nu_{\text{I}} \tau_{\text{syn,I}}/2}\ . \tag{9}$$

[2] The current generated is stepwise constant during each $dt = 0.1\text{ms}$ time step, with Gaussian-distributed amplitude.

Type	Two-variable non-linear dynamic system: membrane potential V, recovery variable U
Subthreshold dynamics	$\dot{V}(t) = \frac{1}{25}V^2(t) + 5V(t) + 140 - U(t) + I_{\mathrm{syn}}(t) + I_{\mathrm{bg}}(t) + I_{\mathrm{ext}}$ (1) $\dot{U}(t) = a\,(bV(t) - U(t))$ (2) Integrated using forward Euler algorithm on fixed time grid t_k.
Spiking	A spike is emitted at t_k if $V(t_k) \geq V_{\mathrm{th}}$ and variables are reset according to $V(t_k) \leftarrow c$, $U(t_k) \leftarrow U(t_k) + d$
Refractoriness	No explicit refractory time
Synapses	δ-current pulses $I_{\mathrm{syn}}(t) = \xi \sum_{n,j} w_n \delta(t - \hat{t}_{n,j})$, where $\{\hat{t}_{n,j}\}$ are spike times of neuron n
Noise current	Approximate Gaussian white noise $I_{\mathrm{bg}}(t)$, cf. Eqs. 8 and 9.
Parameters	a, b, c, d, I_{ext}, ξ (model-dependent weight factor)

Table 1 Summary of Izhikevich model; for parameters, see Table 3.

Type	Leaky integrator with membrane potential V and adaptive threshold V_{th}
Subthreshold dynamics	$\tau_{\mathrm{m}}\dot{V}(t) = -\frac{1}{\tau_{\mathrm{m}}}(V(t) - E_{\mathrm{L}}) + \frac{1}{C_{\mathrm{m}}}I_{\mathrm{syn}}(t)$ (3) $V_{\mathrm{th}}(t) = \sum_k H(t - t_k) + \beta \int_{-\infty}^{t} K(s)\dot{V}(t-s)\mathrm{d}s + \omega$ (4) $H(t) = \left(\alpha_1 e^{-t/\tau_1} + \alpha_2 e^{-t/\tau_2}\right)\Theta(t)$ (5) $K(s) = s e^{-s/\tau_V}\Theta(s)$ (6) Integrated using exact integration on fixed time grid t_k, see Appendix. $\Theta(t)$: Heaviside step function.
Spiking	A spike is emitted at t_k if $V(t_k) \geq V_{\mathrm{th}}(t_k)$ and neuron is not refractory. No reset upon spike.
Refractoriness	After a spike at t_k, the neuron cannot fire a new spike until $t_k + \tau_{\mathrm{ref}}$. V, V_{th}, H, and K evolve freely during the refractory time.
Synapses	Exponentially decaying currents $I_{\mathrm{syn}}(t) = \sum_{n,j} w_n e^{-(t-\hat{t}_{n,j})/\tau^n_{\mathrm{syn}}}\Theta(t - \hat{t}_{n,j})$ where $\tau^n_{\mathrm{syn}} \in \{\tau_{\mathrm{syn,E}}, \tau_{\mathrm{syn,I}}\}$
Parameters	τ_{m}, R, β, $\alpha_{1,2}$, $\tau_{1,2}$, τ_V, τ_{ref}, $\tau_{\mathrm{syn,E}}$, $\tau_{\mathrm{syn,I}}$

Table 2 Summary of AMAT model; for parameters, see Table 4.

For given μ_{bg} and σ_{bg}, we obtain noise input rates by solving Eqs. 8–9 for ν_{E} and ν_{I}.

We consider three background current regimes: first the case without additional background current $I_{\mathrm{bg}}(t) = 0\,\mathrm{pA}$, where all spiking activity is purely stimulus induced. In the second case, $I_{\mathrm{bg}}(t)$ is chosen such that $\mu_{\mathrm{bg}} = 0\,\mathrm{pA}$, and σ_{bg} is large enough to elicit spiking activity with background input alone, i.e., if $I_{\mathrm{stim}}(t) = 0\,\mathrm{pA}$. In the third case, we consider a net inhibitory background current, with $\mu_{\mathrm{bg}} < 0\,\mathrm{pA}$ and sufficient standard deviation σ_{bg} to again elicit baseline spiking in absence of $I_{\mathrm{stim}}(t)$. While the first scenario can be considered a typical situation for neurons in slice preparations, the latter two mimic the situation *in vivo*, e.g., in cortical layer II/III where ongoing spiking activity is sparse (see e.g., Sakata and Harris (2012); Petersen and Crochet (2013)) and input currents are balanced or even inhibition dominated (Haider et al, 2013).

Label	Model	a	b	c	d	ξ	I_{ext}
A	Tonic spiking	0.02	0.2	−65	6	15.1	0
B	Phasic spiking	0.02	0.25	−65	6	4.3	0
C	Tonic bursting	0.02	0.2	−50	2	15.1	0
D	Phasic bursting	0.02	0.25	−55	0.05	4.3	0
E	Mixed mode	0.02	0.2	−55	4	15.1	0
F	Spike frequency adaptation	0.01	0.2	−65	8	15.1	0
G*	Class 1 excitable	0.02	−0.1	−55	6	49	0
H	Class 2 excitable	0.2	0.26	−65	0	5.6	−0.5
I*	Spike latency	0.02	0.2	−65	6	15.1	0
J	Subthreshold oscillation	0.05	0.26	−60	0	1.8	0
K	Resonator	0.1	0.26	−60	−1	2.4	0
L*	Integrator	0.02	−0.1	−55	6	49	0
M	Rebound spike	0.03	0.25	−60	4	4.5	0
N	Rebound burst	0.03	0.25	−52	0	4.5	0
O*	Threshold variability	0.03	0.25	−60	4	4.5	0
P	Bistability	0.1	0.26	−60	0	0.87	0.24
Q	Depolarizing after-potential	1	0.2	−60	−21	17.8	0
R*	Accomodation	0.02	1	−55	4	1	0
S	Inhibition-induced spiking	−0.02	−1	−60	8	4.5	80
T	Inhibition-induced bursting	−0.026	−1	−45	0	4.8	80

Table 3 Parameters for Izhikevich model class obtained from code published by Izhikevich (2003a). Labels refer to subfigure labels in Izhikevich (2004, Fig. 1). Models A and I, G and L, and M and O, respectively, share the same parameters and differ only in their input parameters. For model T, we changed parameter d to $d = 0$ compared to $d = -2$. Instances marked with an asterisk were not included in the study due to repeated parameters sets or non-standard model equations; see text for details. Common parameters: $V_{\text{th}} = 30\,\text{mV}$, $V(t = 0) \sim U(-70\,\text{mV}, 30\,\text{mV})$.

Label	Model	α_1	α_2	β
A	Tonic spiking	10	0	0
B	Phasic spiking	10	0	−0.3
C	Tonic bursting	−0.5	0.35	0
D	Phasic bursting	−0.5	0.35	−0.3
E	Mixed mode	−0.8	0.7	0
F	Spike frequency adaptation	10	1	0
G	Class 1 excitable	15	3	0
H	Class 2 excitable	15	−0.05	0
I	Spike latency	10	0	−1
J	Subthreshold oscillations	1	0	0.2
K	Resonator	10	0	0.5
L*	Integrator	10	0	0
M	Rebound spiking	10	0	−2.5
N	Rebound bursting	−0.5	0.35	−2.5
O	Threshold variability	10	0	−0.5
P	Bistability	20	−0.4	0
Q	Depolarizing after-potential	25	−1	0
R*	Accomodation	10	0	−0.5
S	Inhibition-induced spiking	20	0	2
T	Inhibition-induced bursting	−0.5	0.35	2

Table 4 Parameters for AMAT model class, based on Yamauchi et al (2011, Table 1). Note that models A and L and O and R, respectively, have identical parameters, whence L and R are not included in the study (marked with asterisk). Common parameters: $E_{\text{L}} = -70\,\text{mV}$, $\omega = -65\,\text{mV}$, $C_{\text{m}} = 200\,\text{pF}$, $\tau_{\text{m}} = 10\,\text{ms}$, $\tau_1 = 10\,\text{ms}$, $\tau_2 = 200\,\text{ms}$, $\tau_V = 5\,\text{ms}$, $\tau_{\text{ref}} = 2\,\text{ms}$, $\tau_{\text{syn,E}} = 1\,\text{ms}$, $\tau_{\text{syn,I}} = 3\,\text{ms}$, $V(t = 0) \sim U(-70\,\text{mV}, -65\,\text{mV})$. See text for difference between NEST parameterization and that in Yamauchi et al (2011).

2.3 Characterization of response properties

2.3.1 Sinusoidal rate model

We characterize the response of the neurons by a sinusoidal rate model

$$r(t) = r_0 + r_1 \cos(2\pi f_{\text{stim}} t + \phi_1) + \sum_{m=2}^{\infty} r_m \cos(2m\pi f_{\text{stim}} t + \phi_m) \,, \tag{10}$$

as illustrated in Figure 2. For a purely linear response, r_0 represents the background firing rate of the neuron, r_1 the stimulus response amplitude (with phase shift ϕ_1), and we expect $r_m = 0$ for all higher harmonics ($m \geq 2$). Any nonlinearities in the system will typically be associated with power in the higher harmonics. We consider power at harmonics as significant (z-test, 99% confidence level) if

$$r_m > r_{\text{crit}} = B + 2.34\Sigma \,, \tag{11}$$

where B is the estimated background power of the spike train between the harmonics and Σ the weighted standard deviation of the spike train power spectrum across frequencies. For details, see Sec. 2.2.2 of Heiberg et al (2013).

2.3.2 Linearity

We proceed as follows to characterize the linearity of the firing-rate curve in response to stationary input: We obtain the firing-rate curve $r_0 = f(a_0)$ for a given neuron model, noise regime and synaptic weight by measuring the output rate r_0 as a function of stationary input rate a_0 in the absence of modulation ($a_1 = 0$). To characterize the linearity of f over an interval $[\alpha, \beta]$, we define the linearity measure

$$\bar{L}_1 = \frac{\int_\alpha^\beta [f(x) - \ell(x)]^2 \, dx}{\beta - \alpha} \Big/ \ell^2\left(\frac{\alpha+\beta}{2}\right) \,, \tag{12}$$

as the normalized mean square difference between $f(x)$ and $\ell(x)$, the best linear fit to $f(x)$ over $[\alpha, \beta]$. If $f(x)$ is perfectly linear, we have $\bar{L}_1 = 0$, while $\bar{L}_1 = 1$ means that the average squared distance between firing-rate curve and linear fit is equal to the mean value over the interval. Larger values of $\bar{L}_1$ are difficult to interpret, though. We therefore define

$$L_1 = \frac{1}{1 + \bar{L}_1} \tag{13}$$

as linearity measure. $L_1 = 1$ indicates perfect linearity, $L_1 = 1/2$ a deviation from linearity equal to the mean value, while L_1 approaches 0 for large deviations. For a given mean rate a_0 and modulation depth a_1, we evaluate linearity over $[\alpha, \beta] = [a_0 - a_1, a_0 + a_1]$, i.e., the range of rates spanned by the temporally modulated input.

2.4 Rate model description

The response of a linear, time-invariant (LTI) system to any input can be calculated as a convolution of the input and the *impulse response* of the system. A wide class of non-linear systems can be described by a linear convolution of the input with a kernel $h(t)$ followed by a non-linear *activation function* $g(\cdot)$, so that the response is given by

$$r(t) = g(h(t) * a(t)) \,. \tag{14}$$

To test how well this applies to the neuron models studied here, we fit linear-nonlinear firing-rate models to the responses of the spiking neuron models and compare firing-rate predictions from the linear-nonlinear models to those of the fitted spiking models. We summarize the derivation of the firing-rate model below, based on Heiberg et al (2013) and Nordlie et al (2010).

For each neuron, we find the activation function $g(\cdot)$ and the kernel $h(t)$. For constant input, $a(t) = a_0$, the convolution becomes the identity operation, provided the kernel is normalized ($\int h(t)dt = 1$). We determine $g(\cdot)$ by measuring the response to stationary input, $r_0 = g(a_0)$ for a range of a_0 and obtain a continuous representation of $g(\cdot)$ by interpolation (linear B-spline).

To obtain the kernel $h(t)$, we linearize the activation function around a given *working point* (a_0, r_0). The response to $a(t) = a_0 + a_1 s(t)$ can then be expressed as

$$\begin{aligned} r(t) &= g(h(t) * (a_0 + a_1 s(t))) \\ &\approx r_0(a_0) + h_0(t; a_0, a_1) * (a_1 s(t)) \,, \end{aligned} \tag{15}$$

where the linear impulse response function

$$h_0(t; a_0, a_1) = g'(a_0) h(t; a_0, a_1) =: \gamma h(t; a_0, a_1) \tag{16}$$

combines the normalized kernel with the linear gain γ. In general, this approximation is only valid for small deviations from the working point. However, the limits are not known a priori. For brevity of notation, we will usually drop the explicit reference to stimulus parameters a_0 and a_1 below.

We obtain the transfer function, i.e., the Fourier transform of the linear impulse response $h_0(t)$, from the model responses to sinusoidally modulated input ($s(t) = \sin 2\pi f_{\text{stim}} t$, cf. Eq. (7))

$$H_0(f_{\text{stim}}) = \frac{r(f_{\text{stim}})}{a_1} e^{i\phi(f_{\text{stim}})} \tag{17}$$

where $r(f_{\text{stim}})$ and $\phi(f_{\text{stim}})$ are the Fourier amplitude and phase of the response, respectively.

In Nordlie et al (2010) and Heiberg et al (2013), first-order low-pass filters with delay provided adequate fits to the empirical frequency responses. Here, more complex filter models are needed to fit additional response features. In particular, we expect a second filter time constant $\tau_c = 1/(2\pi f_c)$ to be needed to model some of the response types illustrated in Figure 1. We choose to combine low- and high-pass components of the filter as a sum:

$$\tilde{H}_{0,\mathrm{SUM}}(f) = \gamma_1 e^{-2\pi i f \Delta} \left(\frac{1}{1+i\frac{f}{f_{c,1}}} + \frac{\gamma_2}{1+i\frac{f}{f_{c,2}}} \right) . \tag{18}$$

This form allows for a representation of the filter through a system of linear differential equations, see Sec. 2.4.1.[3]

The filter kernels were fitted to the empirical transfer function to capture it with as few parameters as possible. For each set of stimulus parameters (a_0, a_1, w, μ, σ), we obtained fits for the parameters γ_1, $f_{c,1}$, γ_2, $f_{c,2}$ and Δ. Fitting was performed using basin-hopping hopping optimization provided by the SciPy Optimize toolbox with L-BFGS-B minimization (Jones et al, 2001). To avoid pathological solutions, we imposed the following constraints

$$0.25\mathrm{ms} \le \tau_{c,1,2} \le 175\mathrm{ms} \tag{19}$$
$$\Leftrightarrow \quad 0.909\mathrm{Hz} \le f_{c,1,2} \le 636.6\mathrm{Hz} \tag{20}$$
$$0 \le \Delta \le 75\mathrm{ms} . \tag{21}$$

If a fit resulted in $f_{c,1} > f_{c,2}$, we swapped frequencies and gain coefficients

$$f_{c,1}, f_{c,2} \leftarrow f_{c,2}, f_{c,1} \tag{22}$$
$$\gamma_1, \gamma_2 \leftarrow \gamma_1\gamma_2, 1/\gamma_2 \tag{23}$$

so that $f_{c,1}$ and $f_{c,2}$, respectively, are always the lower and upper characteristic frequencies of the filter. For each parameter combination, we performed 60 independent fits from different starting points and retained the best fit. We also performed 15 independent fits for a pure lowpass filter, but these never yielded better results than fits to the bandpass filter defined by Eq. (18).

We now define the linear-nonlinear rate model as

$$r_{\mathrm{NL}}(t) = \max(0, g(h(t) * a(t))) , \tag{24}$$

[3] We also explored combining the terms in product form

$$\tilde{H}_{0,\mathrm{Prod}}(f) = \gamma_1 e^{-2\pi i f \Delta} \frac{1}{1+i\frac{f}{f_{c,1}}} \left(1 - \frac{\gamma_2}{1+i\frac{f}{f_{c,2}}} \right) ,$$

but did not observe significantly different results.

with the normalized kernel

$$h(t) = \frac{h_0(t)}{\gamma_1(1+\gamma_2)} \tag{25}$$

and correspondingly in Fourier space. We take the maximum solely to avoid negative rates that may result in rare cases from extrapolation of the activation function $g(\cdot)$.

2.4.1 Differential-equation representation

The filter $\tilde{H}_{0,\mathrm{SUM}}(f)$ corresponds to a sum of low-pass filters in the time domain. For this model, the linear-nonlinear model of Eq. (14) can be mapped to a set of delay differential equations using the linear chain trick (Nordbø et al, 2007).

In particular, in the time domain the filter is given by

$$\begin{aligned} h_{0,\mathrm{SUM}}(t+d) &= h_{0,1}(t+d) + h_{0,2}(t+d) \\ &= \Theta(t) \left(\frac{\gamma_1}{\tau_1} e^{-t/\tau_1} + \frac{\gamma_1\gamma_2}{\tau_2} e^{-t/\tau_2} \right) \end{aligned} \tag{26}$$

with Heaviside step function $\Theta(t)$. We introduce

$$u(t) = (a * h_{0,\mathrm{SUM}})(t) = u_1(t) + u_2(t) \tag{27}$$

with

$$u_1(t) = (a * h_{0,1})(t) \quad \text{and} \quad u_2(t) = (a * h_{0,2})(t) . \tag{28}$$

Straightforward differentiation of the two temporal kernels yields

$$\dot{u_1}(t) = -\frac{u_1(t)}{\tau_1} + a(t)\frac{\gamma_1}{\tau_1} \tag{29}$$

$$\text{and} \quad \dot{u_2}(t) = -\frac{u_2(t)}{\tau_2} + a(t)\frac{\gamma_1\gamma_2}{\tau_2} . \tag{30}$$

From this we can solve for $u(t) = u_1(t) + u_2(t)$ and the full rate dynamics then follows by application of the nonlinearity g

$$r(t) = g(u(t)) . \tag{31}$$

The advantage of the differential representation Eq. (29) lies in the fact that it is local in time, whereas the representation by convolution in general relies on knowledge of the complete history of the dynamics.

2.5 Tests against spike trains

We compare the response properties of our rate-based model against spiking neuron models as follows. We use synthetic (Sec. 2.5.1) or experimentally recorded (Sec. 2.5.2) spike trains $S(t)$ as test input. Spiking neuron models are driven by these trains directly and their output spike trains $R(t)$ are recorded as described in Sec. 2.6. We then use the fixed-kernel density estimation method by Shimazaki and Shinomoto (2010) with 0.05 ms bin width to estimate a continuous output firing rate $r_{\text{spike}}(t)$. This is the reference against which we test the rate-based model.

To obtain the response of the rate-based model, we either use the known rate of the synthetic input spike trains or obtain a continuous input rate function $a(t)$ from the input spike trains $S(t)$ using the fixed-kernel density estimation method. Applying Eq. (14) to this rate yields the reponse of the rate model $r_{\text{rate}}(t)$.

We repeat each simulation experiment with five different random seeds and retain only results for which the optimal kernel width obtained by the densitiy estimation methods is 15 ms or less, as wider kernels would lead to an undue smoothing over time.

The difference between responses obtained from rate-based and spiking models is then defined as the mean squared error normalized by the variance of the response of the spiking model (Pillow et al, 2005)

$$\bar{E}_r = \frac{\int_0^T \left(r_{\text{rate}}(t) - r_{\text{spike}}(t)\right)^2 \mathrm{d}t}{\int_0^T \left(r_{\text{spike}}(t) - \bar{r}_{\text{spike}}\right)^2 \mathrm{d}t} \tag{32}$$

where $\bar{r}_{\text{spike}}$ is the average response rate of the spiking model. Corresponding to the linearity measure L_1 (Sec. 2.3.2), we define

$$E_r = \frac{1}{1+\bar{E}_r} \tag{33}$$

as quality measure. $E_r = 1$ indicates perfect agreement, $E_r = 1/2$ an error equal to variation, while E_r approaches 0 for large deviations between spiking and rate model response.

2.5.1 Tests with synthetic spike trains

We first test models using a Poisson spike train input with step changes in rates. Stimulus parameters are given in Table 5. Spike responses are obtained by simulating a population of 4,096 independent model neurons driven by one Poisson process each. The resulting 4,096 output spike trains are pooled to estimate the output rate $r_{\text{spike}}(t)$.

2.5.2 Tests with realistic spike trains

To test the performance of the rate models in response to realistic spike trains, we drive model neurons by spike trains recorded from retinal ganglion cells (RGCs) in cat (Casti et al, 2008). Their data set contained 128 spike trains of 8 s duration recorded during different trials, characterized by low baseline firing and fast transients as illustrated in Figure 3. Because trains from the first trials in the dataset have noticeably lower average firing rates than those from later trials, we only use the last 96 spike trains with an average firing rate of 18.3 ± 1.3 spikes per second.

The Izhikevich models in particular responds weakly to these spike trains in many cases. We therefore increase the rate of the input spike trains by merging pairs of spike trains, resulting in a total of 48 input spike trains with average rates of 36.6 spikes per second. We then drive 48 model neurons independently with one spike train each for 8000 ms and pool the resulting output spike trains for output rate estimation.

2.6 Simulation

Simulations for all model configurations are performed with the NEST Simulator (Gewaltig and Diesmann, 2007; Plesser et al, 2013).

In practice, we simulate N trials by creating N mutually independent Poisson-generator–neuron pairs in a single NEST simulation. Membrane potentials are randomized upon network initialization and data collection is started only after an equilibration period of 1 s simulated time. All simulations are performed with a spike-time resolution of 0.1 ms.

Simulations underlying model fitting are performed using NEST 2.3.r10450, while some scoring of model responses according to Eq. 33 was performed using NEST 2.8.0. Trials are configured using the NeuroTools.parameters package (Muller et al, 2009). Data analysis is performed using NumPy 1.7.1–1.11.1, SciPy 0.18.1, Pandas 0.11.0–0.18.1 and Matplotlib 1.2.1–1.5.3 under Python 2.7.

3 Results

3.1 Response to spike train input

To gain a first impression of the basic response properties of the models, we show the spike responses to stationary and sinusoidally modulated Poisson input in Figures 4 and 5 for Izhikevich and AMAT models, respectively. Each raster plot

Interval [ms]	0–600	600–1000	1000–1200	1200–1500
Rate [1/s]	100	200	40	150

Table 5 Poisson spike train rates applied during different intervals. Rates change instantaneously at interval boundaries.

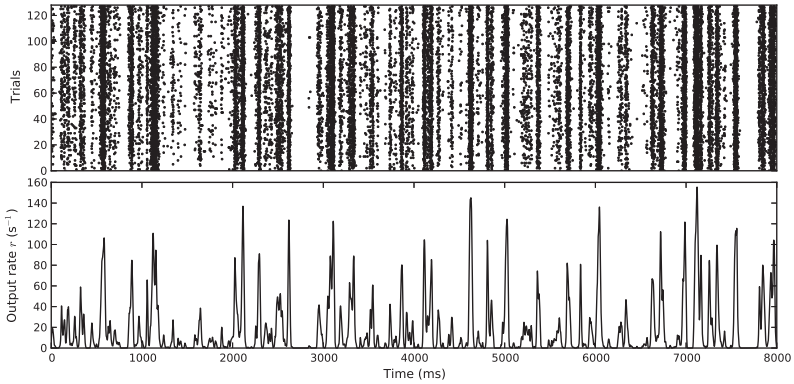

Fig. 3 Spike raster and rate profile for retinal ganglion cell (RGC) data used to test model performance. Rates were estimated by means of kernel density estimation (Shimazaki and Shinomoto, 2010), using the *fixed kernel* method.

shows the response of 30 unconnected neurons, half driven by stationary and half by sinusoidally modulated Poisson spike trains after an equilibration phase of 1000 ms. Each of the 30 neurons receives different realizations of input spike trains and noise, but the same trains and noise are used for all models.

As spiking and bursting variations are included as separate response types in the model classification (Fig. 1), we illustrate the burstiness of the responses by marking spikes fired within $dT = 5$ ms of each other as belonging to a burst, corresponding to the upper limit of intra-burst intervals in LGN (Funke and Wörgötter, 1997, p. 71).

The models that exhibit their characteristic behaviour (Fig. 1) based on "simple" excitatory input current shapes (e.g., steps, ramps, pulses) generally behave as expected when driven by Poisson spike trains; spiking neurons primarily spike and bursting neurons burst, but the nuances of individual models are less visible in the spiking patterns (e.g. tonic vs phasic) due to the input variability. Models that are based on more specific input current pattens or consistent inhibitory input (i.e., bottom rows) do to a lesser extent receive the required input and respond in a less characteristic manner, some even seem erratic (e.g., Fig. 4T and Fig. 5Q). Note, however, that the figures illustrate responses at a single input rate and noise regime combination and that the models to varying degree are sensitive to these conditions.

In contrast to the 20 markedly different responses to current injections (Fig. 1), responses to spiking input show more similar patterns across models, differing in the overall response rate and the proportion of spikes belonging to bursts.

While some Izhikevich and AMAT models that show identical responses to current injections also respond similarly when driven by spiking input (e.g., top two rows), we observe some with very different response patterns (e.g., depolarizing after-potential (Q) and inhibition-induced spiking and bursting (S and T respectively)) across the two model classes.

3.2 Linear-nonlinear models

We now obtain the linear-nonlinear models as defined by Eq. (24).

3.2.1 Activation functions

We first obtain the activation function $g(\cdot)$ by fitting a linear B-spline to the response to stationary input, $r_0 = g(a_0)$, varying a_0 from $0\,\mathrm{s}^{-1}$ to $1000\,\mathrm{s}^{-1}$ in steps of $10\,\mathrm{s}^{-1}$. This yields one activation function fit for

- each model (15 models for the Izhikevich model class, 18 for the AMAT model class);
- each background noise regime

  no noise $\mu = 0, \sigma = 0$

  balanced noise Izhikevich: $\mu = 0, \sigma = 0.1$, AMAT: $\mu = 0\mathrm{pA}, \sigma = 100\mathrm{pA}$

  biased noise Izhikevich: $\mu = -0.1, \sigma = 0.2$, AMAT: $\mu = -100\mathrm{pA}, \sigma = 200\mathrm{pA}$;
- each synaptic weight (Izhikevich: 0.1, 0.25, 0.5, 0.6, 0.75; AMAT 100pA, 300pA, 500pA, 700pA, 900pA).

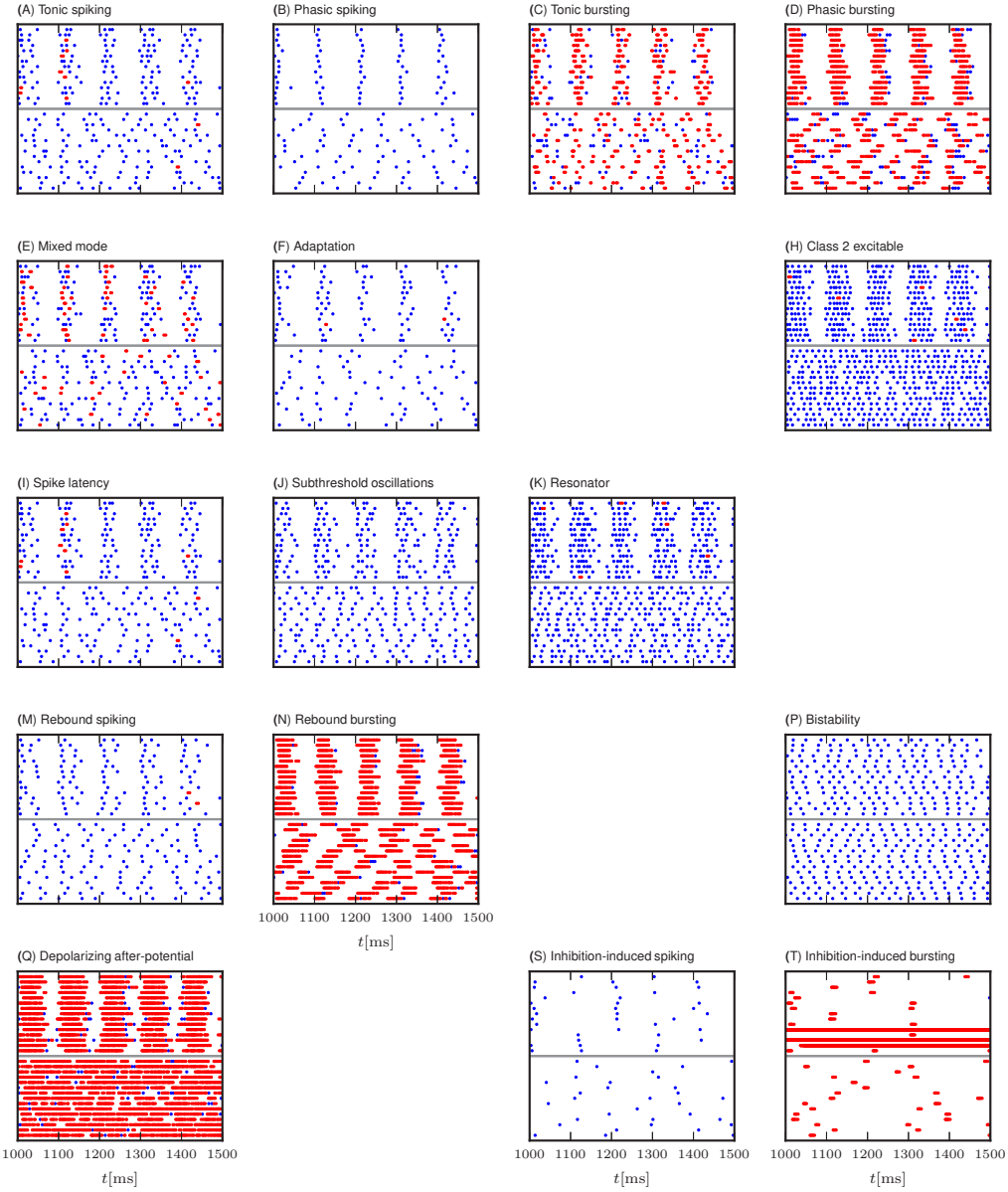

Fig. 4 Spike responses of Izhikevich models driven by stationary (rate $a_0 = 400\,\mathrm{s}^{-1}$) or sinusoidally modulated (rate $a_0 = 400\,\mathrm{s}^{-1}$, modulation amplitude $a_1 = 400\,\mathrm{s}^{-1}$, modulation frequency 10 Hz) Poisson spike trains impinging with synaptic weight $w = 0.6\,\mathrm{pA}$ weighted with ξ, and noise ($\mu = 0\,\mathrm{pA}$, $\sigma = 0.1\,\mathrm{pA}$). The upper part of each panel shows the response of 15 neurons driven by different sinusoidally modulated spike trains, the lower part the response of 15 neurons driven by different stationary trains after 1 s of equilibration time. Isolated spikes are shown in blue, clustered spikes within $dT = 5\,\mathrm{ms}$ from another spike in red.

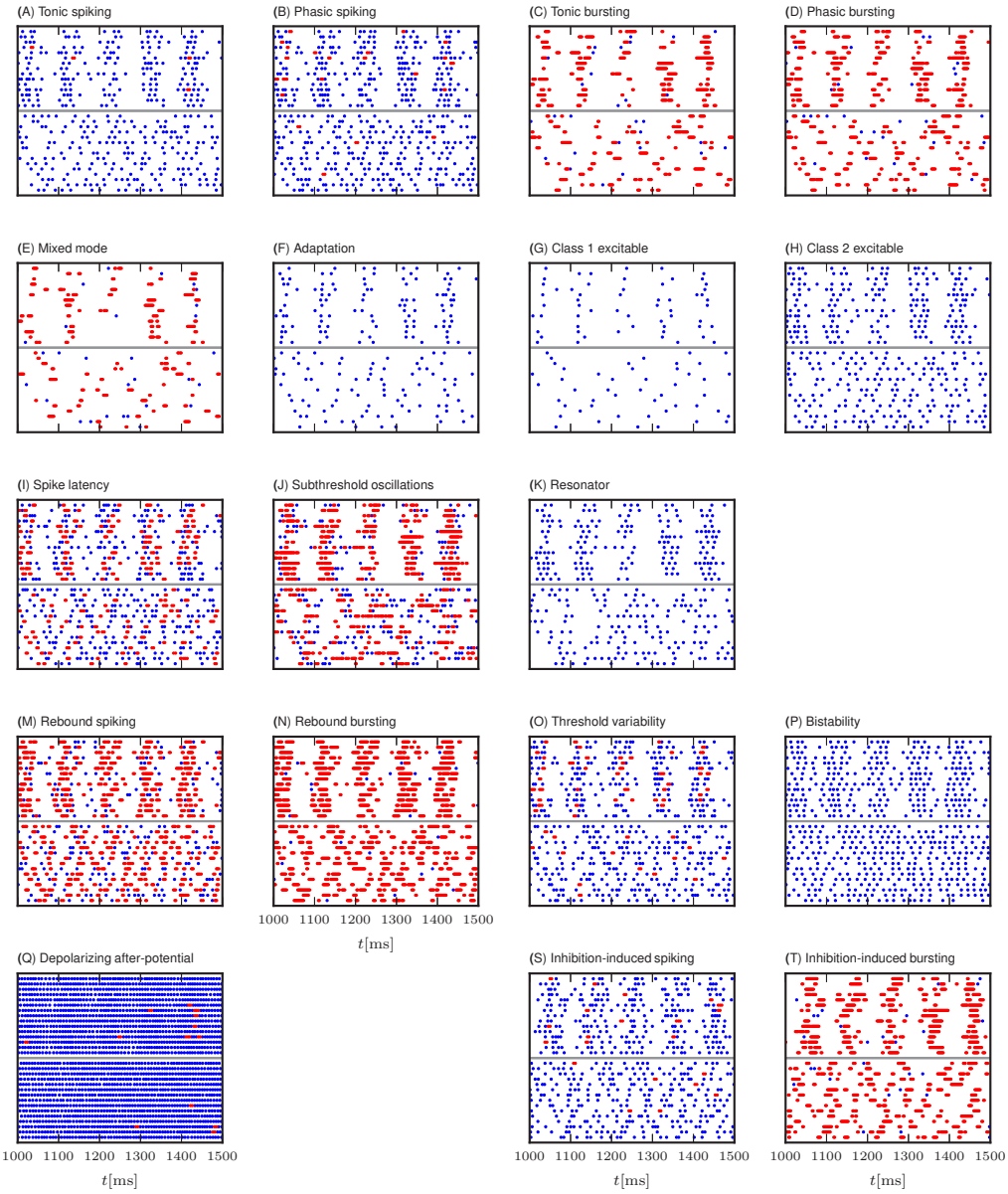

Fig. 5 Spike responses as for AMAT models as in in Fig. 4, using weight $w = 200\,\mathrm{pA}$, and noise with $\mu = 0\,\mathrm{pA}$, and $\sigma = 100\,\mathrm{pA}$.

We thus obtain a total of 225 activation functions for the Izhikevich model class and 270 for the AMAT model class.

The top row of Fig. 6 shows the activation function for the Tonic Spiking and the Phasic Bursting models for the Izhikevich and AMAT model classes, respectively, for all three noise regimes. The spike rates obtained from the simulations are fitted very well by the B-splines. This holds for all models except models S and T in the Izhikevich class (inhibition-induced spiking and bursting), which have rather noisy activation curves with extremely high rates under certain conditions (above $1000\,\mathrm{s}^{-1}$); data not shown.

Before we investigate the response of the models to temporally modulated stimuli, we briefly explore the linearity of the activation functions around different working points $a_0 = \{50\,\mathrm{s}^{-1}, 100\,\mathrm{s}^{-1}, 200\,\mathrm{s}^{-1}, 400\,\mathrm{s}^{-1}, 800\,\mathrm{s}^{-1}\}$ and modulation amplitude $a_1 = \{0.25, 0.5, 0.75, 1\} \times a_0$ about the working point. A working point at $a_0 = 200\,\mathrm{s}^{-1}$ with modulation amplitude $a_1 = 100\,\mathrm{s}^{-1}$ is shaded in the top row of Fig. 6 for illustration. Figures 7 and 8 show the linearity score L_1 for each of the 20 (a_0, a_1) combinations for each response curve.

For the Izhikevich neurons, the stationary linearity metric L_1 indicates that strong synaptic weights w, large mean input rates a_0, and small modulation amplitudes a_1 give the most linear responses. Larger weights and mean rates not only increase the mean input of the Poisson input current, but also its variance. This leads to a linearization of the activation function and moves the activation threshold towards smaller rates (see also Chance et al (2002)). Furthermore, firing-rate modulation amplitudes are more likely to stay within a single region of the sigmoidal firing rate curve for small a_1, and are thus more likely to adhere to a linear fit.

The stationary linearity metric L_1 for the augmented MAT model indicates overall more linear behavior, but the same general pattern of parameter dependence can be seen (Figure 8). One notable difference is the saturation of the AMAT model at output rates of $500\,\mathrm{s}^{-1}$—due to the absolute refractory time of 2 ms—that adds another source of non-linearity in the firing rate curves for some neurons.

3.2.2 Transfer function and linear filters

We obtain empirical transfer functions according to Eq. 17 for 20 combinations of working point and modulation depth (a_0, a_1) for each model, noise regime and synaptic weight using the approach described in detail in Heiberg et al (2013, Sec. 2.2.2), measuring the model response at 28 different stimulation frequencies f_{stim}, logarithmically spaced from 1 Hz to 1000 Hz. We then fit the linear filter $\tilde{H}_{0,\mathrm{SUM}}(f)$ according to Eq. 18 as described in Sec. 2.4, obtaining fit parameters $(f_{c,1}, f_{c,2}, \gamma_1, \gamma_2, d)$ for each model and stimulation parameter combination. Note that γ_1 is fully captured by the activation function, and therefore does not explicitly enter the linear-nonlinear model we construct here, cf. Eq. 25.

The second row of Fig. 6 shows the resulting transfer functions and fitted kernels for the same models and conditions as the activation functions discussed above. The examples reveal bandpass behaviour for three out of four cases, which also show significant power in the second harmonic r_2. The exception is Tonic spiking for the AMAT class, which shows lowpass behavior and no significant power in r_2. Phasic bursting shows a second peak in the spectrum around 200 Hz (Izhikevich) and 500 Hz (AMAT), which our fitted bandpass filter models (thick light lines) cannot capture by construction. These peaks occur as refractory effects regularize firing patterns at high rates. The fitted bandpass filters capture the frequency response of the model neurons well, except for Izhikevich phasic bursting case, where the amplitude of the fitted filter is significantly larger than the power in the first harmonic.

We found that not all model variants responded sufficiently to periodic stimulation under all stimulation conditions to provide sufficient spike data to fit a kernel. Therefore, we only obtained kernel fits for approximately three-quarters of all conditions for the Izhikevich class (3508 out of 4800 possible) and about 90% of all conditions for the AMAT class (4843 out of 5400).

3.3 Grouping of models

To systematize model responses, we cluster the kernel fit parameter sets[4] with k-means clustering using Scikit-Learn (Pedregosa et al, 2011). We cluster Izhikevich and AMAT filters independent of each other, clustering into seven clusters from 100 initial conditions to avoid local minima. Since we are clustering fit parameters obtained for a wide range of simulation conditions, while we are interested in grouping the 16 and 18 model variants, respectively, we assign each model variant to a *model group* as follows: We count how often each model occurs in each k-means cluster and assign each model to the cluster to which it is assigned most often. Each cluster to which at least one model is thus assigned forms a model group. Fig. 9 shows the counts for each model in each cluster, with a maximum possible count of 300 if fit parameters are available for all combinations of μ, σ, w, a_0, a_1 and are assigned to the same cluster.

[4] Each parameter set consists of $f_{c,1}$, $f_{c,2}$, γ_1, γ_2, and d. To compress widely scattering data, we transformed $f_{c,1}$, $f_{c,2}$, and d using $\alpha(x) = \log_{10} x$ and γ_1 and γ_2 using $\beta(x) = \mathrm{sgn}\, x \log_{10} 100|x|$ before applying k-means clustering.

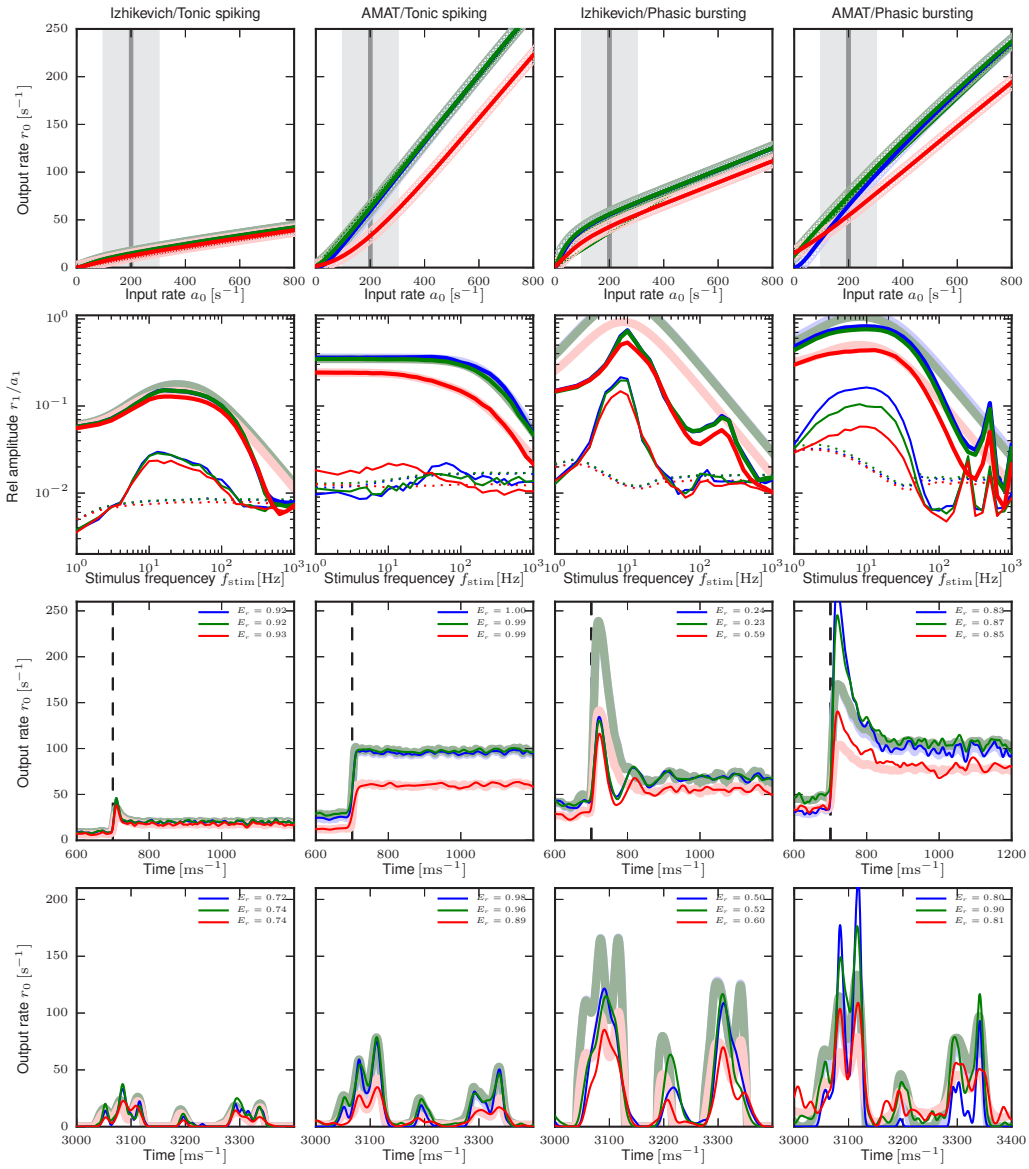

Fig. 6 Response properties for exemplary model neurons. Columns show from left to right response properties of Izhikevich and AMAT tonic spiking and Izhikevich and AMAT phasic bursting models. Top row: stationary output firing rate response r_0 as function of input rate a_0 for three noise regime levels (blue: no noise, green: balanced noise, red: biased noise). Light symbols show responses from simulations, solid lines the fitted B-splines. Second row: Frequency response to sinusoidally modulated Poisson input with mean $a_0 = 200$ s^{-1} and modulation amplitude $a_1 = 100$ s^{-1} as function of modulation frequency f_{stim}; thick solid lines: first harmonic r_1, thick shaded lines: fitted filter $H_0(f)$, thin solid lines: second harmonic r_2, dotted lines: significance level r_{crit}. Mean input rate a_0 and modulation range $a_0 \pm a_1$ are marked gray in the top row. Fit parameters are given in Table 6. Third row: Response of spiking model (thin solid lines) and rate-model prediction (light thick lines) to Poisson spike trains with rate 100 s^{-1} for $t < 700$ ms and 300 s^{-1} for $t \geq 700$ ms. Fit quality E_r shown as inset. Bottom row: Response to realistic spike trains, 400 ms section starting at 3000 ms (cf. Figure 3) with the same line types as for step responses. Connection weight w from left to right: 0.75, 700, 0.75, 500.

Model	Noise	γ_1	γ_2	$f_{c,1}$[Hz]	$f_{c,2}$[Hz]	Δ[ms]
Izh/Tonic spiking	none	−0.152	−1.328	9.988	61.577	0.987
	balanced	−0.150	−1.334	9.959	63.535	1.009
	biased	−0.110	−1.442	8.397	68.001	1.003
AMAT/Tonic spiking	none	0.468	−0.225	224.270	636.620	0.183
	balanced	0.386	−0.107	181.140	636.620	0.181
	biased	0.088	1.748	28.946	149.427	0.222
Izh/Phasic bursting	none	−25.548	−1.002	8.745	9.043	1.709
	balanced	−23.825	−1.002	8.817	9.134	1.670
	biased	−21.662	−1.003	8.601	8.892	1.936
AMAT/Phasic bursting	none	−0.718	−1.486	3.067	22.380	0.913
	balanced	−0.672	−1.488	3.159	21.450	0.832
	biased	−0.304	−1.884	3.697	21.139	0.836

Table 6 Fit parameters for filters $H_0(f)$ shown in the second row of Fig. 6.

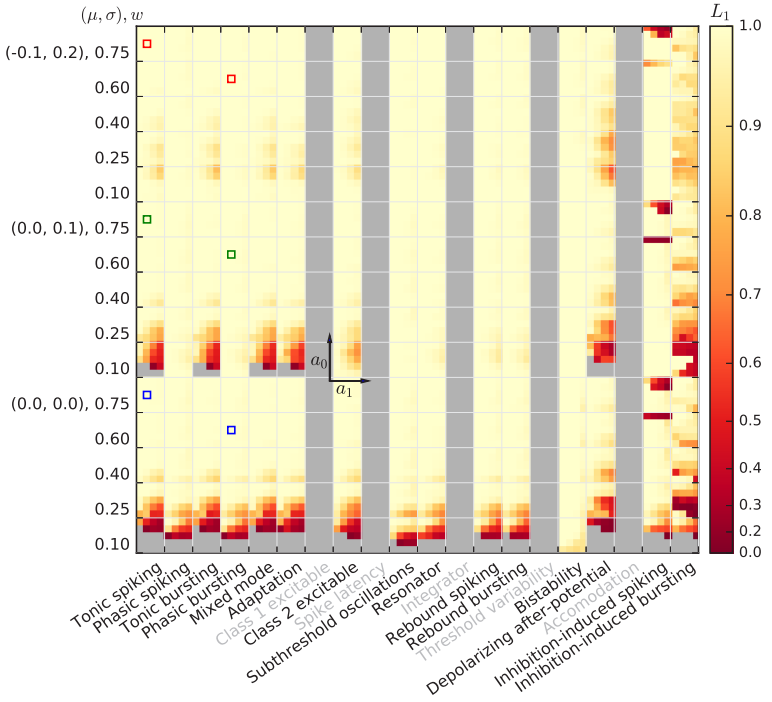

Fig. 7 Linearity measure L_1 for the Izhikevich model class for different model parameterizations (major columns), and five different synaptic weights for each of three noise regimes (major rows). Each major row/column block shows data for five different average input rates ($a_0 = \{50, 100, 200, 400, 800\}\mathrm{s}^{-1}$), minor rows) and four different modulation amplitudes ($a_1 = \{0.25, 0.5, 0.75, 1.0\} \times a_0$, minor columns), as indicated by the small coordinate axes shown for one major square. Thus, the bottom left minor square of each major square is the L_1 value computed over $37.5\,\mathrm{s}^{-1} \le a \le 62.5\,\mathrm{s}^{-1}$, while the upper right minor square is the L_1 value computed over $0\,\mathrm{s}^{-1} \le a \le 1600\,\mathrm{s}^{-1}$. $L_1 = 1$ indicates perfect linearity of the firing-rate curve $F(a)$ over the relevant input range, cf. Sec. 2.3.2. Grey indicates missing data, either because neurons were unresponsive or because the model variants are described by non-standard differential equations or have duplicate parameters. Blue, green, and red squares correspond to the examples shown in the first and third columns of Fig. 6.

The resulting grouping into six groups per model class is shown in Table 7, with median kernel parameter values for each group in Table 8. Grouping is clearly different for the Izhikevich and AMAT classes, supporting our previous observation that these models respond differently to spike input even though they show identical responses to the current injection protocol of Fig. 1.

Comparing the grouping of models to the spike responses shown in Figs. 4 and 5, we can roughly identify the groups found by k-means clustering of filter parameters to firing patterns, as indicated in the right column of Table 7. This classification is far from perfect, as several models show firing patterns different from the groups into which they have been placed, especially for the AMAT class. It should also be noted that the firing patterns are for a single stimulus configuration only and that models may behave differently under

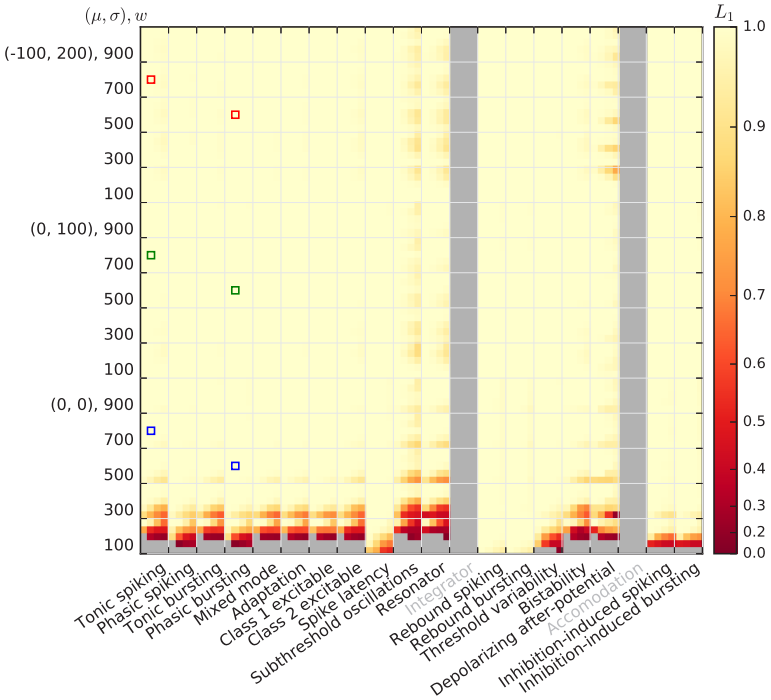

Fig. 8 Linearity measure L_1 for the AMAT model; the figure is constructed as Fig. 7.

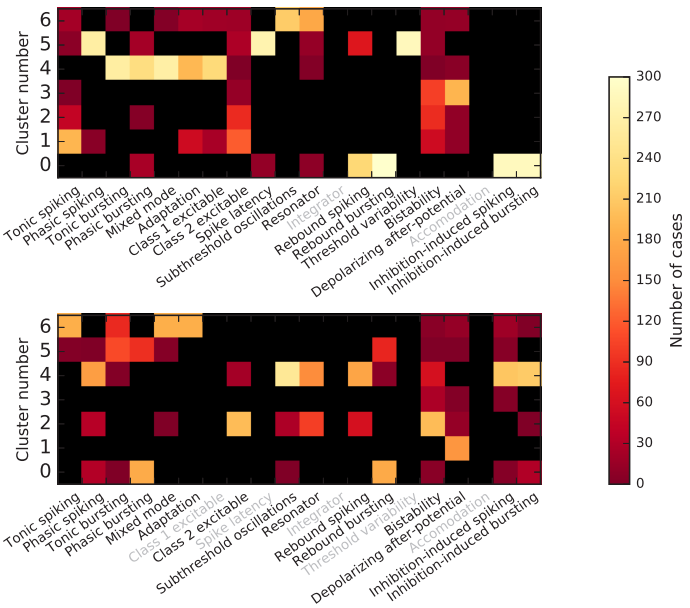

Fig. 9 Result of k-means clustering of linear filter fit parameters for the Izhikevich (top) and AMAT (bottom) model classes. Rows represent clusters, columns model variants and the color of each square indicates how many stimulation configurations were assigned to a given cluster for of each model variant. Each model variant is assigned to the cluster for which it reached the highest count of stimulation configurations. Black means zero count, and models not considered are indicated by greyed-out labels.

Group	Firing pattern	Izhikevich	AMAT
1	Isolated spikes, rare mini bursts	A/Tonic spiking E/Mixed mode F/Adaptation	B/Phasic spiking I/Latency O/Threshold variability
2	Isolated spikes	B/Phasic spiking J/Subthreshold oscillations K/Resonator M/Rebound spiking S/Inhibition-induced spiking T/Inhibition-induced bursting*	A/Tonic spiking H/Class 2
3	Short bursts	C/Tonic bursting	C/Tonic bursting D/Phasic bursting E/Mixed mode F/Adaptation* G/Class 1*
4	Long bursts	D/Phasic bursting N/Rebound bursting	M/Rebound spiking N/Rebound bursting S/Inhibition-induced spiking* T/Inhibition-induced bursting
5	Long bursts	Q/Depolarizing after-potential	J/Subthreshold oscillations K/Resonator*
6	Regular isolated spikes	H/Class 2 P/Bistability	P/Bistability Q/Depolarizing after-potential*

Table 7 Models grouped by k-means clustering of linear filter parameters as illustrated in Fig. 9. Groups for Izhikevich and AMAT models are paired according to the predominant firing pattern for each group for one test case as shown Figs. 4 and 5. Models with a different firing pattern than their group are marked with an asterisk. Filter kernel parameters for the groups are shown in Table 8.

Izhikevich					
Group	γ_1	γ_2	$f_{c,1}$[Hz]	$f_{c,2}$[Hz]	Δ[ms]
1	−11.98	−1.41	8.57	61.67	1.35
2	−1315.67	−1.01	17.09	18.77	4.29
3	−154.58	−1.21	10.51	23.28	0.91
4	−2273.17	−1.02	6.70	7.33	6.54
5	54.98	0.19	17.26	403.19	0.74
6	−1462.74	−1.02	36.15	38.72	4.24
AMAT					
Group	γ_1	γ_2	$f_{c,1}$[Hz]	$f_{c,2}$[Hz]	Δ[ms]
1	−90.59	−1.52	16.03	36.65	0.21
2	2.46	0.50	34.47	161.85	0.22
3	−34.88	−1.65	1.53	21.41	0.35
4	−1436.78	−1.00	16.06	18.20	1.90
5	32.98	0.29	8.56	407.10	0.27
6	3.89	0.90	12.77	190.14	0.20

Table 8 Median values of parameters for filter kernels fitted to the six groups described in Table 7 for Izhikevich and AMAT models.

other conditions; the k-means clustering, on the other hand, is based on a wide range of stimulus conditions.

3.4 Performance of rate models

We evaluate the perfomance of the linear-nonlinear firing rate models by testing them against the corresponding spiking model as described in Sec. 2.5, using the fit quality E_r as criterium, with $E_r = 1$ indicating a perfect fit.

The third row of Fig. 6 shows the response to a Poisson spike train with a step in rate from $100\,\mathrm{s}^{-1}$ to $300\,\mathrm{s}^{-1}$. We use the filters fitted for the same noise regime and synaptic weight and $a_0 = 200\,\mathrm{s}^{-1}$ and $a_1 = 100\,\mathrm{s}^{-1}$, corresponding to the step height. For the Tonic spiking case, the firing rate models capture the spiking neuron response very well, with $E_r > 0.9$ in all cases (see legend). For the Phasic bursting models, we find that the rate models overshoot massively for the Izhikevich variant with no or balanced noise, while the ratemodels "undershoot" somewhat for the AMAT variant. The stationary rate attained after the step is captured well in all cases. These examples also provide an illustration of how to interpret the fit quality measure E_r.

Figures 10 and 11 show the fit quality observed for responses to Poisson input with piecewise constant rates as described in Sec. 2.5.1. For each model, we simulate responses under 15 input conditions (three noise regimes (μ,σ) and five different synaptic weights w), yielding 15 firing-rate estimates $r_{\mathrm{spike}}(t)$. We then test each firing-rate estimate against the 20

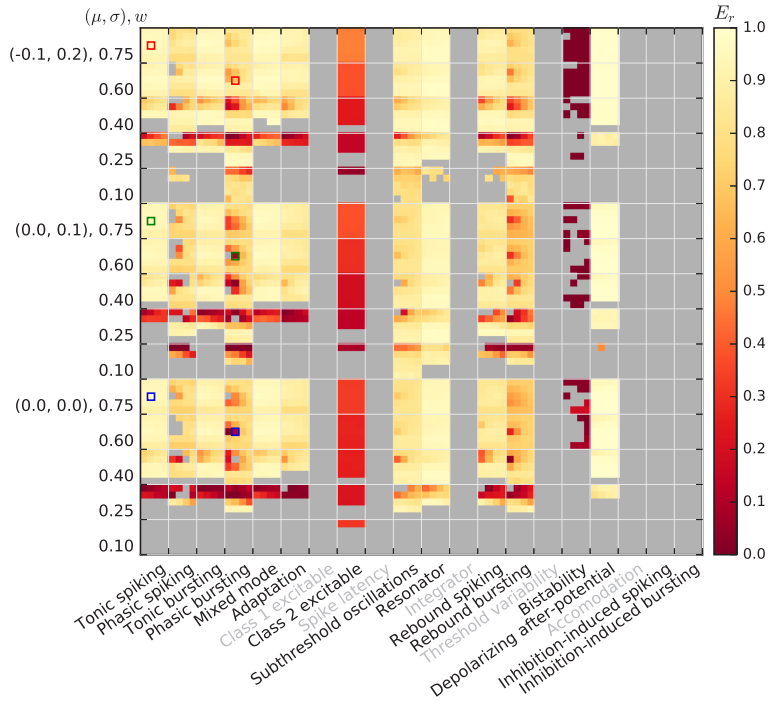

Fig. 10 Fit quality E_r for Izhikevich model class responses to a Poisson process with firing rate changing in steps, cf. Tab. 5, where $E_r = 1$ indicates a perfect fit. Each major column corresponds to one model, each major row to one of 15 input conditions; thus, each major cell corresponds to one firing-rate estimate $r_{\text{spike}}(t)$. Each entry inside a major cell represents the fit against one of 20 filter models obtained for the same μ, σ, w and different combinations of a_0, a_1 as in Fig. 7. Missing results (grey) are either due to models excluded (grey labels) or insufficient responses.

linear-nonlinear rate models obtained for the same μ, σ, w and all a_0, a_1 combinations, yielding 20 fit quality values E_r.

For the Izhikevich class, the Inhibition-induced spiking and bursting models, as well as most models with the lowest weight, $w = 0.1$, produced too few spikes to confidently estimate firing rates from the spiking model. We also observe very poor responses for the Bistability model. Class 2 excitable stands out with poor scores, $E_r < 0.5$, while the remaining models provide reasonable fits, $E_r > 0.7$ at least for most cases with sufficiently strong weights ($w \geq 0.4$).

The AMAT model class performs significantly better: Results are available for almost all stimulus conditions except for $w = 100\,\text{pA}$ in the absence of noise and all models except the Depolarizing after-potential model yield excellent fits ($E_r > 0.9$) for almost all conditions.

Figures 12 and 13 show the fit quality E_r for responses to real spike trains from cat retinal ganglion cells as described in Sec. 2.5.2. We again stimulate under 15 different conditions and obtain the fit quality for each of 20 different linear-nonlinear model fits.

For Izhikevich-class models we find noticeably worse fit quality, mostly $E_r < 0.7$, with the worst results mostly for the same conditions that also yielded low fit quality in response to Poisson input with piecewise constant rate. The main differences are that the Depolarizing after-potential model, which fitted stepped Poissonian input very well does not perform better than other models for the real spike trains, and that we obtain quality of fit values, albeit very poor ones, for the Inihibition-induced bursting model.

AMAT class responses to real spike trains show all over better fit quality than the Izhikevich class, but also for the AMAT class fit quality is lower in response to real spike trains than to stepped Poisson input. The distribution of good and bad fits is similar to the one observed for stepped Poisson input, with the worst performance for the Depolarizing after-potential model. Furthermore, more models require $w \geq 300\,\text{pA}$ to yield a fit quality result for real spike trains.

We summarize these observations in Fig. 14, which shows the cumulative distribution $P(E_r)$ of all individual results from Figs. 10–13 (thin lines). This clearly shows that our linear-nonlinear rate models are much more faithful for the AMAT class than for the Izhikevich class, and that within each class, responses to stepped Poisson input are rendered more faithfully than to real spike trains.

These observations pertain to all (up to 20) linear-nonlinear models obtained for each input configuration μ, σ, w. In prac-

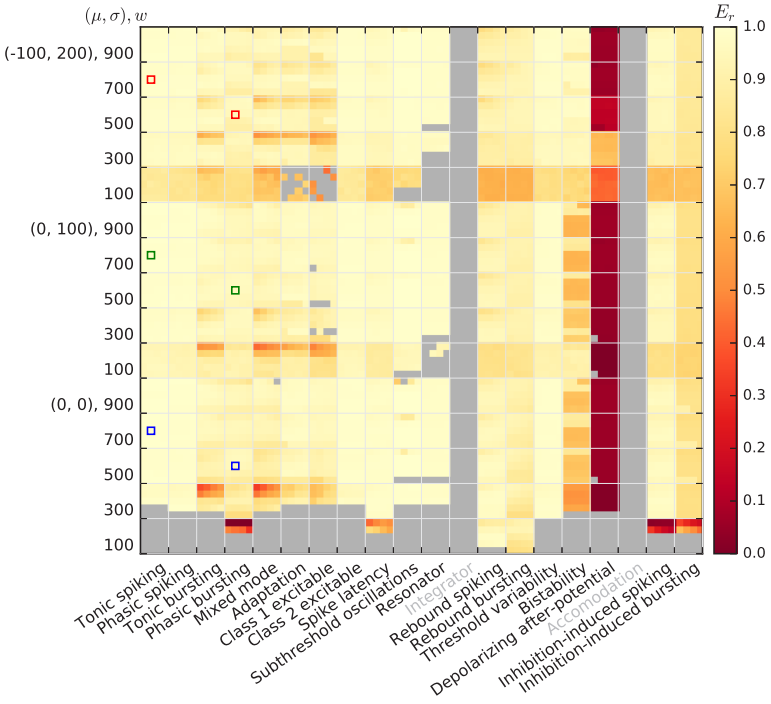

Fig. 11 Fit quality E_r for AMAT model class responses to a Poisson process with firing rate changing in steps; all else as in Fig. 10.

	Izhikevich	AMAT
Stepped Poisson trains	56%	84%
Real spike trains	26%	59%

Table 9 Proportion of linear-nonlinear rate models achieving $E_r^{\text{opt}} \geq 0.8$ across all model variants, noise regimes and synaptic weights.

tice, we would only be interested in the optimal linear-nonlinear model for each input configuration, i.e., for given μ, σ, w we would choose the model with

$$E_r^{\text{opt}} = \max_{a_0, a_1} E_r \,, \tag{34}$$

the highest E_r across all a_0, a_1 combinations. The cumulative distribution of fit quality for these optimal models is shown as thick lines in Fig. 14 and provides noticeably better fit quality for stepped Poisson and real train responses for both model classes. Table 9 shows the proportion of cases for which we reach high fit quality ($E_r^{\text{opt}} \geq 0.8$) for the optimal models. We find that the linear-nonlinear rate models perform well for the majority of conditions for the AMAT model class, but mostly poorly for the Izhikevich model class.

3.5 Model generalizations

As we have shown above, our linear-nonlinear rate models can capture the responses of spiking neuron models to real spike trains quite accurately, especially for the AMAT model class. Unfortunately, to find the optimal linear-nonlinear model for each input configuration μ, σ, w, we had to test a set of 20 different linear-nonlinear models to then pick the best one. This is impractical. We will now consider how to generalize our linear-nonlinear rate models, so that we can select an optimal model *a priori*.

We consider four different types of generalization:

per model (M) one linear-nonlinear model for each of the 15 Izhikevich class and 18 AMAT class models;

per model and noise (MN) one linear-nonlinear model for each Izhikevich/AMAT model and each noise regime;

per model, noise, and weight (MNW) one linear-nonlinear model for each Izhikevich/AMAT model, each noise regime, and each synaptic weight selected a priori;

MNW selected by stepped response (MNWS) one linear-nonlinear model for each Izhikevich/AMAT model, each noise

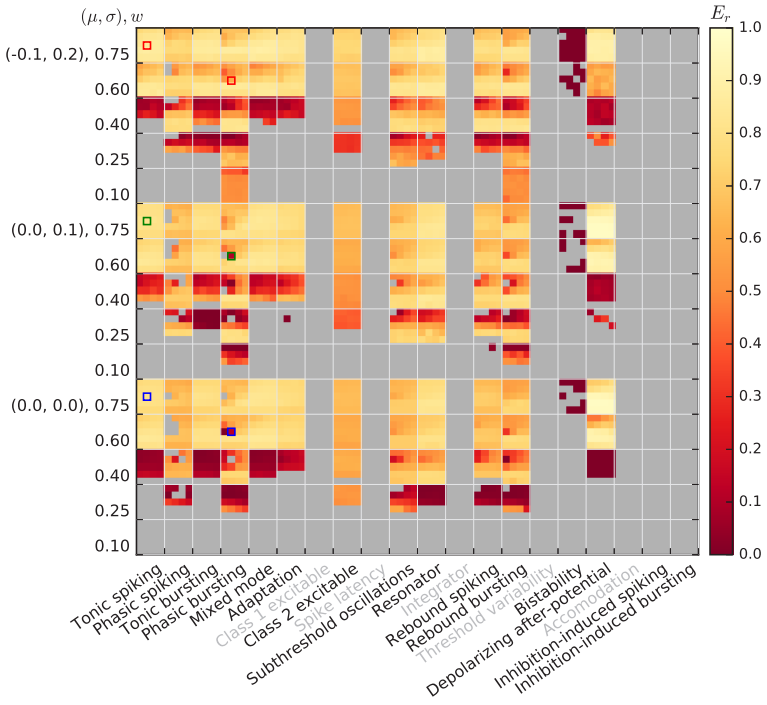

Fig. 12 Fit quality E_r for Izhikevich model class responses to the real spike trains from Fig. 3; all else is as in Fig. 10.

regime, and each synaptic weight selected based on the stepped Poisson test.

For the M and MN generalizations, we exploit that the activation functions $g(a)$ for many models and conditions scale roughly linear in the synaptic weight. We thus pool the scaled activation function data $g(a)/w$ for a given model across all input conditions (M) or just all synaptic weights for given noise (MN) and fit a single spline $\bar{g}(a)$ to the pooled data. We then use $w\bar{g}(a)$ as activation function in the linear-nonlinear model. For MNW and MNWS we use the original splines fitted directly against measurements.

To generalize the linear kernels, we take the median value for each of the kernel fit parameters $f_{c,1}, f_{c,2}, \gamma_1, \gamma_2, d$ and use these median parameters as parameters of our generalized kernel; using the median instead of the mean avoids problems with outliers. For M generalization, we take the median across all μ, σ, w, a_0, a_1 combinations, for MN across all w, a_0, a_1 for given μ, σ and for MNW across all a_0, a_1 for given μ, σ, w.

For MNWS generalization, we proceed differently: For each combination of μ, σ, w we select the filter parameters $f_{c,1}, f_{c,2}, \gamma_1, \gamma_2, d$ which yielded the highest fit quality $E_r = E_r^{\text{opt}}$ in response to the stepped Poisson input, our test stimulus.

While these generalizations, especially of the M and MN type, may seem rather crude, they perform reasonably, as indicated by the examples shown in Fig. 15. In one case shown there, the Phasic Bursting variant of the Izhikevich model, the model generalizations actually perform better than the specific model fits: The model responses to a firing rate step and to real spikes trains show significant overshoots in low noise regimes (blue and green curves) for the input parameters chosen for illustration ($w = 0.75$, $a_0 = 200\text{s}^{-1}$, $a_1 = 100\text{s}^{-1}$). This is consistent with the overly large amplitudes of the fitted filters. The corresponding generalized model filters fit the experimental data better, avoid the overshoot and thus track the response of the spiking model better.

To systematically quantify the quality of our generalizations, we compute the fit quality in response to stepped Poisson and real spike train input for all input configurations μ, σ, w for each generalization variant. Then

$$\rho_X = E_r^X / E_r^{\text{opt}} \tag{35}$$

measures how close the model generalization X is to the optimal linear-nonlinear model, where $\rho_X = 1$ is best.

Results are shown in Figs. 16 and 17. The coarser the generalization, the more frequently do we observe low generalization quality ρ_X. Interestingly, differences between the vari-

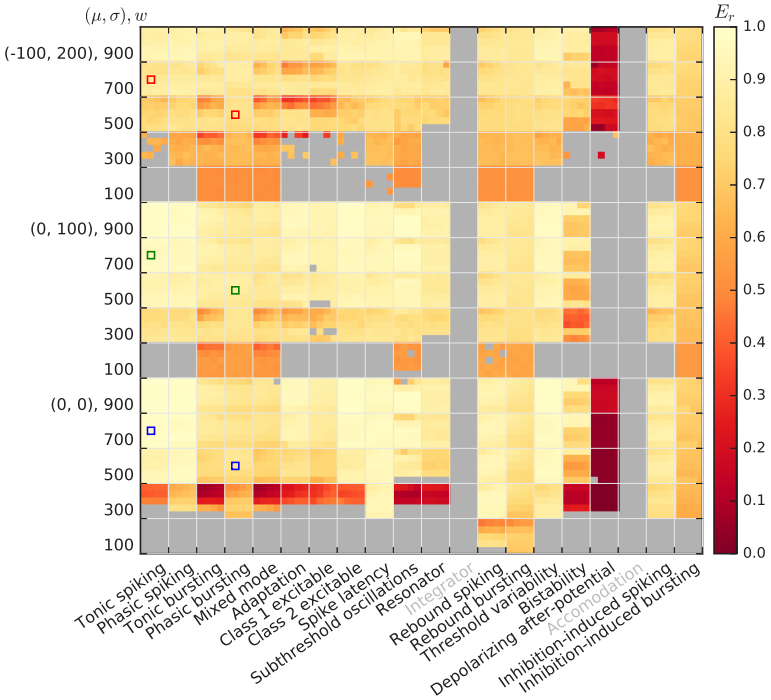

Fig. 13 Fit quality E_r for AMAT model class responses to the real spike trains from Fig. 3; all else as in Fig. 10.

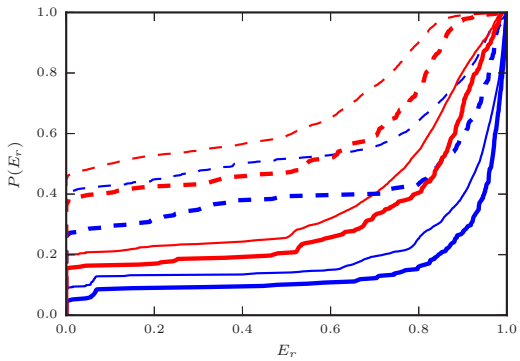

Fig. 14 Cumulative distribution $P(E_r)$ of the fit quality in response to stepped Poisson (blue) and real spike train (red) input for the Izhikevich (dashed) and AMAT classes (solid). Thin lines show the distribution of all individual results from Figs. 10–13, while thick lines show the distribution of optimal scores E_r^{opt} for each input configuration μ, σ, w. If all fits were perfect, $P(E_r)$ would hug the x axis until jumping to 1 for $E_r = 1$.

ous generalizations are larger for the AMAT class than for the Izhikevich class, and generalization seems to fail for the AMAT class mostly for biased noise and Inhibition-induced spiking. For the Izhikevich class, on the other hand, generalization mostly fails for low synaptic weights.

The most important observation, though, is that MNWS generaliztion works well, with $\rho_{\text{MNWS}} > 0.9$ in almost all cases for both model classes. This means that by selecting a filter model based on a fixed stepped Poisson protocol, we will obtain a linear-nonlinear rate model that is close to the optimal model for given noise regime and synaptic weight when applied to real neuronal dynamics.

Combined with the observation from Tab. 9 that the optimal model will provide a good approximation to actual neuronal firing rates in roughly two thirds of all conditions, we can thus use our fitting approach together with the stepped Poisson test to select a reasonably reliable linear-nonlinear neuron model.

4 Discussion

In this paper we numerically investigated the response properties of two neuron model classes, the Izhikevich model and the AMAT model, to noisy spiking input. Both neuron models can reproduce a wide range of experimentally observed

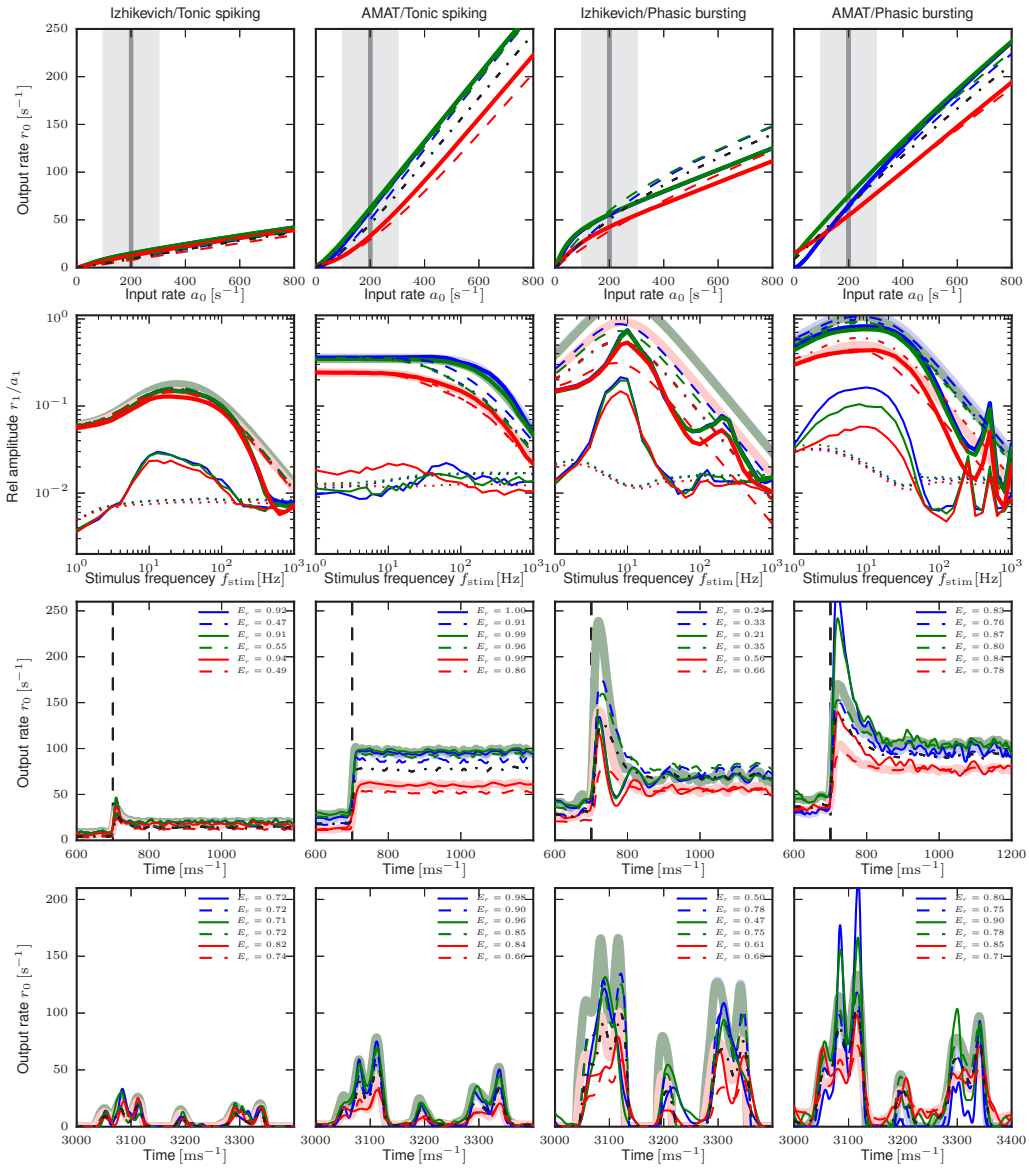

Fig. 15 Response properties for exemplary model neurons including responses of model generalizations. This figure is identical to Fig. 6, except that it also shows the response of model generalizations. Top row: activation function for no noise (blue), balanced noise (green) and biased noise (red). Solid lines show original spline fit (also used for MNW and MNWS generalizations), dashed lines responses from MN-generalization and the black dash-dotted line the response for the M-generalization. Second row: Frequency response to sinusoidally modulated Poisson input. Thick solid lines: first harmonic r_1, thin solid lines: second harmonic r_2, dotted lines: significance level r_{crit}, light thick lines: fitted filter function $\tilde{H}$, dashed lines: filter function for MN-generalizations, dash-dotted lines: filter function for M-generalization. Third row: Response of spiking model (thin solid lines) and rate-model prediction (light thick lines) to Poisson spike trains with rate step. Dashed lines show the response of the MN-generalization, the black dash-dotted line of the M-generalization. Bottom row: Response to real spike trains, 400 ms section starting at 3000 ms with the same line types as for step responses. Connection weight w from left to right: 0.75, 700, 0.75, 500.

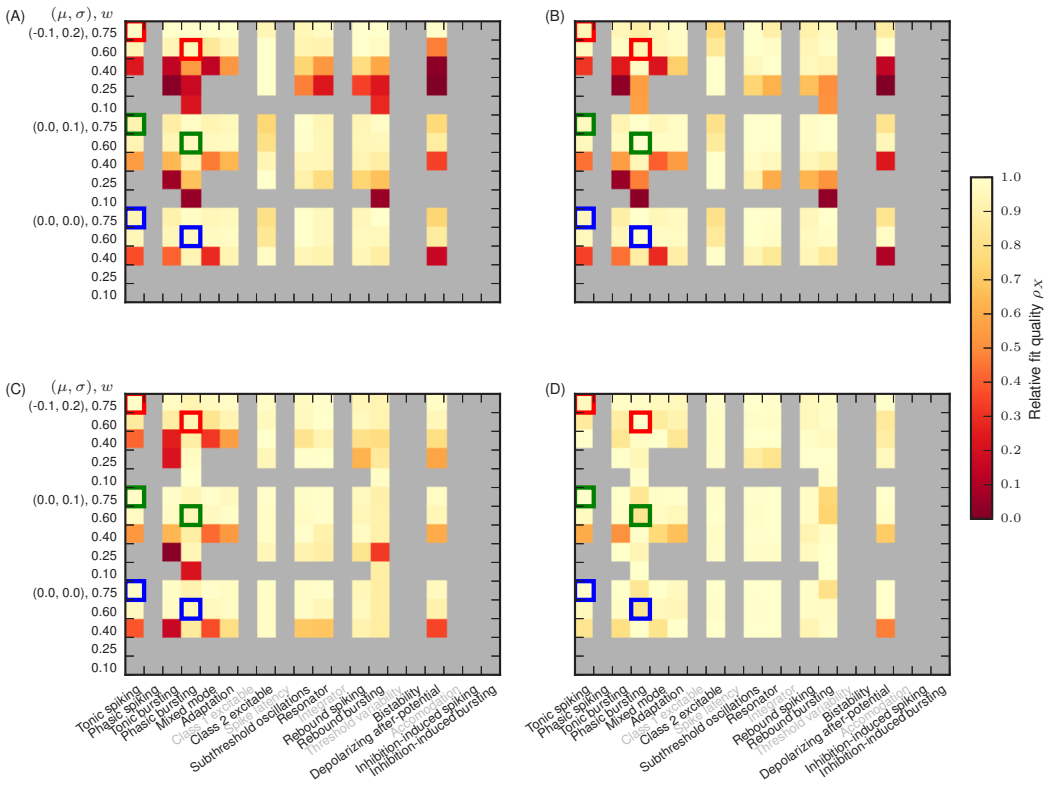

Fig. 16 Fit quality relative to optimum, ρ_X for Izhikevich class model generalizations: (A) M, (B) MN, (C) MNW, and (D) MNWS. For details, see text.

spike response patterns when stimulated with current injections. However, how these neurons behave with more natural synaptic inputs has so far not been studied systematically. We considered three different background noise regimes, one with no background noise at all, one balanced and one biased with enough background noise to put neurons in a spontaneously active state at low output rates. The first scenario can be considered to represent the situation in slice preparations, the other two correspond to neurons embedded in a network with ongoing excitatory and inhibitory activity. The stimulus spikes were modeled as stationary and sinusoidally modulated excitatory Poisson input spike trains, mimicking afferent inputs from sensory pathways with different synaptic connection strengths w.

We found that the response complexity observed under current injection collapses to only a few response types when the neurons are driven by stationary or sinusiodally modulated Poisson input. This is not entirely surprising, since some of the models are parametrically quite similar, and variations in response behavior to current stimulation depend on very specific current injection patterns that are not realizable in terms of Poisson spike inputs. Still, actual neurons receive inputs that often are well-described by Poissonian statistics and this can thus be considered the functionally more relevant input scenario. It is hence of interest to see which, possibly quite different, neuron models behave approximately equivalent.

The respective groupings for Izhikevich and AMAT are all-in-all very different. In particular, direct comparison of the individual corresponding neuron models reveals completely different response properties for most neuron models. This is in part explained by the differences in subthreshold dynamics which are linear for the AMAT model but nonlinear for the Izhikevich model. Individual spikes thus have quite different effects in the two models: Any input spike to an AMAT neuron will always evoke the same postsynaptic membrane-potential response and these responses simply superimpose due to the subthreshold linearity. For the

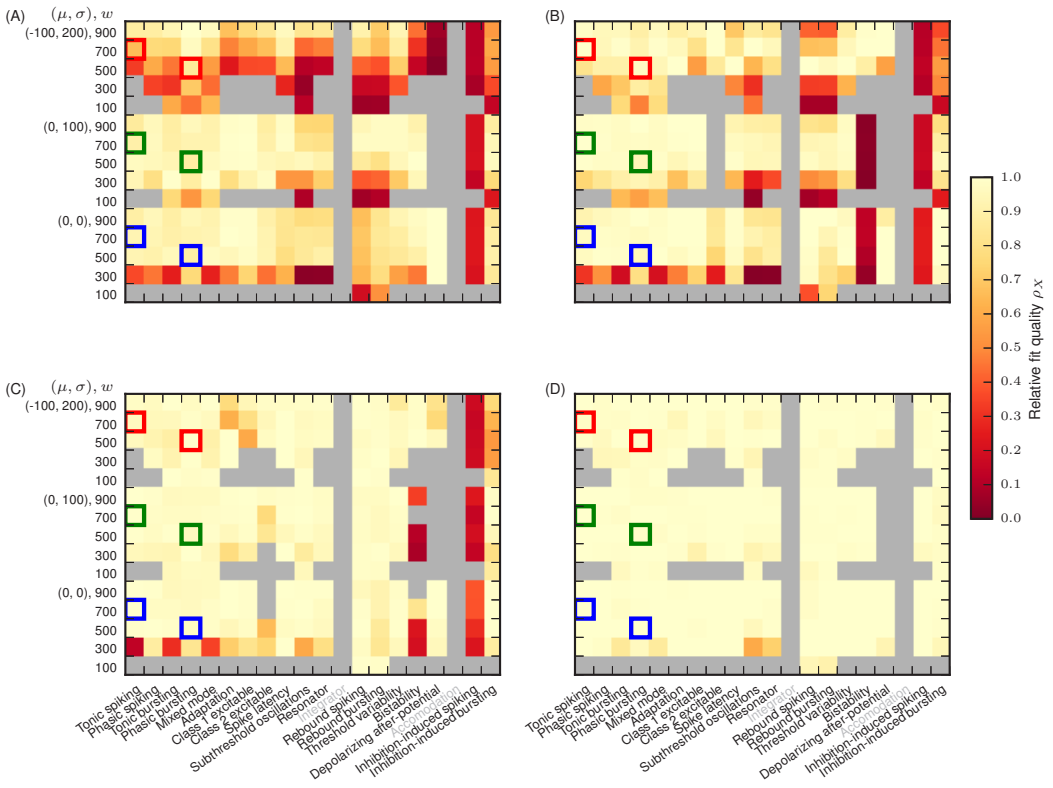

Fig. 17 Fit quality relative to optimum, ρ_X for AMAT class model generalizations: (A) M, (B) MN, (C) MNW, and (D) MNWS. For details, see text.

Izhikevich models, on the other hand, the postsynaptic response depends intricately on the value of the dynamic variables, such as the membrane potential, and the effect of several incoming excitatory spikes of same weight at one moment might be smaller than that of just one such spike at another moment. These differences hence make it hard, or even impossible, to set up synaptic weights w for the two neuron model classes that are directly comparable.

We therefore chose to gauge synaptic strengths in terms of the minimal weight w_θ needed to evoke a spike from rest, cf. Sec. 2.2, and to use weights spanning roughly from 10% to 75% of w_θ. This allowed us to quantify and compare input coupling strength within and between model classes. In general we observed that output rates for Izhikevich neurons were much lower than for AMAT neurons for the same input frequency and relative synaptic strength. It is therefore possible that model classes might become more similar if the Izhikevich neurons were driven at higher input rates or at other background noise levels, although we did not observe such a trend.

We observed here that neuron models can show very similar responses to spike input, even though they show very different responses to current injections, and in particular that models of different mathematical nature, showing *identical* current responses can respond very differently to spiking input. Given that neurons are mainly driven by spike input *in vivo*, this raises the intriguing question of how valuable a classification of neuronal response types based purely on current injection experiments is. It appears that a systematic classification based on a neuron's response to spiking input may be required.

In the second part of the paper, we made use of the measured stationary and frequency responses to fit linear-nonlinear firing-rate models to the data. It was previously shown that the firing-rate dynamics in response to complex spiking input can be well described by such models (Paninski et al, 2004;

Ostojic and Brunel, 2011; Weber and Pillow, 2017; Østergaard et al, 2018). In particular, Nordlie et al (2010) studied simple leaky integrate-and-fire (LIF) models with strong current-based synapses. They showed that a lowpass fit to the frequency response together with the nonlinear activation function yielded linear-nonlinear rate models that predicted responses to arbitrary inputs with high accuracy. Heiberg et al (2013) adapted this approach and studied two LIF-like models, one with current-based, the other with conductance-based synapses, that were fit to actual data recorded from cat and macaque LGN in response to retinal stimulation. They found a good performance of linear-nonlinear rate models as well.

Here, we presented results of the same basic approach for the Izhikevich and AMAT neuron model classes. Frequency responses were in most cases more complex than simple lowpass behavior and we employed fits to bandpass filters that better capture the non-monotonous passband structure observed in simulations. We then used novel test stimuli, i.e., step responses and more structured, highly-variable spike input sampled from actual recordings of retinal ganglion cells (Casti et al, 2008) to study rate-model performance. The main finding is that the AMAT neuron model class is approximated much better than the Izhikevich class by our linear-nonlinear rate models: for the former, good rate model responses ($E_r \geq 0.8$) were obtained in 64% of all cases tested, while the latter provided such good results in only 15% of cases tested. This difference might again be explained by the fact that the AMAT model class has subthreshold linear dynamics. However, the AMAT class is not completely linear either, because its firing threshold depends on the history of the membrane-potential dynamics. Therefore, neuronal transfer is not expected to be linear in any model class.

Some of the model variants gave consistently poor results, typically those that show very nonlinear behavior in response to direct current stimulation, e.g., the *Bistability*, *Inhibition-induced spiking* and *Inhibition-induced bursting* models for the Izhikevich class, and the *Depolarizing afterpotential* and *Inhibition induced spiking* models for the AMAT class.

To estimate the effects of linearity on rate-model performance, we measured the linearity of the stationary response function $r_0(a_0)$ in terms of L_1, cf. Eq. (12). If the stationary response function is linear, the activation function $g(\cdot)$ is also linear and only its slope is relevant, independent of the working point, cf. Section 2.4. We computed L_1 for all background noise regimes as a function of synaptic strength w and working point a_0, and find that the AMAT model generally is more linear than the Izhikevich model with respect to L_1. We further find that the linearity measure L_1 does not predict rate-model performance (data not shown). Thus, a nonlinear activation function does not imply poor rate-model performance, nor does linearity in terms of L_1 necessarily predict a good rate-model performance.

Furthermore, despite exploration of many potential performance predictors, we were unable to identify any single quantity or group of quantities that reliably predicted whether the response of a neuron model in a given input regime could be captured well by a linear-nonlinear rate model. We found, though, that a relative simple protocol, testing the rate model's performance in response to a Poisson spike train input with piecewise constant rate (stepped Poisson), allowed us to reliably identify rate models that render spiking neuron model responses to realistic spike input with reasonable accuracy.

Acknowledgements We are grateful to Alex Casti for permission to use data from his recordings. Partially funded by the Research Council of Norway (Grant 178892/V30 eNeuro) and EU Grants 269921 (BrainScaleS), 604102 (Human Brain Project RUP), and 720270 (Human Brain Project SGA1), and the Helmholtz Association portfolio theme SMHB and the Jülich Aachen Research Alliance (JARA). Simulations were performed using NOTUR resources.

Appendix

The AMAT model as specified by Equations 1–3, 16, 17, and A1–A7 of Yamauchi et al (2011) models input as instantaneous jumps in the membrane potential (δ-synapses) or as α-function post-synaptic currents (PSCs). We adapt the model to synapses injecting exponentially decaying PSCs and add a piecewise-constant input current. We further re-parameterize the model from membrane resistance R and time constant τ_m to membrance capacitance C and time constant τ_m by setting $R = \tau_m/C$; this brings the model equations in line with conventions for the NEST Simulator (Gewaltig and Diesmann, 2007; Morrison et al, 2007). The resulting set of differential equations are then integrated using the exact integration technique (Rotter and Diesmann, 1999; Plesser and Diesmann, 2009).

The AMAT model with two adaptive thresholds (AMAT2 model), two exponential-current synapses and piecewise-constant input current is defined by the following equations

$$\dot{V} = -\frac{V}{\tau_m} + \frac{I}{C} \tag{36}$$

$$\dot{\theta}_1 = -\frac{\theta_1}{\tau_1} + \alpha_1 \sum_k \delta(t - \hat{t}_k) \tag{37}$$

$$\dot{\theta}_2 = -\frac{\theta_2}{\tau_2} + \alpha_2 \sum_k \delta(t - \hat{t}_k) \tag{38}$$

$$\ddot{\theta}_V + \frac{2\dot{\theta}_V}{\tau_V} + \frac{\theta_V}{\tau_V^2} = \beta \dot{V} = -\frac{\beta V}{\tau_m} + \frac{\beta I}{C} \,. \tag{39}$$

Here, $\hat{t}_k$ are the times of the spikes fired by the neuron itself. A spike is fired whenever

$$V(t) \geq \theta(t) = \omega + \theta_1 + \theta_2 + \theta_V \,, \tag{40}$$

provided the neuron is not refractory. To be precise, let $\hat{t}_k$ be the time of the most recent spike and τ_{ref} the duration of the absolute refractory period. Then the time of the next spike is given by

$$\hat{t}_{k+1} = \min\{t > \hat{t}_k + \tau_{\text{ref}} | V(t) \geq \theta(t)\} \,. \tag{41}$$

Note that the membrane potential is *not* reset upon a spike.

To obtain first-order differential equations for θ_V (Rotter and Diesmann, 1999), we define

$$\eta = \dot{\theta}_V + \frac{\theta_V}{\tau_v} \tag{42}$$

and arrive at the equations

$$\dot{\eta} = -\frac{\beta V}{\tau_m} + \frac{\beta I}{C} \tag{43}$$

$$\dot{\theta}_V = \eta - \frac{\theta_V}{\tau_V} \tag{44}$$

as can be verified by inserting the first differential equation into the time derivative of the second and comparing with Eq. (39).

We treat spike input as follows: We assume that the PSC evoked by input through any synapse on the neuron will decay either with time constant τ_E or τ_I. Let $\{(\hat{t}_{X,j}, w_{X,j})\}$ be the set of all spike arrival times and weights of spikes arriving through synapses with time constant τ_X where $X \in \{E,I\}$. If we further assume that all PSCs are independent of each other, we can express the total input as

$$I(t) = I_E(t) + I_I(t) + I_{\text{ext}}(t) \tag{45}$$

where

$$I_X(t) = \sum_j w_{X,j} e^{-\frac{t-\hat{t}_{X,j}}{\tau_X}} \Theta(t-\hat{t}_{X,j}) \tag{46}$$

and $I_{\text{ext}}(t)$ is a piecewise-constant external current and $\Theta(t)$ the Heaviside step function. We will commonly refer to I_E as excitatory and I_I as inhibitory input. For efficient integration of the synaptic currents (Plesser and Diesmann, 2009), we describe them by differential equations

$$\dot{I}_X + \tau_X I_X = \sum_j w_{X,j} \delta(t-\hat{t}_{X,j}) \,. \tag{47}$$

We can summarize the resulting system of eight first-order linear differential equations as

$$\dot{\mathbf{y}} = \mathbf{A}\mathbf{y} + \mathbf{x} \tag{48}$$

with state and input vectors

$$\mathbf{y} = \begin{pmatrix} I_{\text{ext}} \\ I_E \\ I_I \\ V \\ \theta_1 \\ \theta_2 \\ \dot{\theta}_V + \frac{\theta_V}{\tau_V} \\ \theta_V \end{pmatrix} \qquad \mathbf{x} = \begin{pmatrix} \Delta I_{\text{ext}}(t) \\ \sum_j w_j^E \delta(t-\hat{t}_j^E) \\ \sum_j w_j^I \delta(t-\hat{t}_j^I) \\ 0 \\ \alpha_1 \sum_k \delta(t-\hat{t}_k) \\ \alpha_2 \sum_k \delta(t-\hat{t}_k) \\ 0 \\ 0 \end{pmatrix} \tag{49}$$

and system matrix

$$\mathbf{A} = \begin{pmatrix} 0 & 0 & 0 & 0 & 0 & 0 & 0 & 0 \\ 0 & -\frac{1}{\tau_E} & 0 & 0 & 0 & 0 & 0 & 0 \\ 0 & 0 & -\frac{1}{\tau_I} & 0 & 0 & 0 & 0 & 0 \\ 0 & \frac{1}{C} & \frac{1}{C} & -\frac{1}{\tau_m} & 0 & 0 & 0 & 0 \\ 0 & 0 & 0 & 0 & -\frac{1}{\tau_1} & 0 & 0 & 0 \\ 0 & 0 & 0 & 0 & 0 & -\frac{1}{\tau_2} & 0 & 0 \\ 0 & \frac{\beta}{C} & \frac{\beta}{C} & -\frac{\beta}{\tau_m} & 0 & 0 & -\frac{1}{\tau_V} & 0 \\ 0 & 0 & 0 & 0 & 0 & 0 & 1 & -\frac{1}{\tau_V} \end{pmatrix} . \tag{50}$$

$\Delta I_{\text{ext}}(t)$ represents the jumps in the piecewise constant external input current.

We can solve this system exactly (to the limits of machine precision) on a fixed time grid $t_j = jh$ for $h > 0$ using exact integration (Rotter and Diesmann, 1999), provided that $I_{\text{ext}}(t)$ only changes at grid points t_j, i.e., $\Delta I_{\text{ext}}(t) = \sum_j \delta I_j \delta(t-t_j)$. Starting from the initial state $\mathbf{y_0} = \mathbf{y}(\mathbf{t}=\mathbf{0})$, exact integration updates the state according to

$$\mathbf{y_{j+1}} = \mathbf{A}\mathbf{y_j} + \mathbf{x_{j+1}} \tag{51}$$

where $\mathbf{A}$ is the propagator matrix

$$\mathbf{P} = e^{\mathbf{A}h} = \sum_{j=0}^{\infty} \frac{(\mathbf{A}h)^j}{j!} \,. \tag{52}$$

The $\delta(t_j - \hat{t}_k)$-functions in the input vector $x(t)$ are replaced by Kronecker symbol $\delta_{j,k}$ upon discretization, restricting spike times to the time grid; see Morrison et al (2007) for an extension to off-grid spikes.

The propagator matrix $\mathbf{P}$ can be obtained numerically, e.g., using the `expm` functions provided by SciPy or Matlab, using an algorithm due to Higham (2005). These methods can, though, fail under certain circumstances (Moler, 2012; Al-Mohy and Higham, 2009) and we have not performed any systematic tests regarding their reliability with respect to model neuron dynamics. We used the Mathematica symbolic algebra system (Wolfram, 1999) to obtain an explicit expression for the propagator matrix $\mathbf{P}$ and generate C++-code for the matrix elements. Note that the expression obtained in this way requires that all time constants except τ_1 and τ_2 differ, i.e., $\tau_m \neq \tau_V \neq \tau_E \neq \tau_I$. Other expressions for $\mathbf{P}$ pertain if any two time constants are equal. The resulting model is implemented in NEST as `amat2_psc_exp`.

While our implementation of the AMAT2 model is based on the equations given by Yamauchi et al (2011), we found that we needed to modify some model parameters to reproduce the responses in Figs. 6 and 7 of that paper:

- all models: membrane time constant $\tau_m = 10$ ms instead of $\tau_m = 5$ ms
- *subthreshold oscillations*: $\alpha_1 = 1$, $\beta = 0.2$ instead of $\alpha_1 = 10$, $\beta = 0.1$
- *resonator*: $\beta = 0.5$ instead of $\beta = 0.1$
- *threshold variability*: $\beta = -0.5$ instead of $\beta = -0.1$

Parameters used in our model are given in Table 4.

We further needed to make some adjustments to stimulus parameters to reproduce Figs. 6 and 7 in Yamauchi et al (2011):

- *tonic spiking*: $I_c = 0.118$ nA instead of $I_c = 0.15$ nA
- *phasic spiking*: $I_c = 0.1$ nA instead of $I_c = 0.08$ nA
- *phasic bursting*: $I_c = 0.1$ nA instead of $I_c = 0.08$ nA
- *class 1 excitable*: $dI/dt = 150$ pA/s instead of $dI/dt = 2.5$ pA/s
- *class 2 excitable*: $dI/dt = 150$ pA/s instead of $dI/dt = 2.5$ pA/s
- *latency*: $I_p = 1$ nA instead of $I_c = 0.58$ nA
- *subthreshold oscillations*: $I_p = 0.8$ nA instead of $I_p = 0.2$ nA
- *resonator*: $I_p = 0.6$ nA instead of $I_p = 0.36$ nA
- *integrator*: $I_p = 0.45$ nA instead of $I_p = 0.28$ nA
- *rebound spiking*: $I_p = -1.5$ nA instead of $I_p = -0.6$ nA
- *rebound bursting*: $I_p = -1.5$ nA instead of $I_p = -0.6$ nA
- *threshold variability*: $I_p = \pm 0.35$ nA instead of $I_p = \pm 0.2$ nA
- *bistability*: $ISI = 222$ ms instead of $ISI = 22$ ms
- *depolarizing after-potential*: $I_p = 0.5$ nA instead of $I_p = 0.2$ nA
- *accomodation*: $dI/dt = 0.54$ nA/s, 2.43 nA/s, $\Delta_{\text{ramp}} = 180$ ms, 40 ms instead of $dI/dt = 1$ nA/s, 4.5 nA/s, $\Delta_{\text{ramp}} = 90$ ms, 20 ms
- *inhibition-induced spiking*: $I_p = -0.4$ nA instead of $I_p = -0.3$ nA
- *inhibition-induced bursting*: $I_p = -0.3$ nA instead of $I_p = -0.16$ nA

The changes in stimulation currents are only relevant for the illustrative Fig. 1 and do not directly affect the remainder of the results presented here.

We can only speculate about why these parameters changes were necessary. We inferred the time axis of Figs. 6 and 7 of Yamauchi et al (2011) from the scale bars given in panel A of each figure. This clearly indicates that pulse/ramp durations given in Table 1 of that paper are inconsistent with the figures for, e.g., *bistability* (Fig. 6F) and *accomodation* (Fig. 7I). Concerning the membrane time constant τ_m, the authors tested various values of this parameter (Yamauchi et al, 2011, p. 2, right column) and this may have led to a mix-up.

References

Al-Mohy AH, Higham NJ (2009) A new scaling and squaring algorithm for the matrix exponential. SIAM J Matrix Anal Appl 31:970–989, DOI 10.1137/09074721X

Avermann M, Tomm C, Mateo C, Gerstner W, Petersen CCH (2012) Microcircuits of excitatory and inhibitory neurons in layer 2/3 of mouse barrel cortex. J Neurophysiol 107(11):3116–3134, DOI 10.1152/jn.00917.2011

Blomquist P, Devor A, Indahl UG, Ulbert I, Einevoll GT, Dale AM (2009) Estimation of thalamocortical and intracortical network models from joint thalamic single-electrode and cortical laminar-electrode recordings in the rat barrel system. PLoS Computational Biology 5(3):e1000328, DOI 10.1371/journal.pcbi.1000328

Brette R, Gerstner W (2005) Adaptive exponential integrate-and-fire model as an effective description of neuronal activity. J Neurophysiol 94(5):3637–3642, DOI 10.1152/jn.00686.2005

Brunel N (2000) Dynamics of sparsely connected networks of excitatory and inhibitory spiking neurons. J Comput Neurosci 8(3):183–208

Brunel N, Chance FS, Fourcaud N, Abbott LF (2001) Effects of synaptic noise and filtering on the frequency response of spiking neurons. Phys Rev Lett 86(10):2186–2189

Burkitt AN (2006a) A review of the intergrate-and-fire neuron model: I. Homogeneous synaptic input. Biol Cybern 95:1–19

Burkitt AN (2006b) A review of the intergrate-and-fire neuron model: II. Inhomogeneous synaptic input and network properties. Biol Cybern 95:97–112

Casti A, Hayot F, Xiao Y, Kaplan E (2008) A simple model of retina-LGN transmission. J Comput Neurosci 24(2):235–252, DOI 10.1007/s10827-007-0053-7

Chance FS, Abbott LF, Reyes AD (2002) Gain modulation from background synaptic input. Neuron 35:773–782

Coombes S (2005) Waves, bumps, and patterns in neural field theories. Biological Cybernetics 93:91–108

Ermentrout B (1998) Neural networks as spatio-temporal pattern-forming systems. Reports on Progress in Physis 61:353–430

FitzHugh R (1961) Impulses and physiological states in theoretical models of nerve membrane. Biophys J 1:445–466

Funke K, Wörgötter F (1997) On the significance of temporally structured activity in the dorsal lateral geniculate nucleus (LGN). Prog Neurobiol 53:67–119

Gerstein GL, Mandelbrot B (1964) Random walk models for the spike activity of a single neuron. Biophys J 4:41–68

Gewaltig MO, Diesmann M (2007) NEST (NEural Simulation Tool). Scholarpedia 2(4):1430

Haider B, Häusser M, Carandini M (2013) Inhibition dominates sensory responses in the awake cortex. Nature 493:97–100

Heiberg T, Kriener B, Tetzlaff T, Casti A, Einevoll GT, Plesser HE (2013) Firing-rate models capture essential response dynamics of LGN relay cells. J Comput Neurosci 35:359–375, DOI 10.1007/s10827-013-0456-6

Helias M, Kunkel S, Masumoto G, Igarashi J, Eppler JM, Ishii S, Fukai T, Morrison A, Diesmann M (2012) Supercomputers ready for use as discovery machines for neuroscience. Front Neuroinform 6:26, DOI 10.3389/fninf.2012.00026

Higham NJ (2005) The scaling and squaring method for the matrix exponential revisited. SIAM J Matrix Anal Appl 26:1179–1193

Hodgkin AL, Huxley AF (1952) A quantitative description of membrane current and its application to conduction and excitation in nerve. J Physiol 117:500–544

Ikegaya Y, Sasaki T, Ishikawa D, Honma N, Tao K, Takahashi N, Minamisawa G, Ujita S, Matsuki N (2013) Interpyramid spike transmission stabilizes the sparseness of recurrent network activity. Cereb Cortex 23(2):293–304, DOI 10.1093/cercor/bhs006

Izhikevich EM (2003a) Figure 1.m MATLAB script. URL http://www.izhikevich.org/publications/figure1.m, last accessed 2017-08-18

Izhikevich EM (2003b) Simple model of spiking neurons. IEEE Trans Neural Netw 14(6):1569–1572, DOI 10.1109/TNN.2003.820440

Izhikevich EM (2004) Which model to use for cortical spiking neurons? IEEE Trans Neural Netw 15(5):1063–1070, DOI 10.1109/TNN.2004.832719

Izhikevich EM (2010) Hybrid spiking models. Philos Transact A Math Phys Eng Sci 368(1930):5061–5070, DOI 10.1098/rsta.2010.0130

Jansen BH, Rit VG (1995) Electroencephalogram and visual evoked potential generation in a mathematical model of coupled cortical columns. Biol Cybern 73(4):357–366

Johannesma PIM (1968) Diffusion models of the stochastic activity of neurons. In: Caianiello ER (ed) Neural Networks, Springer, Berlin, pp 116–144

Jolivet R, Rauch A, Lüscher HR, Gerstner W (2006) Predicting spike timing of neocortical pyramidal neurons by simple threshold models. J Comput Neurosci 21(1):35–49, DOI 10.1007/s10827-006-7074-5

Jolivet R, Schürmann F, Berger TK, Naud R, Gerstner W, Roth A (2008) The quantitative single-neuron modeling competition. Biol Cybern 99(4-5):417–426, DOI 10.1007/s00422-008-0261-x

Jones E, Oliphant T, Peterson P, et al (2001) SciPy: Open source scientific tools for Python. URL http://www.scipy.org/, [Online; accessed 2015-03-09]

Kobayashi R, Tsubo Y, Shinomoto S (2009) Made-to-order spiking neuron model equipped with a multi-timescale adaptive threshold. Front Comput Neurosci 3:9, DOI 10.3389/neuro.10.009.2009

Kunkel S, Schmidt M, Eppler JM, Plesser HE, Masumoto G, Igarashi J, Ishii S, Fukai T, Morrison A, Diesmann M, Helias M (2014) Spik-

ing network simulation code for petascale computers. Frontiers in Neuroinformatics 8(78), DOI 10.3389/fninf.2014.00078

Lapicque L (1907) Considérations préalables sur la nature du phénomene par lequel l'électricité excite les nerfs. J Physiol Pathol Gen 9:565–578

Lefort S, Tomm C, Sarria JCF, Petersen CCH (2009) The excitatory neuronal network of the C2 barrel column in mouse primary somatosensory cortex. Neuron 61(2):301–316, DOI 10.1016/j.neuron.2008.12.020

Mainen ZF, Sejnowski TJ (1996) Influence of dendritic structure on firing pattern in model neocortical neurons. Nature 382:363–366

Markram H, Toledo-Rodriguez M, Wang Y, Gupta A, Silberberg G, Wu C (2004) Interneurons of the neocortical inhibitory system. Nature reviews Neuroscience 5:793–807, DOI 10.1038/nrn1519

Moler C (2012) A balancing act for the matrix exponential. URL http://blogs.mathworks.com/cleve/2012/07/23/a-balancing-act-for-the-matrix-exponential/

Morris C, Lecar H (1981) Voltage oscillations in the barnacle giant muscle fiber. Biophys J 35(1):193–213, DOI 10.1016/S0006-3495(81)84782-0

Morrison A, Straube S, Plesser HE, Diesmann M (2007) Exact subthreshold integration with continuous spike times in discrete time neural network simulations. Neural Comput 19:47–79

Muller E, Davison AP, Brizzi T, Bruederle D, Eppler JM, Kremkow J, Pecevski D, Perrinet L, Schmuker M, Yger P (2009) NeuralEnsemble.Org: Unifying neural simulators in Python to ease the model complexity bottleneck. In: Frontiers in Neuroscience Conference Abstract: Neuroinformatics 2009, DOI 10.3389/conf.neuro.11.2009.08.104

Nordbø Ø, Wyller J, Einevoll GT (2007) Neural network firing-rate models on integral form: effects of temporal coupling kernels on equilibrium-state stability. Biol Cybern 97(3):195–209, DOI 10.1007/s00422-007-0167-z

Nordlie E, Tetzlaff T, Einevoll GT (2010) Rate dynamics of leaky integrate-and-fire neurons with strong synapses. Front Comput Neurosci 4:149, DOI 10.3389/fncom.2010.00149

Østergaard J, Kramer MA, Eden UT (2018) Capturing spike variability in noisy izhikevich neurons using point process generalized linear models. Neural Computation 30(1):125–148, DOI 10.1162/neco_a_01030

Ostojic S, Brunel N (2011) From spiking neuron models to linear-nonlinear models. PLoS Comput Biol 7(1):e1001056, DOI 10.1371/journal.pcbi.1001056

Paninski L, Pillow JW, Simoncelli EP (2004) Maximum likelihood estimation of a stochastic integrate-and-fire neural encoding model. Neural Comput 16:2533–2561

Pedregosa F, Varoquaux G, Gramfort A, Michel V, Thirion B, Grisel O, Blondel M, Prettenhofer P, Weiss R, Dubourg V, Vanderplas J, Passos A, Cournapeau D, Brucher M, Perrot M, Duchesnay E (2011) Scikit-learn: Machine learning in Python. Journal of Machine Learning Research 12:2825–2830

Petersen C, Crochet S (2013) Synaptic computation and sensory processing in neocortical layer 2/3. Neuron 78:28–48

Pillow JW, Paninski L, Uzzell VJ, Simoncelli EP, Chichilnisky EJ (2005) Prediction and decoding of retinal ganglion cell responses with a probabilistic spiking model. J Neurosci 25(47):11003–11013, DOI 10.1523/JNEUROSCI.3305-05.2005

Plesser HE, Diesmann M (2009) Simplicity and efficiency of integrate-and-fire neuron models. Neural Comput 21:353–359, DOI 10.1162/neco.2008.03-08-731

Plesser HE, Diesmann M, Gewaltig MO, Morrison A (2013) NEST: the Neural Simulation Tool. In: Jaeger D, Jung R (eds) Encyclopedia of Computational Neuroscience: SpringerReference, Springer-Verlag, Berlin Heidelberg, DOI 10.1007/SpringerReference_348323

Richardson MJE (2007) Firing-rate response of linear and nonlinear integrate-and-fire neurons to modulated current-based and conductance-based synaptic drive. Physical Review E 76(021919):1–15

Richardson MJE, Swarbrick R (2010) Firing-rate response of a neuron receiving excitatory and inhibitory synaptic shot noise. Phys Rev Lett 105(17):178102

Rotter S, Diesmann M (1999) Exact digital simulation of time-invariant linear systems with applications to neuronal modeling. Biol Cybern 81:381–402

Roxin A (2011) The role of degree distribution in shaping the dynamics in networks of sparsely connected spiking neurons. Frontiers Comput Neurosci 5(8), DOI 10.3389/fncom.2011.00008

Sakata S, Harris KD (2012) Laminar-dependent effects of cortical state on auditory cortical spontaneous activity. Frontiers in Neural Circuits 6(109):1–10

Shimazaki H, Shinomoto S (2010) Kernel bandwidth optimization in spike rate estimation. J Comput Neurosci 29(1-2):171–182, DOI 10.1007/s10827-009-0180-4

Song S, Sjöström P, Reigl M, Nelson S, Chklovskii D (2005) Highly nonrandom features of synaptic connectivity in local cortical circuits. PLoS Biology 3(3):e68

Stein RB (1965) A theoretical analysis of neuronal variability. Biophys J 5:173–194

Tuckwell HC (1988) Introduction to Theoretical Neurobiology, vol 1. Cambridge University Press, Cambridge, UK

Weber AI, Pillow JW (2017) Capturing the dynamical repertoire of single neurons with generalized linear models. Neural Computation 29(12):3260–3289, DOI 10.1162/neco_a_01021

Wilson HR, Cowan JD (1972) Excitatory and inhibitory interactions in localized populations of model neurons. Biophys J 12(1):1–24, DOI 10.1016/S0006-3495(72)86068-5

Wolfram S (1999) The Mathematica Book, 4th edn. Wolfram Media/Cambridge University Press, Cambridge

Yamauchi S, Kim H, Shinomoto S (2011) Elemental spiking neuron model for reproducing diverse firing patterns and predicting precise firing times. Front Comput Neurosci 5:42, DOI 10.3389/fncom.2011.00042

Paper III

Heiberg T, Hagen E, Halnes G, Einevoll GT (2016) Biophysical Network Modelling of the dLGN Circuit: Different Effects of Triadic and Axonal Inhibition on Visual Responses of Relay Cells. PLoS Comput Biol 12(5):e1004929, doi: 10.1371/journal.pcbi.1004929

PLOS | COMPUTATIONAL BIOLOGY

RESEARCH ARTICLE

Biophysical Network Modelling of the dLGN Circuit: Different Effects of Triadic and Axonal Inhibition on Visual Responses of Relay Cells

Thomas Heiberg[1], **Espen Hagen**[1,2], **Geir Halnes**[1], **Gaute T. Einevoll**[1,3]*

1 Department of Mathematical Sciences and Technology, Norwegian University of Life Sciences, Ås, Norway, **2** Institute of Neuroscience and Medicine (INM-6) and Institute for Advanced Simulation (IAS-6) and JARA BRAIN Institute I, Jülich Research Centre, Jülich, Germany, **3** Department of Physics, University of Oslo, Oslo, Norway

* gaute.einevoll@nmbu.no

OPEN ACCESS

Citation: Heiberg T, Hagen E, Halnes G, Einevoll GT (2016) Biophysical Network Modelling of the dLGN Circuit: Different Effects of Triadic and Axonal Inhibition on Visual Responses of Relay Cells. PLoS Comput Biol 12(5): e1004929. doi:10.1371/journal.pcbi.1004929

Editor: Arnd Roth, University College London, UNITED KINGDOM

Received: August 29, 2015

Accepted: April 20, 2016

Published: May 20, 2016

Data Availability Statement: All relevant data are within the paper and its Supporting Information files.

Funding: This work was funded by the Research Council of Norway (NFR) (ISP-Fysikk, project no. 216699; NOTUR), European Union Seventh Framework Programme (FP7/2007-2013) under grant agreement no. 604102 (HBP), and the Helmholtz Portfolio Supercomputing and Modeling for the Human Brain (SMHB). The funders had no role in study design, data collection and analysis, decision to publish, or preparation of the manuscript.

Abstract

Despite its prominent placement between the retina and primary visual cortex in the early visual pathway, the role of the dorsal lateral geniculate nucleus (dLGN) in molding and regulating the visual signals entering the brain is still poorly understood. A striking feature of the dLGN circuit is that relay cells (RCs) and interneurons (INs) form so-called triadic synapses, where an IN dendritic terminal can be simultaneously postsynaptic to a retinal ganglion cell (GC) input and presynaptic to an RC dendrite, allowing for so-called triadic inhibition. Taking advantage of a recently developed biophysically detailed multicompartmental model for an IN, we here investigate putative effects of these different inhibitory actions of INs, i.e., triadic inhibition and standard axonal inhibition, on the response properties of RCs. We compute and investigate so-called area-response curves, that is, trial-averaged visual spike responses vs. spot size, for circular flashing spots in a network of RCs and INs. The model parameters are grossly tuned to give results in qualitative accordance with previous in vivo data of responses to such stimuli for cat GCs and RCs. We particularly investigate how the model ingredients affect salient response properties such as the receptive-field center size of RCs and INs, maximal responses and center-surround antagonisms. For example, while triadic inhibition not involving firing of IN action potentials was found to provide only a non-linear gain control of the conversion of input spikes to output spikes by RCs, axonal inhibition was in contrast found to substantially affect the receptive-field center size: the larger the inhibition, the more the RC center size shrinks compared to the GC providing the feedforward excitation. Thus, a possible role of the different inhibitory actions from INs to RCs in the dLGN circuit is to provide separate mechanisms for overall gain control (direct triadic inhibition) and regulation of spatial resolution (axonal inhibition) of visual signals sent to cortex.

Competing Interests: The authors have declared that no competing interests exist.

Author Summary

While the basic receptive-field structure of cells in the dorsal lateral geniculate nucleus (dLGN), the station between retina and visual cortex in the early visual pathway, was mapped out half a century ago, the function of this nucleus in molding the visual signals is still poorly understood. One reason is that the dLGN contains enigmatic inhibitory interneurons which can act with different inhibitory action on the excitatory relay cells. In addition to standard axonal inhibition, relay cells and interneurons form so-called triadic synapses, where an interneuron dendritic terminal can be simultaneously postsynaptic to a retinal input and presynaptic to a relay-cell dendrite, opening up for so-called triadic inhibition. Taking advantage of a recently developed biophysically detailed multicompartmental model for an interneuron, we here use a network model to investigate putative effects of these inhibitory actions on the response properties of relay cells stimulated by circular flashing spots. Our results suggest a possible role of the different inhibitory actions in providing separate mechanisms for overall gain control (triadic inhibition) and regulation of spatial resolution (axonal inhibition) of visual signals sent to cortex.

Introduction

The dorsal lateral geniculate nucleus (dLGN) acts as a gateway for visual signals that reach cortex. The principal cells, the relay cells (RCs), constitute about 75–80% of the cells in the nucleus, while the remaining 20–25% are intrageniculate interneurons (INs) [1]. The RCs receive synaptic inputs from a variety of sources: direct *feedforward excitation* from retinal ganglion (GC) cells [2–8], indirect *feedforward inhibition* via the INs, which in turn are excited by GC cells [7, 9], *feedback inhibition* from the thalamic reticular nucleus (TRN) [1] and *feedback excitation* from primary visual cortex [10, 11]. Both the IN and TRN cells further receive excitatory feedback from cortex opening up for *feedback inhibition* of RCs involving the entire thalamocortical loop [1]. Despite its prominent position in the early visual pathway, and the relative abundance of anatomical and physiological data recorded from the nucleus, the functional role of the dLGN circuit is still poorly understood. Mathematical modeling of the properties of the network will clearly have to be a key component in elucidating its function.

A striking feature of the dLGN circuit is that INs and RCs are known to form so-called triadic synapses [12–16]. Such triadic synapses are typically formed at sites that are proximal on the RC dendrites and distal on the IN dendrites. At these sites, a single retinal terminal contacts postsynaptic terminals on both an IN dendrite and an RC dendrite. The IN terminal is, at the same time, postsynaptic to the GC input and presynaptic to the RC [14]. In the triads, GABA-release from the IN may be triggered directly by local GC input, providing a localized source of inhibition of RCs, which may be functionally decoupled from the IN soma [12, 13, 15, 16]. In addition to the complex triadic action, the INs also provide standard, axonal inhibition of RCs [14].

Until now, there has to our knowledge been no dLGN network study investigating the functional role of these triadic circuit elements. A key reason is that while several biophysically detailed neuron models for RCs have been developed [17–23], models of INs have been more scarce. However, recently our group developed the first comprehensive multicompartmental IN models including active dendritic conductances placed on anatomically reconstructed dendritic morphologies [24], opening up for investigations of the functional role of the different putative inhibitory action by INs on RCs in the dLGN network.

Various types of visual stimuli have been used to probe the response properties of the dLGN circuit: light or dark bars, gratings, and spots of various sizes [25]. Based on experiments with

flashing circular spots [26], Einevoll and Heggelund [27] developed a mechanistic firing-rate model to account for the changes in the spatial response properties of RC cells in cat compared to its GC input. In qualitative accordance with known anatomy and physiology for cat X cells, the RC neurons in the model received excitatory input from single GC neurons and indirect feedforward inhibition from INs, which in turn received input from of a handful of GC neurons. While this model successfully accounted for the observed area-summation curves in RC cells, i.e., the experimentally observed response vs. spot-diameter curves, it could not distinguish between the various possibilities of inhibitory action from INs to RCs, i.e., whether the inhibition was predominantly triadic or axonal.

To investigate the putatively different roles of triadic and axonal inhibitory action from INs in the dLGN circuit, we here develop and investigate a biophysically detailed, spiking neuron network model designed to be analogous to the firing-rate network model in [27]. A key component of the network is an adapted version of the recent multicompartment IN model [24] allowing for explicit studies of how the various modes of inhibition affect the shape of measured spot-response curves for dLGN cells [26].

In the next section we introduce the circuit model and describe the models of the GC input, the IN and the RC, as well as their synaptic connections. In Results we first investigate and describe the behavior of the IN model, then probe the functional behavior of the triadic circuit. Next, we illustrate how the various modes of inhibition affect the area-summation curves and finally explore differences between the transient (onset) and sustained (steady-state) responses to spot stimulation. Our findings are then discussed in the final Discussion.

Materials and Methods

dLGN circuit model

Input to the dLGN circuit was provided by a layer of five retinal ganglion neurons (GCs), spatially organized with one center cell and four peripheral cells equidistant from the center cell (Fig 1). Each GC axon was assumed to synapse at two different locations, i.e., (i) in a triadic synapse where the interneuron (IN) and one of the relay cells (RCs) both receive excitatory input, and (ii) in a 'conventional' synapse on the proximal IN dendrite. The IN formed two inhibitory synapses on each of the five RCs, (i) a dendrodendritic synapse (part of the triad) and (ii) an axodendritic synapse.

In the present application of the model we only computed the response of the central RC. In addition to the local triadic inhibitory action due to synaptic inputs from the central GC (called *direct triadic inhibition* below), this cell received extra 'back-propagating' triadic inhibition (called *soma-driven triadic inhibition* below) and axonal inhibition following firing of action potentials in the IN. Thus the RCs were decoupled in the sense that firing of action potentials in one RC did not affect the firing of the other RCs. Therefore, the only effect of the four peripheral (non-central) GCs came from their proximal inputs to the IN. For simplicity we here assumed that these four synaptic weights are the same, an approximation which is unlikely to bear out in real biological situations. However, the use of circular flashing spot stimuli concentric with the receptive field of the central RC, implies that the response of the central RC will largely be determined by the *sum* of these four weights, not their individual variation [27].

The spike trains of GCs were modeled descriptively as non-stationary Poisson processes. The visual input driving the GCs were circular light spots centered on the middle GC. The outputs were spike trains with mean rate and temporal profile fitted to experimental data.

The components that make up our circuit were modeled at different levels of detail. To allow for local processing in the dendrites and because the IN is known to be electrotonically

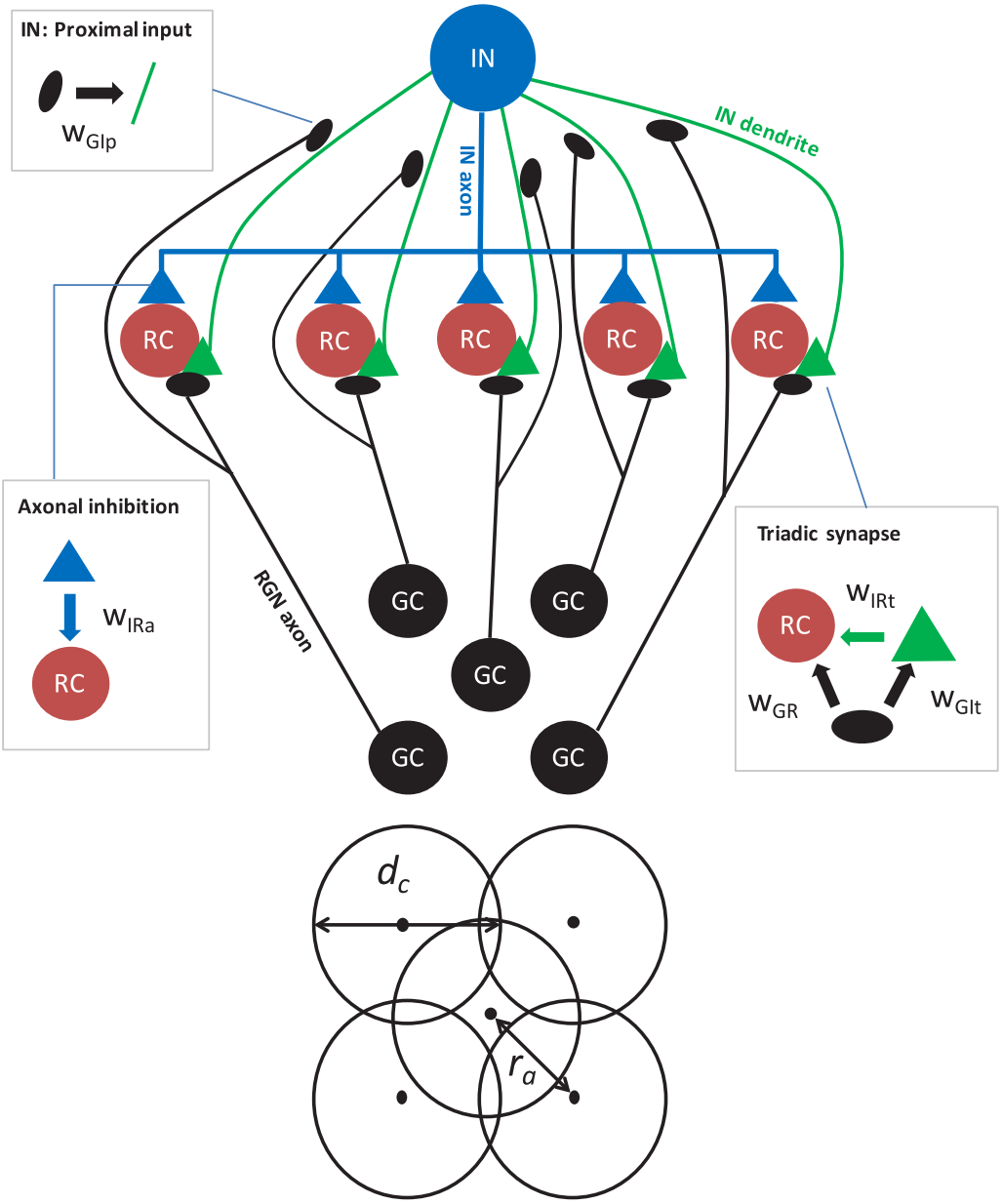

Fig 1. Schematic of the dLGN circuit model. (Top) Five relay cells (RCs) receive input from one retinal ganglion (GC) cell each. All inputs to RCs arrive in triadic synapses, involving the one and same IN. In addition, the IN receives proximal input from all five GCs. The boxes highlight the synaptic connections in the networks and the associated connection weights *w*. Note that in the present model application, only responses for the central RC cell is considered so that the only effect of the four peripheral GCs comes from the proximal inputs to the IN. (Bottom) The GCs are organized with four peripheral GCs all located at distance r_a from the center GC.

doi:10.1371/journal.pcbi.1004929.g001

extensive [28], a multicompartment model was needed. We selected an existing model [24] and simplified its morphology. Some of the parameters were adjusted to otherwise preserve the model's properties.

The RC spikes constitute the main output from our network model. A single-compartment RC model was decided to be sufficient as these neurons are thought to be electrotonically compact [28]. With slight modifications discussed below, a previously published model was used [29].

The IN and RC models were both based on standard cable theory (see e.g., [30]), and the complete dLGN circuit model was implemented in the NEURON simulation environment [31–33]. Both neuron models were based on previously published models and are available from ModelDB [34]: IN model from [24] (ModelDB accession number 140249) and RC model from [29] (ModelDB accession number 3343).

In the following section, the individual components of the circuit and their parameterizations are presented in detail.

Input from retinal ganglion (GC) cells

As in the firing-rate based circuit model of [27], a descriptive filter model was used to generate the input from the GC cells to our model dLGN circuit. Specifically, the input spike trains from the five GC cells were generated by non-stationary Poisson processes with rates determined by a response function $R_g(t, d)$ describing the firing rate for a circular spot of radius d as a function of time. This response function was in turn modeled as a product over a spatial part $G_g(d)$ and a temporal part $F_g(t)$ [35], i.e., $R_g(t, d) = G_g(d)F_g(t)$.

Spatial part of GC input response function. Following [27] we modeled the shape of the spatial receptive-field (point-spread) functions $g_g(r)$ by means of the difference-of-Gaussians (DOG) model [36],

$$g_g(r) = \frac{1}{\pi a_1^2} e^{-r^2/a_1^2} - \frac{\omega}{\pi a_2^2} e^{-r^2/a_2^2} \quad , \tag{1}$$

where the first and second terms term correspond to the center and surround terms, respectively. Further, ω represents the relative strengths of these terms, and a_1 and a_2 are the corresponding width parameters.

We further assume that the total neuronal response is given as a sum of the inputs caused by the spot with luminance L_{spot} and the infinite background surrounding the spot with luminance L_{bkg}. For the single GC cells with receptive-field center concentric with the spot stimulus (see Fig 1), the response function is then found to be [27]:

$$\begin{aligned} G_g(d;0) &= S\Big[l_{bkg}(1-\omega) \\ &+ \Big(l_{spot} - l_{bkg}\Big)\big(1 - e^{-d^2/4a_1^2} - \omega(1 - e^{-d^2/4a_2^2})\big)\Big] \end{aligned} \tag{2}$$

where the halfwave rectification function $S[x] = x\Theta(x)$ has been introduced to enforce non-negative firing rates. Here $\Theta(x)$ is the Heaviside step function, and an activity function $l(L)$ converting luminance to firing rates has been introduced, i.e., $l_{bkg} \equiv l(L_{bkg})$, $l_{spot} \equiv l(L_{spot})$. The '0' in the notation $G_g(d;0)$ signifies that the spot and receptive fields are concentric, i.e., a distance zero between their centers.

Four of the GC neurons driving the dLGN circuit have receptive fields that are not concentric with the spot, however. Rather, their receptive field centers are displaced a distance r_a from

the spot center (Fig 1). In this situation the spot-response function is instead given by [27]

$$\begin{aligned} G_g(d;r_g) \;=\; & S\Big[\, l_{bkg}(1-\omega) + (l_{spot}-l_{bkg})\times \\ & \Big(e^{-r_a^2/a_1^2} \sum_{m=0}^{\infty} \frac{1}{m!} \left(\frac{r_a}{a_1}\right)^{2m} \gamma(m+1, d^2/4a_1^2) \\ & -\omega\, e^{-r_a^2/a_2^2} \sum_{m=0}^{\infty} \frac{1}{m!} \left(\frac{r_a}{a_2}\right)^{2m} \gamma(m+1, d^2/4a_2^2) \Big) \Big] \end{aligned} \tag{3}$$

where $\gamma(n, x)$ is the so-called incomplete gamma function given by

$$\gamma(n,x) = \frac{1}{(n-1)!} \int_0^x u^{n-1} e^{-u}\, du \tag{4}$$

when n is an integer larger than zero. Note that for $r_a = 0$, Eq (3) simplifies to Eq (2). Note also that since we only consider visual stimuli with circular symmetry, i.e., circular spots, the model response does not depend on the perfect square arrangement of the non-concentric GC inputs as depicted in Fig 1B. The magnitude of a particular peripheral GC input only depends on the distance r_a from the central GC cell.

The spatial characteristics of the GC inputs to the circuit can thus be parameterized by the GC parameters ω, l_{bkg}, l_{spot}, a_1, and a_2, as well as the distance between central and peripheral GC centers r_a. Here we assumed the five GC neurons providing the inputs to the dLGN circuit to have the same response properties, i.e., the same values of ω, l_{bkg}, l_{spot}, a_1, and a_2. The parameters used here were found in [27] from fitting the GC response function in Eq (2) to experimental data in [27] (see cell no. 2 depicted in Fig 5 therein). This parameterization was selected because it is close to the mean of the results reported there and also the parameterization used in examples throughout that paper. The parameters are listed in Table 1.

Temporal part of GC input response function. The temporal profile of the GC spike trains was modeled as a difference of two exponential functions,

$$F_g(t) = \Theta(t-t_s)\,\alpha\left(1 - e^{-(t-t_s)/\tau_1} - \beta\left(1 - e^{-(t-t_s)/\tau_2}\right)\right) \tag{5}$$

to incorporate the overshoot seen in experiments (e.g. [26], see Fig 3 and 4 therein) following stimulus onset (or more precisely onset of stimulus-evoked response in the GCs in our model) at time t_s. The parameters (see Table 1) were chosen to approximate the magnitude and width of the peak in the experiments of [26] (see Fig 4B therein), with a maximum of about 2.5 times

Table 1. Model parameters for input from retinal ganglion cells (GCs).

Parameter	Description	unit	value
ω	relative strength between surround and center		0.85
$l_{bkg}(1-\omega)$	activity function (background)	s^{-1}	36.8
$l_{spot}(1-\omega)$	activity function (spot)	s^{-1}	56.5
a_1	center width	deg	0.62
a_2	surround width	deg	1.26
r_a	peripheral GC receptive-field center displacement	deg	0.99
τ_1	time constant of first exponential	ms	10.0
τ_2	time constant of second exponential	ms	22.0
α	global scaling		12.0
β	relative scaling of second exponential		11.26

doi:10.1371/journal.pcbi.1004929.t001

the sustained rate, i.e., the firing rate long after stimulus onset, while retaining the mean rate for the stimulus period given by the spatial response function.

Interneuron model

Model and calibration. An adapted and simplified version of the multicompartmental IN model by [24] was used. In particular, we employed a simplified dendritic morphology consisting of a cylindrical soma (with radius 8.72 μm and length 15.3 μm) with five identical linear 'stick'-like dendrites protruding out from it. These dendrites had linearly tapered diameters going from 4 μm adjacent to the soma to 0.3 μm at a distance of 100 μm, and from there on a constant diameter up to a total length of 500 μm.

We employed a set of passive membrane properties and active channel conductances with corresponding kinetics from [24] (Parameter set 1). The seven active ion-channels included the traditional Hodgkin-Huxley sodium and delayed-rectifier potassium channels (with conductances g_{Na} and g_{Kdr}, respectively), a hyperpolarization-activated cation channel (g_h), a low-threshold, T-type calcium channel (g_{CaT}), a high-threshold, L-type calcium channel (g_{CaL}), a medium-duration, calcium-dependent afterhyperpolarization channel (g_{AHP}), and a long-lasting calcium-activated non-specific cation channel (g_{CAN}). The intracellular Ca^{2+}-concentration was modeled as a leaky integrator [24].

To adjust for the simpler morphology compared to the morphologies used in [24], and account for recent experimental findings, some parameter values were modified: (i) The reversal potential of the passive leak current (E_{pas}) was modified to adjust the resting membrane potential, which was kept at -63 mV. (ii) The dendritic conductances g_{Na} and g_{Kdr} were set so that a somatically generated action potential (AP) reliably invaded distal dendrites (backpropagating APs), while synaptically evoked AP propagation from distal dendrites to the soma reliably failed. This was done to accommodate recent experimental findings [37]. (iii) In [24], g_{CaT} was set to increase linearly with distance from soma. However, with high values for g_{CaT} in distal dendrites, synaptic activation was likely to induce Ca^{2+} spikes and bursts of APs that originated locally in distal dendrites [38]. Such effects were not observed in experimental studies of dendritic signalling [37]. We here therefore assumed that g_{CaT} and g_{CAN} were uniformly distributed over the dendritic membrane, as this significantly reduced locally induced AP-firing in the dendrites. A uniform distribution of g_{CaT} also agreed better with another experimental study, which showed that somatically elicited Ca^{2+}-spikes evoked Ca^{2+} transients that were of the same magnitude across the entire dendritic tree [37]. (iv) In [24], g_{CAN} was assumed to have the same distribution as g_{CaT}. Here, we kept this assumption, and used a uniform distribution also for g_{CAN}.

Model parameters for passive and active membrane properties for the somatic compartment and dendritic sections are summarized in Table 2. With these parameters, the simplified IN model preserved the qualitative response properties of the original model to somatic current injection [24]. Further, the resting membrane potential of this IN model is –63 mV, and for this membrane-potential value the model responded to depolarizing current injections into the soma with tonic AP-firing, with a slightly higher firing rate immediately after current onset, see Fig 2. This resembles the tonic firing mode described for dLGN cells [39].

Input. Each GC was assumed to synapse onto the IN in two spatially separated locations, contacting the IN dendrites (i) at the proximal IN synapse (50 μm from the soma; weight denoted w_{GIp}), and (ii) in the triadic synapse located at the distal IN dendrite (450 μm from the soma; weight denoted w_{GIt}). Each GC projected to one of the five dendritic sections on the IN unit.

Conductance-based synapses were assumed, i.e.,

$$I_{syn}(t) = w f_{syn}(t)(V - E_{syn}) \ , \tag{6}$$

Table 2. Interneuron (IN) parameters.

Parameter	Description	unit	soma	dendrites
r_{ax}	axial resistivity	Ω·cm	113	113
c_m	membrane capacitance	$\mu F/cm^2$	1.1	1.1
r_m	membrane resistivity	$\Omega \cdot cm^2$	22000	22000
E_{pas}	passive leak reversal potential	mV	-67.5	-67.5
g_{Na}	max Na^+ conductance	S/cm^2	0.1	0.0074
E_{Na}	Na^+ reversal potential	mV	50	50
SH_{Na}	Na activation threshold	mV	-52.6	-52.6
$g_{K,\ dr}$	max K_{dr} conductance	S/cm^2	0.37	0.037
$SH_{K,\ dr}$	K_{dr} activation threshold	mV	-51.2	-51.2
E_K	K^+ reversal potential	mV	-90	-90
g_{CaT}	max CaT conductance (permeability)	cm/s	$1.8 \cdot 10^{-4}$	$1.8 \cdot 10^{-4}$
g_{CaL}	max CaL conductance (permeability)	cm/s	$9.0 \cdot 10^{-4}$	$2.25 \cdot 10^{-4}$
[Ca]	basal Ca^{2+} concentration	nM	50	50
τ_{Ca}	Ca^{2+} decay time constant	ms	50	50
g_{AHP}	max I_{AHP} conductance	S/cm^2	$6.4 \cdot 10^{-5}$	$6.4 \cdot 10^{-6}$
g_{CAN}	max I_{CAN} conductance	S/cm^2	$6.8 \cdot 10^{-7}$	$6.8 \cdot 10^{-7}$
g_h	max I_h conductance	S/cm^2	$1.1 \cdot 10^{-4}$	$1.1 \cdot 10^{-4}$

doi:10.1371/journal.pcbi.1004929.t002

where the weight w corresponds to the maximal conductance, and the temporal envelope $f_{syn}(t)$ of the synaptic conductance is given as the difference between two exponentially decaying functions specified by rise (τ_{rise}) and decay (τ_{decay}) times and normalized so that the maximum value of $f_{syn}(t)$ is unity, cf. Eqs. 6.4–6.6 in [40].

The properties of the proximal synapse were adapted to give responses in accordance with experimental data where EPSPs have been found to be dependent on AMPA and NMDA activation, but not on mGluR activation [41]. The joint AMPA and NMDA response was modeled as a sum of two exponentials [40, ch.6]. We used an AMPA reversal potential of 10 mV [15], and adapted the time constants of synaptic rise and decay, as well as maximum conductance to *in vitro* EPSC-traces in [41]. With these values, the time course of the somatic EPSCs in INs resembled those observed experimentally. We adjusted the synaptic weights so that the IN model required simultaneous activation of both the proximal and distal synapses on four dendrites in order to produce an action potential. This agrees with experiments, where typically 3–4 simultaneous synapse activations were required to evoke action potentials in INs [41]. The synaptic parameters are summarized in Table 3.

The response properties of the distal synapse (IN-side of triadic synapse) was initially modeled after [41] like the proximal synapses. However, in the triad the parameters were adjusted so that the triad supported so-called 'locked' (i.e., 'time-locked') inhibition of RC cells following the excitatory GC input input spike by $\sim$1 ms [15], see below. As triadic synapses are located in the distal part of IN dendrites, triadic synaptic activation were found not have any strong impact on the membrane potential in the soma of the IN (postsynaptic potential amplitudes $\sim$1 mV)

Output. Axonal GABA release from INs was assumed to occur whenever the soma elicited an AP, detected by somatic voltage crossings at –10 mV, with a 1 ms conduction delay. All five relay cells were contacted by the axon, and received the same axonal inhibition (although only the inhibition of the central RC was of relevance in the present model application focusing solely on the response of the central RC).

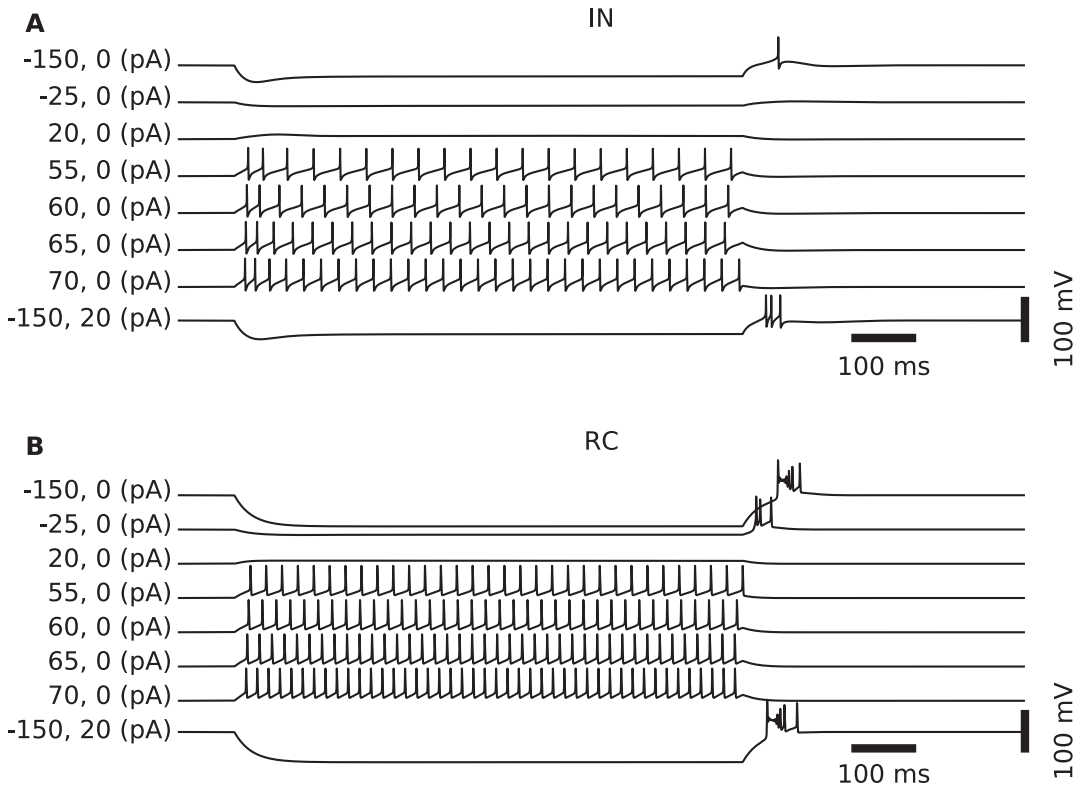

Fig 2. Spiking patterns of model neurons following somatic current injection. (A) Somatic membrane potentials of the IN model following injection of depolarizing and hyperpolarizing (positive and negative values, respectively, of first of two numbers in parenthesis) step currents lasting 900 ms. Results illustrate the overall tonic-firing response to depolarizing input currents. For the case with a strong hyperpolarizing current (–150 pA), a rebound spike is observed at offset (top trace). In the case where the offset of the strong hyperpolarizing step current (–150 pA) is combined with a constant but weak depolarizing current (+20 pA), a rebound burst is observed instead (bottom trace). (B) Similar to the IN cell, the RC cell generates spikes in a tonic pattern when the soma receives depolarizing currents. However, compared to the IN, the RC cells respond with more spikes for similar-amplitude depolarizing soma currents (and also more rebound spikes after offset of hyperpolarizing currents).

doi:10.1371/journal.pcbi.1004929.g002

Table 3. Synaptic parameters, cf. Eq 6. The listed parameters for the weights w_{GR}, w_{GIp}, w_{IRt}, and w_{IRa} are only the default values, other values are also considered, cf. Table 5. The other parameters are kept fixed in the study.

Presyn.	Postsyn.	Weight label	w (nS)	E_{syn} (mV)	τ_{rise} (ms)	τ_{decay} (ms)
GC	IN triad	w_{GIt}	2	10	0.3	2.0
GC	RC	w_{GR}	11.6	10	0.2	1.2
GC	IN proximal	w_{GIp}	0.6	10	1.6	3.6
IN triad	RC	w_{IRt}	4	-80	0.7	4.2
IN axon	RC	w_{IRa}	4	-80	0.7	4.2

doi:10.1371/journal.pcbi.1004929.t003

It has been suggested that GABA release from IN dendrites in the triad is mediated by a depolarization of the presynaptic terminal [42]. We assumed that GABA release from dendritic sites was triggered whenever the local voltage exceeded a threshold of –10 mV. With this threshold, the model reproduced two independent experimental observations. Firstly, synaptic GC input to triadic terminals in most cases (yet dependent on the history the IN activity) resulted in local GABA release from IN terminals. RCs typically responded to triadic GC input by an EPSP (synaptic excitation) followed by an IPSP about 1 ms after, as has been observed experimentally and coined 'locked' inhibition [15]. We refer to this input-induced inhibition as *direct triadic* inhibition. Secondly, local GABA release could also in some instances be evoked by back-propagating action potentials or Ca^{2+} spikes with somatic origin [41]. We refer to this as *soma-driven triadic* inhibition.

Relay-cell model

Model and parameter calibration. In contrast to INs, relay cells (RCs) appear to be electrotonically compact [28], and we thus use a single-compartment model. The membrane mechanisms were taken from an existing model [29], and included the standard (Hodgkin-Huxley type) sodium and potassium channels for generating action-potentials, as well as T-type Ca^{2+}-channels. The conductances g_{Na}, g_K and g_{CaT} were tuned so as to obtain qualitatively typical responses to somatic current injections for cells resting at a relatively depolarized membrane potential (–60 mV) [39] set by adjusting the reversal potential of the passive (leak) current (E_{pas}). In this relatively depolarized state, the RC model responded to somatic current injections by tonic firing of spikes as shown in Fig 2. The final parameter set is summarized in Table 4.

Input and output. As illustrated in Fig 1, the RC received (i) excitatory input from GCs in triadic synapses, (ii) inhibitory input from INs via dendritic GABA release in triadic synapses, and (iii) inhibitory input from INs via axonal GABA release.

The postsynaptic model response of RCs to glutamatergic input from the GCs was adapted to experimental data, i.e., monosynaptic excitation was assumed mediated by AMPA receptors with a reversal potential of 10 mV [15]. We constrained synaptic parameters (time constants, maximum conductance) to reproduce experimentally obtained EPSCs (Fig 4 in [15]).

Table 4. Model parameters for relay cell (RC).

Parameter	Description	unit	value
L	soma length	μm	35
d	soma diameter	μm	47
c_m	membrane capacitance	$\mu F/cm^2$	1.0
r_m	membrane resistivity	$\Omega \cdot cm^2$	26000
E_{pas}	passive leak reversal potential	mV	-63
g_{Na}	max. Na conductance	S/cm^2	0.015
E_{Na}	Na reversal potential	mV	50
SH_{Na}	Na activation threshold	mV	-50
g_K	max. K conductance	S/cm^2	0.0025
E_K	K reversal potential	mV	-100
[Ca]	t_∞ Ca^{2+}-concentration	nM	240
g_{CaT}	max. CaT conductance	S/cm^2	0.001
SH_{CaT}	Shift for ext. [Ca] = 2mM	mV	2
E_{Ca}	Ca^{2+} reversal potential	mV	120

doi:10.1371/journal.pcbi.1004929.t004

The postsynaptic model response of RCs to dendritic GABA release from INs in the triadic synapses was adapted to experimental data on direct triadic ('locked') inhibition [15]. The synaptic response was assumed mediated by $GABA_A$ receptors with a reversal potential of –80 mV. We constrained synaptic parameters (time constants, maximum conductance) to reproduce experimentally obtained IPSCs (Fig 4 in [15]).

In the experimental study of [15] the shapes of IPSCs produced by dendritic and axonal GABA-release were observed to be similar. We therefore modeled the synaptic response of RCs to axonal inhibition from INs to have the same functional shapes as for the triadic inhibition. Parameter values for all synapse models are summarized in Table 3.

Stimulus protocol

Neuron and synapse parameters were initially set up according to the calibrated (default) parameters listed in Tables 1–4. As in [27] we modeled the response to circular spots concentric with the receptive field of the central GC input (cf. Fig 1). The only stimulus parameter varied was thus the spot diameter d, with the spot sizes ranging from much smaller than, to much larger than the receptive-field center. In the simulations each trial consisted of a 500 ms period of full-field background luminance followed by a 500 ms stimulus period with the circular spot added on top.

In accordance with [27], mean firing rates from GC, IN, and RC cells over the entire or selected parts of the stimulus period were computed. (These firing-rates were found from time-averaging post-stimulus time histograms (PSTHs) and correspond to what is more precisely referred to as 'spike-count' firing rates [43], but in the present paper we will for simplicity generally refer to them as firing rates.) However, all spike trains were also stored for further analysis. In addition, membrane potentials from relevant neural compartments (i.e., RC and IN soma compartments as well as IN triad compartments) were recorded for a subset of the trials.

For each spot diameter several simulations ('trials') were run, and the spike-count firing rate for each trial computed. So called area-summation response curves of the type considered in [26] and [27], i.e., spike-count firing rates averaged over numerous trials as functions of spot diameter, were produced (cf. Fig 3). Unless otherwise noted, ten trials were used in the computation of the trial-average firing rate for each parameter set and spot size, and the response vs. spot-diameter curves were filtered with a seven-point rectangular window to produce smoother area-summation curves. Such area-summation curves were calculated for a large set of parameter values (cf. Table 5) to investigate the link between model parameters and response curves.

Analysis of simulation results

In the present application of the model we only considered the response of the IN and the central RC.

The receptive-field center diameter d_c was determined numerically by identifying the spot diameter that produced the maximum response r_c, see Fig 3. Here we were interested both in maximal responses for the RC (r_c^R) and IN (r_c^I). Similarly, the surround diameter d_s was given by the spot size diameter producing the minimum response r_{cs}, and at the same time fulfilling $d_s > d_c$.

From these four quantities we calculated several response measures: The ratio d_c^R/d_c^G was calculated to measure the effect of inhibition on RC receptive-field tuning [26, 27]. In the absence of inhibition, one would expect the relay cell to inherit the receptive-field size from the GC cell, and this ratio would be close to 1.0.

As a measure of how much the center response is reduced by the surround (center-surround antagonism), we also calculated the normalized difference between the maximum response to

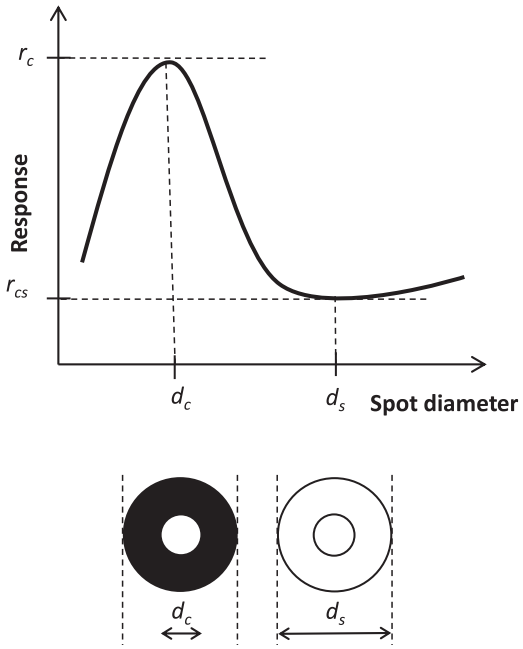

Fig 3. Illustration of area-response curves and metrics used to quantify key properties. Center diameter d_c, surround diameter d_s, peak response rate r_c, center-surround minimum rate r_{cs}. Illustration adapted from Fig 1 in [26].

doi:10.1371/journal.pcbi.1004929.g003

center stimulation (r_c) and the minimum response when the surround is stimulated as well (r_{cs}) [26, 27]:

$$\alpha = (r_c - r_{cs})/r_c \cdot 100\%. \quad (7)$$

Finally, we also investigated temporal aspects of the response and computed area-response curves both for the transient (onset) response, i.e., trial-averaged spike-count firing rate for the first 100 ms after stimulus onset, and the sustained (steady-state) response corresponding to the averaged rate in the time interval from 400 to 500 ms after stimulus onset.

Table 5. Parameter space explored for spot size and synaptic weights (maximal synaptic conductances, cf. Eq 6) in simulations. † denotes default values.

Parameter	Description	Unit	Values
d	Stimulus (spot) diameter	deg	0.05, 0.1, . . ., 10.0
w_{GR}	GC → RC	nS	†11.6/13.6/15.6/17.6
w_{GIp}	GC → IN proximal	nS	0.3/†0.6/1.2/1.8
w_{IRt}	IN triad → RC	nS	0/†4
w_{IRa}	IN axon → RC	nS	0/2/†4/6/8

doi:10.1371/journal.pcbi.1004929.t005

Implementation

Simulation and data acquisition of the dLGN circuit model was fully implemented as class objects in Python [44], using the Python package LFPy [45] for object-representations of individual cells post-synaptic to GC units. LFPy relies on the NEURON simulation environment [33] to solve the membrane potentials for the multicompartment IN unit and single-compartment RC units. NEURON also intrinsically allows specification of neuron-to-neuron connectivity, i.e., building network models.

With a relatively low total segment count (177) for the multi-compartment IN model, each network instance was simulated serially in a matter of seconds at a temporal sampling rate of f_s = 16 kHz, resulting in realtime factors as high as $\sim$10% for our computer hardware described below. Parallel execution was therefore only incorporated on the parameter scan level, as discussed below. Typically, only spike times and resulting rates were returned from each network element, but readouts such as membrane voltages were readily available if needed. All simulations for each parameter set (and spot size) were repeated 10 times or more (see above) with different seeds resulting in a total of more than one million simulations.

The GC model was implemented in NEST [46] as a spike generator (rather than a neuron model) named `exp_onset_generator`.

Simulations were performed on a compute cluster with Intel Xeon 2 CPUs running Linux 2.6.32 using NEURON 7.3 and NEST 2.3.r10450. Software was compiled with the GNU Compiler v. 4.7.2 and linked against the GNU Science Library v. 1.14. Trials were configured using the NeuroTools.parameters package [47]. Data analysis was performed on the same computers and Apple MacBook Pro computers using NumPy 1.7.1, Pandas 0.11/0.12, and Matplotlib 1.2.1/1.3.0 under Python 2.7.3.

Results were stored in HDF5 files using the PyTables package. Further analysis was performed using Pandas/NumPy and Matplotlib for visualization.

Results

Synaptic integration in interneurons (INs)

Before embarking on the dLGN circuit behavior, we demonstrate in Fig 4 the salient integrative properties of the interneuron (IN) model. The simplified ball-and-sticks morphology of the IN is illustrated in Fig 4 with the soma (black square) in the center, and the five dendrites protruding out from it with locations of both the distal, i.e., triadic, and proximal synapses marked (panel A). In the remaining panels (B–E), the membrane potential in only two selected dendrites are considered for figure clarity reasons.

When a single GC spike arrives at a distal IN synapse (panel B), the response is partly mediated by local, active ion channels. The distal dendrites undergoes a rapid, local depolarization (up to $\sim$0 mV) due to activation of local Na^+ channels, after which the potential decays from subsequent activation of K^+ (and deactivation of Na^+) channels. The distal-dendrite membrane potential is observed to remain at a relatively depolarized level, i.e., above –50 mV, for an extended period of time (about 20 ms, see inset panel B). The endured response is partly due to the activation of local T-type Ca^{2+} channels, as we have shown previously [38]. Due to the widening of the dendritic stick, i.e., increase of stick diameter in the central direction, the EPSP is strongly attenuated upon its propagation towards the soma, and is not sufficient for driving the soma above the action potential threshold (panel B).

A single spike arriving at a proximal synapse results in only a small depolarization of the membrane potential (panel C), i.e., too little to evoke either triadic inhibition or generate a somatic action potential which in turn would provide axonal inhibition. Further, when a single

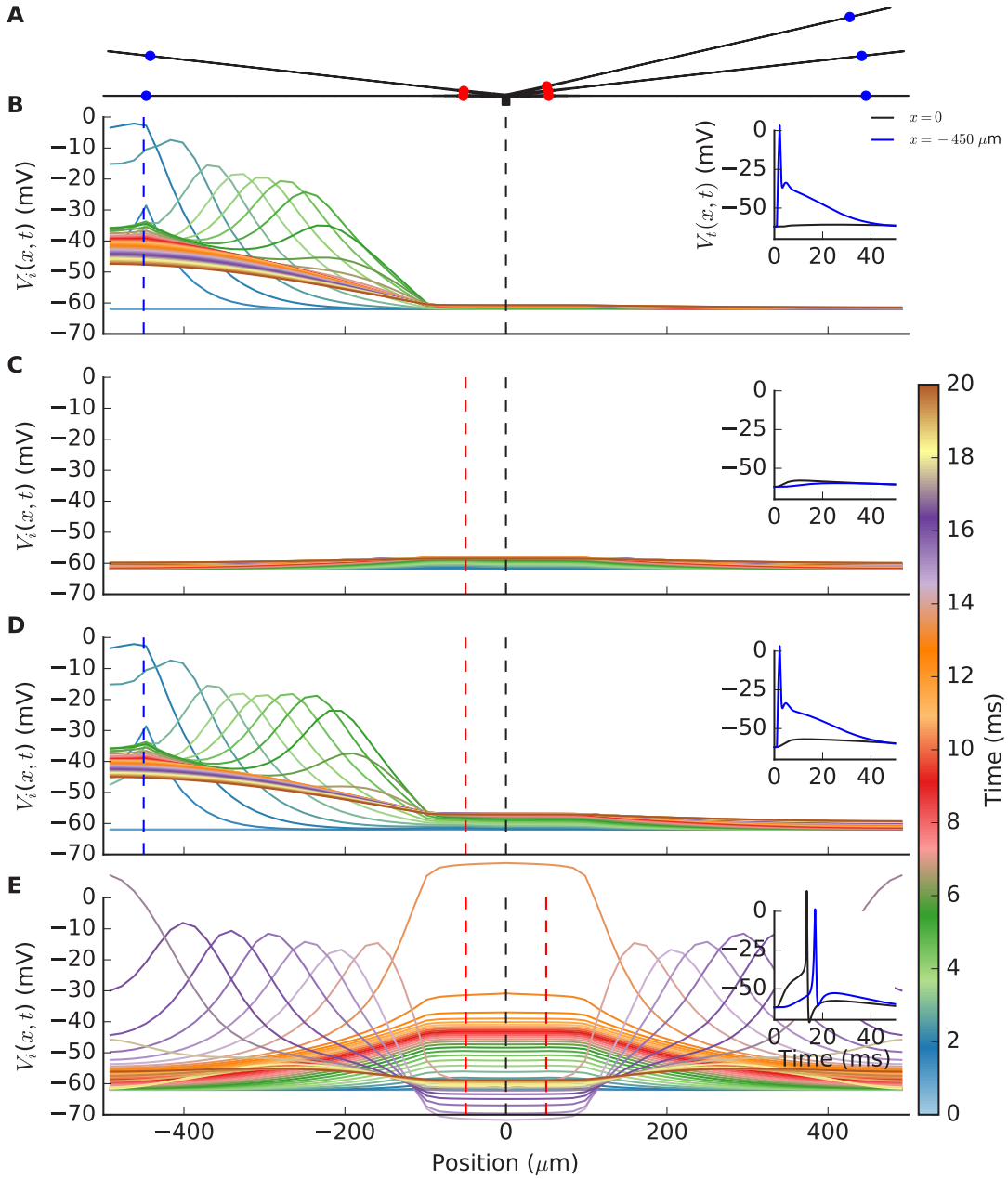

Fig 4. Synaptic integration properties of interneuron (IN) model. (A) Ball-and-sticks IN model consisting of a point-like soma (black square) with five dendritic sticks protruding out from it. Distal (triadic; blue dots) and proximal (red dots) synapse locations are illustrated. Panels B–E shows spatiotemporal spread of IN membrane potential along two (of five) dendritic sticks following activation by single RC spiking on inputs distal (triadic)

and/or proximal synapses. Each colored line represents a snapshot of the membrane potential taken each half millisecond from 0 to 20 milliseconds with the GC spike(s) arriving at t_{syn} = 1 ms. The synapse position(s) are denoted by vertical, red or blue dashed lines, while the black dashed line marks the location of the soma compartment. The small inset axes show the membrane potential in the soma ($V_i(0, t)$) and in the distal dendrite ($V_i(-450\ \mu m, t)$), respectively, as a function of time. (B) GC spike onto distal synapse on lower left dendritic stick. (C) GC spike onto proximal synapse on lower left dendritic stick. (D) GC spike arriving simultaneously on distal and proximal synapses on lower left dendritic stick. (E) GC spikes arriving simultaneously at all five proximal synapses, including those on the two depicted dendritic sticks.

doi:10.1371/journal.pcbi.1004929.g004

distal and a single proximal synapse positioned on the same branch are activated at the same time (panel D), the resulting soma potential is still too small to generate an action potential. However, when all five proximal synapses are activated by simultaneous spikes (panel E), a somatic axon potential is generated which next provides axonal inhibition on postsynaptic RC cells. Moreover, this axonal action potential back-propagates into the dendrites where it also activates triadic inhibition. This latter type of triadic inhibition is here denoted soma-driven triadic inhibition.

Triadic circuit dynamics

The mechanism behind the two types of triadic inhibition, i.e., 'direct' and 'soma-driven', is illustrated in Fig 5. In panel B, a single incoming GC spike input to a distal (triadic) synapse (illustrated in panel A) triggers a large postsynaptic response in the distal IN dendrite. If the response is sufficiently large, as in the current example, it will lead to direct triadic inhibition from the IN to the RC partner in the triadic circuit. While the excitatory GC input to the RC cell alone would give an immediate RC action potential (red curve in panel C), this action-potential firing is prevented when this excitatory input is accompanied by direct triadic inhibition (black curve in panel C). (For the present model example we find that the triadic inihibition must arrive within 1.3 millisecond after the excitatory GC input to prevent the generation of an RC spike.)

In soma-driven triadic inhibition a somatic action potential in the IN, induced by sufficiently synchronous excitatory GC inputs onto the proximal dendrites (cf. Fig 4), results in a back-propagating action potential which in turn induces triadic inhibition (panel D in Fig 5). However, this type of triadic inhibition takes a few milliseconds to occur, i.e., too late to prevent the firing of an RC action potential (panel E). This inhibition can thus only affect GC spikes reaching the dLGN circuit at a later time.

Fig 5 illustrates the importance of timing of the triadic inhibition in the regulation of RC firing: when a GC spike impinges on the dLGN circuit (RC and IN cells), only the direct triadic inhibition acts fast enough to affect the immediate spike generation in RC cells. Such direct triadic inhibition probably underlies what is known as *time-locked*, or simply *locked* inhibition in the experimental literature [15].

Some key features of the dynamics of the triadic circuit when stimulated by a flashing circular post, are illustrated in Fig 6. While our numerical experiments each last for 1000 milliseconds, the figure focuses on the spiking activity in the half-second window around the stimulus onset at 500 milliseconds. Panel A shows the membrane-potential dynamics of the IN for an example trial, both in the soma (blue line) and in the distal part of the dendritic segment (green) receiving synaptic input from the central GC cell. This panel also shows the time stamps of the GC input spikes driving the circuit, both from the center GC cell (top row of tiny triangles) and from the four peripheral GC cells combined (bottom row of triangles). A first observation is that in the typical case, an input spike from the central GC cell causes direct triadic inhibition (see, for example, arrow 1 in panel A) while a fairly synchronous barrage of four spikes from the set of GC cells is needed to evoke a somatic action potential (see, for example, arrow 2 in panel A). Given the much higher firing-rate of the central GC cell compared to

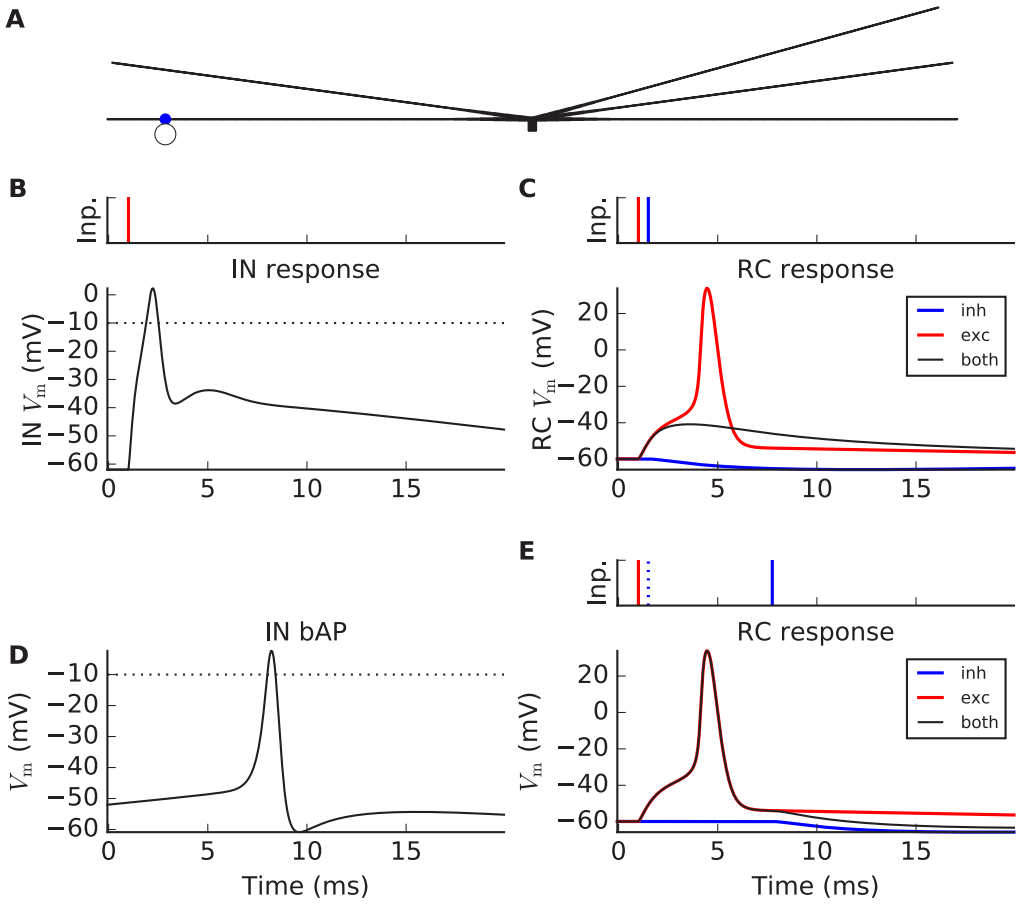

Fig 5. Illustration of two pathways for triadic inhibition of relay cells (RCs). Curves show membrane potentials of the IN dendrite (panels B,D) at the distal synapse position (blue dot in panel A) and in RC soma (panels C,E), respectively. (A) Illustration of interneuron (IN) with triadic connection with RC shown as open circle. (B) Single incoming GC spike input to distal (triadic) synapse (time stamp t_{syn} = 1 ms denoted as red bar in small display on top) triggers a large postsynaptic response in distal IN dendrite, effectively resulting in a dendritic action potential. (C) Same GC input spike as in (B) now also projecting to the RC partner of the triadic circuit with a short time delay resulting in *direct triadic inhibition* of the RC (starting at time shown as blue time-stamp bar above): without inhibition the GC input to the RC cell gives an immediate RC action potential (red curve), while no action potential occurs if the excitatory input is accompanied by direct triadic inhibition (black curve). (D) Back-propagating action potential in IN dendrite(s) triggered by a strong synapse input to the IN soma (activation time t_{syn} = –8 ms, g_{max} = 300 nS, E_{syn} = 10 mV, τ = 1 ms, $I_{syn}(t) = g_{max} \cdot \exp(-(t - t_{syn})/\tau) \cdot (V_m - E_{syn})$ for $t \geq t_{syn}$). For illustration purposes, the distal activation of the IN dendrite by the GC input is here absent, i.e., $w_{Glt} = 0$. (E) Same GC input spike as in panels B and C now also projecting to an RC cell, gives an RC action potential both without (red curve) and with *soma-driven triadic inhibition* (black curve) as the inhibition occurs too late (blue time-stamp bar above) to prevent action-potential firing in the RC.

doi:10.1371/journal.pcbi.1004929.g005

the peripheral GC cells in the present example, the direct triadic inhibition will occur more often than firing of somatic action potentials. As a consequence, the soma-driven inhibition (soma-driven triadic and axonal) will occur less frequently than direct triadic inhibition. Note, however, that the involvement of dendritic Na^+ and K^+ channels in mediating the local

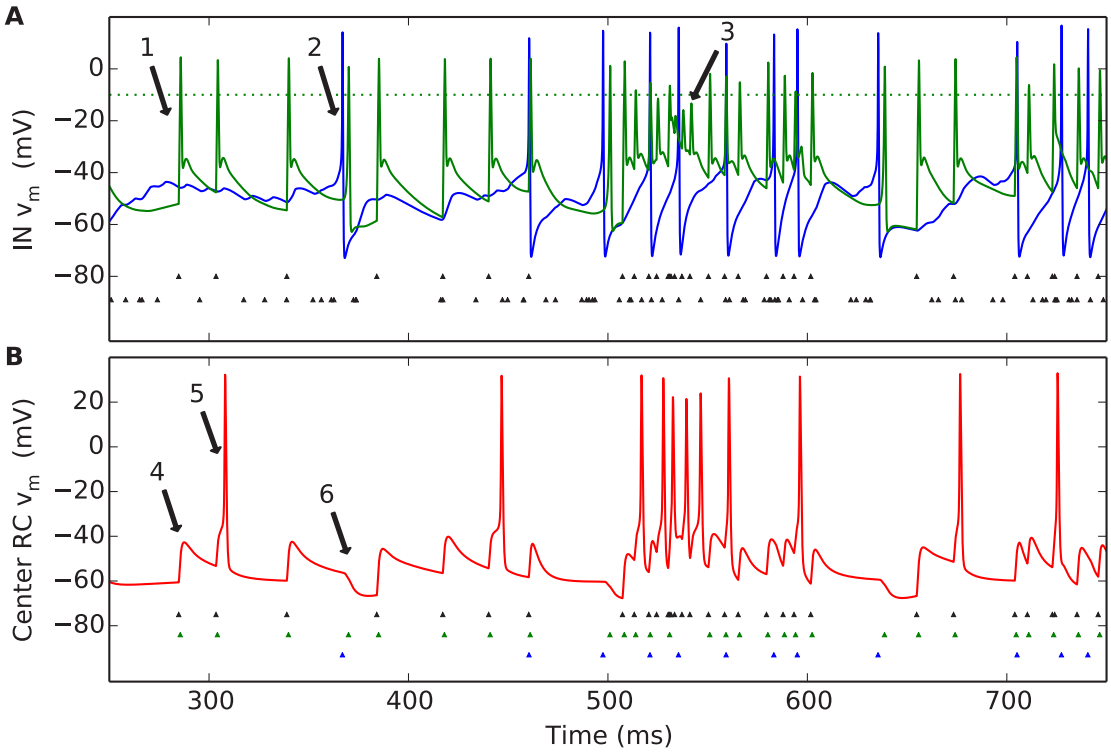

Fig 6. Illustration of temporal response in dLGN model circuit. A stimulus spot of diameter $d = 1$ deg is turned on at 500 ms. (A) Example of (single-trial) IN membrane-potential dynamics (soma: blue line; distal part of dendritic segment receiving synaptic input from central GC cell: green line). Also shown are GC input spikes driving the circuit, both from the center GC cell (top row of tiny triangles) and from the four peripheral GC cells (bottom row of triangles). (B) Corresponding RC membrane-potential dynamics. Also shown are input spikes from the central GC input (top row of tiny black triangles), IN dendritic (triadic) action potentials (middle row of green triangles), and IN somatic action potentials (bottom row of blue triangles). See text for explanation of arrows. Default model parameters are used, cf. Tables 2–4.

doi:10.1371/journal.pcbi.1004929.g006

response induces an effective refractory period (the channels do not have time to reset between two input spikes). This is evident during the first 50 milliseconds or so after stimulus onset, when the firing-rate of the central GC cell is so high that not all incoming spikes result in the distal-dendrite membrane potential passing firing threshold (see, for example, arrow 3 in panel A). Direct triadic inhibition will therefore not occur at every input spike. Such a depression of triadic inhibition for high input rates was also seen experimentally [15].

Panel B in Fig 6 illustrates the corresponding RC response. When there has been a long time since the previous excitatory GC input spike (see, for example, arrow 4 in panel B), direct triadic inhibition prevents the firing of an RC spike. However, if a new GC input spike arrives before the RC membrane potential has returned to its resting value, the direct triadic inhibition may not be sufficient to prevent the firing of an RC action potential (see, for example, arrow 5 in panel B). The chance for an incoming GC spike to generate an RC spike can be further reduced by soma-driven inhibition leading to a transiently hyperpolarized RC membrane potential (see, for example, arrow 6 in panel B). We also note that the inhibition is more efficient at preventing

the firing of RC action potentials in the background state, i.e., prior to stimulus onset at 500 milliseconds, than immediately after stimulus onset: For example, during the depicted background state (250–500 ms) only two of the seven incoming GC spikes result in the firing of an RC spike, corresponding to a transfer ratio [48] of $2/7 \approx 0.29$. In contrast, in the first 75 milliseconds after stimulus onset (500–575 ms), six of thirteen incoming GC spikes result in an RC spike, corresponding to a transfer ratio of $6/13 \approx 0.46$. This transfer ratio smaller than unity value reflects that two or more incoming GC spikes are normally needed to elicit an RC spike [48–50].

As the spiking response to individual stimulus presentations typically varies between trials, the post-stimulus time histogram (PSTH) [43] is commonly used to characterize neural spiking responses. Examples of such PSTHs for the set of experiments underlying the experimental area-response curve measurements for the GC and RC on which the present model is tuned (cf. Fig 5 in [27]), can be found in [26] (Fig 3 and 4 therein). Fig 7 shows PSTHs for the GC, IN and RC cells in Fig 6 found by binning spikes found from many repetitions, i.e., many trials of our numerical 'experiment'. Panel A shows the PSTH from the central GC cell in a 500 ms window around the spot onset, while panel B similarly shows the corresponding PSTH for the IN cells. The two lower panels show corresponding PSTHs for the RC cell for two extreme situations: only axonal inhibition (i.e., triadic inhibition turned off, $w_{\mathrm{IRt}} = 0$) in panel C, and only triadic inhibition (i.e., axonal inhibition turned off, $w_{\mathrm{IRa}} = 0$) in panel D. For these particular model parameters we see that the peak response in the PSTH following stimulus onset is largest for the GC ($\sim 200\ \mathrm{s}^{-1}$) and smallest for the IN ($\sim 50\ \mathrm{s}^{-1}$). For the RC we see that both the background (i.e., response before stimulus onset) and peak responses are larger for the case with axonal inhibition (panel C) than for triadic inhibition (panel D), implying that for the present choice of model parameters the triadic inhibition is more efficient than axonal inhibition in reducing RC firing.

Area-summation curves

We now move on to compute and investigate area-summation curves, that is, the time-average of PSTHs of the type shown in Fig 7, as a function of spot diameter. These time-averaged PSTHs correspond to what is more precisely referred to as 'spike-count' firing rates [43], but in the following we will for simplicity refer to them as firing rates.

In the present modeling study we in particular investigate the effects of various types of inhibition on the area-summation curves of the RC and IN neurons. Examples of such calculated area-response curves are given in Fig 8. Here the black line gives the area-response curve of the central GC cell providing the input, the blue line the corresponding curve for somatic spikes for an IN, while the solid, dashed and dotted red lines show RC response curves for different choices of model parameters specifying inhibitory effects from the IN. The response curves shown here correspond to the 'raw' data, i.e., prior to filtering by a seven-point rectangular window (see Methods), and the jagged response curves serve to illustrate the inherent variability of the trial-averaged response. The bottom panel in Fig 8 shows the data normalised to the maximal response for each cell, thus highlighting the shapes of the area-response curves rather than their response magnitudes.

Fig 8 shows example area-summation curves for the three different types of inhibition considered here:

(RC-i) **Direct triadic inhibition:** Triadic inhibition driven by GC input on same distal IN dendrite only, i.e., $w_{\mathrm{IRt}} > 0$, $w_{\mathrm{GIp}} = 0$, $w_{\mathrm{IRa}} = 0$

(RC-ii) **Direct & soma-driven triadic inhibition:** Triadic inhibition driven both by GC input on same distal IN dendrite and back-propagated soma activation in turn stemming from proximal inputs on the IN, i.e., $w_{\mathrm{IRt}} > 0$, $w_{\mathrm{GIp}} > 0$, $w_{\mathrm{IRa}} = 0$

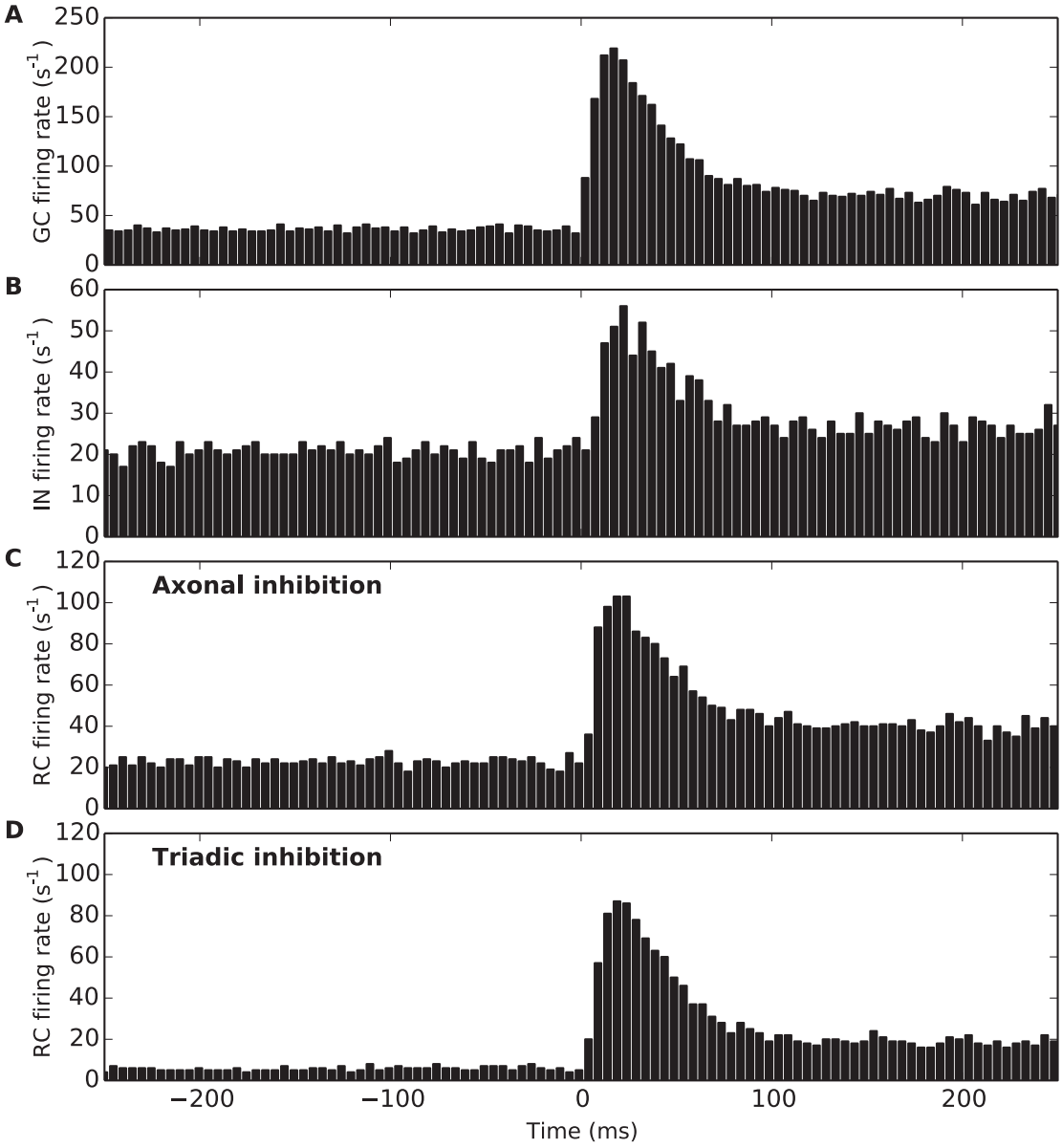

Fig 7. Example post-stimulus time histograms (PSTS) for cells in dLGN model circuit. Stimulus spot of diameter $d = 1$ deg is turned on at 500 ms. (A) PSTH for central GC cell. (B) PSTH for IN cell. (C) PSTH for RC cell with axonal inhibition only ($w_{IRa} = 4$ nS, $w_{IRt} = 0$). (D) PSTH for RC cell with triadic inhibition only ($w_{IRa} = 0$, $w_{IRt} = 4$ nS). Results correspond to 1000 trials, bin size: 5 ms. Default model parameters are used, cf. Tables 2–4.

doi:10.1371/journal.pcbi.1004929.g007

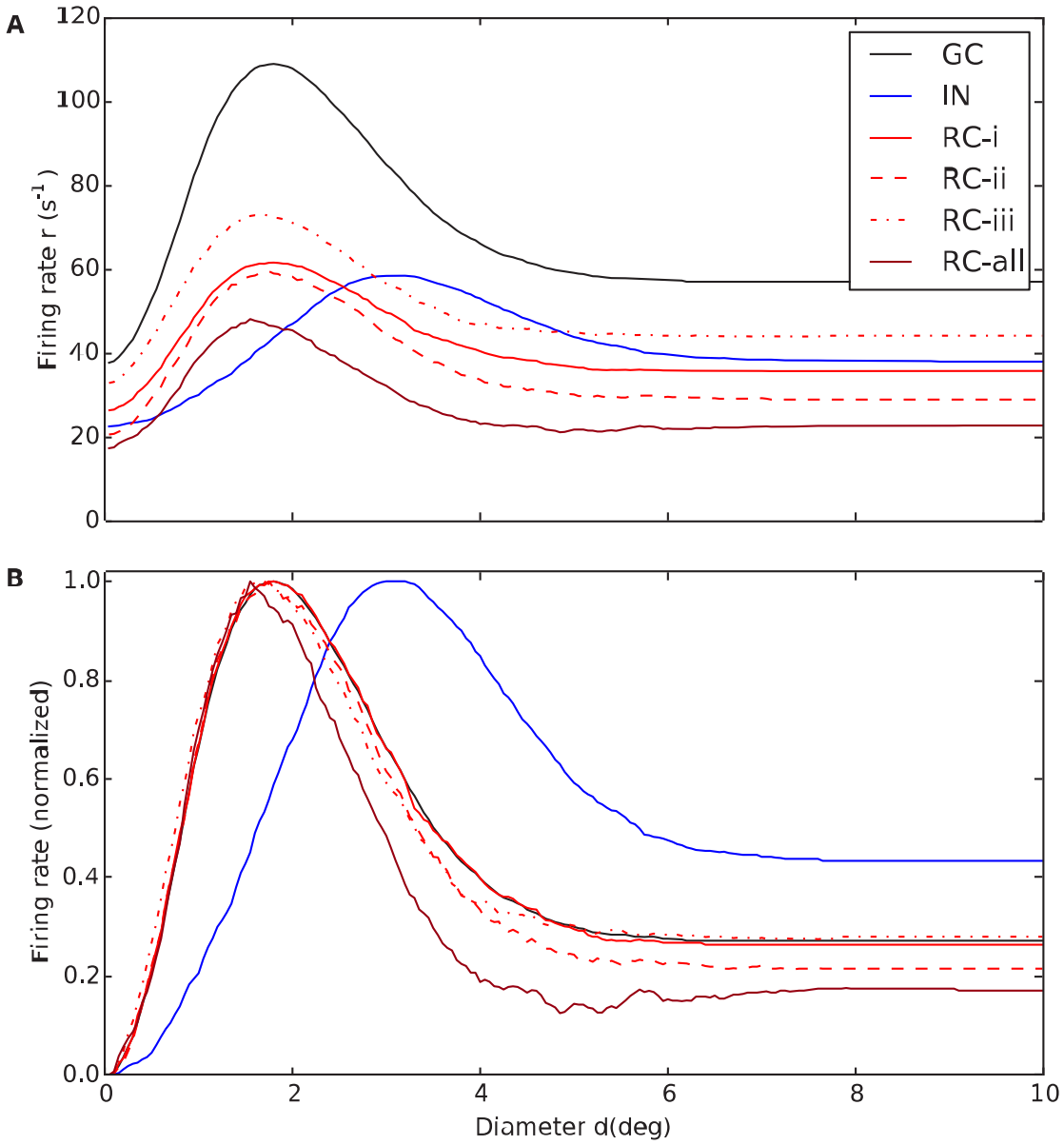

Fig 8. Example area-summation curves illustrating effects of various types of inhibition on relay-cell (RC) response. (A) Trial-averaged spike-count firing rate vs. spot diameter, for central retinal ganglion cell (GC, solid black), interneuron (IN, solid blue), and relay cell (RC, red lines). Red solid line: RC response for *direct triadic inhibition* (RC-i) with $w_{IRt} = 4$ nS, $w_{Glp} = 0$, $w_{IRa} = 0$. Red dashed line: RC response for *direct & soma-driven triadic inhibition* (RC-ii) with $w_{IRt} = 4$ nS, $w_{Glp} = 0.6$ nS, $w_{IRa} = 0$. Red dotted line: RC response for *axonal inhibition* (RC-iii) with $w_{IRt} = 0$, $w_{Glp} = 0.6$ nS, $w_{IRa} = 4$ nS. Dark red line (RC-all) corresponds to results from all three types of inhibition combined, i.e., $w_{IRt} = 4$ nS, $w_{Glp} = 0.6$ nS, $w_{IRa} = 4$ nS. $w_{GR} = 15.6$ nS is used in all cases. Other parameters correspond to default values. Note that the depicted IN response does not apply to case (RC-i) as the IN is only

synaptically activated at the triads in this case as $w_{GIp} = 0$. (B) Area-response curves in A normalised to have maximal values of unity. The receptive-field center diameters d_c corresponds to the spot diameter giving the largest response. The spike-count firing rates are found by averaging PSTHs of the type in Fig 7 over the entire 500-ms time window the stimulus is on.

doi:10.1371/journal.pcbi.1004929.g008

(RC-iii) **Axonal inhibition**: Axonal inhibition of RC following firing of action potential in the IN, i.e., $w_{IRt} = 0$, $w_{GIp} > 0$, $w_{IRa} > 0$.

The figure also shows the resulting area-summation curve when all these three types of inhibition is included at the same time.

A first observation in Fig 8 is that the GC response in all cases is larger than the RC response, essentially reflecting that the transfer ratio at the retinogeniculate relay always is less than one [26, 27, 48, 49]. The spot diameter with the largest responses corresponds to the size of *receptive-field center*, and we observe that while the central GC cell has a center diameter d_c^G of about 2 degrees, the IN center diameter d_c^I is about 3 degrees, cf. panel B. This larger center size reflects that the IN is driven by multiple, spatially separated GCs.

For the case with direct triadic inhibition only (RC-i) we observe that while this inhibition reduces the RC firing rate by about a factor two compared to the GC input (solid curves in Fig 8A), the shape of the response curves, i.e., normalized response, is essentially identical (panel B). Thus the direct triadic inhibition essentially acts as a gain control, only. With soma-driven inhibition included as well (RC-ii), some changes in the shape is observed (dashed red curve in panel B). In particular, a close inspection of panel B reveals that the receptive-field center size d_c^R of the RC cell now is seen to be somewhat smaller than the GC center size. An even larger reduction of the center size is observed in the case of axonal inhibition only (RC-iii). This reduction in receptive-field center size seen for cases (RC-ii) and (RC-iii) (as well as the example in Fig 8 with all three types of inhibition included, RC-all) reflects the larger resulting receptive-field size of the IN providing the inhibitory action on the RC cell [26, 27].

Another key qualitative feature observed in Fig 8 is the larger *center-surround antagonism*, i.e., large relative dampening of the full-field response (e.g., $d = 10$ degrees) compared to the peak response, seen for the cases where the inhibitory effects are the strongest (RC-ii and RC-all for the example model in Fig 8). For IN this center-surround antagonism is instead reduced compared to the GC input.

In the following we show area-summation curves results both when only triadic or axonal inhibition are active like in Fig 8, and in the likely more realistic case when both types of inhibitions simultaneously affect the relay-cell response.

For reference we show in the top row of Fig 9 the RC response for the case with neither triadic nor axonal IN inhibition. Here we observe that the overall RC response changes only moderately when increasing the excitatory connection strength w_{GR} between the central GC cell and the RC cell with almost 50% from the lowest value considered ($w_{GR} = 11.6$ nS). The reason is that the transfer ratio, i.e., the fraction of incoming GC spikes resulting in an outgoing RC spike, is already quite high even for this lowest weight. This leaves limited room for further increase in the response. Another observation is that without inhibition the RC and GC response curves always have their maxima at the same spot diameter, i.e. $d_c^R \approx d_c^G$.

With direct triadic inhibition included (second row in Fig 9) we see that the RC response curves drop substantially, e.g., about 50% for the peak response and even more for the full-field (large-spot) response for the lowest value of w_{GR} (11.6 nS). Unlike in the case with no inhibition, increased excitation strength w_{GR} is seen to increase the RC response as extra excitation will compensate for the added direct triadic inhibition. We further see that the shapes of the RC response curves are similar to the 'no-inhibition' curves, the main difference is a vertical shift of the response curves. Such a vertical shift implies a larger relative reduction of the full-field

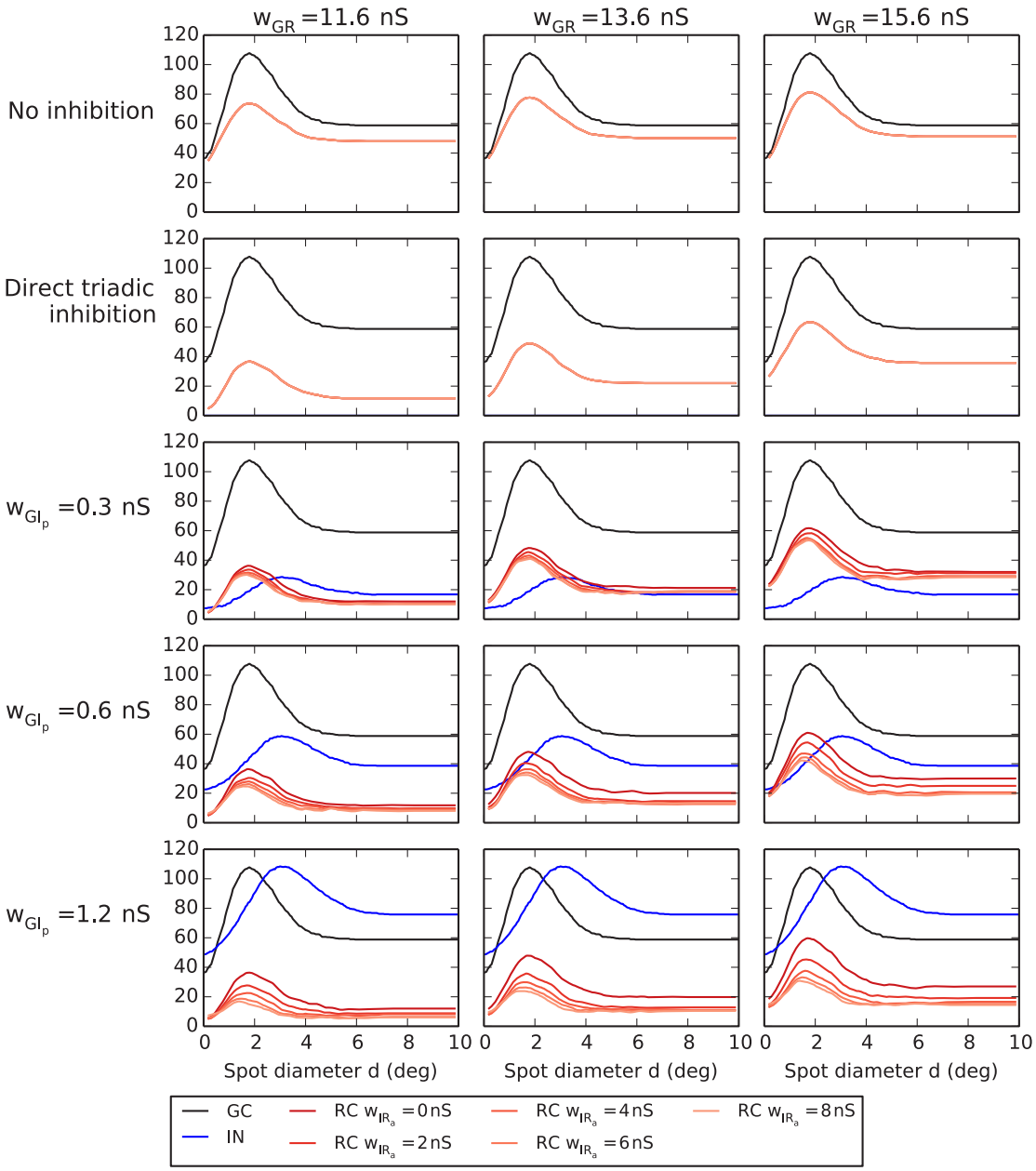

Fig 9. Area-response curves with triadic inhibition. Row 1: no inhibition. Row 2: direct triadic inhibition only (case (RC-i)). Rows 3–5: triadic or triadic +axonal inhibition for different values of weight proximal ganglion-cell input to the interneuron w_{GIp}. Black curves correspond to central retinal ganglion cell (GC), blue curves to interneuron (IN), and red/orange curves to relay cell (RC). The four RC curves in the panels in rows 3–5 correspond to w_{IRa} = 0/2/4/8 nS with w_{IRa} = 0 (no axonal inhibition) and w_{IRa} = 8 nS (maximal axonal inhibition) corresponding to the top and bottom of the four curves, respectively.

doi:10.1371/journal.pcbi.1004929.g009

response compared to the center response, i.e., an increased center-surround antagonism. Thus direct triadic inhibition increases the RC center-surround antagonism α_R, particularly for the lower excitatory weights. The RC receptive-field center size d_c^R is essentially unaffected by the direct triadic inhibition. This follows from the fact that in our IN model, excitation of the distal IN dendrite results in small EPSP amplitudes at the soma (Fig 4B). Thus direct triadic inhibition on the RC cell can only occur due to spiking inputs from the central GC cell, and such inhibition can only affect the gain control within the triadic synapse structure (as was clearly illustrated in the normalized response plot for the direct triadic case in Fig 8B). Since distal IN excitation barely affects the somatic membrane potential and does not generate IN somatic action potentials, an IN area-summation curve is likewise absent from the second row of Fig 9.

The three lower rows of Fig 9 depict area-response curves for various combinations of direct and soma-driven triadic inhibition and axonal inhibition. The different rows correspond to different values of the proximal excitation of INs (w_{GIp}), while different columns still correspond to different values of the retinogeniculate excitation (w_{GR}). The area-response curve of the IN is, of course, independent of the value of w_{GR}, so the same IN response curve is seen in the same-row panels. By comparing area-response curves for increasing values of proximal IN excitation w_{GIp} we see, as expected, a large increase in the IN response. The increased response is also accompanied by a reduction in center-surround antagonism of the IN neuron. However, the IN receptive-field center size d_c^I is much less affected.

In each of the nine panels in the lower three rows in Fig 9 there are four (red/orange) RC area-summation curves corresponding to different values of the axonal inhibition weight w_{IRa}. The topmost curves correspond to the situation without axonal inhibition ($w_{IRa} = 0$), while the three other curves corresponds to different non-zero values of w_{IRa} (2/4/8 nS) with the lowest curve corresponding to the largest weight considered ($w_{IRa} = 8$ nS). It is seen that not only does increased axonal inhibition reduce the RC response, it also reduces the RC receptive-field center size d_c^R. Both effects are seen to be strongest when the proximal excitation w_{GIp} of the IN is largest.

The effects of the various model components and parameters on key response measures for the results in Fig 9 are summarized in Fig 10. This figure shows how the RC and IN receptive-field center sizes (d_c^R, d_c^I), center-surround antagonisms (α_R, α_I), and maximum firing rates vary with the axonal inhibition weight (w_{IRa}) for a set of different values of the weight of ganglion-cell activation of the RC (w_{GR}) and of the proximal dendrites of the IN (w_{GIp}, color coded according to legend box below figure).

A first observation is that the receptive-field center size of the RC (d_c^R) is substantially reduced both when the proximal excitation of the proximal IN dendrites (w_{GIp}) and when the axonal inhibition weight from the IN to the RC (w_{IRa}) are increased (panel A). This is as expected as both these weights determine the overall axonal inhibition of the RC providing the shrinkage of the RC receptive-field center [27]. In contrast, the receptive-field center size of the IN (d_c^R) can naturally only depend on the weight of the proximal synapse from the GC (w_{GIp}). This increase is quite modest, however, and most of the observed variation in the ratio between the IN and RC center sizes (d_c^I/d_c^R) (panel B) comes from the variation of the RC center size.

The center-surround antagonism for the RC (α_R) is seen to be almost independent of the axonal inhibition weight w_{IRa} (panel C). This implies that the RC center-surround antagonism is little affected by axonal inhibition.

For the smallest values of the weight of the ganglion-cell input to the RC ($w_{GR} = 11.6$ nS), α_R does not depend much on somatic IN activity (panel C): α_R is large, about 0.7, for all considered values for w_{GIp}. However, for the two largest values of the ganglion-cell input weight to the RC ($w_{GR} = 13.6$ nS, $w_{GR} = 15.6$ nS) some variation with w_{GIp} is observed: For example, for

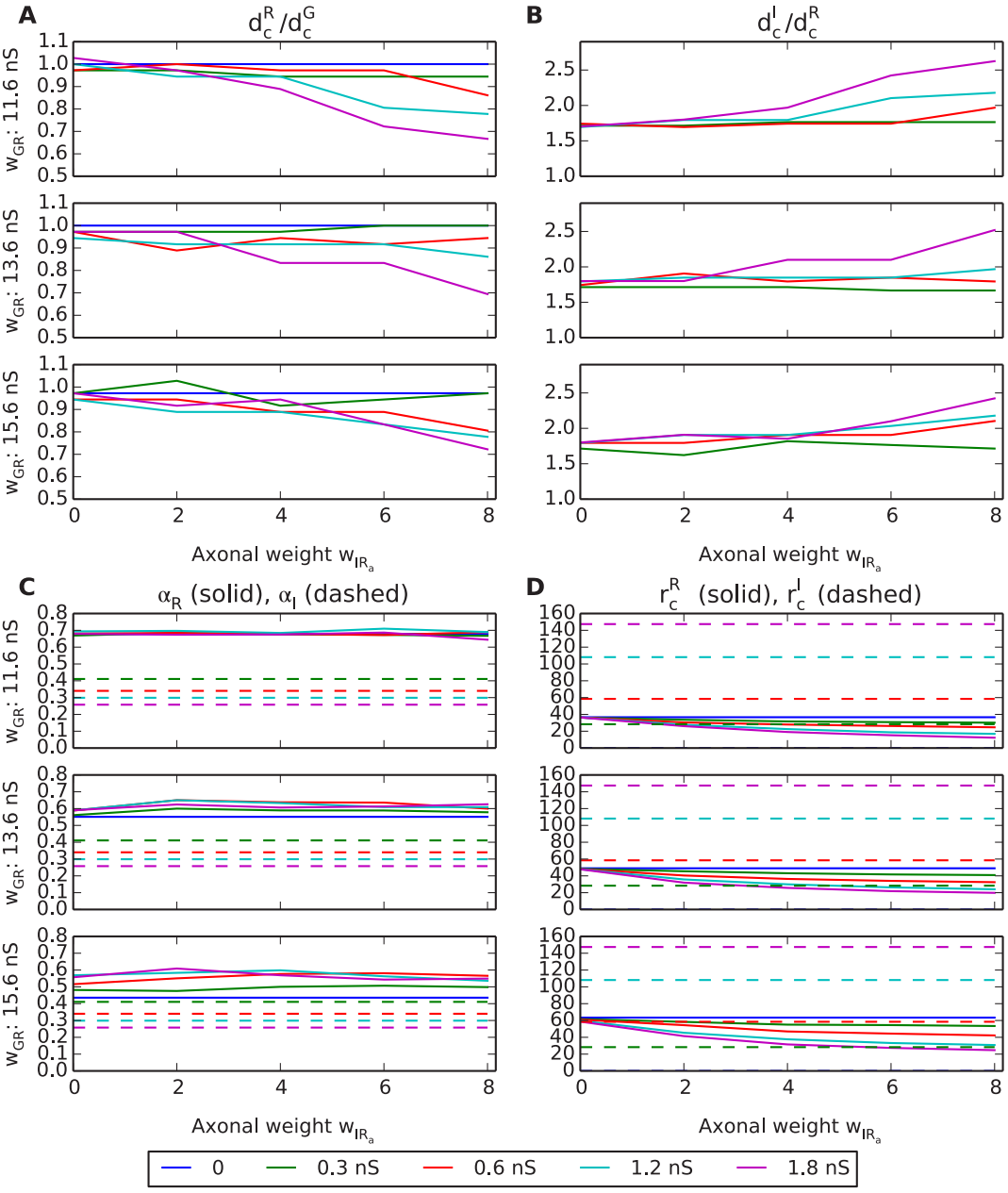

Fig 10. Summary of response measures from area-response curves with triadic inhibition present. (A) Ratio of receptive-field center diameter of relay cell (RC) and (central) retinal ganglion cell (GC), d_c^R/d_c^G; receptive-field center diameter measured as the spot diameter corresponding to the largest firing rate in the area-summation curves in Fig 9. (B) Ratio of receptive-field center diameter of interneuron (IN) and

relay cell (RC), d_c^I/d_c^R. (C) Relay-cell α_R (solid) and interneuron α_I (dashed) center-surround antagonisms, cf. Eq 7. (D) Maximal firing rate r_c, i.e., firing rate for spot exactly covering receptive-field center, for relay cell (r_c^R, solid) and interneuron (r_c^I, dashed). The colored lines correspond to different values of w_{GIp}, see legend below panels. Note also that interneuron (IN) results are absent for the case with $w_{GIp} = 0$ (blue lines) since in this case the IN only receives triadic input and does not fire any action potentials.

doi:10.1371/journal.pcbi.1004929.g010

$w_{GR} = 15.6$ nS, α_R is seen to vary between ~ 0.4 for $w_{GIp} = 0$ to ~ 0.6 for $w_{GIp} = 1.8$ nS. As $w_{GIp} = 0$ corresponds to the case with direct triadic inhibition only (and it is also seen that α_R is essentially independent of w_{IRa}) this substantial increase in α_R must be due to soma-driven triadic inhibition. Thus while direct triadic inhibition alone is seen to be sufficient to assure a large centre-surround inhibition when the retinogeniculate excitation w_{GR} is weak, soma-driven triadic inhibition can provide the same when the retinogeniculate excitation is strong.

The center-surround antagonism for the IN (α_I) is generally much lower than for the RC [27] and is seen to vary between ~ 0.25 and ~ 0.4 depending on the value of w_{GIp} (panel C, dashed lines).

The maximum firing rate r_c^R of the RC, i.e., the firing rate at the peak of the area-summation curve, is as expected seen to decrease both with increasing axonal inhibition weight (w_{IRa}) and increasing synaptic input onto the proximal dendrites of IN (w_{GIp}) (solid lines in Fig 10D). For the IN, the maximum firing rate r_c^I is correspondingly seen to increase when the weight of proximal synaptic input from GCs (w_{GIp}) increases (panel D, dashed lines).

In Fig 11 we show, in analogy to Fig 9, the same set of area-summation curves in the absence of triadic inhibition, i.e., $w_{IRt} = 0$. In this case where only axonal inhibition acts on the RCs, we observe as expected less reductions of RC responses, particularly for the smallest considered values of w_{GIp} and w_{GR}. However, as confirmed by the corresponding parameter dependence of the key response measures shown in Fig 12, most qualitative effects of increasing the inhibitory synaptic weights are similar to what was seen for the case with triadic inhibition included, cf. Fig 10: The receptive-field center size of the RC (d_c^R) (panel A) decreases with increasing axonal inhibition (w_{IRa}) and increasing ganglion-cell drive onto proximal IN dendrites (w_{GIp}). This is also the case for the maximal RC firing rate r_c^R (panel D), but here the firing rates are as expected overall higher compared to the case with triadic inhibition.

A final observation in Fig 12 is that the center-surround antagonism for the RC (α_R, panel C) is seen to generally be lower when triadic inhibition is absent, cf. Fig 10C. This is in accordance with the previous observation for the results *with* triadic inhibition (Fig 10C) where α_R was seen to be largely independent of the axonal inhibition weight w_{IRa}. This was interpreted to reflect dominance of triadic inhibition over axonal inhibition in determining the RC center-surround antagonism. *Without* triadic inhibition we observe in Fig 12C that α_R instead increases with the value for the axonal inhibition weight w_{IRa}.

Transient vs. sustained response

So far we have only considered the spike-count rate pooling all spikes within the whole 500 ms time interval following stimulus onset in our simulations. As seen in Fig 7 there is a strong *transient* component of the response with a peak in the PSTHs around 25 ms after stimulus onset while the generally much lower *sustained* (steady-state) response is reached around 100 ms after onset. This is in qualitative accordance with observations in flashing-spot experiments on cat RCs [26, 35, 51]. We thus next asked the question of whether triadic and axonal inhibition have differential effects on the transient and sustained responses of the RC.

In Fig 13 we compare area-response curves computed for the transient phase (0–100 ms after stimulus onset) to the sustained phase (400–500 ms after stimulus onset) for the same model examples as in Fig 8. Comparison of the (unnormalized) responses in the top row

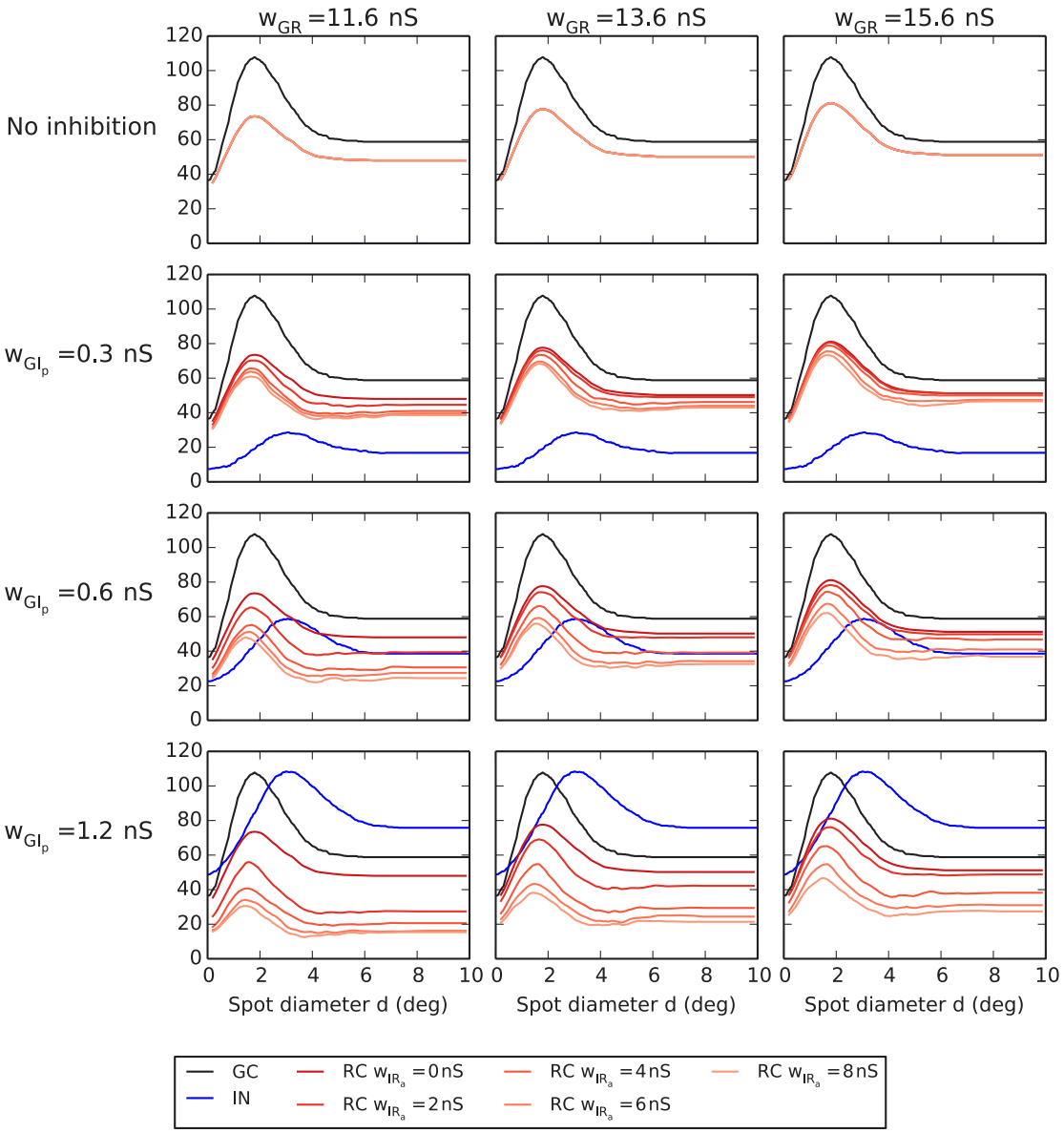

Fig 11. Area-response curves without triadic inhibition. Row 1: no inhibition. Rows 2–4: axonal inhibition for different synaptic weight values of proximal ganglion-cell input to the interneuron w_{GIp}. Black curves correspond to central retinal ganglion cell (GC), blue curves to interneuron (IN), and red/orange curves to relay cell (RC). The four RC curves in the panels in rows 2–4 correspond to w_{IRa} = 0/2/4/8 nS with w_{IRa} = 0 (no axonal inhibition) and w_{IRa} = 8 nS (maximal axonal inhibition) corresponding to the top and bottom of the four curves, respectively.

doi:10.1371/journal.pcbi.1004929.g011

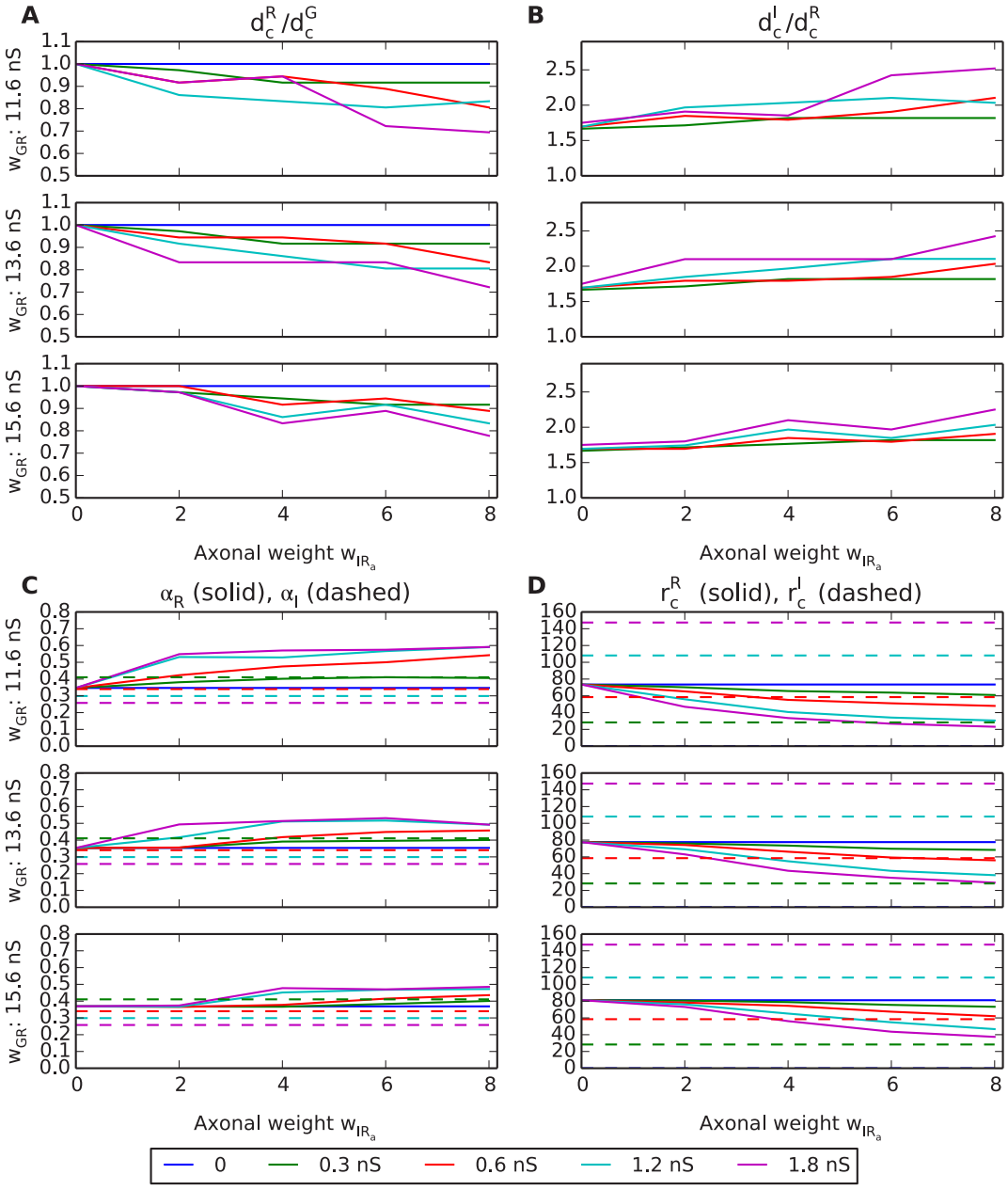

Fig 12. Summary of response measures from area-response curves without triadic inhibition. For explanation of panels, see caption of Fig 10.

doi:10.1371/journal.pcbi.1004929.g012

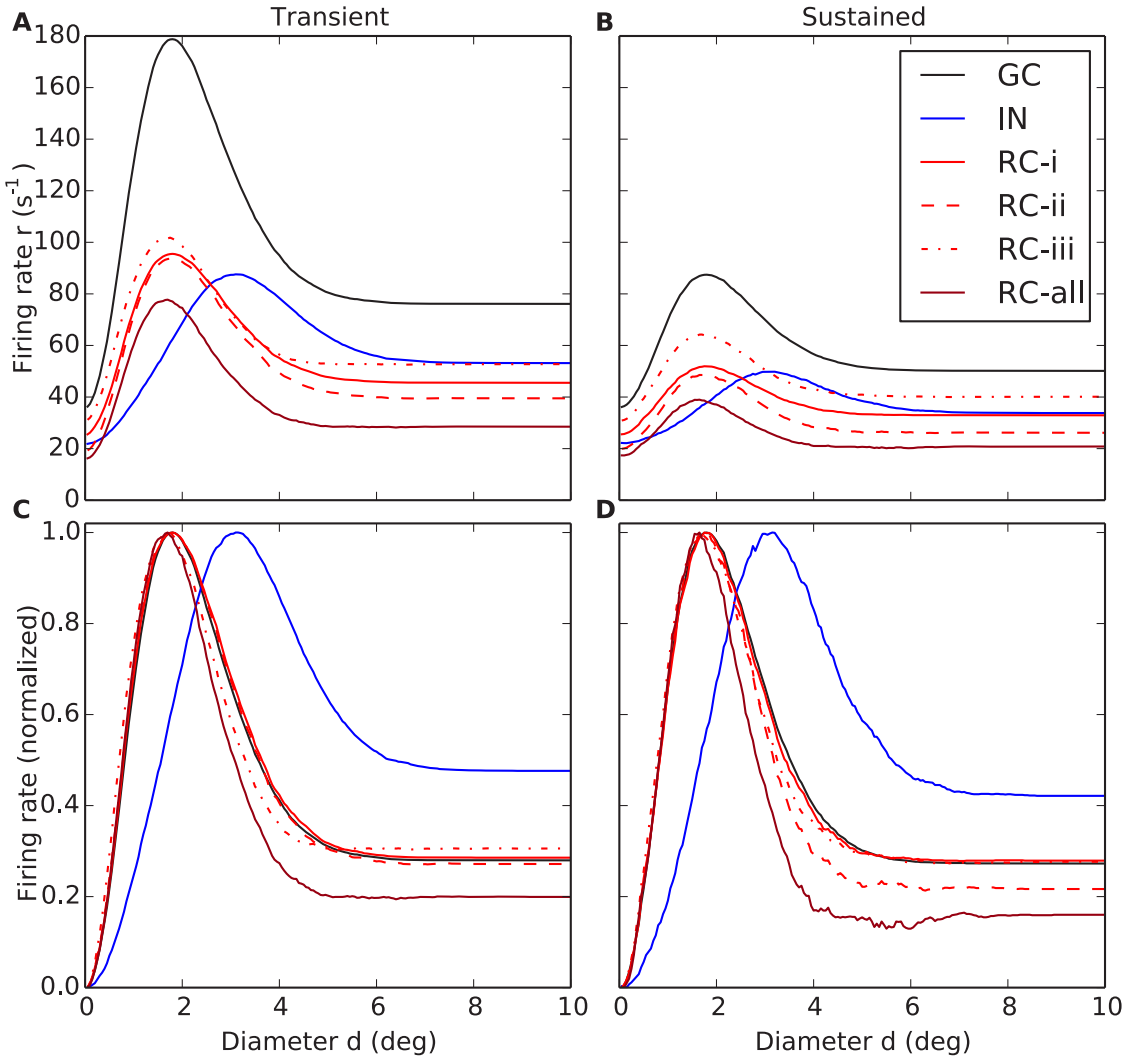

Fig 13. Area-summation curves for transient response and sustained response for relay-cells (RCs). (A–B) Trial-averaged spike-count firing rate vs. spot diameter, for central retinal ganglion cell (GC, solid black), interneuron (IN, solid blue), and relay cell (RC, red lines) for transient (A) and sustained responses (B). (C–D) Area-summation curves in A and B normalized to the maximum firing rate for each cell. The transient response corresponds to the trial-averaged spike-count firing rate for the first 100 ms after stimulus onset, while the sustained response corresponds to the averaged rate in the time interval from 400 to 500 ms after stimulus onset, cf. Fig 7. The depicted models examples are the same as in Fig 8: Red solid line: RC response for *direct triadic inhibition* (case (RC-i)) with $w_{IRt} = 4$ nS, $w_{Glp} = 0$, $w_{IRa} = 0$. Red dashed line: RC response for *direct & soma-driven triadic inhibition* (case (RC-ii)) with $w_{IRt} = 4$ nS, $w_{Glp} = 0.6$ nS, $w_{IRa} = 0$. Red dotted line: RC response for *axonal inhibition* (case (RC-iii)) with $w_{IRt} = 0$, $w_{Glp} = 0.6$ nS, $w_{IRa} = 4$ nS. Dark red line (RC-all) corresponds to results from all three types of inhibition combined, i.e., $w_{IRt} = 4$ nS, $w_{Glp} = 0.6$ nS, $w_{IRa} = 4$ nS. $w_{GR} = 15.6$ nS is used in all cases. Other parameters correspond to default values. Note that the depicted IN response does not apply to case (RC-i) as the IN is only synaptically activated at the triads in this case as $w_{Glp} = 0$. Note also that 500 trials, not the default value of 10 trials, were used to compute each depicted trial-averaged spike-count rate, and that no seven-point filtering was employed to smooth the area-summation curves.

doi:10.1371/journal.pcbi.1004929.g013

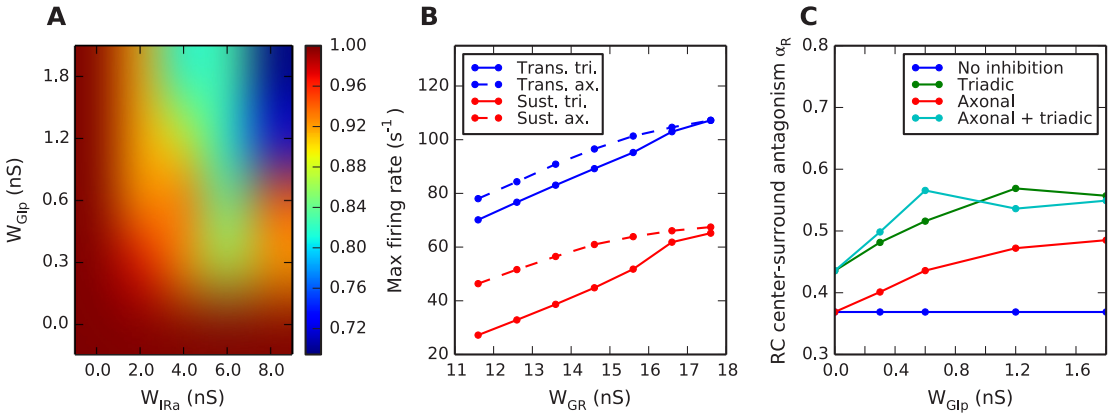

Fig 14. Summary of key results on different effects of triadic and axonal inhibition on relay-cell (RC) response. (A) Dependence of diameter of RC receptive-field center d_c^R on two key model parameters (w_{GIp}, weight of proximal excitation of the interneuron (IN); w_{IRa}, weight of axonal inhibition) for the case of axonal inhibition only (i.e., $w_{IRt} = 0$). For this example the diameter of the ganglion-cell receptive-field center d_c^S is fixed to 1.8 deg, and the retinogeniculate excitation is set to $w_{GR} = 11.6$ nS. (B) Transient and sustained RC responses for center-filling spots, corresponding to maximal responses in the area-response curves, for the cases of only triadic or only axonal inhibition. Dependence of maximal response on retinogeniculate excitation weight w_{GR} is depicted. Other parameters: $w_{IRa} = 4$ nS, $w_{GIp} = 0.6$ nS. (C) Dependence of center-surround antagonism, quantified by the coefficient α_{RC} (Eq 7), on w_{GIp}, the weight of the GC excitation of INs on the proximal dendrites. Dark-blue line: No inhibition, $w_{IRa} = w_{IRt} = 0$. Red line: Axonal inhibition only, $w_{IRt} = 0$, $w_{IRa} = 8$ nS. Green line: Triadic inhibition only, $w_{IRa} = 0$. Light-blue line: Both triadic and axonal inhibition, $w_{IRa} = 8$ nS. Retinogeniculate excitation is set to $w_{GR} = 15.6$ nS. In B and C simulation data points are marked with dots, and lines are added as a guide for the eye. Note that 500 trials, not the default value of 10 trials, were used to compute the depicted trial-averaged spike-count rate in panel B.

doi:10.1371/journal.pcbi.1004929.g014

demonstrates the large differences in firing rates, the transient response (panel A) being up to a factor two larger than the sustained response (panel B). For the present model examples, the triadic and axonal inhibition are seen to be roughly equally effective in dampening the RC response for the transient response for spots filling the receptive-field center (panel A). Interestingly, however, the triadic inhibition is seen to be more effective than axonal inhibition in dampening this response to center-filling spots for the sustained response. This feature is seen also for other values of retinogenculate excitation w_{GR} than the one used in this example, cf. Fig 14B.

Comparison of the normalized area-response curves (panels C and D in Fig 13) reveals only subtle differences in the area-response shapes. One observation is that soma-driven triadic inihibition seems slightly more effective in suppressing the sustained than the transient RC responses for the largest spot diameters.

For the sustained response we also observe in panel D a weak 'noisy' minimum in the response for spot diameters d around 5–6 degrees for the case with both triadic and axonal inhibition (RC-all), a feature not present for the transient response (panel C). This minimum stems from the strong activation of the INs for these spot sizes (cf. blue curve in panel D) compared to for the larger spot sizes, i.e., $d \sim 8$–10 degrees. While this feature of the IN response curve is also present for the transient response, it is slightly less so. The more prominent role of the combined triadic and axonal inhibition in modifying the receptive-field of the RC (compared to the GC) in the sustained response than in the transient response is also manifested by the slightly smaller receptive-field center size (d_c^R) and widths of the peak of the area-summation curves, cf. panels C and D in Fig 13.

Discussion

In the present modeling work we have investigated putative roles of triadic and axonal inhibition from dLGN interneurons (INs) on the visual response properties of dLGN relay cells (RCs) relaying visual information to cortex. Taking advantage of a recently developed biophysically detailed multicompartmental model for an IN, the study is the first investigating the effects of different inhibitory actions of INs, i.e., triadic inhibition due to dendrodendritic contacts between INs and RCs and standard axonal inhibition. The interplay of these two inhibitory pathways is expectedly essential for understanding the functional role of inhibition in the dLGN circuit [52, 53]. To compare with (i) *in vivo* data of responses to flashing spot stimuli for cat RC cells of the X-type [26] and (ii) previous firing-rate models of the dLGN circuits [27], we have focused on a minimal network motif consisting of five RCs, modeled as single-compartment neurons, receiving inhibition from a single multicompartmental IN. These dLGN neurons are in turn driven by spiking inputs from five neighbouring retinal ganglion cells (GCs).

As in [27] we have computed and investigated area-response curves for circular flashing spots and studied how the model ingredients and parameters affect their detailed shapes and features, in particular (i) the *receptive-field center size* d_c of RCs and INs, identified as the flashing spot diameter giving the largest spike-count firing-rate reponse, (ii) the *maximal firing rate* (occuring for spots exactly filling the receptive-field centers), and (iii) the *center-surround antagonism* α measuring the suppression of large-field responses compared to the maximal responses. A particular focus of our study has been the investigation of differential effects of triadic and axonal inhibition on the response properties of RCs, and key findings are summarized in Fig 14 and discussed below.

Triadic vs. axonal inhibition

Our model contains three distinct types of inhibition, (i) direct triadic inhibition, (ii) soma-driven triadic inhibition and (iii) axonal inhibition, each with putatively different inhibitory effects on the RCs.

Gain control vs. shaping of RC spatial receptive fields. One of the findings is the different roles played by direct triadic and axonal inhibition in shaping the spatial receptive fields of RCs. Direct triadic inhibition was found to essentially only provide a simple non-linear gain control of the conversion of input spikes to output spikes by RCs (cf. two top rows of Fig 9), with no qualitative changes on the shape of the area-response curve (cf. RC-i in Fig 8B). The receptive-field center size was unchanged compared to the no-inhibition situation, reflecting the assumed spatially local inhibitory action on a single dendritic branch.

Axonal inhibition, on the other hand, was found to have a substantial effect on the size of the receptive-field center: the larger the inhibition, the more the RC center size shrinks compared to the center size of the retinal ganglion cell (GC) providing the feedforward excitation, see, e.g., panel A of Fig 12. This shrinking follows from the larger receptive-field center size of the IN compared to the central GC [26, 27]. Thus the exact magnitude of the receptive-field shrinking will in our model depend on the parameter values for the proximal GC excitation of INs (w_{GIp}) and the weight of the axonal inhibition of the central RCs by the IN (w_{IRa}) as shown in Fig 14A. These results for the ratio d_c^R/d_c^G show that the product of these two model parameters is a good predictor of the receptive-field shrinkage resulting from axonal inhibition.

As soma-driven triadic inhibition is activated by the same IN action potentials that drive axonal inhibition, this type of triadic inhibition will also contribute to the shrinking of the RC receptive-field center. This is for example observed for the example with both direct and soma-

driven triadic in Fig 8B (RC-ii) where the receptive-field center is smaller than for direct triadic inhibition only (RC-i) (but larger than for axonal inhibition only, RC-iii).

Thus, a possible role of the different inhibitory actions from INs to RCs in the dLGN circuit is to provide separate mechanisms for affecting gain control only (direct triadic inhibition) and regulation of receptive-field center size (axonal inhibition, soma-driven inhibition) of visual signals sent to cortex. A smaller receptive-field center size suggests higher spatial resolution, but see [54].

Center-surround antagonism. The center-surround inhibition has been observed to be larger for LGN RCs compared to the retinal GCs driving them, see [26] and references therein. Both triadic and axonal inhibition contribute to increasing the RC center-surround antagonism compared to GC input, but triadic inhibition was found to be the most efficient mechanism in doing so. This is further illustrated in Fig 14C where we compare the center-surround antagonism coefficient α_R measuring the dampening effect of the inhibitory surround on the RC response compared to the maximal RC response (Eq 7). With axonal inhibition only, α_R increases from the no-inhibition value of 0.37 to 0.49 found for the maximal values considered for w_{GIp} (1.8 nS) and w_{IRa} (8 nS) in this study. With direct triadic inhibition only (i.e., triadic-inhibition curve for $w_{GIp} = 0$), α_R is at a modest value of 0.44. With soma-driven triadic inhibition included as well (i.e., triadic-inhibition curve for $w_{GIp}>0$), α_R gradually increases with increasing excitation of the IN (i.e., increasing value for w_{GIp}) up to a maximum value of α_R = 0.56. Interestingly, addition of axonal inhibition on top of this triadic inhibition is seen in Fig 14C to have little effect on the total value of α_R, even with our maximum weight for the inhibition of the RC (w_{IRa} = 8 nS). Thus while direct triadic inhibition alone is seen to be sufficient to assure some extra centre-surround inhibition, the addition of soma-driven triadic inhibition increases α_R, substantially. Note, however, that the model example in Fig 14C has a fairly strong retinogeniculate excitation, i.e., w_{GR} = 15.6 nS. For weaker retinogeniculate excitation, e.g., w_{GR} = 11.6 nS, we observed in Fig 10C that direct triadic inhibition alone was sufficient to provide a large value of center-surround antagonism.

Transient vs. sustained response. Another difference between the effects of axonal and triadic inhibitions were observed when comparing area-response curves computed for the transient phase (0–100 ms after stimulus onset) with corresponding responses in the sustained phase (400–500 ms after stimulus onset) (Fig 8). As found for the example in Fig 13, triadic inhibition seems, compared to axonal inhibition, to be particularly efficient in inhibiting the sustained RC response. As demonstrated in Fig 14B this is also observed for other values of retinogeniculate excitation, parameterized in our model by w_{GR}, and is particularly prominent for weaker excitation. Here the maximum RC response, i.e., occurring for spots filling the receptive-field center, is shown both for the transient and sustained responses for different values of the retinogeniculate excitation w_{GR}. Only the cases with direct triadic inhibition or axonal inhibition (cases (RC-i) and (RC-iii)) are considered. For all values of w_{GR} less than 15.6 nS, the value used in the example in Fig 13, we see that the reduction of the sustained response compared to the transient response is particularly prominent for the case with triadic inhibition only.

Timing of inhibitory action. Direct triadic inhibition where time-locked dendrodendritic inhibition occurs due to the same GC spike that provides the excitatory input, was the fastest-acting of the three types of inhibition presently considered. Both soma-driven triadic and axonal inhibition follow only after the generation of IN action potentials which, in our model, required multiple simultaneously arriving GC spikes at the proximal dendrites of the IN. Following this simultaneous input volley it took in our model on the order of ten milliseconds for the action potential occur, a time lag mainly set by the time needed to activate the calcium currents involved in driving the neuron above the action-potential initiation threshold. Thus

effects both from soma-driven triadic and axonal inhibition are substantially delayed compared to putative excitatory effects of the same GC input spikes. In our model the time constant of activation of the axonal inhibition was on the order of 1 ms (cf. Table 3), much shorter than the time it takes for the IN action potential to backpropagate from the IN soma to the triad and activate soma-driven triadic inhibition (∼ 5 ms, cf. Fig 5). Thus axonal inhibition was a faster mode of inhibition than soma-driven triadic inhibition in our model.

Role of soma-driven inhibition. Finally, it should be noted that of the three types of inhibition, soma-driven triadic inhibition is both conceptually and biophysically less understood than the two others: Although somatically elicited APs in INs are known to successfully invade distal dendrites [37], it has still not been proven that they actually do trigger dendritic GABA release directly, although this seems likely [41]. It might nevertheless be that the key role of soma-controlled dendritic signals is to regulate the release probability, e.g., via the activation of local dendritic NMDA receptors [41] or metabotropic glutamate receptors [42]. These mechanisms were not included in the current model, and more experimental studies are clearly needed to constrain this aspect of the model.

Future model applications and extensions

We consider the present investigation to be only the first of several applications of the present modeling approach. Until recently, dLGN circuit models lacked a key ingredient, namely an IN model incorporating the key dual-action inhibitory features of this cell type. With the arrival of the first multicompartmental dual-action IN model [24], we can now, with the combined use of existing (single-compartment) Hodgkin-Huxley type models for relay cells (see [55] for an overview), investigate dLGN circuitry in models at a new level of biological realism. This will not only enable elucidation of the role of dLGN circuitry in shaping spatial response features like here, but also the key role played by the circuit in temporal processing of the incoming spike trains from retina [39, 52]. Below we discuss various directions where the present modeling approach should be considered.

Brain state—tonic vs. bursty spiking. The neurons in the dLGN receive modulatory input from other parts of the brain which, among other things, may cause the dLGN circuit to shift between drowsy and attentive cognitive states [56, 57]. Such state-regulating modulation can shift the resting membrane potential of both RCs and INs, which in turn can switch the firing mode of these neurons between tonic and bursty [13, 39, 56–60]. In the current study, our RC and IN models were based on data from RC and IN neurons that both rested on relatively depolarized membrane potentials (–60 mV and –63 mV, respectively) and were characterized by tonic response modes, cf. Fig 2. One obvious step in future investigations would be to explore how the conclusions we arrived at in the current work depend on the processing state of the dLGN.

Firing regime and receptor activation. The signal processing in the dLGN depends in non-trivial manners on external conditions. In [14], the author distinguishes between two input regimes in the dLGN: (i) a low-input regime (low GC firing frequency), where the glutamatergic input to relay cells and INs is thought to be primarily mediated by AMPA receptors, and (ii) a high-input regime that also triggers the slower NMDA and metabotropic glutamate receptors (mGluRs). Although recent experiments have indicated that a sharp distinction between low and high-input regimes may be questionable [61], it is still likely that the input intensity determines which receptor subtype that dominates in generating the dLGN response. Our model was adapted to experimental data where the observed IN and RC responses were found not to depend on mGluR-activation [15, 41]. The model predictions are therefore expectedly most valid for signal processing in the low-input regime. However, mGluR

activation could have numerous additional effects on the signal processing in the dLGN [12, 42, 61–63], and a natural step in future investigations would be to investigate effects of mGluR activation in the current model.

A subclass of RC cells, the so-called *lagged* cells, has been found to have delayed visual-response onset and an initial suppression of response until it reaches a maintained firing level [5], contrasting the fast and strong transient response found for the presently studied non-lagged cells, cf. the PSTHs in panels C and D in Fig 7. This property has been linked to dominance of NMDA receptors over AMPA receptors at the excitatory part of the retinogeniculate synapse [64]. Again, the effect of various combinations of these ionotropic glutamate receptors at this synapse could directly be studied in a modified version of our model.

Retinal input. In the present model application we have focused on the situation with a single dominant retinal GC input to each RC as in the analogous firing-rate based model in [27]. RCs receiving input from multiple GCs have also been observed [7, 8]. However, our present model assumption of a single GC input naturally accounts for the experimental observation that the receptive-field centers for the RCs typically have similar or smaller sizes than those of the GCs (as measured by S-potentials) [26]. With strong inputs from several spatially displaced GCs, the receptive-field centers of the RCs would instead be larger than those of the GCs and thus at odds with the experimental data set on which the present version of the model is tuned. The study of the effect of having multiple GC inputs would be a natural future application [65], as would the study of the effect of having a set of discrete units describing the receptive field of the GC rather than the circularly symmetric DOG model [66].

Further, the present retinal input was described by a spatiotemporally separable filter model, i.e., the spatiotemporal GC receptive field was assumed to be described by a spatial function (in this case a DOG-model [36]) multiplied by a temporal function. However, several studies have demonstrated receptive fields in the GCs driving the LGN which are non-separable in space and time [51, 67, 68]. In [35] a new non-separable spatiotemporal receptive-field model, consisting of a sum of a transient and sustained component, was derived based on high-resolution, time-resolved area-summation curves for LGN RCs from [51]. As qualitatively similar area-summation curves was observed for the GC input, a future project would be to explore the LGN circuit response to GC input described by such non-separable filter models.

In our model application we have also assumed a (time-modulated) Poissonian distribution of the incoming GC spikes. Experimental recordings have revealed a more regular spike-train input than Poissionian [48, 69, 70]. The effect of this regularity could be investigated by considering input GC spike trains instead obeying a gamma-process statistics, as in the model study of [50].

Feedback from cortex and thalamic reticular nucleus (TRN). Both RCs and INs receive excitatory feedback from cortex, both via ionotropic and metabotropic receptors, and inhibitory feedback from the GABAergic neurons in the thalamic reticular nucleus [11, 39, 71–74]. The effect of the feedback on circuit behaviour will likely depend strongly on whether the feedback arrives on distal dendrites or close to the soma. This is again a question that can be directly investigated with a network model of the present type including a spatially extended multicompartment IN model incorporating both triadic and axonal actions.

Local dendritic processing is particularly important in the electrotonically extensive INs [28], but recent experiments have indicated it also plays an important role in processing cortical input to distal RC dendrites [75]. In the current study, we explored the LGN response to retinal input, and kept a particular focus on the processing by the triadic synapse which tends to be located distally at IN dendrites and proximally at RC dendrites. We therefore used an extensive, multicompartmental IN model, while we assumed that a single-compartment model was sufficient for the (generally more compact [28]) RC. However, to properly explore modulatory

input to LGN arriving at distal dendritic sites, it is likely that our model should be expanded to include a more comprehensive, multicompartmental model also for the RCs (see, e.g., [23]).

Synaptic plasticity. The present model assumes static synapses while *in vitro* studies have demonstrated short-term synaptic plasticity throughout the circuit. The feedforward excitatory synapse from GCs to RCs has been found to be short-term depressing [76] as has the feedback excitatory synapse from cortical cells to INs [73]. In contrast, the feedback excitatory synapse from cortical cells to RCs is short-term facilitating [77]. This suggests the possibility for interesting and varied dynamics in the dLGN circuit, a dynamics that likely will require detailed circuit modeling to unravel.

'Same-sign' vs. 'push-pull' inhibition. In the present model the IN has been assumed to receive GC input with symmetry of the 'same sign', i.e., ON or OFF, as the RC it inhibits. For the direct triadic input this 'same-sign' follows directly, but it is also possible that the proximal synaptic input to the IN which drive the generation of IN action potentials, has the opposite 'push-pull' symmetry [6, 78]. If so, the axonal inhibition (as well as the soma-driven triadic inhibition) from the IN onto the RC will have the opposite symmetry compared to the excitatory input to the RC from the GC, an arrangement suggested in [53, 65, 79]. While this arrangement seems difficult to reconcile with the observed shrinking of the RC receptive-field center compared to the GC input [26, 27], the consequences of driving IN action-potential firing with proximal GC inputs with opposite or mixed symmetries (cf. [65]), should also be explored in a model of our type.

Outlook

The present model is based on data from several animal species: the target RC and GC area-response curves are from cat dLGN [26, 27], the RC single-compartment neuron model was developed to investigate network dynamics in ferret slices [29], while the multicompartment IN model is based on data from mice [24]. Main features of thalamic physiology seem to be well conserved across species [52]. However, the applicability of the present 'chimeric' model to account for data from different species is presently unknown, in particular since different arrangements of the LGN circuit elements may give very different signal-transformation properties [65, 78]. This will have to be explored by comparison of model predictions with experimental data from the various species.

With the advent of ever more sophisticated techniques for controlling gene expression in mice (accompanied by the possibility for optogenetic activation [80]), the mouse dLGN has emerged as a particularly interesting model system [52]. The full mouse dLGN has only about 18.000 neurons, so network simulations of a sizable fraction of the visual field is feasible with present-day computers. However, 'no nucleus is an island' [52], and a comprehensive understanding of the function of the dLGN circuit likely also will require simultaneous modeling of the primary visual cortex (with 360.000 neurons [81]) and maybe also other brain areas. Such modeling of the visual thalamocortical system in mice can be facilitated by joint application of models at different levels of resolution. In the present model, for example, the GC input was modeled by means of stochastically generated spike trains obeying spatiotemporal probability distributions found from descriptive firing-rate models. The RC cells were modeled as single-compartment Hodgkin-Huxley type neuron models producing spikes, but the connection to the previous firing-rate model of the same system [27] was apparent as very similar trial-averaged area-response curves were produced. In the same vein one could envision modeling the effects of cortical feedback to the dLGN circuit by means of firing-rate models for populations of cortical cells feeding back to spiking network models in the dLGN (rather than firing-rate models [74]). With a comprehensive mapping of the physiological and anatomical properties

of the cells (and their connections) in mouse dLGN and visual cortex on the way [81, 82], the time seems ripe for comprehensive efforts to finally build mechanistic models mimicking signal processing in the dLGN.

Acknowledgments

We thank Hans Ekkehard Plesser, Paul Heggelund, Marianne Fyhn, Torkel Hafting, Milad Mobarhan and Pablo Martinez-Cañada for very useful inputs and discussions.

Author Contributions

Conceived and designed the experiments: TH EH GH GTE. Performed the experiments: TH EH. Analyzed the data: TH EH. Contributed reagents/materials/analysis tools: TH EH GH GTE. Wrote the paper: TH EH GH GTE.

References

1. Sherman S, Guillery R. Exploring the Thalamus. New York: Academic; 2001.
2. Cleland BG, Dubin MW, Levick WR. Sustained and transient neurones in cat's retina and lateral geniculate nucleus. Journal of Physiology. 1971; 217:473–496. doi: 10.1113/jphysiol.1971.sp009581 PMID: 5097609
3. Coenen AML, Vendrik AJH. Determination of the transfer ratio of cat's geniculate neurons through quasi-intracellular recordings and the relation with the level of alertness. Experimental Brain Research. 1972; 14:227–242. doi: 10.1007/BF00816160 PMID: 4340696
4. Cleland BG, Lee BB. A comparison of visual responses of cat lateral geniculate nucleus neurones with those of ganglion cells afferent to them. Journal of Physiology. 1985; 369:249–268. doi: 10.1113/jphysiol.1985.sp015899 PMID: 4093882
5. Mastronarde DN. Two classes of single-input X-cells in cat lateral geniculate nucleus. I. Receptive-field properties and classification of cells. Journal of Neurophysiology. 1987; 57:357–380. PMID: 3559684
6. Mastronarde DN. Two classes of single-input X-cells in cat lateral geniculate nucleus. II. Retinal inputs and the generation of receptive-field properties. Journal of Neurophysiology. 1987; 57:381–413. PMID: 3559685
7. Mastronarde DN. Non-lagged relay cells and interneurons in the cat lateral geniculate nucleus:Receptive field properties and retinal inputs. Visual Neuroscience. 1992; 8:407–441. doi: 10.1017/S0952523800004934 PMID: 1586644
8. Usrey WM, Reppas JB, Reid RC. Specificity and strength of retinogeniculate connections. J Neurophysiol. 1999 Dec; 82(6):3527–3540. PMID: 10601479
9. Dubin MW, Cleland BG. Organization of visual inputs to interneurons of lateral geniculate nucleus of the cat. J Neurophysiol. 1977 Mar; 40(2):410–427. PMID: 191574
10. Murphy PC, Sillito AM. Corticofugal feedback influences the generation of length tuning in the visual pathway. Nature. 1987; 329(6141):727–729. doi: 10.1038/329727a0 PMID: 3670375
11. Briggs F, Usrey WM. Emerging views of corticothalamic function. Curr Opin Neurobiol. 2008 Aug; 18(4):403–407. doi: 10.1016/j.conb.2008.09.002 PMID: 18805486
12. Cox CL, Zhou Q, Sherman SM. Glutamate locally activates dendritic outputs of thalamic interneurons. Nature. 1998 Jul; 394(6692):478–482. doi: 10.1038/28855 PMID: 9697770
13. Zhu J, Heggelund P. Muscarinic regulation of dendritic and axonal outputs of rat thalamic interneurons: a new cellular mechanism for uncoupling distal dendrites. J Neurosci. 2001 Feb; 21(4):1148–1159. PMID: 11160385
14. Sherman SM. Interneurons and triadic circuitry of the thalamus. Trends Neurosci. 2004 Nov; 27(11):670–675. doi: 10.1016/j.tins.2004.08.003 PMID: 15474167
15. Blitz DM, Regehr WG. Timing and specificity of feed-forward inhibition within the LGN. Neuron. 2005 Mar; 45(6):917–928. doi: 10.1016/j.neuron.2005.01.033 PMID: 15797552
16. Crandall SR, Cox CL. Local Dendrodendritic Inhibition Regulates Fast Synaptic Transmission in Visual Thalamus. Journal of Neuroscience. 2012 Feb; 32(7):2513–2522. Available from: http://www.jneurosci.org/cgi/doi/10.1523/JNEUROSCI.4402-11.2012. doi: 10.1523/JNEUROSCI.4402-11.2012 PMID: 22396424

17. Rose RM, Hindmarsh JL. A model of a thalamic neuron. Proceedings of the Royal Society of London Series B, Containing papers of a Biological character Royal Society (Great Britain). 1985 Aug; 225(1239):161–93. Available from: http://www.ncbi.nlm.nih.gov/pubmed/19285053. doi: 10.1098/rspb.1985.0057

18. McCormick DA, Huguenard JR. A model of the electrophysiological properties of thalamocortical relay neurons. J Neurophysiol. 1992; 68(4):1384–1400. Available from: http://jn.physiology.org/content/68/4/1384.long. PMID: 1331356

19. Destexhe A, Babloyantz A, Sejnowski TJ. Ionic mechanisms for intrinsic slow oscillations in thalamic relay neurons. Biophys J. 1993; 65(4):1538–1552. doi: 10.1016/S0006-3495(93)81190-1 PMID: 8274647

20. Antal M, Acuna-Goycolea C, Pressler RT, Blitz DM, Regehr WG, Antal K, et al. Model of a thalamocortical neurone with dendritic voltage-gated ion channels. Neuroreport. 1997 Mar; 8(4):1063–1066. PMID: 9141093

21. Destexhe A, Neubig M, Ulrich D, Huguenard J. Dendritic low-threshold calcium currents in thalamic relay cells. J Neurosci. 1998; 18(10):3574–3588. Available from: http://www.jneurosci.org/content/18/10/3574. PMID: 9570789

22. Emri Z, Antal K, Crunelli V. The impact of corticothalamic feedback on the output dynamics of a thalamocortical neurone model: the role of synapse location and metabotropic glutamate receptors. Neuroscience. 2003; 117(1):229–239. doi: 10.1016/S0306-4522(02)00759-5 PMID: 12605909

23. Rhodes PA, Llinás R. A model of thalamocortical relay cells. J Physiol. 2005 Jun; 565(Pt 3):765–781. doi: 10.1113/jphysiol.2004.070888 PMID: 15613378

24. Halnes G, Augustinaite S, Heggelund P, Einevoll GT, Migliore M. A Multi-Compartment Model for Interneurons in the Dorsal Lateral Geniculate Nucleus. PLoS Computational Biology. 2011; 7(9). doi: 10.1371/journal.pcbi.1002160 PMID: 21980270

25. DeAngelis GC, Ohzawa I, Freeman RD. Receptive-field dynamics in the central visual pathways. Trends Neurosci. 1995; 18:451–458. doi: 10.1016/0166-2236(95)94496-R PMID: 8545912

26. Ruksenas O, Fjeld IT, Heggelund P. Spatial summation and center-surround antagonism in the receptive field of single units in the dorsal lateral geniculate nucleus of cat: comparison with retinal input. Vis Neurosci. 2000; 17(6):855–870. Available from: http://journals.cambridge.org/abstract_S0952523800176059. doi: 10.1017/S0952523800176059 PMID: 11193102

27. Einevoll GT, Heggelund P. Mathematical models for the spatial receptive-field organization of nonlagged X-cells in dorsal lateral geniculate nucleus of cat. Vis Neurosci. 2000; 17(6):871–885. Available from: http://arken.umb.no/~gautei/forskning/einevoll-2000b.pdf. doi: 10.1017/S0952523800176060 PMID: 11193103

28. Bloomfield SA, Sherman SM. Dendritic current flow in relay cells and interneurons of the cat's lateral geniculate nucleus. Proc Natl Acad Sci U S A. 1989; 86(10):3911–3914. Available from: http://www.ncbi.nlm.nih.gov/pmc/articles/PMC287251/. doi: 10.1073/pnas.86.10.3911 PMID: 2542955

29. Destexhe A, Bal T, McCormick DA, Sejnowski TJ. Ionic mechanisms underlying synchronized oscillations and propagating waves in a model of ferret thalamic slices. J Neurophysiol. 1996 Sep; 76(3):2049–2070. Available from: http://www.ncbi.nlm.nih.gov/pubmed/8890314. PMID: 8890314

30. Niebur E. Neuronal cable theory. Scholarpedia. 2008; 3(5):2674. revision #121893. doi: 10.4249/scholarpedia.2674

31. Carnevale NT, Hines ML. The NEURON Book. Cambridge University Press; 2006.

32. Carnevale T. Neuron simulation environment. Scholarpedia. 2007; 2(6):1378. revision #91576. doi: 10.4249/scholarpedia.1378

33. Hines ML, Davison AP, Muller E. NEURON and Python. Front Neuroinform. 2009; 3:1. doi: 10.3389/neuro.11.001.2009 PMID: 19198661

34. Hines ML, Morse T, Migliore M, Carnevale NT, Shepherd GM. ModelDB: A Database to Support Computational Neuroscience. J Comput Neurosci. 2004; 17(1):7–11. doi: 10.1023/B:JCNS.0000023869.22017.2e PMID: 15218350

35. Einevoll GT, Jurkus P, Heggelund P. Coarse-to-fine changes of receptive fields in lateral geniculate nucleus have a transient and a sustained component that depend on distinct mechanisms. PLoS One. 2011; 6(9):e24523. doi: 10.1371/journal.pone.0024523 PMID: 21931739

36. Rodieck RW. Quantitative analysis of cat retinal ganglion cell response to visual stimuli. Vision Research. 1965; 5:583–601. doi: 10.1016/0042-6989(65)90033-7 PMID: 5862581

37. Casale AE, McCormick DA. Active Action Potential Propagation But Not Initiation in Thalamic Interneuron Dendrites. Journal of Neuroscience. 2011 Dec; 31(50):18289–18302. Available from: http://www.jneurosci.org/cgi/doi/10.1523/JNEUROSCI.4417-11.2011. doi: 10.1523/JNEUROSCI.4417-11.2011 PMID: 22171033

38. Allken V, Chepkoech JL, Einevoll GT, Halnes G. The subcellular distribution of T-type Ca2+ channels in interneurons of the lateral geniculate nucleus. PLoS One. 2014; 9(9):e107780. doi: 10.1371/journal.pone.0107780 PMID: 25268996

39. Sherman SM. Tonic and burst firing: dual modes of thalamocortical relay. Trends Neurosci. 2001 Feb; 24(2):122–126. doi: 10.1016/S0166-2236(00)01714-8 PMID: 11164943

40. Roth A, van Rossum MCW. Modeling synapses. In: De Schutter E, editor. Computational Modeling Methods for Neuroscientists. 1st ed. MIT Press, Cambridge, MA; 2009. p. 139–159. Available from: http://mitpress.mit.edu/books/computational-modeling-methods-neuroscientists.

41. Acuna-Goycolea C, Brenowitz SD, Regehr WG. Active dendritic conductances dynamically regulate GABA release from thalamic interneurons. Neuron. 2008 Feb; 57(3):420–31. Available from: http://www.ncbi.nlm.nih.gov/pubmed/18255034. doi: 10.1016/j.neuron.2007.12.022 PMID: 18255034

42. Cox CL, Sherman SM. Control of dendritic outputs of inhibitory interneurons in the lateral geniculate nucleus. Neuron. 2000 Sep; 27(3):597–610. doi: 10.1016/S0896-6273(00)00069-6 PMID: 11055441

43. Dayan P, Abbott L. Theoretical Neuroscience. The MIT Press; 2001.

44. Langtangen HP. A Primer on Scientific Programming with Python. Mathematics and Statistics. Springer-Verlag Berlin Heidelberg; 2009. Available from: http://books.google.no/books?id=cVof07z_rA4C.

45. Lindén H, Hagen E, Łęski S, Norheim ES, Pettersen KH, Einevoll GT. LFPy: A tool for biophysical simulation of extracellular potentials generated by detailed model neurons. Frontiers in Neuroinformatics. 2014; 7(41):41. Available from: http://www.frontiersin.org/neuroinformatics/10.3389/fninf.2013.00041/abstract. doi: 10.3389/fninf.2013.00041 PMID: 24474916

46. Gewaltig MO, Diesmann M. NEST (NEural Simulation Tool). Scholarpedia. 2007; 2(4):1430. Revision #130182. doi: 10.4249/scholarpedia.1430

47. Muller E, Davison AP, Brizzi T, Bruederle D, Eppler JM, Kremkow J, et al. NeuralEnsemble.Org: Unifying neural simulators in Python to ease the model complexity bottleneck. In: Frontiers in Neuroscience Conference Abstract: Neuroinformatics 2009; 2009. p. –.

48. Casti A, Hayot F, Xiao Y, Kaplan E. A simple model of retina-LGN transmission. Journal of computational neuroscience. 2008; 24(2):235–252. doi: 10.1007/s10827-007-0053-7 PMID: 17763931

49. Carandini M, Horton JC, Sincich LC. Thalamic filtering of retinal spike trains by postsynaptic summation. Journal of Vision. 2007; 7(14):20. doi: 10.1167/7.14.20 PMID: 18217815

50. Heiberg T, Kriener B, Tetzlaff T, Casti A, Einevoll G, Plesser H. Firing-rate models capture essential response dynamics of LGN relay cells. J Comp Neurosci. 2013; 35:359–375. doi: 10.1007/s10827-013-0456-6

51. Ruksenas O, Bulatov A, Heggelund P. Dynamics of spatial resolution of single units in the lateral geniculate nucleus of cat during brief visual stimulation. J Neurophysiol. 2007 Feb; 97(2):1445–1456. doi: 10.1152/jn.01338.2005 PMID: 16914606

52. Scrubb MS. Physiology of the mouse dorsal lateral geniculate nucleus. In: Chalupa LM, Williams RW, editors. Eye, retina, and visual system of the mouse. MIT Press; 2008. p. 219–232.

53. Wang X, Sommer FT, Hirsch JA. Inhibitory circuits for visual processing in thalamus. Curr Opin Neurobiol. 2011 Oct; 21(5):726–733. doi: 10.1016/j.conb.2011.06.004 PMID: 21752634

54. Foffani G, Chapin JK, Moxon KA. Computational role of large receptive fields in the primary somatosensory cortex. J Neurophysiol. 2008 Jul; 100(1):268–280. doi: 10.1152/jn.01015.2007 PMID: 18400959

55. Einevoll GT, Halnes G. Lateral Geniculate Nucleus (LGN) Models. In: Jaeger D, Jung R, editors. Encyclopedia of Computational Neuroscience. Springer; 2014. p. 1–7.

56. Sherman SM. Dual response modes in lateral geniculate neurons: mechanisms and functions. Vis Neurosci. 1996; 13(2):205–213. Available from: http://www.ncbi.nlm.nih.gov/pubmed/8737271. doi: 10.1017/S0952523800007446 PMID: 8737271

57. McCormick DA, Bal T. Sleep and arousal: thalamocortical mechanisms. Annu Rev Neurosci. 1997; 20:185–215. doi: 10.1146/annurev.neuro.20.1.185 PMID: 9056712

58. McCormick DA, Pape HC. Acetylcholine inhibits identified interneurons in the cat lateral geniculate nucleus. Nature. 1988 Jul; 334(6179):246–248. doi: 10.1038/334246a0 PMID: 3398922

59. Zhu JJ, Lytton WW, Xue JT, Uhlrich DJ. An intrinsic oscillation in interneurons of the rat lateral geniculate nucleus. J Neurophysiol. 1999 Feb; 81(2):702–711. Available from: http://www.ncbi.nlm.nih.gov/pubmed/10036271. PMID: 10036271

60. Antal M, Acuna-Goycolea C, Pressler RT, Blitz DM, Regehr WG. Cholinergic activation of M2 receptors leads to context-dependent modulation of feedforward inhibition in the visual thalamus. PLoS Biol. 2010; 8(4):e1000348. doi: 10.1371/journal.pbio.1000348 PMID: 20386723

61. Pressler RT, Regehr WG. Metabotropic Glutamate Receptors Drive Global Persistent Inhibition in the Visual Thalamus. Journal of Neuroscience. 2013 Feb; 33(6):2494–2506. Available from: http://www.jneurosci.org/cgi/doi/10.1523/JNEUROSCI.3458-12.2013. doi: 10.1523/JNEUROSCI.3458-12.2013 PMID: 23392677

62. Govindaiah G, Cox CL. Metabotropic glutamate receptors differentially regulate GABAergic inhibition in thalamus. J Neurosci. 2006 Dec; 26(52):13443–13453. doi: 10.1523/JNEUROSCI.3578-06.2006 PMID: 17192427

63. Errington AC, Giovanni GD, Crunelli V, Cope DW. mGluR control of interneuron output regulates feed-forward tonic GABAA inhibition in the visual thalamus. J Neurosci. 2011 Jun; 31(23):8669–8680. doi: 10.1523/JNEUROSCI.0317-11.2011 PMID: 21653871

64. Heggelund P, Hartveit E. Neurotransmitter receptors mediating excitatory input to cells in the cat lateral geniculate nucleus. I. Lagged cells. Journal of Neurophysiology. 1990; 63:1347–1360. PMID: 2162923

65. Martinez LM, Molano-Mazón M, Wang X, Sommer FT, Hirsch JA. Statistical wiring of thalamic receptive fields optimizes spatial sampling of the retinal image. Neuron. 2014 Feb; 81(4):943–956. doi: 10.1016/j.neuron.2013.12.014 PMID: 24559681

66. Martin PR, Grünert U. Ganglion cells in mammalian retinae. In: Chupra LM, Werner JS, editors. The Visual Neurosciences. vol. 1. MIT (Bradford); 2004. p. 410–421.

67. Dawis S, Shapley R, Kaplan E, D T. The receptive field organization of X-cells in the cat: Spatiotemporal coupling and asymmetry. Vision Research. 1984; 24:549–564. doi: 10.1016/0042-6989(84)90109-3 PMID: 6740975

68. Frishman LJ, Freeman AW, Troy JB, E STD, Enroth-Cugell C. Spatiotemporal frequency responses of cat retinal ganglion cells. Journal of General Physiology. 1987; 89:599–628. doi: 10.1085/jgp.89.4.599 PMID: 3585279

69. Troy JB, Einstein G, Schuurmans RP, Robson JG, Enroth-Cugell C. Steady discharges of X and Y retinal ganglion cells of cat under photopic illuminance. Visual Neuroscience. 1992; 9:535–553. doi: 10.1017/S0952523800001784 PMID: 1450106

70. Victor JD. Temporal aspects of neural coding in the retina and lateral geniculate nucleus. Network: Comput Neural Syst. 1999; 10:R1–R66. doi: 10.1088/0954-898X_10_4_201

71. Cudeiro J, Sillito AM. Looking back: corticothalamic feedback and early visual processing. Trends Neurosci. 2006 Jun; 29(6):298–306. doi: 10.1016/j.tins.2006.05.002 PMID: 16712965

72. Wang W, Jones HE, Andolina IM, Sillito AM. Functional alignment of feedback effects from visual cortex to thalamus. Nature Neurosci. 2006; 9:1330–1336. doi: 10.1038/nn1768 PMID: 16980966

73. Augustinaite S, Yanagawa Y, Heggelund P. Cortical feedback regulation of input to visual cortex: role of intrageniculate interneurons. The Journal of physiology. 2011 Jun; 589(Pt 12):2963–77. Available from: http://www.ncbi.nlm.nih.gov/pubmed/21502287. doi: 10.1113/jphysiol.2011.205542 PMID: 21502287

74. Einevoll GT, Plesser HE. Extended difference-of-Gaussians model incorporating cortical feedback for relay cells in the lateral geniculate nucleus of cat. Cognitive Neurodynamics. 2012; 6:307–324. doi: 10.1007/s11571-011-9183-8 PMID: 24995047

75. Augustinaite S, Kuhn B, Helm PJ, Heggelund P. NMDA spike/plateau potentials in dendrites of thalamocortical neurons. J Neurosci. 2014 Aug; 34(33):10892–10905. doi: 10.1523/JNEUROSCI.1205-13.2014 PMID: 25122891

76. Kielland A, Heggelund P. AMPA and NMDA currents show different short-term depression in the dorsal lateral geniculate nucleus of the rat. J Physiol. 2002 Jul; 542(Pt 1):99–106. doi: 10.1113/jphysiol.2002.019240 PMID: 12096054

77. Lindström S, Wróbel A. Frequency dependent corticofugal excitation of principal cells in the cat's dorsal lateral geniculate nucleus. Exp Brain Res. 1990; 79(2):313–318. Available from: http://www.ncbi.nlm.nih.gov/pubmed/2323378. doi: 10.1007/BF00608240

78. Hirsch JA, Wang X, Sommer FT, Martinez LM. How inhibitory circuits in the thalamus serve vision. Annu Rev Neurosci. 2015 Jul; 38:309–329. doi: 10.1146/annurev-neuro-071013-014229 PMID: 26154979

79. Wang X, Vaingankar V, Sanchez CS, Sommer FT, Hirsch JA. Thalamic interneurons and relay cells use complementary synaptic mechanisms for visual processing. Nat Neurosci. 2011 Feb; 14(2):224–231. doi: 10.1038/nn.2707 PMID: 21170053

80. Jurgens CWD, Bell KA, McQuiston AR, Guido W. Optogenetic stimulation of the corticothalamic pathway affects relay cells and GABAergic neurons differently in the mouse visual thalamus. PLoS One. 2012; 7(9):e45717. doi: 10.1371/journal.pone.0045717 PMID: 23029198

81. Koch C, Reid C, H Z, S H, Hawrylycz A, Philips J, et al. Project Mindscope. In: Marcus G, Freeman J, editors. The Future of the Brain. Princeton University Press, Princeton; 2014. p. 25–39.

82. Markram H. The human brain project. Scientific American. 2012 Jun; 306(6):50–55. doi: 10.1038/scientificamerican0612-50 PMID: 22649994

ISBN: 978-82-575-1512-6
ISSN: 1894-6402

Norwegian University
of Life Sciences

Postboks 5003
NO-1432 Ås, Norway
+47 67 23 00 00
www.nmbu.no

98764 / ANDVORDGRAFISK.NO